Comportement des tunnels pressurisés en milieu urbain

Christian Noubissi Kountchou

To cite this version:

Christian Noubissi Kountchou. Comportement des tunnels pressurisés en milieu urbain. Géotechnique. Université Paris-Saclay, 2022. English. NNT : 2022UPAST150 . tel-04320138

HAL Id: tel-04320138
https://theses.hal.science/tel-04320138v1

Submitted on 4 Dec 2023

Pressurized tunnels behavior in an urban area

Comportement des tunnels pressurisés en milieu urbain

Thèse de doctorat de l'université Paris-Saclay

École doctorale n° 579, sciences mécaniques et énergétiques, matériaux et géosciences (SMEMAG)
Spécialité de doctorat: Génie Civil
Graduate School: Sciences de l'ingénierie et des systèmes
Référent: CentraleSupélec

Thèse préparée dans l'unité de recherche LMPS - Laboratoire de Mécanique Paris-Saclay (Université Paris-Saclay, CentraleSupélec, ENS Paris-Saclay, CNRS), 91190, Gif-sur-Yvette, France, sous la direction de **Guillaume Puel**, Professeur des universités, le co-encadrement de **Fernando Lopez-Caballero**, Professeur des universités et **Reza Taherzadeh**, Directeur technique.

Thèse soutenue à Paris-Saclay, le 02 Décembre 2022, par

Christian Noubissi Kountchou

Composition du jury

Membres du jury avec voix délibérative

Olivier DECK Professeur des universités, Ecole des Mines de Nancy	Président & Rapporteur
Fabrice EMERIAULT Professeur des universités, Université de Grenoble	Rapporteur
Emmanuel BOURGEOIS Maître de conférences, IFSTTAR	Examinateur
Filippo GATTI Maître de conférences, CentraleSupélec	Examinateur

Thèse de doctorat

NNT: 2022UPASAT150

ÉCOLE DOCTORALE
Sciences mécaniques et énergétiques, matériaux et géosciences (SMEMAG)

Title: Pressurized tunnels behavior in urban areas

Keywords: TBM, numerical simulation, soil heterogeneity, metamodel, building damage

Abstract: Nowadays, the use of pressurized tunnel boring machines in urban areas has enabled the possibility of limiting soil deformations due to tunnel constructions. However, due to the heterogeneous nature of the soils and the application of inappropriate pressures by the tunnel boring machine, irreversible scenarios (damage to the surrounding area) can occur. In order to avoid this, it appears essential to predict the ground displacements due to tunnel construction.

Analytical, empirical and numerical methods have been developed for the prediction of tunnel-induced settlement. Among these methods, numerical ones have proven their effectiveness with the three-dimensional (3D) approach. However, this approach has a major drawback which is its cost in computation time. To overcome this problem, the two-dimensional (2D) approach, which is a simplification of the three-dimensional approach, is often adopted. However, this approach requires the transformation of the pressures applied by the TBM into a fictitious pressure to be applied with the 2D approach. Concerning the consideration of soil heterogeneity in the numerical prediction, this latter requires a large number of 2D simulations and consequently a high cost in terms of calculation time, which limits the use of this expensive approach.

In this thesis, a numerical simulation methodology (two- and three-dimensional) with finite elements capable of predicting the response of soils to tunneling with a TBM by taking into account the heterogeneity of soils was proposed. To achieve this, a formulation allowing simplifying the pressures of the TBM into a 2D fictitious pressure has also been proposed in order to respect a defined settlement threshold and thus ensure the stability of the nearby structures. According to this formulation, the fictitious pressure is mainly related to the pressure around the shield and the grouting pressure to fill the gap between the mortar and the excavated soil.

During the construction of the tunnels, measurements of soil deformations are compared with the predictions and very often there is a discrepancy between the two settlement troughs. This phenomenon was observed on the extension of the Paris metro Line 12 where the tunnel was excavated in a stratified soil layer. This thesis also proposes a back-analysis methodology to find the adequate set of parameters with which it is possible to obtain the numerical settlement trough closest to the measurements.

Subsequently, a sensitivity analysis applied to the extension of the Parisian metro Line 12 was also conducted, which allowed studying the influence of the soil layers on the settlement trough.

Other 3D and 2D numerical simulations allowed to understand the influence of the excavation phenomenon on the soil response (settlement, stress evolution and strain evolution). A methodology that takes into account the heterogeneous nature of the soil was also proposed in order to study the influence of this character on the displacement of the soil and on the damage to the structures located in the vicinity of the tunnel. Finally, metamodels have been developed using a coupling between neural networks and clustering algorithms (k-means) on the one hand and the multi-fidelity approach on the other hand to predict the surface settlement trough and the level of damage to nearby buildings.

université
PARIS-SACLAY

ÉCOLE DOCTORALE
Sciences mécaniques et
énergétiques, matériaux
et géosciences (SMEMAG)

Titre: Comportement des tunnels préssurisés en milieu urbain

Mots clés: Tunnelier, modélisation numérique, hétérogénéité des sols, méta-modélisation, endomagement des avoisinants

Résumé: De nos jours, l'utilisation des tunneliers à front pressurisé en zones urbaines a permis de limiter les déformations dues à la construction de tunnels. Toutes fois à cause de la nature hétérogène parfois mal connue des sols ainsi que l'application des pressions souvent inappropriées par le tunnelier, des scénarios irréversibles (dégâts sur les avoisinants) peuvent se produire. Afin d'éviter cela, la prédiction des déplacements du sol engendrés par le creusement de tunnel est indispensable.

Des méthodes analytiques, empiriques et numériques ont été développées pour la prédiction des tassements dus au creusement de tunnel. Parmi ces méthodes, les méthodes numériques ont prouvé leur efficacité avec l'approche tridimensionnelle (3D). Cependant, cette approche présente un inconvénient majeur qui est son coût en temps de calcul. Pour pallier ce problème, l'approche bidimensionnelle (2D) qui est la simplification de l'approche tridimensionnelle est très souvent adoptée. Cette approche nécessite toutefois la transformation des pressions appliquées par le tunnelier en une pression fictive à appliquer en 2D. Concernant la prise en compte de l'hétérogénéité des sols dans la prédiction numérique, elle requiert un grand nombre de simulations 2D, ce qui limite l'utilisation de cette approche coûteuse en temps de calcul.

Dans cette thèse, une méthodologie de simulation numérique (bidimensionnelle et tridimensionnelle) aux éléments finis capable de prédire au mieux la réponse des sols au creusement de tunnel au tunnelier en prenant en compte l'hétérogénéité des sols a été proposée. Pour y parvenir, une formulation permettant de simplifier les pressions du tunnelier en une pression fictive 2D a également été proposée afin de respecter un seuil de tassement défini permettant ainsi d'assurer la stabilité des avoisinants. D'après cette formulation la pression fictive est principalement dépendante de la pression autour du bouclier et de la pression d'injection du coulis de remplissage du vide créée entre le mortier et le sol excavé.

Lors de la construction des tunnels, des mesures de déformations des sols sont comparées aux prédictions et très souvent, il existe un écart entre les deux cuvettes de tassement. Ce phénomène a été observé sur le prolongement de la ligne de métro 12 dans le nord de la ville de Paris où le tunnel a été creusé dans un sol stratifié. Cette thèse propose également une méthodologie d'analyse inverse permettant de retrouver le jeu de paramètres adéquat avec lequel il est possible d'obtenir la cuvette de tassement numérique la plus proche des mesures.

Par la suite, une analyse de sensibilité appliquée sur le prolongement de la ligne 12 du métro Parisien a également été menée ce qui a permis d'étudier l'influence des couches de sol sur la cuvette de tassement.

D'autres simulations numériques 3D et 2D ont permis de comprendre l'influence du phénomène de creusement sur la réponse du sol (tassement, évolution des contraintes, déformations). Une méthodologie de prise en compte de la nature hétérogène des sols (Figure 3) a été également proposée afin d'étudier l'influence de ce caractère sur le déplacement du sol et sur l'endommagement des structures situées au voisinage du tunnel (Figure 4). Enfin, des méta-modèles ont été développés à l'aide d'un couplage entre les réseaux de neurones et les algorithmes de clustering (k-means) d'une part et l'approche par multi-fidélité d'autre part pour prédire la cuvette de tassement en surface ainsi que le niveau d'endommagement des bâtiments.

Remerciemments

Qu'il me soit permis d'adresser mes sincères remerciements à toutes ces personnes qui ont œuvré d'une quelconque manière à l'accomplissement de ce travail de recherche.

Je tiens à exprimer ma profonde gratitude à Guillaume Puel, Fernando Lopez-Caballero et Reza Taherzadeh pour avoir accepté de diriger et d'encadrer cette thèse. J'ai eu la grâce d'être encadré par des personnes dotées d'une rigueur scientifique accrue, d'une grande capacité d'écoute et de nombreuses autres qualités humaines. Ils se sont fortement impliqués dans l'élaboration de ce travail par leur directives, leur remarques, leur suggestions et leur encouragements et ceci dans des moments difficiles de pandémie mondiale. Qu'ils trouvent en l'accomplissement de ce travail, le résultat de leur rigueur scientifique et de leur soutien inconditionnel.

Je remercie également d'une part M. Olivier Deck et M. Fabrice Emeriault pour avoir accepté de rapporter ce travail et d'autre part M. Emmanuel Bourgeois et M. Filippo Gati d'avoir accepté de l'examiner.

Je tiens également à remercier mes collègues du Laboratoire LMPS avec qui nous avions passé de très bons moments. Je pense ainsi à Christina Khalil, Michail Korres, Amar Al Yaman, Valeria Soto, Ramon Alcala, Yilun Li, Martin Colvez, et tous les autres.

Mes sincères remerciements vont également à l'endroit de mes collègues de TRACTEBEL pour ces trois ans pensées ensemble. Merci à Samy Mahdi, Sami Khodr, Xuan-Son Ngeyen, Natalia Katsaiti et Elio EL Kahi pour leur apport inconditionnel dans l'accomplissement de ce travail.

Je tiens en fin à remercier ma famille et plus particulière ma très chère et tendre épouse pour son soutien et ses encouragements sans faille à qui je dédie ce travail de thèse.

General introduction

The world is increasingly an urban environment. Since 2008 more than half of the world population lives in cities. As the world's rural population is projected to remain stable in this period, that increase will occur in urban areas (Division, 2019; Until, 2013). The increase in population and consequently the congestion in urban areas, has led to a consensus among governments and politicians to improve transportation systems and reduce greenhouse gas emissions. Public transportation in general and underground transportation systems as tunnels in particular, are crucial in addressing climate change and play an important role in reducing traffic jams, pollution and noise, lack of space and preservation of heritage and environment and protection against natural disasters(Broere, 2016).

The introduction of the tunnel boring machine (TBM) in 1857 by Charles Wilson mitigated the risks associated with the use of conventional methods by better controlling the ground deformations. In urban areas, soil deformations i.e. settlements due to excavation can have serious consequences on the buildings and the infrastructures located in the vicinity of the tunnel. Hence the need for an adequate prediction in order to anticipate these effects or if possible to avoid them. Three methods exist for the prediction of TBM-induced settlement:

- Empirical methods: these methods are based on feedback from past projects. In their work, O'Reilly and New (1982), Guglielmetti et al. (2008) and, Mair et al. (1993) showed that the settlement trough shape recorded during tunneling depends on the type of soil (sand or clay). However, certain factors limit the use of these methods; uncertainties on the nature of the soil and, the inability to take into account the pressures applied by the TBM in the case of mechanized excavation.

- Analytical methods: these methods are based on some simplifications and strong assumptions as explained by Peck (1969), Sagaseta (1987), and Verruijt (1997) which are rarely observed in real situations and even less in urban areas. For example, the settlement trough is assumed to be a symmetrical curve which is not the case in reality. Like the empirical methods, the analytical does not take into account the TBM pressures.

- Finally, the numerical methods: these methods appear to be the most realistic today with the three-dimensional (3D) method. The advantage of this method lies in the fact that it is able to represent the real phenomena that occur when excavating with a TBM. This method also considers the TBM pressures.

Despite the ability of the 3D numerical method to consider the complex phenomena that occur during the tunnel excavation, this approach has one drawback: it is time-consuming. To overcome this limitation, the bi-dimensional (2D) method is generally used. According to Panet and Guenot (1983), Rowe and Kack (1983) and Addenbrooke and Potts (2001) several methods exist to conduct a 2D simulation. The convergence confinement method, the stiffness reduction method, the disk calculation method, the gap volume and the loss method can be listed. Karakus (2007) compared these methods and concluded that the best one to simulate the TBM-induced surface settlement is the convergence confinement method with the explicit approach. This approach requires the transformation of the TBM pressures applied by the machine to excavate the soil into a 2D fictitious pressure.

Predicting TBM-induced soil displacement mainly depends on the boundary conditions, the lack of knowledge of the soil behavior and the constitutive model used to simulate this behavior. According to Gilleron and Bourgeois (2018), among the constitutive models implemented in the current finite element (FE) software, the nonlinear elastoplastic Hardening Soil Model (HSM) is commonly used. However, the settlement trough from the numerical simulations is generally larger than the observations although the maximum settlement can be well fitted. Several works on existing constitutive models and the development of new constitutive models to improve the shape of the settlement curve resulting from the FE simulation are constantly increasing (Gilleron and Bourgeois, 2018). These constitutive models require some simplified parameters whose calibration is done on the results of laboratory tests. However, these tests are not always available because of their cost. To overcome this limitation, correlations are generally adopted between the $in-situ$ tests and the parameters of the constitutive model. The latter does not all have the same influence on the settlement. For this reason, it is important to determine the most influential parameters and concentrate on them during the project design, namely in risk evaluation.

Even if the soils in nature are heterogeneous, in practice they are modeled as homogeneous stratified layers and the parameters are determined in a judicious way, sometimes with uncertainties. The determination of the influence of the parameters requires a large number of numerical simulations which makes the process costly and time-consuming. Thanks to models built with the Machine Learning approach (meta-models), it is possible to consider a large number of simulations to study the soil response to Tunnel construction in a very short time (Suwansawat and Einstein, 2006; Gao et al., 2019; Ghiasi and Koushki, 2020; Mahmoodzadeh et al., 2021; Zhang et al., 2021a).

This thesis aims at achieving the following objectives:

- Adopting the advanced version of the HSM known as the Hardening Soil with Small Strain

Model in order to improve the settlement shape and amplitude of the FE results.

- Proposing a formulation to obtain the 2D fictitious pressures from the TBM pressures.
- Developing a meta-model for the determination of the surface settlement trough created by TBM tunneling.
- Studying the influence of the spatial variability of soils on the TBM-induced soil displacement and building damage.

This thesis is organized into 5 chapters. The first chapter recalls the existing works related to tunneling, the phenomena that occur during the excavation process, and the existing methods that allow the prediction of the soil response. Then, several works developed on the consideration of uncertainties and the explicit modeling of the heterogeneous nature of soils are presented. Finally, the chapter briefly presents some artificial intelligence techniques for meta-models construction.

The second chapter describes the process of tunneling with a TBM. This chapter explains the 3D and the 2D model procedures and proposes a formulation to determine the fictitious pressure knowing the real pressures applied by the TBM. The soil behavior is simulated with the Hardening Soil with Small Strain Model (HSSM). The application is based on Line 16 of the Grand Paris Express project in France.

In the third chapter, 3D and 2D FE simulations are firstly conducted with the homogeneous stratified soil layer to predict the TBM-induced surface settlement on the Paris Metro Line 12 extension. The 2D FE simulation is used to apply back analysis to determine the set of parameters that offer good agreements with the field measurement and sensitivity analysis to determine the most influential parameters. The 3D FE simulation is conducted to study the longitudinal settlement curve evolution and the stress field is compared to 2D one. Then, due to the heterogeneity character of the soil, spatially variable models are used in addition to 2D FE simulation to study the heterogeneity effect of soils on TBM-induced surface settlement.

Chapter 4 develops meta-model based on coupling the Artificial Neurel Network (ANN) and the K-means algorithm to predict the TBM-induced surface settlement. Two approaches are used in this analysis to consider soil behaviour. The soil is firstly considered as a homogeneous and stratified profile and secondly, the spatial variability models are adopted to account for the heterogeneity of soil. In this two approaches, the training data are generated with 2D FE simulations.

As the soil displacement may cause risk to the building in the vicinity of the tunnel, chapter 5 finally studies the effect of the TBM pressure and the building location on the TBM-induced building damage. The 2D FE simulations are used to predict the building damage. After that, the Multi-fidelity approach is applied in order to enhance the 2D FE result to better predict the damage level.

Contents

List of Tables

List of Figures

Chapter 1

General background on tunneling

Contents

1.1 Introduction

In congested and old cities, there is a need for better utilization of the underground space especially with the strong demand for new infrastructures due to the population increase. The current situation of urban areas has reached such a level that the best use of the underground urban areas has to be made. Within years, there has been an increasing number of the underground public transport infrastructures. In urban areas, tunnels are mostly located at low depths and in soft soil. During the excavation, the safety of the buildings located in the vicinity of the tunnel has to be guaranteed. Excavating in hard rocks seems to be well controlled by the tunnel engineers. On the other hand, tunnel constructed in soft soil are more difficult to be managed. To overcome this limitation, tunnel boring machines (TBM) are generally adopted.

There has been considerable development in tunnel construction in the past 200 years, especially since Marc Brunel used a tunneling shield to construct the tunnel under the River Thames in London in 1825 (Chapman et al., 2017). The introduction of mechanized tunnel excavation with the use of TBM in 1857 by Charles Wilson mitigated the dangers associated with traditional excavations methods that used explosives and other machines and improved construction efficiency by automatizing soil removal and lining support installation (Hemphill, 2012). However tunneling remains a challenge even today, as it is quite difficult to control and predict tunnel deformations, especially when excavating in unstable conditions involving soft soils with multiple layers at low depth. Moreover, the deformations caused by tunnel construction with a TBM depend in part on the type of TBM used.

In this chapter, The different types of TBMs and the selection criteria for each type is discussed. Subsequently, the influence of the TBM components on the longitudinal settlement curve is also presented. In order to anticipate the deformations and take corrective measures, some methods to predict the settlement curve caused by the tunnel construction are explained.

According to its natural formation, soils are heterogeneous in nature. This soil characteristic implies an uncertainty on its parameters. Taking into account these uncertainties in the prediction of soil response requires a large number of models. By using numerical methods, this requires a large number of simulations and consequently it is time consuming. In order to overcome this problem of computational cost, meta models are generally developed. In this chapter, Some meta model techniques are also presented in tunneling applications.

1.2 TBM classification and choice

TBMs exist in many different diameters, ranging from microtunnel boring machines with diameters smaller than 1 m to machines for large tunnels, whose diameters are greater than 15 m (Chapman et al., 2017). TBMs are available for many different geological conditions. TBM can be classified according to the support provided at the excavated face. Depending on the soil condition, different types of TBM can be identified (Founta, 2018). Figure 1.1 represents the types of TBM according to the nature of soil.

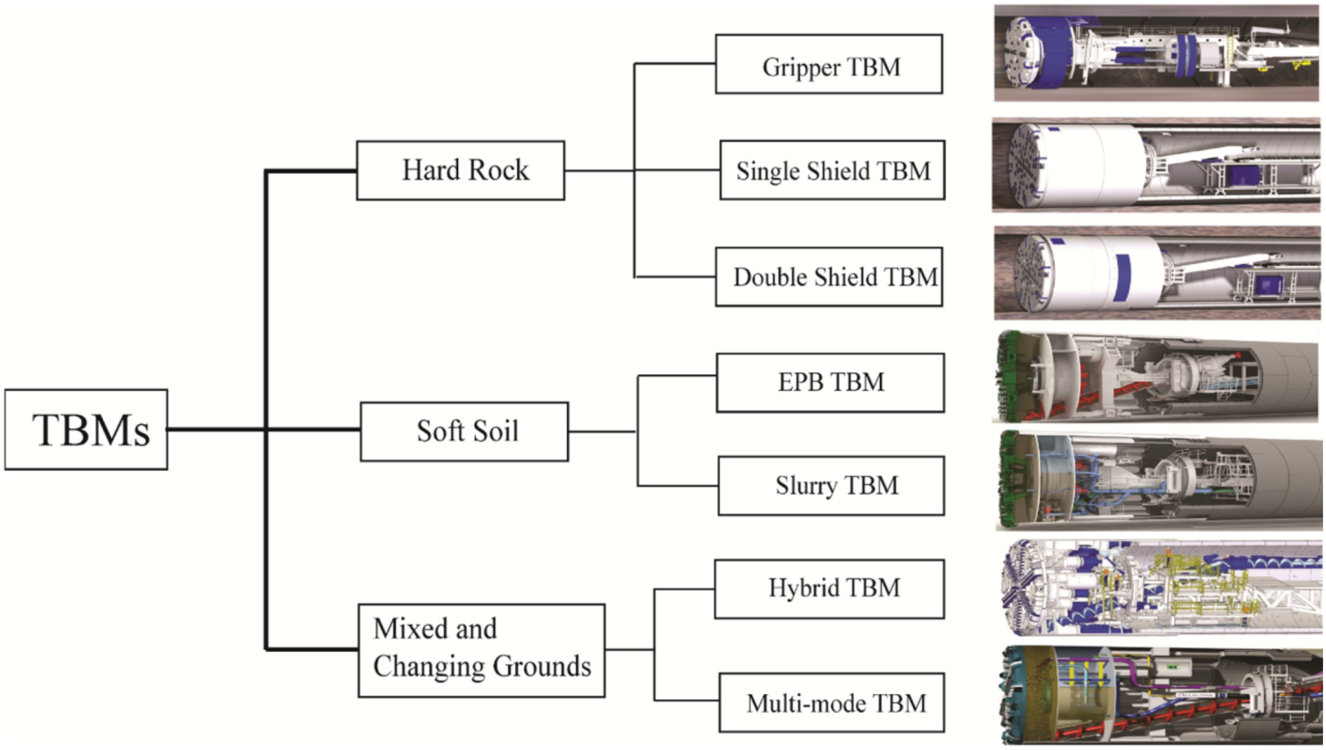

Figure 1.1: Classification of TBM from (Zheng et al., 2016)

- TBMs in hard rock
  There are various mechanized full face tunneling techniques for hard rock and these depend on the quality of the ground. The final decision on the type of the machine to be used in hard rock depends on the expected quantity of water ingress (Chapman et al., 2017). Gripper TBM can be used in stable condition with low water ingress. Single shield TBM can be used in unstable conditions where there is a risk of ground collapse. Double shield TBM combines the ideas of the gripper and the single-shield techniques and can be applied to a variety of geological conditions.

- TBMs in soft soil
  In soft soil where the tunnel head requirement is generally low, different types of TBM based on the face support system are used. Slurry Pressure Balanced (SPB) TBMs use a pressurised fluid to stabilise the face during excavation of the ground. There are two systems to maintain a balanced face pressure. One simply uses the fluid in the pressurized chamber behind the cutter head and the other one uses an air bubble system. The slurry has three functions; firstly, it helps stabilize the face; secondly, it penetrates the face to form a 'filter cake' that reduces the hydraulic conductivity of the ground and permits to reduce water ingress and thirdly, it mixes with the excavated material to allow it to be transported out of the machine more easily. This type of TBM is more suitable for coarse grained-soil where the permeability is high. Earth Pressure Balance (EPB) TBM uses the excavated material to support the tunnel face during the excavation. The ideal material for the EPB TBM is the cohesive soil with stiff consistency (consistency index between 0.5-0.75). Moreover the pressure applied in the excavation chamber is limited to 5 bar. EPB technology has made significant progress over the past couple of decades. This is the particularly in the area of ground conditioning which has enabled the EPB machines to be used in coarser-grained materials. Making a choice between the SPB and the EPB TBM is critical and does not only include the ground conditions. The experience of contractors, the logistics and configuration of the works, and the requirements to meet the client specifications also play a factor in the choice (Chapman et al., 2017). In some project, it is economical that the tunnel is excavated with one TBM. However, the geotechnical context is heterogeneous making difficult the use one type of TBM. For this reason, a multi-mode machine is recently developed.

- Mixed and changing grounds
  In order to overcome the problem of excavating with the different ground conditions without a limitation on the confinement pressure, the Hybrid and multi-mode TBMs have been developped. This TBM is able to switch from one mode to another within a short time.

Despite the difference in the operation system of the TBMs, they are all constituted by almost the same equipment. Figure 1.2 and figure 1.3 present respectively the longitudinal section of the EPB and the SPB TBMs.

1.3 Soil disturbance by tunnel excavation

Tunnel excavation modifies the internal equilibrium of the soil. Depending on the intensity of the disturbance, soil movement generally occurs in the 3 directions. This section focuses on soil settlement. Excavating with TBMs requires the application of pressures by the machine. The face pressure applied in the excavation chamber and the grouting pressure to fill the mortar between

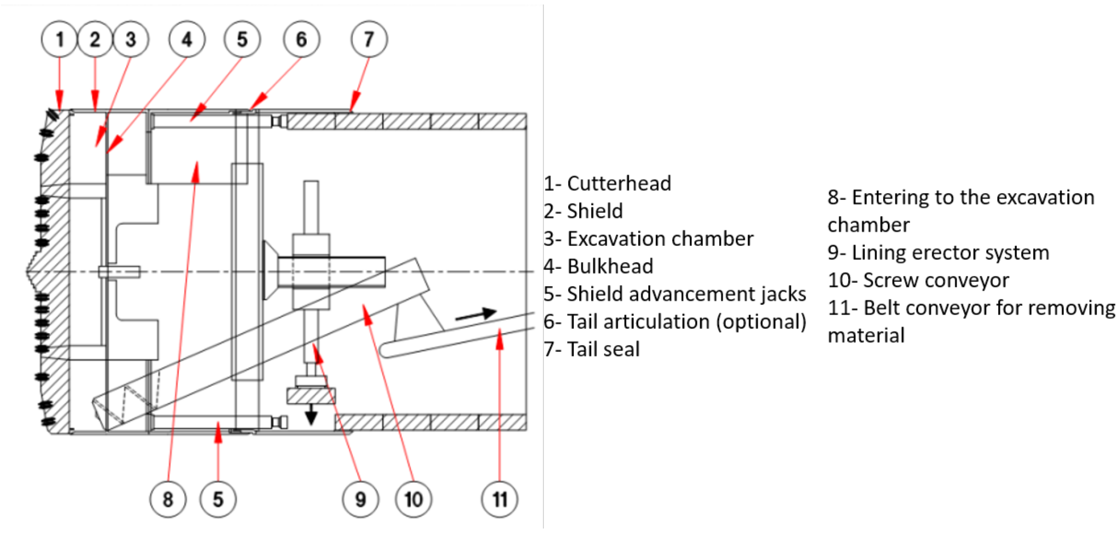

Figure 1.2: Longitudinal section through an EPB TBM after (Grasso and Pelizza, 1994)

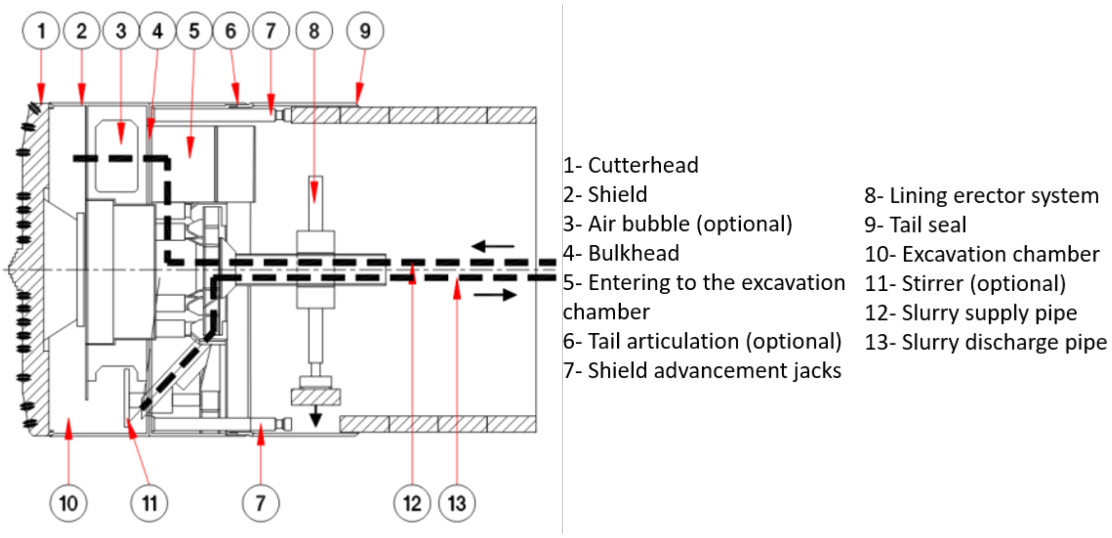

Figure 1.3: Longitudinal section through an SPB TBM (Grasso and Pelizza, 1994)

the linings and the surrounding soil constitute the main pressures. Sometimes, pressure along the shield can be applied if the TBM encountered deformable cohessionless soil. If the pressures are higher than the total stress, soil uplift can occur. On the other hand, if the applied pressures are low, settlement may arise on the ground surface.

In the case of settlement, in general, ground movements result in the soil stresses modification around the excavated soil and, also from the over-excavation of the tunnel structure which is known as ground loss. Lunardi and Bindi (2004) illustrated the three components of the deformation response: the preconvergence that takes place behind the front of the TBM inside the soil, the extrusion that takes place at the TBM front and the convergence that happens due to the conicity of the shield. Mair and Taylor (1999), Loganathan (2011), and Hashimoto et al. (2002) summarized the causes of ground movements due to tunneling process by tunneling boring machines. The final settlement trough is an addition of different factors that can be summarized in 4 groups as represented on figure 1.4

- Instantaneous deformation at the front; this is a consequence of preconvergence and the extrusion of the tunnel face: its amplitude essentially depends on the value of the face pressure.
- Deformation along the shield; the displacement along the shield is generally caused by the convergence of the soil due to the shield conicity: the shield conicity prevents the machine from direct contact with the surrounding soil, accordingly the development of shear stresses.
- Deformation at the shield tail: filling the gap between the linings and the surrounding soil with mortar limits the soil displacement. But if the gap is not well filled, it can be a source of displacement.
- Long-term displacement: this secondary displacement depends on the nature of soil. In cohesive soil, the final value of the displacement can be due to consolidation (Soga et al., 2017). In coarse-grain soils, this aspect does not occur.

The contraction of the lining that happens could be another source of displacement. But it was shown by Metwally (2016) that this settlement is too small compared to the other sources and depends mainly on the design and rigidity of the tunnel lining.

Chapman et al. (2017) classified the tunnel into two main categories according to the ratio between the tunnel cover (C) depth and the tunnel diameter (D). The tunnel is shallow when $C < 2D$, and deep when $C > 3D$. The soil behavior during the excavation process differs from shallow to deep tunnels. The excavation process can create a softening zone in the crown area, which for shallow tunnels in soft ground reaches the ground surface. As a result, no arching can develop over the crown. The ground in this area has no bearing capacity and acts only as a load on the tunnel lining. For the unsupported area, an angle of 90° is assumed at the tunnel crown as shown on figure 1.5. For deep tunnel, the ground is able to form an arch and transfer loads on both sides of the tunnel. In the range $2D < C < 3D$, the ground above the tunnel crown either act as a support or not depend upon the geological conditions.

Hashimoto et al. (2002) summarized the results of some case studies of TBM excavation in soil near the surface. The conclusion of this study is presented in figure 1.6, illustrating the mechanism of soil displacement. Due to the continuously development in TBM design, the deformation in front of the cutting face δ_1 can be restrained to a very small quantity by a good control of the earth balance at the cutting face. The deformation δ_2 is caused by the over-cut during the passage of the shield. This deformation can be small if the advancement of the TBM is well controlled.

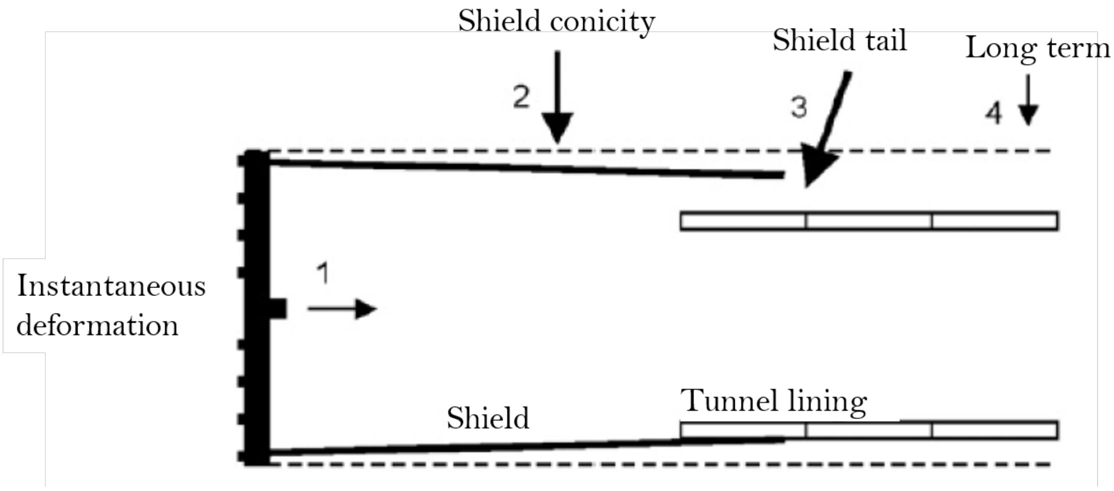

Figure 1.4: Different factors responsible of the soil displacement due to TBM excavation (Mair and Taylor, 1999)

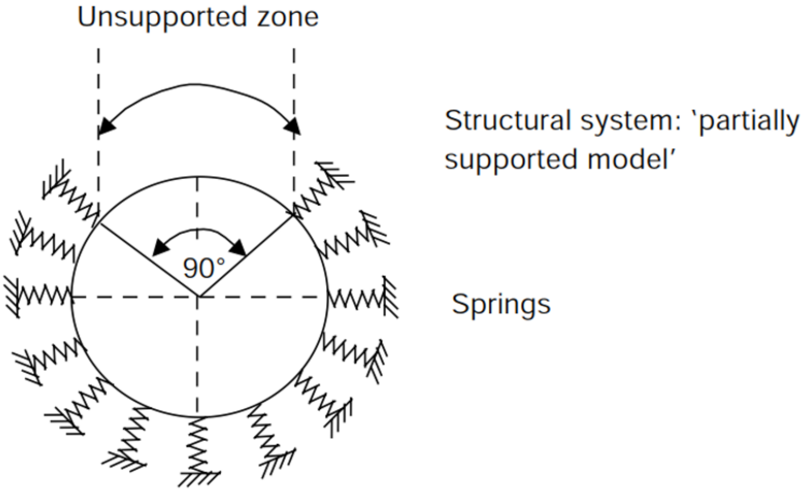

Figure 1.5: Representation of the non supported zone with the spring model for shallow tunnel from Chapman et al. (2017)

The deformation due to the tail void δ_3 can also be reduced to a very small value by simultaneous back-fill grouting. The overall deformation caused by the stress release is the sum of δ_1, δ_2, and δ_3. δ_4 could be produced due to consolidation procedure in cohesive soils.

In urban areas, it is critical to identify the sources of the ground movement and to control them by measurements. Different technologies are adopted to mitigate the response of the adjacent structures and facilities. The prediction of the damages by the soil movements due to tunneling is the main factor in the design and choice of tunnels constructions methods (Bernat, 1996; Metwally, 2016). According to Guglielmetti et al. (2008); Vahdatirad et al. (2010); Janin (2012); Marto et al.

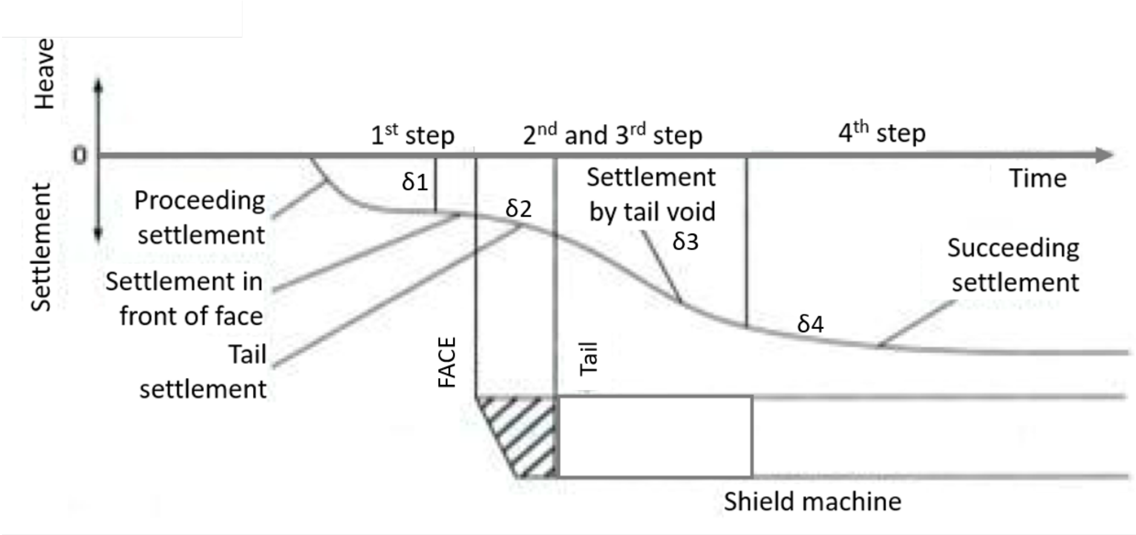

Figure 1.6: Mechanism of the deformation due to TBM (Hashimoto et al., 2002)

(2015); Zheng et al. (2017), an essential part of a tunnel project design is also the prediction of the ground movements and the assessment of the impacts on the nearest structures and infrastructures, especially for shallow tunnels.

1.4 Prediction methods

Some researchers worked on the prediction of the settlement caused the tunnel construction. Among others, Grasso and Pelizza (1994) and Vlachopoulos and Diederichs (2009) studied the prediction of the longitudinal settlement profile due to tunneling and they concluded on a relationship between the settlement profile, the distance to the tunnel face and, the tunnel cover. Predicting the longitudinal profile of the settlement trough is not enough. Another factor appears more critical i.e. the width of the settlement trough. Traditional methods of predicting surface settlement have historically been based on the cross-section settlement trough (Janin, 2012). The ground displacement problems have been studied using three different approaches, i.e., analytical, empirical, and numerical modeling (see the works of Lee et al. (1999), Founta (2018) and, Loganathan (2011)).

1.4.1 Empirical approach

To better predict the ground displacement due to tunneling, it is important to understand the tunneling-induced settlements in a greenfield configuration as mentioned by Guglielmetti et al. (2008). The problem of tunnel-induced settlements has interested many researchers in the last 40 years and many notable review papers have been published (among others, Peck (1969),Cording et al. (1976), Mair and Taylor (1999), Attewell et al. (1986), Norgrove and Attewell (1984), Rankin (1988),Leca and New (2007) can be listed). The settlement evolves from the tunnel crown to the surface. In this sense, the surface settlement and the subsurface settlement can be distinguished.

1.4.1.1 Surface settlements

The well-established empirical methods are used primarily to estimate surface settlements in soft ground. The one used most commonly was proposed by Peck (1969). Peck found that based on a number of field measurements, the surface settlement trough could be well represented by a Gaussian distribution curve as shown in equation 3.2.1 where s represents the surface settlement at a distance of x from the tunnel axis, s_{max} represents the maximum settlement at the axis and i the inflection point.

$$s = s_{max}\exp(\frac{-x^2}{2i^2}) \tag{1.4.1}$$

$$s = s_{max}\exp\left(-0.334(\frac{|x|}{i})^{3/2}\right) \tag{1.4.2}$$

$$s = \frac{s_{max}}{1+(\frac{|x|}{a})^b} \tag{1.4.3}$$

$$s = \frac{ns_{max}}{n-1+\exp\left(a\frac{x^2}{i^2}\right)} \tag{1.4.4}$$

Following the work of Peck, several researchers Celestino et al. (2000); jacobsz (2003); Vorster et al. (2005) suggested different curves for different soil types to better fit the empirical ground surface prediction to the real case studies. In equation 1.4.2 Jacobsz proposed a new equation to predict the surface settlement trough. The modified gaussian model in equation 1.4.4 was developed to cover the lack of fit in gaussian curve for the results of soil settlements in some centrifuge experiments conducted by Vorster et al. (2005). The parameter n in modified gaussian is the shape function parameter controlling the width of the profile and a is a parameter to ensure that i remains the distance of the inflection point. The modified gaussian curve becomes the gaussian curve when the shape function n is equal to 0.5. The yield density in equation 1.4.3 was developed to better predict the ground distortion since the gaussian curves tend to predict lower ground distortions than the measurements (Celestino et al., 2000). The ground distortion is a parameter used to predict the building damage due to settlement (Celestino et al., 2000). In the yield density method, the parameter a strongly influences the settlement width, whereas b influences the shape of the curve and this latter was found to vary in the ranges 2-3 for soft clay, and 2-2.8 for stiff clay.

The difficulty of these methods lies in the determination of the two main factors of the formulation i.e the maximum settlement and the volume loss. The maximum settlement can be

Table 1.1: Matrix approach for assessing the volume loss in non conventional media for TBM tunneling Guglielmetti et al. (2008).

Overburden condition	Geological condition of the tunnel face			
	1) Soil like material	2) Mixed condition (soil and rock mass)	3) Faults and/or weathered bands	4) Discontinuous rock mass and weak rock
Soil like material	$c = 0, V_L = 1\%$	$c = 0, V_L = 1.2\%$	$c = 0, V_L = 1\%$	$c = 0, V_L = 0.8\%$
	$c > 0, V_L = 0.8\%$	$c > 0, V_L = 1\%$	$c > 0, V_L = 0.8\%$	$c > 0, V_L = 0.5\%$
Mixed condition	$V_L = 0.5 - 0.7\%$	$V_L = 0.6 - 0.8\%$	$V_L = 0.5 - 0.8\%$	$V_L < 0.5\%$
Weathered band/faults	$V_L = 0.4 - 0.8\%$	$V_L = 0.5 - 0.9\%$	$V_L = 0.6 - 1.2\%$	$V_L = 0.4 - 0.9\%$
Discontinuous and weak rock	$V_L = 0.3 - 0.5\%$	$V_L = 0.4 - 0.6\%$	$V_L < 0.4\%$	$V_L < 0.2\%$

Table 1.2: Empirical formulas to predict the inflection point.

Authors	Soil types	Formulas
Attewell (1977)	cohesive soil	$i = 0.5z_0$
Atkinson and Potts (1979)	loose sand	$i = 0.25(c + d)$
	dense sand and over consolidated clay	$i = 0.25(1.5c + d)$
Clough and Schmidt (1981)	cohesive soil	$i = 0.5z_0^{0.8}D^{0.2}$
O'Reilly and New (1983)	granular soil	$i = 0.25z_0$ or $0.28z_0 - 0.1$
	cohesive soil	$i = 0.5h$ or $0.43h + 1.1$
Mair et al. (1993)	cohesive soil	$i = 0.175z_0 + 0.325\frac{z}{z_0}$

estimated using equation 1.4.5 as proposed by Mair et al. (1993). V_L represents the ratio between the volume loss and the tunnel volume per linear meter and D is the tunnel diameter.

$$s_{max} = \frac{0.313V_L D^2}{i} \tag{1.4.5}$$

Guglielmetti et al. (2008) summarized in Table 1.1 the results of different works that used the geological conditions at the tunnel face, with respect to the overburden conditions to assess the volume loss. In this table, c is the soil cohesion.

Some authors proposed some formulations to determine the inflection point. The tunnel cover (c), the tunnel diameter (d) and the depth of the tunnel (h) are the input parameters as presented in table 1.2.

1.4.1.2 Subsurface settlements

A few empirical methods are available to predict subsurface settlement profiles (Loganathan, 2011; O'Reilly and New, 1983). The two most widely used are those proposed by Mair et al. (1993) and Atkinson and Potts (1979).

Mair et al. (1993) proved that the shapes of subsurface settlement profiles developed during tunnel construction are characterized by a Gaussian distribution in the same manner as for surface settlement profiles. They proposed in figure 1.7 an adaptation of the Peck formulation for the subsurface settlement and in equation 1.4.6 the related formulation.

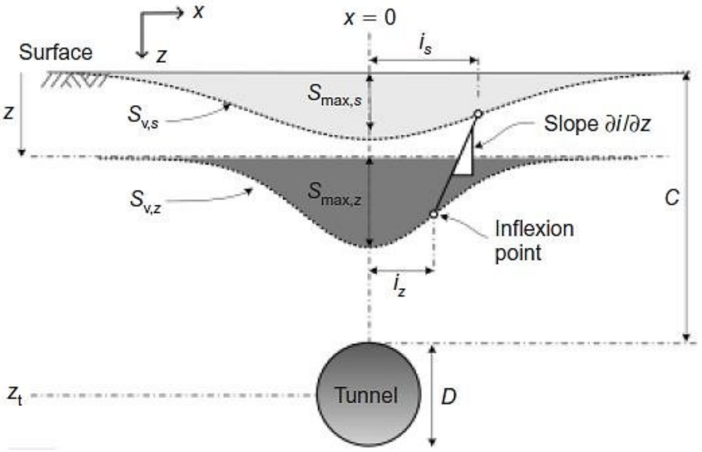

Figure 1.7: The surface and the subsurface representation of the settlement trough (Mair et al., 1993)

$$s = s_{max,z} \exp(\frac{-x^2}{2i_z^2}) \tag{1.4.6}$$

where $i_z = k(z_0 - z)$ and $k = \frac{0.175+0.325(1-\frac{-x^2}{2i_z})}{1-\frac{z}{z_0}}$. Atkinson and Potts (1979) proposed the equation 1.4.7 to estimate subsurface settlement for shallow tunnels based on experimental model tests:

$$\frac{s_z}{s_{max,z}} = 1.0 - \alpha\frac{z-R}{2R} \tag{1.4.7}$$

where
$\alpha = 0.57$ for dense sand
$\alpha = 0.40$ for loose sand
$\alpha = 0.13$ for over-consolidated clays
S_z = settlements at depth z
$S_{z,max}$ = maximum settlement at depth z.
Norgrove and PB (1979) and Leblais et al. (1995) were interested in the determination of the lateral deflection of the soil. Their conclusions are presented in figure 1.8 and in the equation 1.4.8.

$$s_x = \frac{x}{z_0} s_z \tag{1.4.8}$$

where

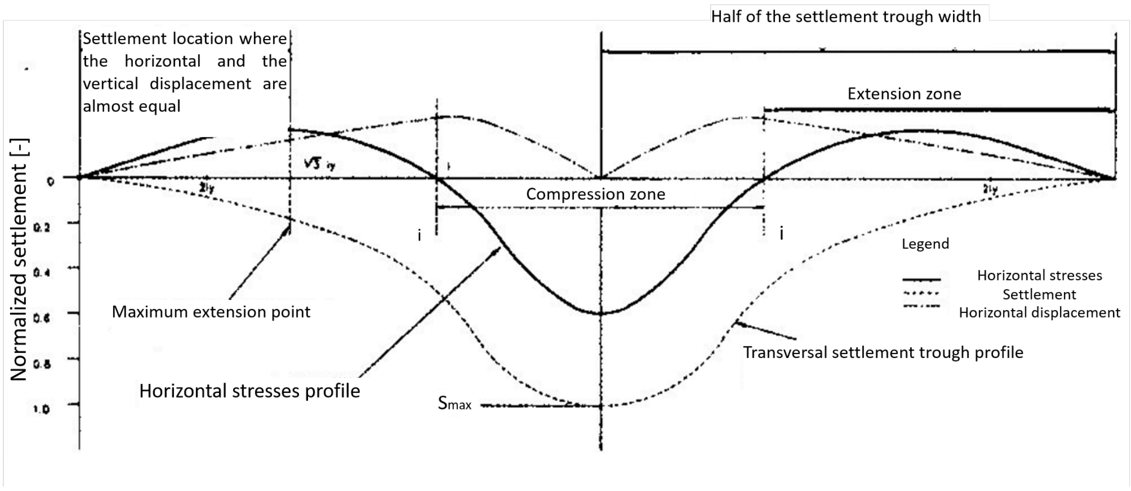

Figure 1.8: Horizontal and vertical displacement relationships due to tunnel excavation (Leblais et al., 1995)

s_x = lateral deflection
s_z = settlement at depth z
x = lateral distance from the tunnel axis
z_0 = Tunnel depth.

These empirical methods do not give highly accurate results as they are subjected primarily to some important limitations:

- The construction techniques are not taken into account
- The ground conditions are not included in the formulations
- The formulations do not consider the TBM pressures
- The limited relationships to predict the horizontal and the subsurface displacement

1.4.2 Analytical approach

1.4.2.1 Analytical approach for deep tunneling

Some analytical formulations are provided in the literature to predict the tunneling-induced soil movement. In most of the cases, the authors are interested in the study of the modification of the stress field generated by the tunnel excavation as presented in figure.1.9. However, some formulations have also been proposed for the evaluation of the soil displacements in the soil mass. They rely on the general principles of mechanics as well as on strong hypotheses concerning the geometry (circular with horizontal axis at great depth), the stratigraphy (a single homogeneous layer), the constitutive law (Tresca) and the initial stress state (non-weighted and isotropic).These methods are only valid for deep tunnel excavated in soils or rocks that fulfilled the previous hypotheses. Equation 1.4.9 with $p = \sigma'_v = \sigma'_h$ (respectively the vertical and the horizontal effectif stress) represents the radial displacement and the relative volume loss of the medium.

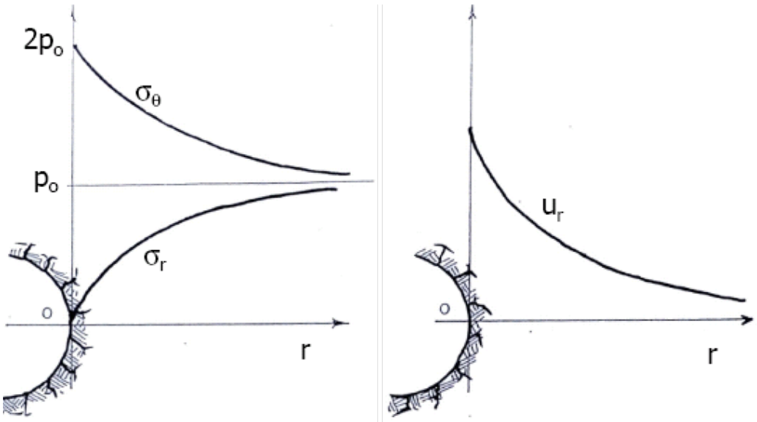

Figure 1.9: Stresses and radial displacement evolution with respect to the distance (r) from the tunnel (Janin, 2012)

$$\begin{aligned} U(r) &= -\frac{1+\nu}{E} p \frac{R^2}{r} \\ V_t &= 2\frac{1+\nu}{E} p \pi R^2 \end{aligned} \tag{1.4.9}$$

Other authors like Peck (1969), Sagaseta (1987), O'Reilly and New (1983) and Verruijt (1997) have proposed for shallow tunnel, elastic solutions to assess the settlement and the horizontal displacement . Poulos (1974) and Berry (1977) were interested in the case of an anisoptropic medium. Some studies on the behavior of tunnels in an elasto-plastic medium were also conducted by González and Sagaseta (2001), Panet (1973), Panet (1976), and Detournay and Fairhurst (1987). Franza and Marshall (2019) summarized the literature review for a better explanation concerning this issue. As a conclusion, the tunnel excavation can create two zones; the plastic and the elastic zones. The plastic zone if it exists, surrounds the excavation area.

1.4.2.2 Convergence-confinement method

The convergence-confinement method is an analytical method which is generally adopted to simplify the three-dimensional problem of the conventional tunnel excavation into a two-dimensional plane deformation problem of the ground-support interaction (Panet et al., 2001; Vlachopoulos and Diederichs, 2009). It is commonly introduced in 2D numerical calculations of tunnel excavation projects in order to estimate the deformations of the soil and to validate the support

(Karakus, 2007; Do et al., 2014; De La Fuente et al., 2019).

The convergence-confinement method which accounts for the 3D effects by replacing the ground to be excavated by a fictitious pressure is the one that has been widely used among the available equivalent approaches. The radial stress, σ_r, acting on the tunnel periphery is given as follows:

$$\begin{aligned} \sigma_r &= (1-\lambda)\sigma_0 \\ \lambda &= \frac{U_r^x}{U_r^{\text{inf}}} \\ U_r^{\text{inf}} &= \frac{1+\nu_s}{E_s}\sigma_0 r \end{aligned} \tag{1.4.10}$$

where λ is the stress relaxation coefficient also known as the confinement loss; σ_0 is the initial radial stress; U_r^x is the radial component of displacement at a distance x behind the face; U_r^{inf} is the radial component of displacement at a distance behind the face considered as infinite;E_s and ν_s are respectively the elastic modulus and Poisson's ratio of the ground; r is the tunnel radius. In the case of an unsupported tunnel, the confinement loss varies from 0, for a section far ahead of the front, to 1 for a section far behind. By considering a section between the two mentioned above, the problem becomes three-dimensional since the influence of the front has to be considered. In this case, the choice of the confinement loss, which is directly related to the distance of the section to the front, constitutes the main difficulty of the method. Many authors have been interested in the formulation of the radial displacement in an elastoplastic medium. Panet and Guenot (1983) related the confinement loss, and the displacement, to the value of the plastic radius. Corbetta et al. (1991) proposed a principle of similarity in order to determine the function U_r^x from the corresponding elasticity curve. Carranza-Torres and Fairhurst (2000) provided an exponential formulation of the radial displacement in the case of a massive with Hoek-Brown failure criterion.

Figure 1.10 shows the main characteristics of the convergence-confinement method. The convergence curve corresponds to the internal pressure versus the tunnel radial displacement. The tunnel radial displacement increases as the internal pressure decreases. The tunnel can be self-stabilized without a liner (curve a) or the surrounding ground can fail which leads to an increase in the ground load acting on the tunnel lining (curve b).

Tunnel construction is a more complex operation than it seems to be. The ground deformation should account for the effects of a number of parameters. These parameters include:

- The construction method and the tunnel driving details
- Tunnel depth and diameter
- Ground water condition
- The initial stress state

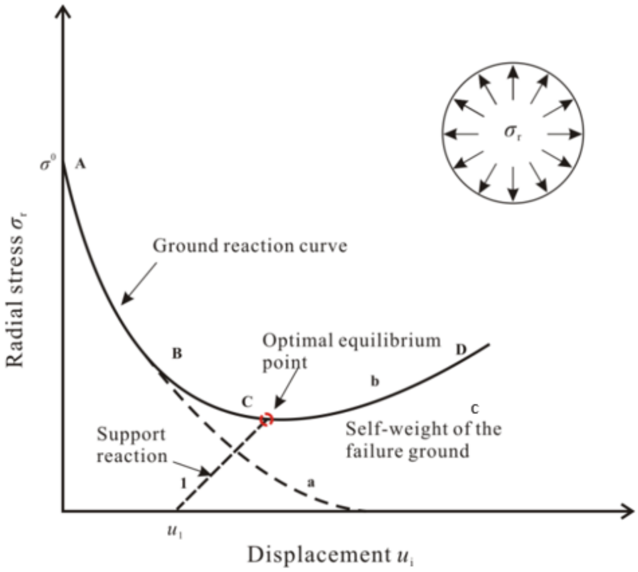

Figure 1.10: Ground reaction curve of a tunnel and reaction line of the support (Panet et al., 2001; De La Fuente et al., 2019)

- The stress-strain-strength behavior of the soil around the tunnel excavation

For these reasons, the adoption of analytical methods to predict the soil response to tunnel excavation is not recommended in urban areas where the isotropic configuration can not be assumed.

1.4.3 Numerical simulation

Some limitations of empirical and analytical methods may lead to the application of numerical methods. Numerical simulations have been widely used for tunneling analyses. There are several types of numerical approaches among which the finite element method, the differential elements method, and the distinct elements method can be listed. This section focuses on the finite element method (FE).

Rowe and Kack (1983) found in their analyses of some cases that, the FE techniques generally give good estimates of soil settlements as compared with the measurements. Successful predictions of the lateral soil movements by the FE method were also reported by Lee et al. (1992). Gunn (1993) found that the surface settlement trough was too wide compared to the field measurements. Simpson and Jovicis (1993) concluded from their analyses of excavation in London clay that the predicted surface settlement trough was substantially influenced by the anisotropic shear modulus, and that it was little influenced by non-linearity of ground stiffness. Addenbrooke and Puzrin (1997) reported that better predictions could be achieved by using sophisticated soil models that accounted for nonlinear soil behavior at small strain. To succeed a numerical simulation some key aspects have to be considered with great seriousness:

- Soil heterogeneity
- The water level
- The tunnel geometry
- The excavation techniques and sequences
- The soil and the lining behavior
- The boundary conditions

The 3D numerical modeling is able to study the TBM excavation phenomenon in all its complexity. This gives the possibility to explicitly consider the tri-dimensional geometry of the project, the state of the initial stresses, the excavation method, the sequence of work, and the surface loads. Moreover, for the TBM tunneling, it is possible to consider the excavation by the cutter head, the pressure applied by the excavation chamber, the progression of the TBM, the injection of the mortar through the tail shield, the percolation of the bentonite and the grouting along the skin and the consolidation procedure in the simulation (Mollon et al., 2013; Do et al., 2014; Janin et al., 2017).

The constant progress of computer tools and numerical codes makes it possible today to use them for the design of underground structures, with a calculation time that is becoming shorter and shorter. However, the two-dimensional modeling approach, for its speed and relative simplicity, is the most widespread in the current practice of tunnel project calculations. Different methods have been studied to simulate the tunnel-induced settlement with 2D approach (convergence-confinement method, GAP method, soil softening method). Karakus (2007) compared the different methods for the 2D simulation tunnel construction with the $in-situ$ measurements recorded on the Heathrow Express tunnel in London (New Austrian Tunneling Method NATM). He concluded that the best fit with the shape of the trough is obtained with the convergence-confinement method with the lining modeled with beam elements.

There are two approaches to conduct the convergence-confinement method. The first is an implicit technique where a confinement loss of the soil assimilates the convergence of the surrounding ground and the grouting pressure. The second method is the explicit technique where the grouting pressure is applied. Here, the confinement loss is used to simulate only the convergence of the tunnel before injecting mortar to fill the gap between the surrounding soil and the lining segments. Aristaghes and Autuori (2001) showed that it is better to use the explicit technique when the TBM pressures are available. However, there is always a gap between predictions and measurements. This gap can be due to the uncertainties on the soil parameters (because of the heterogeneity of soils).

1.5 Heterogeneity of soils

The methods used in geotechnics in general and in underground works in particular are based on simplified approaches that consider the soil as a homogeneous medium even though the natural medium is heterogeneous at all scales (Okhulkova, 2015). In the literature, there are few works done on the modeling of the heterogeneous character of soils. Lombardi et al. (2017) demonstrated that the spatial variability analysis is able to consider soil heterogeneity. The work of Bolle (2000) on the investigation and allowance for the spatial variability can also be cited. Despite these few references, some authors have attempted to quantify the variability of soil parameters. In this section, The origins of the variability in geotechnical engineering is first explained. Then some examples concerning uncertainties on soil parameter i.e cohesion, internal friction angle, deformation modulus and also the influential zone in which these parameters are highly correlated (auto-correlation distance) are presented. Finaly, the methodology to generate a random field in order to construct a spatial variable model is briefly explained and an example is presented.

1.5.1 Origins of variability in geotechnical engineering

Kulhawy (1993) summarized the uncertainty in geotechnical engineering in three sources as presented in figure 1.11:

- The natural variability of the soil which is an intrinsic property of the geological formations (random error) related to its evolution and the processes of genesis.
- Measurement error that is related to sampling and field investigations, such as errors due to measuring equipment (epistemic errors), operator, lack of knowledge related to measurements or geotechnical identifications.
- The modeling error that comes from the interpretation of the test results, their transformation into geotechnical parameters and the approximation of the real behavior by constitutive models.

In this thesis, the analysis will be focus on the natural variability of soils.

1.5.2 Quantification of the spatial variability

The spatial variability of a given geotechnical property can be characterized with 3 statistical parameters; the mean, the variance (or standard deviation or coefficient of variation), and the auto-correlation distance (or auto-correlation function) (Vanmarcke, 1977).

The mean and the variance (the standard deviation or the coefficient of variation) allow to represent the soil property by a random variable that follows a certain statistical distribution

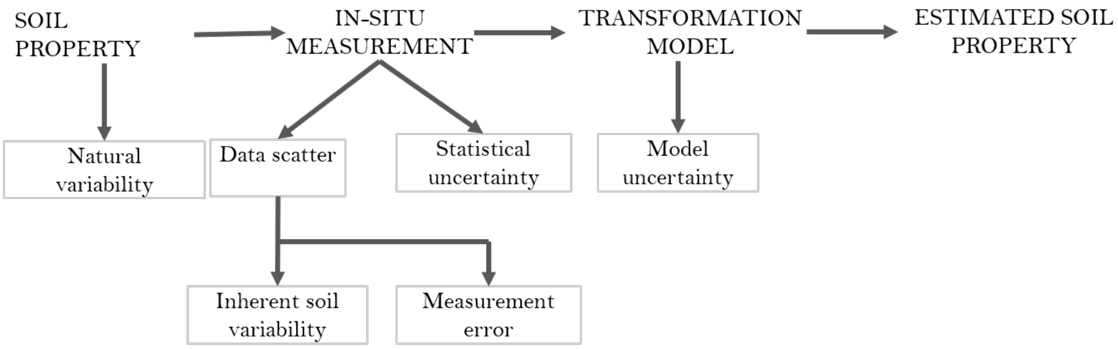

Figure 1.11: Uncertainty in soil property estimates (Kulhawy, 1993)

(Gaussian, Exponential, Lognormal, Beta...) (Guerra, 1973). If in addition, the auto-correlation distances and the correlation functions are taken into account, the property is then modeled by a random field that reflects the spatial variability of the soil. For this purpose, the property at a point would depend on its position. Determining the first statistical moments requires a statistical study on the results of the geotechnical investigations including $in-situ$ and/or laboratory tests. In the literature, different statistical distributions are used to represent the soil properties (Griffiths and Fenton, 2001; Griffiths et al., 2002; Fenton and Griffiths, 2003; Fenton G.A., 2005). Lognormal and beta distributions are recommended for representing Young's modulus, Poisson's ratio, and the shear parameters, since these quantities only admit positive values.

1.5.2.1 Cohesion

Phoon and Kulhawy (1999) conducted a series of $in-situ$ and laboratory tests and showed that the coefficient of variation of the undrained cohesion, due only to the natural variability, ranges from 10% to 55%. Cherubini et al. (1993) found that the variability decreases with increasing the soil cohesion and recommended a range of 12% to 45% for stiff clays. As for soft clays, they present a greater variability with a coefficient of variation that can reach 80%. Table 1.3 summarizes the value of the coefficient of variation of the cohesion proposed by different authors in the literature.

1.5.2.2 Internal friction angle

Phoon and Kulhawy (1999) showed that in the case of friction angle, the range of the coefficient of variation is narrower than that of cohesion. For soils with a frictional angle between 20° and 40°, the coefficient of variation is between 5% and 15%. Table 1.4 summarizes the value of the coefficient of variation of the frictional angle proposed by different authors in the literature.

Table 1.3: Coefficient of variation of the cohesion proposed in literature (Houmadi, 2011)

Authors	Coefficient of variation (cv) [%]
Lumb (1972)	30-50 (UC test) 60-85 high variation clay
Morse (1971)	30-50 (UC test)
Fredlund and Dahlman (1972)	30 - 50 (test UC)
Lee et al. (1983)	20-50 (Clay) 25-30 (sand)
Ejezie and Harrop-Williams (1984)	28 - 96
Cherubini et al. (1993)	12 - 45 (medium to stiff clay)
Lacasse and Nadim (1996)	5 - 20 (clay, triaxial test)
Phoon and Kulhawy (1999)	10 - 55
Duncan (2000)	13 - 40

Table 1.4: Coefficient of variation of the friction angle proposed in literature (Houmadi, 2011)

Authors	Coefficient of variation (cv) [%]	Soil nature
Lumb (1966)	9	Different types of soils
Harr (1984)	7-12	Coarse sand
Wolff (1996)	16	Clay
Lacasse and Nadim (1996)	2-5	Alluvial
Phoon and Kulhawy (1999)	4-12	Sand

1.5.2.3 Deformation Modulus

Bauer and Puła (2000a) proved that the deformation modulus variability increases with the decrease of its value. Table 1.5 summarizes the values of the coefficient of variation of the stiffness proposed by different authors in the literature.

1.5.2.4 Auto-correlation distance

The auto-correlation distance is a parameter that represents the natural spatial variability of a soil property and the influential zone in which values are highly correlated with each other. A small auto-correlation length implies a rapid and strong variation of the soil property from one point

Table 1.5: Coefficient of variation of the deformation stiffness proposed in literature (Houmadi, 2011)

Authors	Coefficient of variation (CV) [%]
Baecher and Christian (2005a)	2-42
Nour et al. (2002)	40-50
Bauer and Puła (2000b)	15
Phoon and Kulhawy (1999)	30

Table 1.6: Horizontal and vertical auto-correlation length

Authors	Auto-correlation length [m]	
	Vertical	Horizontal
Chiasson et al. (1995)	2	
Soulie et al. (1990)	3	7-30 for clay
Popescu (1995)		12 for sand and 5 for clay
Lacasse and Nadim (1996)	3-10	5-38
Phoon and Kulhawy (1999)	0.5-6	40-60

to another. A large auto-correlation length indicates rather homogeneous values. Some authors studied the spatial variability of the soil properties and Houmadi (2011) summarized in his thesis the horizontal and the vertical auto-correlation length as presented in table 1.6.

1.5.3 Random field discretization

In this section, the methodology to generate a spatially variable model is explained and some applications are also illustrated.A random field is defined either by an autocorrelation function or by a power spectral density . Some applications of random field using autocorrelation functions are proposed in the literature for different engineering fields (Goff and Jordan, 1988; Holliger and Levander, 1992) but very few in tunneling (Gong et al., 2018). Three types of autocorrelation functions are generally adopted:

- The Gaussian function; $\exp(-r^2)$
- The Exponential function; $\exp(-r)$
- The Von Karman function; $\frac{G_H(r)}{G_H(0)}$

In these equations, H is the Hurst exponent, K_H the modified Bessel function of the first kind (order H), and $r = \sqrt{\frac{x^2}{a_x^2} + \frac{z^2}{a_z^2}}$, $G_H(r) = r^H K_H(r)$.

After generating the random field, this latter is introduced into the models either as a continuous function or a discrete function. Several methods exist to affect a random field to a numerical model. In the literature three main categories can be distinguished:

- discretization by point values: these methods consist in applying a discrete value directly at specific points, either at the centroid of the element (Mid-Point method) or to the nodes of the mesh (Nodal Point method),
- discretization by average values: these methods use a spatial averaging of the field on the elements of the model Vanmarcke (1983),

- discretization by series development: these methods are used to represent the random field in a series of random variables, such as the orthogonal series expansion method (OSE), the method of discretization by optimal linear estimation (EOLE) and the Karhunen-Loeve (K-L) method.

The discretization by point values and the discretization by mean values give non-optimal solutions for the discretization of the random fields since they require a large number of random variables which is a function of the size of the deterministic model. The series developments solve this problem as they are satisfied with an optimal number of random variables (Hamrouni et al., 2021).

Concerning an application in tunneling, Gong et al. (2018) worked on the tunnel longitudinal performance. They adopted the random field theory to simulate the spatial variation of soil properties along the tunnel longitudinal direction, in which the soil properties at borehole locations can be explicitly considered. Figure 1.12 presents the longitudinal soil properties generated with a 2D continuous random field theory. In their work, Gong et al. (2018) used the finite difference method to generate the model by assigning to each element of the model a value generated according to its position in the space.

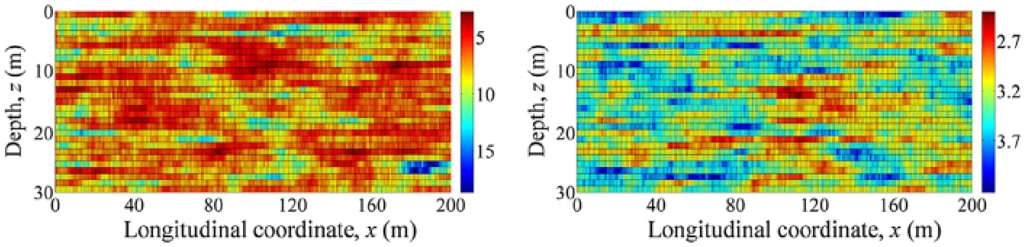

(a) Effective cohesion (c, kPa) (b) Effective friction (ϕ, ×10 °)

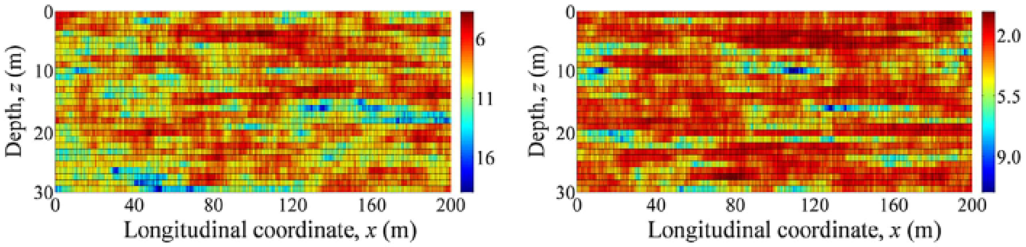

(c) Horizontal ground stiffness (k_h, $\times 10^3$ kN/m^3) (d) Vertical ground stiffness (k_v, $\times 10^4$ kN/m^3)

Figure 1.12: ‘True’ soil properties presented by Gong et al. (2018)

As it has been shown, nowadays some tools are able to represent explicitly the heterogeneity of soils. To achieve this, it is important to have enough well-distributed $in-situ$ tests to cover the whole space. Due to the cost of the overall investigation, it is impossible in practice to conduct them in their entirety during projects. As soil heterogeneity has an impact on the prediction of ground deformation and displacement during tunneling, it is therefore important to be able to study the effect of this characteristic on the stability of surrounding structures. Today, numerical approaches allow to simulate soil heterogeneity and the calculations are faster thanks to the 2D modeling. However, studying the effect of the spatial variability model requires a large number of simulations that makes the process time consuming. The evolution of the Machine Learning tools has allowed over the years to build meta-models capable of completing and substituting numerical simulations.

1.6 Meta-modeling

In tunneling, meta models are used to predict the effects induced by excavation such as surface settlements in the case of a shallow tunnel, building vulnerability, tunnel convergence or even for the adjustment of the control parameters of the TBM during excavation. According to Ejday (2011), the term ”meta model” characterizes the use of a mathematical equation to express the relationship between the input and the output variables of a complex model, allowing an approximation of functions by knowing the exact value, at a certain number of points of these functions . Two main ways of building meta models can be distinguished; supervised learning and unsupervised learning methods. Supervised meta models consist of the labeling of the input data and the corresponding output data. This generally involves a learning phase. In the case of unsupervised meta models, the algorithm analyzes the data and draws its own conclusions. According to the distribution of meta models mentioned in the literature, the most commonly used are:

- Supervised models
  - Polynomial regression (PR)
  - Support Vector Regression (SVR)
  - Radial Basis Function (RBF)
  - Artificial Neural Network (ANN)
  - Decision Tree (DT)
  - Random Forest (RF)
- Unsupervised models
  - K-means clustering
  - Principal Component Analysis (PCA)
  - Singular Value Decomposition (SVD)
  - Hierachical clustering

In tunneling, meta models are developed for the prediction of the settlement, the vulnerability of the nearby structures, the rock mass parameters, the convergence of the soil, and the advancement rate of the TBM.

1.6.1 Prediction of the soil response to excavation

Some researches on Machine Learning have been developed with the aim of predicting tunnel excavation-induced settlements in urban areas using meta models. Mohammadi et al. (2015) presented two meta models (Multi Layer Perceptron MLP ANN and MLR Multi Linear Regression) in the case of the shallow Niayesh tunnel in urban area excavated by NATM method. Due to the lack of site data, the development of the meta models was based on the finite element results. The input variables are the deformation modulus, the tunnel cover, the friction angle, the cohesion, the grain density, the soil type, and the output variable is maximum settlement. Ghiasi and Koushki (2020) developed the MLP ANN to predict the maximum surface settlement induced by the excavation of a circular cross-section tunnel from the depth to diameter ratio, the permeability, the friction angle, and the cohesion. They compared the accuracy of the MLP ANN with other intelligent networks and regression methods like the imperialist competitive algorithm ICA-ANN a new hybrid model of artificial neural network. According to the determination coefficient, the MLP ANN appears to be the best performing model.

1.6.2 Rock mass and TBM parameters

In the literature, some authors have proposed to determine the geological soil parameters with meta models. Liu et al. (2020) developed a meta model based on the coupling between the BPNN and the simulated annealing (SA a meta heuristic algorithm based on the search method) to predict rock mass parameters of the Songhua River water conveyance from the TBM advance control parameters (revolutions per minute, thrust of TBM cutterhead, torque of TBM cutterhead, and the advance rate). The Rock mass parameters is constituted by the uni axial compression strength (UCS), the brittleness index, the distance between plane of weakness, and the orientation of the discontinuities. Mahmoodzadeh et al. (2021) used several meta models among which the Gaussian Process regression- GPR to predict the geological parameter of Rock Quality Designation along the tunnel route. The meta models have been studied based on data obtained from 51 tunnels all over the world. Fifty data sets were utilized for intelligent modeling, while one was used to evaluation the prediction approach. They compared the result obtained with the different meta models at the end of the analysis. The proposed GPR, on the whole, performs better than the support vector regression (SVM), artificial neural network (ANN) and linear regression (LR) in predictive analysis of the RQD parameter. Gao et al. (2019) used the Long-Short term memory networks (LSTM), the traditional RNN, and the Gated Recurrent Unit (GRU) to deal with the real-time prediction of the TBM operating parameters based on the TBM $in-situ$ operating data. Avunduk et al. (2014) used the ANN to predict the Instantaneous cutting rate (ICR) of the roadheader. A data set including UCS, RQD, and the measured ICR were established in detail for the Kucuksu sewage tunnel thanks to the measurements and to the empirical models.

1.7 Conclusion

In this chapter, based on literature review, several works that are related to the problematic of this thesis have been presented. The criteria for choosing the type of TBM according to the nature of the soil in which it will be used is first discussed. Then, the advantages of using TBM for the tunnel construction have been clearly demonstrated. These include the control of ground deformation, i.e. settlement, and the reduction of project duration. However, it has been shown that even with the use of a TBM, important settlements can occur and affect the safety of the nearby structures and infrastructures. In order to prevent these displacements, analytical, empirical and numerical prediction methods have been presented (Lu and Liu, 2008; Zamora Hernández et al., 2019; Huo et al., 2019; Aygar and Gokceoglu, 2021).

Between these three methods, Mollon et al. (2013), Do et al. (2014), Galli et al. (2004), Yeo et al. (2009), and Janin (2017) have shown that the most appropriate one with a wide range of application is the numerical method with the 3D approach. It has also been demonstrated that, the success of a 3D approach depends on the ability to consider the excavation process - the excavation with the ground passing through the cutter head, the progression of the TBM, and the injection of the mortar, among others -. For this reason 2D simplification approach are generally adopted with the convergence-confinement method in order to obtain very good result (Karakus, 2007). However, there is still a gap between numerical prediction result i.e settlement and field measurements. In this thesis, soil heterogeneity has been assumed to be the cause of this difference.

This chapter also explained some methodologies that allow to explicitly consider the heterogeneity of the soils in the numerical analyses with random field theory. This method aims to develop models with spatial variability representing soil heterogeneity. In order to study the influence of soil heterogeneity on the TBM-induced settlement, several spatially variable models have to be generated and calculated (Miranda, 2011). This study is time consuming due to the large number of calculations that is required. At the end of this chapter, methods based on machine learning tools are presented as a solution to save calculation time.

As mentioned in this chapter two approaches exist to conduct a convergence-confinement method. In this thesis, the explicit approach is adopted. This approach required a 2D fictitious pressure. In the next chapter the methodology to simplify the 3D approach by the 2D one with the explicit approach convergence-confinement method will be explained. At the end this chapter, a formulation will be proposed in order to obtain the 2D fictitious pressure from the TBM pressures.

Chapter 2

Numerical simulation of TBM excavation and model simplification

Contents

2.1 Introduction

As already explained in chapter 1, numerical simulations are generally used to predict TBM-induced settlement in order to prevent the impact of this later on the safety of structures. Among numerical simulations, the Finite Element method (FE) appears to be the most widely used today. Nevertheless, some challenges remain to achieve a successful FE simulation.

In FE simulation, the constitutive model used to simulate soil behavior plays an essential role in the model response. Pande and Pietruszczak (1986), Vakili et al. (2014), Mousivand and Maleki (2018), Javadi et al. (2020) and Cao et al. (2021) conducted FE simulations with different constitutive models to evaluate the surface settlement trough induced by tunneling. Pande and Pietruszczak (1986) concluded that the use of models based on nonlinear elastoplasticity theory, such as the Hardening Soil with Small Strain Model (HSSM) (Benz et al., 2009; Schanz et al., 2019) is always suitable since they represent a rational mechanical process. However, parameter identification remains a great challenge with this type of constitutive model due to generally the lack of $in-situ$ and laboratory tests.

Two approaches, three-dimensional (3D) and two-dimensional (2D), exist for conducting a FE simulation. Mollon et al. (2013), Do et al. (2014), and Janin (2017) demonstrate that the 3D FE approach appears to be the most accurate. The success of a 3D simulation depends on its ability to represent the complex phenomena that occur during the construction of the tunnel, i.e. the excavation with the ground passing through the cutter head, the progression of the TBM, and the injection of the mortar, among others. Despite current progress and the advantages offered by the 3D approach, this method remains time-consuming, and numerical problems frequently appear. It also generally requires a lot of parameters (the TBM pressures), thus, limiting its usage as explained by Galli et al. (2004) and Yeo et al. (2009). To overcome this limitation, 2D FE modeling is generally adopted.

Among the 2D methods, the explicit approach of the convergence-confinement method proposed by Aristaghes and Autuori (2001) is used in this thesis with a plane strain analysis to evaluate the TBM-induced settlement. The success of a 2D simulation depends on its ability to represent the different steps of the 3D simulation which is characterized by the third dimension deformation. This approach requires the use of a confinement loss rate to represent the stress relief due to the excavation, and a fictitious pressure to represent the pressures applied by the TBM during the tunnel construction. While certain researches try to explain the relationship between the TBM pressures and the settlement trough, others try the study the influence of the 2D fictitious pressure on the settlement (Kasper and Meschke, 2006; Chortis et al., 2014). It appears from these works that the relationship between the TBM pressures and the 2D fictitious pressure needed to conduct the 2D explicit approach of the convergence confinement is not yet established. The goal of this chapter is to determine the 2D fictitious pressure of the convergence confinement method knowing the TBM pressures (The face pressure, the pressure around the shield and the grouting or injection pressure).

In order to achieve this goal, the data used in this chapter is based on the Paris Metro Line 16 and the chapter is organized as follows. In section 2.3, real process of the tunnel construction is presented. Based on this description, a procedure for 3D modeling and 2D modeling is proposed in section 2.4 and section 2.5 respectively. Several 3D and 2D FE models are conducted in order to obtain the fictitious pressure by fitting the maximum settlement. The models are calculated with the FE code ZSoil V18.05, the HSSM is used to simulate the soil behavior. In section 2.7, the influence of the TBM pressure on the 2D fictitious pressure is analyzed and a formulation to obtain a 2D fictitious pressure from the TBM pressures is proposed before concluding in section 2.8.

2.2 Project description of the Paris Metro Line 16

The Grand Paris Express (GPE) is one of the largest urban projects in Europe, with 200 km of automatic lines and 68 stations. Located in the Paris area in France, this project will help solve transportation issues by considerably reducing transportation time, pollution and traffic jams. The GPE consists of new lines, and the extension of some existing lines. Specifically, this chapter is based on the data recorded during the construction of the Paris Metro Line 16.

The Paris Metro Line 16 is divided into three different parts:

- The main path of Line 16: Consists of 21.3 km of tunnel infrastructure located between the back station of ‘Le Bourget RER’ station and the north of the back station of the ‘Noisy-Champs station’.
- The overlap between Line 16 and Line 17: Extends over approximately 6.1 km between the back station of ‘Saint-Denis Pleyel’ and the entrance to ‘Le Bourget RER’ station.
- The overlap with Line 14: covers 1.7 km of the tunnel between the ‘Mairie de Saint-Ouen’ station and the ‘Saint-Denis Pleyel’ station.

The studied area of the Line 16 project and its characteristics are presented in more detail in figure 2.1. This thesis is focused on the third part. Along this part, Line 16 has connections with line 14. The tunnel was excavated with an Earth Balance Pressure Tunnel Boring Machine (EPB TBM). The longitudinal profile of the tunnel alignment encountered a multi-layer soil configuration located below water level. This mixed front soil is constituted either by the ‘Saint Ouen/Beauchamp sand, marls and sandstones/coarse limestone or coarse limestone/Beauchamp sand. The tunnel cover varies between twice the diameter and 4.5 times the diameter.

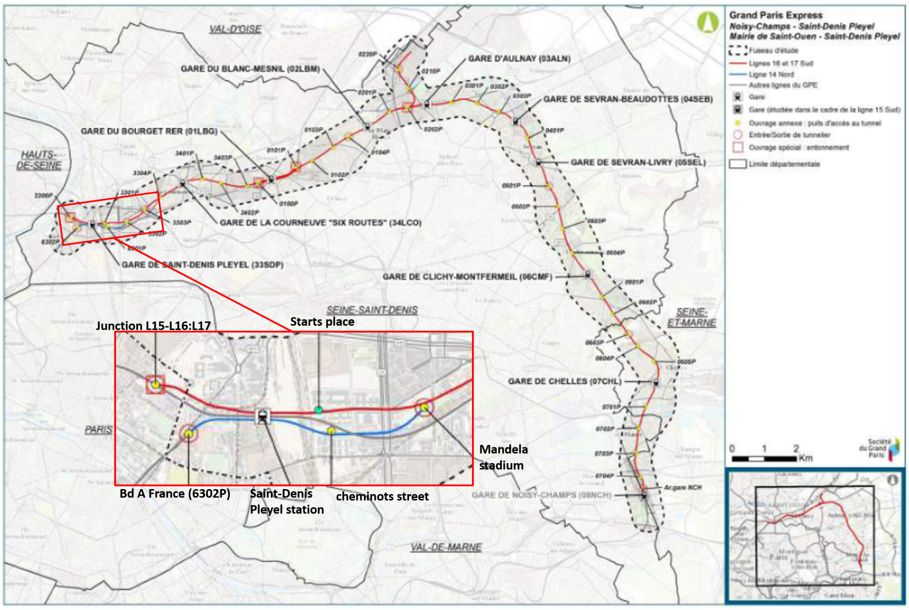

Figure 2.1: Studied area of Line 16 of the Grand Paris Express (Giroux et al., 2022)

All along its path, Line 16 encounters structures and infrastructures that may have been affected by the tunnel construction. Finite element (FE) methods offer the possibility of efficiently predicting ground deformation, particularly the settlement due to tunneling. In order to accurately simulate the tunneling procedure and to be successful with FE numerical prediction, it is important to understand how the TBM tunneling phenomenon occurs in reality.

2.3 Tunnel construction procedure

By observing in detail the construction of full-scale tunnels, Leca (1987) and Chapeau (1991) have shown that the tunnel construction procedure can be simplified into two main phases: the excavation phase and the lining phase.

2.3.1 Excavation phase and pressure distribution around the TBM

The construction of a tunnel with a TBM is a set of repetitive operations. The tunnel boring machine excavates the ground with the cutting wheel while moving forward. To facilitate its advance, the tunnel boring machines are designed with a conical shape. Table 2.1 presents the main characteristic of the TBM used to excavate the Paris Metro Line 16. Note, the TBM head is larger than the TBM tail. With this kind of design, it is expected to avoid friction between the TBM and the surrounding soil that comes from the convergence due to stress release. With the rotation of the cutting wheel, the TBM excavates the soil and removes the material from the

Table 2.1: Main characteristics of TBM used for the GPE Line 16

Characteristics	L16 GPE
Excavation diameter [m]	8.92
Shield tail diameter [m]	8.87
Shield + shield tail length [m]	10.2
Conicity of the shield over the diameter [mm]	50
Conicity around the linings over the diameter [mm]	370
Maximum pressure of the TBM [bars]	5

excavation chamber. Depending on the soil conditions, the excavation chamber can be full or partially full.

In the case of a full excavation chamber, the stability of the face is entirely ensured by the excavated soil which is maintained under pressure in the chamber. The determination of the equilibrium pressure depends on the pressure distribution of the soil. The pressure applied by the TBM has the main goal of balancing the total stress of the soil as presented in figure 2.2 (Founta, 2018; El Jirari, 2021).

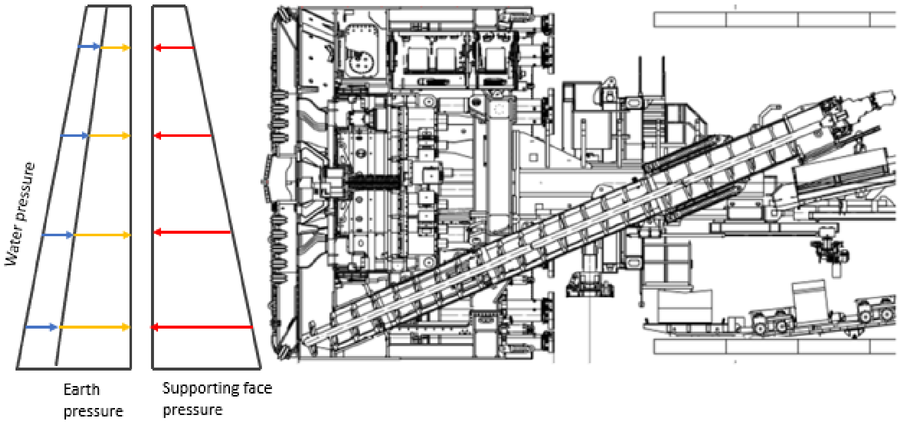

Figure 2.2: Pressure diagram for a full excavation chamber: configuration adopted during the excavation of line 16

In the case of a chamber partially filled with excavated soil, during the excavation of the Paris Metro Line 16, the material located at the crown is put in place by the application of compressed air or foam pressure. This application modifies the pressure distribution at the tunnel face as shown in figure2.3.

According to Aristaghes and Autuori (2001) whenever TBM crosses soils with good quality, i.e. soils whose mechanical parameters can ensure stability, it is necessary to control the water inflow. For this reason, a minimum pressure equal to the hydrostatic pressure must be applied at the front. During the excavation of the Paris Metro Line 16, sensors were installed on the cutting

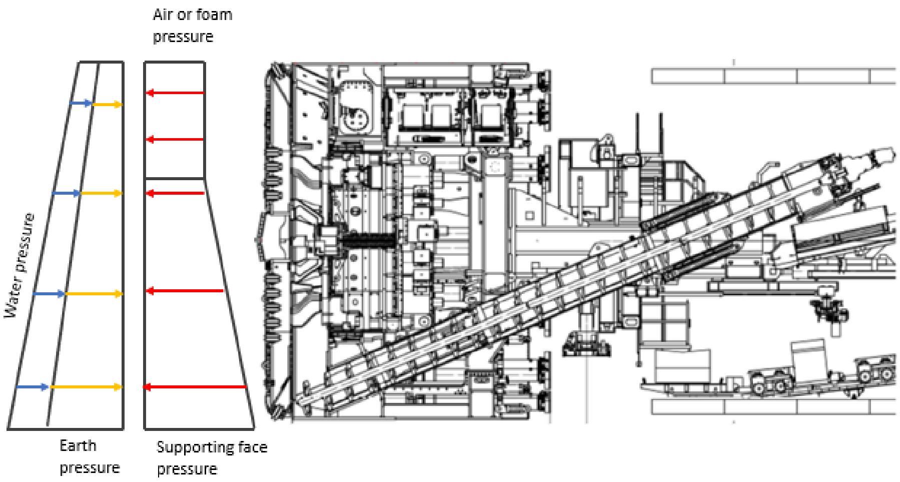

Figure 2.3: Pressure diagram for a partially full excavation chamber: configuration adopted during the excavation of line 16

wheel to record the value of the face pressure. Figure 2.5 presents the location of the sensor on the cutting wheel. The face pressure distribution is deduced from recorded pressure with a linear regression function as presented in figure 2.4. The measurements of the face pressure at some sections of the tunnel path are compared with the value of the hydrostatic pressure along the cutting wheel. Two face pressure distributions can be distinguished:

- For the first distribution, the value of the face pressure at the crown is equal to the hydrostatic pressure. The mechanical properties of the soil are able to ensure stability. There is no need for additional pressure at the front.
- For the second distribution, there is a need of additional pressure to ensure the face stability. Thus, the value of the face pressure at the crown is greater than the hydrostatic pressure.

By analyzing the pressure distribution evolution as a function of TBM position, it can be seen that the pressure distribution depends on the tunnel cover and the type of soil in which passes the tunnel. When the tunnel is deep enough and excavated in good soil quality, the hydrostatic pressure is sufficient and has the role only to counterbalance the water inflow. When the cover decreases, the pressure at the excavation face is higher than the hydrostatic pressure. Based on this conclusion, the tunnel path can be divided into two zones as presented on figure 2.6.

- Zone 1: where the face pressure at the crown is equal to the hydrostatic pressure ($P_{min} = P_w$).
- Zone 2: where the face pressure at the crown is higher than the hydrostatic pressure ($P_{min} = P_w + P_{add}$)

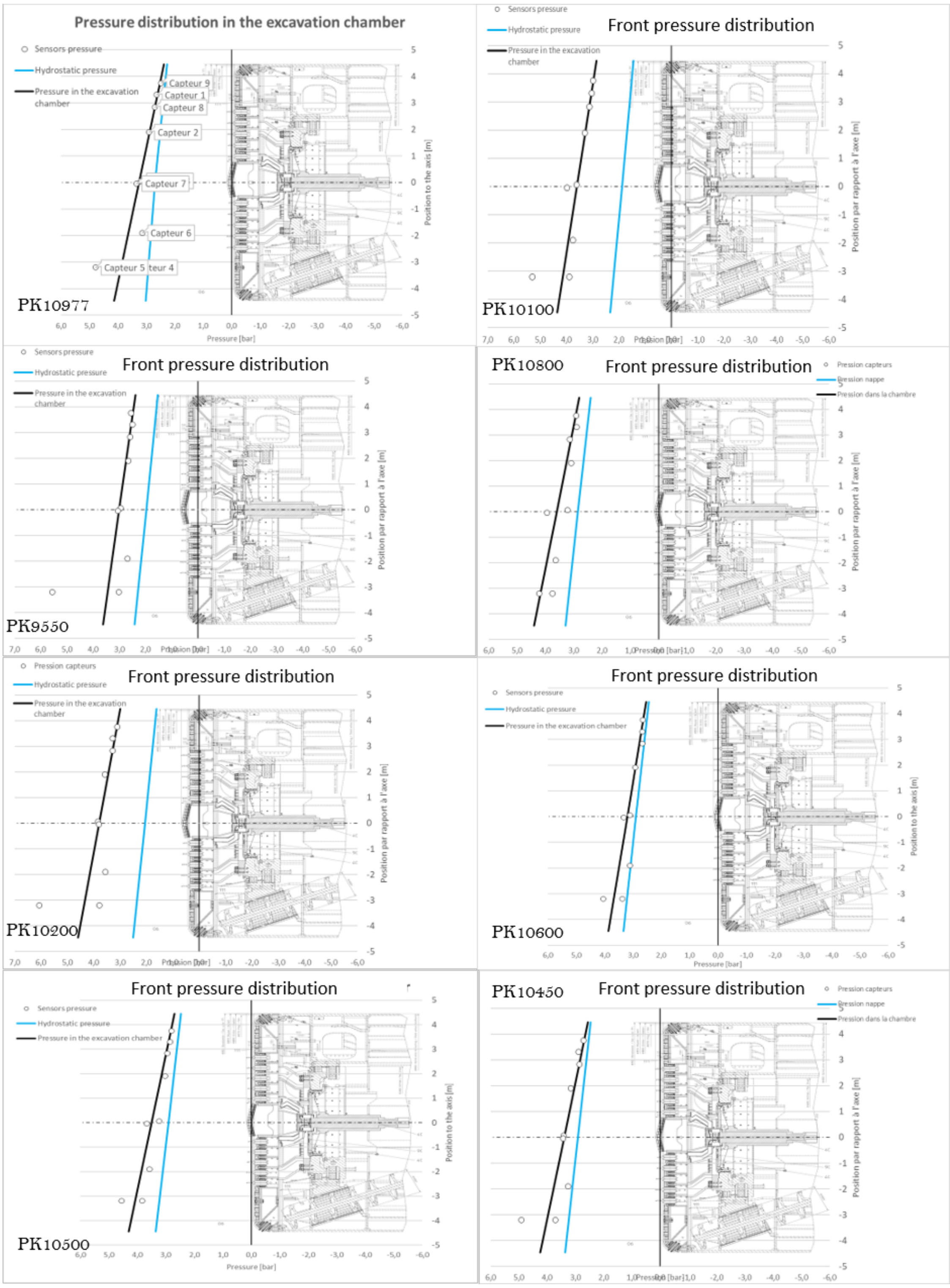

Figure 2.4: Pressure distribution in the excavation chamber at some sections of the Line 16

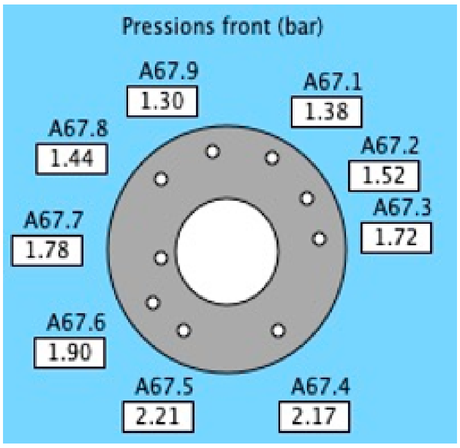

Figure 2.5: Location of the sensors along the cutting wheel

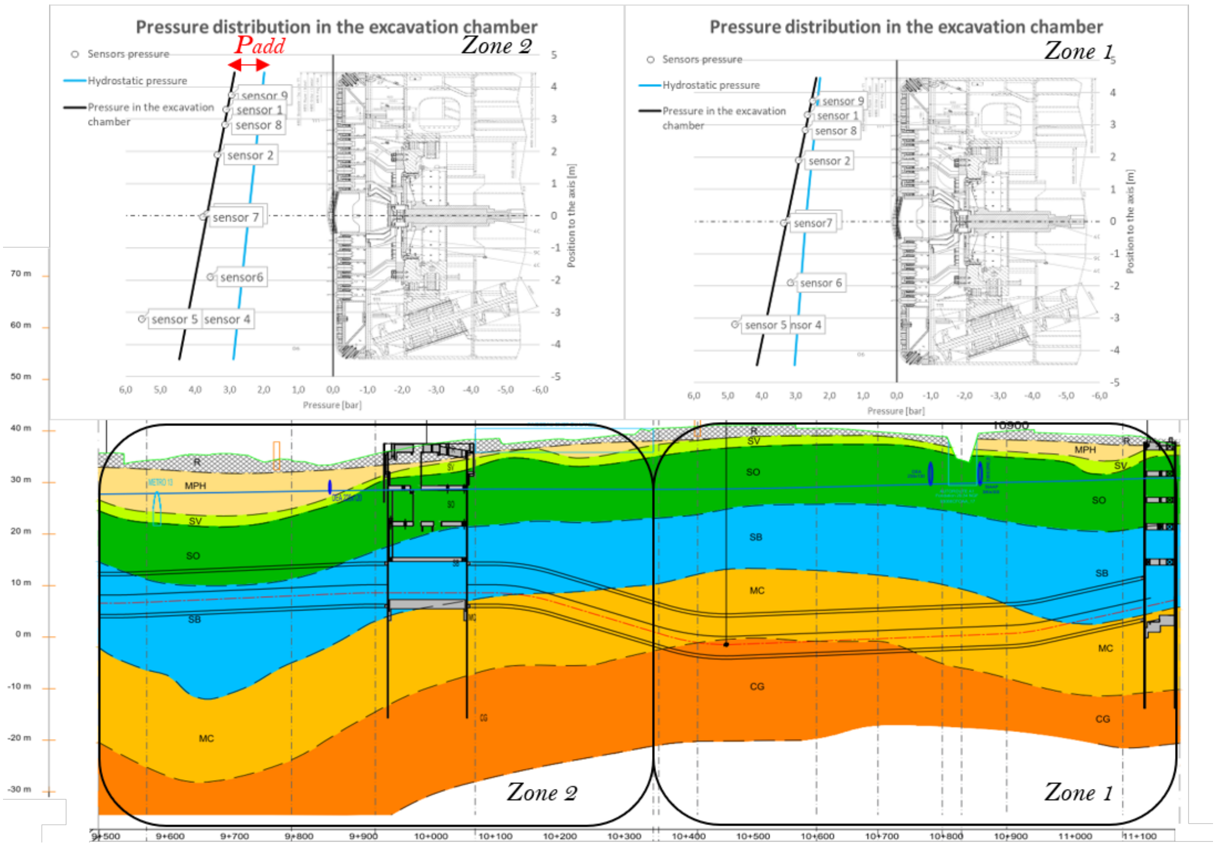

Figure 2.6: 2D Simulation steps for the plane strain method

Due to the conical shape of the TBM, there is a continuous connection between the excavation chamber and the free space around the shield. This creates pressure around the shield as presented in figure 2.7. The value of that pressure is generally unknown unless sensors are installed for

recording. Given the origin of this pressure, it could not be higher than the pressure of the excavation chamber unless there is an injection along the shield.
After the excavation procedure, the TBM moves forward and the linings are immediately installed behind the shield tail to control the soil displacement and prevent it from collapsing.

2.3.2 Lining construction procedure

The concrete lining rings are formed by 1.8 m wide and approximately 35 cm thick segments. The TBM erector is used to move, fix, and stick the segment linings together.

The difference in diameter between the cutting wheel, the shield, and the tail creates an annular gap between the external face of the lining and the excavated soil. This gap is necessary for the shield to adapt to the curvature of the tunnel alignment, and prevents any friction that may block advancement. In order to limit settlement and soil confinement loss, the annular gap is filled by grouting (inert, active, or in a coarse form such as sand or gravel) through a pressure injection at the end of the shield tail. The injection can be done either through the linings once they have been removed from the tail, or directly at the shield tail. A gasket system (in general three rows of steel brushes) prevents a grout extrusion from the gap between the segments and the shield (Guglielmetti et al., 2008).

Figure 2.7 presents the distribution of pressures applied by the TBM during the excavation and the installation of the lining segments. It is important to describe in detail this configuration in order to propose compatible FE models able to effectively predict settlement. The 3D model best represents complex phenomena (excavation with the ground passing through the cutter head and progression of the TBM, among others), as well as the pressures applied by the TBM, explained in Galli et al. (2004), Yeo et al. (2009) and, Do et al. (2014).

2.4 Three dimensional simulation of TBM construction

3D simulation can consider different and complex phenomena that occur during tunnel construction with a TBM such as the excavation by the cutter head, the pressure applied by the excavation chamber, the progression of the TBM, and the injection pressure or grouting pressure through the tail shield, among others. Other aspects that can be taken into account with this approach include the three-dimensional geometry of the project, the initial stress, the excavation method, the different steps, and the external surface load.

In this section, three-dimensional modeling is adopted to conduct the numerical simulation of the pressurized tunneling at a given cross-section of the 10 m diameter of the Paris Metro Line 16. Figure 2.8 shows the general view of the 3D FE model. The symmetry of the model allows for the size reduction of the model, with a mesh of 97000 cubic elements, each with eight nodes.

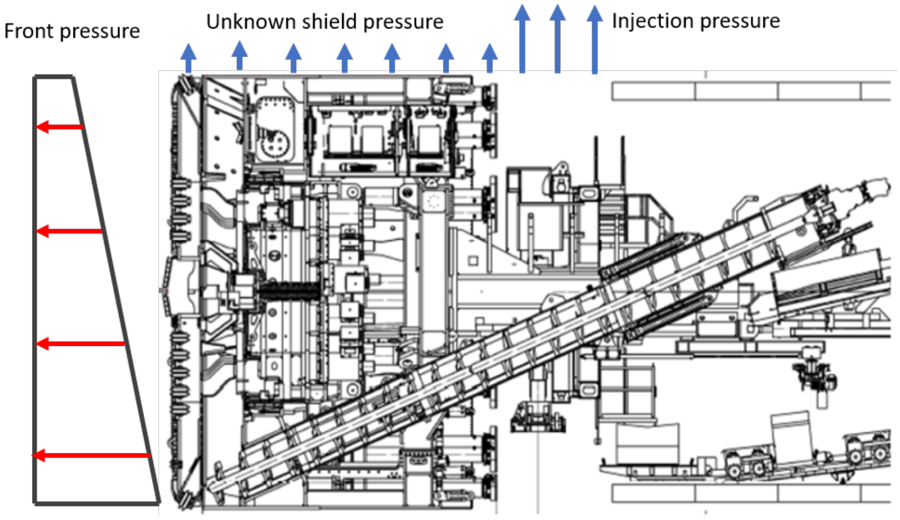

Figure 2.7: Pressure distribution around the shield

At the two vertical faces, no horizontal displacement is allowed, with the lower boundary between them being fixed both vertically and horizontally. For a successful 3D FE simulation, a precise procedure must be followed. This procedure starts with the initialization of the $in - situ$ stresses and is followed by the construction process.

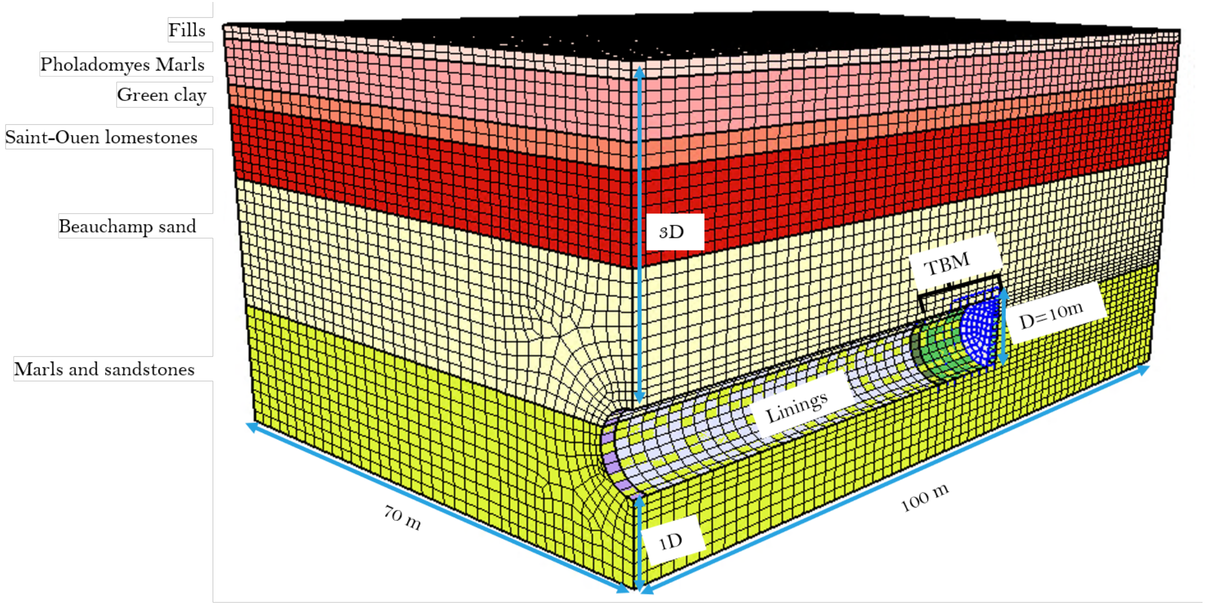

Figure 2.8: General view of the 3D numerical model

2.4.1 Excavation procedure in the 3D approach

The progression of the TBM in the ground is simulated in successive steps. At the tunnel face, soil elements are removed at each step along a 1.8 m length of the lining segment. At the same time, the face pressure is applied. This pressure originates from the action exerted by the TBM against the soil to maintain stability. In general, the pressure distribution results from the superposition of the mechanical supporting action of the cutting wheel and a supporting action exerted by the material contained in the excavation chamber. This material corresponds to a mixture of the excavated soil with different compounds (water, foam, and polymers in the case of EPB TBM). In the numerical model, increasing pressure with depth P_f^* is applied at the TBM face following equation 2.4.1:

$$P_f^*(z) = P_f + \Delta_{front} \cdot z \tag{2.4.1}$$

where P_f corresponds to the face pressure at the crown, Δ_{front} is the unit volume weight of the mixture inside the excavation chamber, and z is between 0 and d_{exc} (the excavated diameter in this case equal to 10 m). During the excavation, sensors were installed on the cutting wheel to monitor the input parameters P_f, and Δ_{front} is determined by analyzing the face pressure's evolution.

As the TBM advances, there is a connection between the excavation chamber and the void around the shield. This connection generates a pressure distribution around the shield. Determining the pressure condition around the shield is not apparent as it depends on many factors, as explained in the previous section. Additionally, according to El Jirari (2021), the backflow of the mortar along the shield and the inflow of the mixture from the excavation chamber are low for an EBP TBM. By considering the face pressure distribution where the value at the crown is equal to the hydrostatic pressure, and based on the conclusion of El Jirari (2021), the water pressure is considered around the shield in the 3D simulation.

After some steps of excavation, when the length of the excavation is equal to the length of the shield, the lining rings are put in place.

2.4.2 Lining construction in the 3D approach

In reality, after excavating the soil, the lining segments are installed at the shield tail, and a mortar is injected between the concrete lining ring and the surrounding soil to fill the annular void. In this thesis, the lining ring is simulated as a continuous elastic linear isotropic shell with Young's modulus of 13.5 GPa. The longitudinal and transversal joints between the lining segments are not explicitly modeled. The mortar injection is simulated by applying a radial pressure against the soil. As shown in equation 2.4.2, a gradient governs the radial injection pressure. In this equation, P_{inj} represents the value at the crown and Δ_{mortar} the volume weight of the mortar:

$$P_{inj}^*(z) = P_{inj} + \Delta_{mortar} \cdot z \tag{2.4.2}$$

It is considered that the injection pressure of the mortar mainly governs the soil deformation at the shield tail. This hypothesis implies two assumptions: the lining segments are impermeable and, under real-life conditions, the mortar is liquid enough to exert pressure on the lining ring. To consider the possibility of pressure losses between the crown and the invert due to friction between the mortar and the soil, the vertical gradient Δ_{mortar} is assumed to equal 14 kN.m^{-3}. Note that this value is lower than the unit weight of the mortar which is around 22 kN.m^{-3}. For every advancement step, the injection pressure moves forward, and the lining rings follow behind (see figure 2.9).

The complete simulation of the tunnel excavation in 3D is sometimes costly in calculation time.

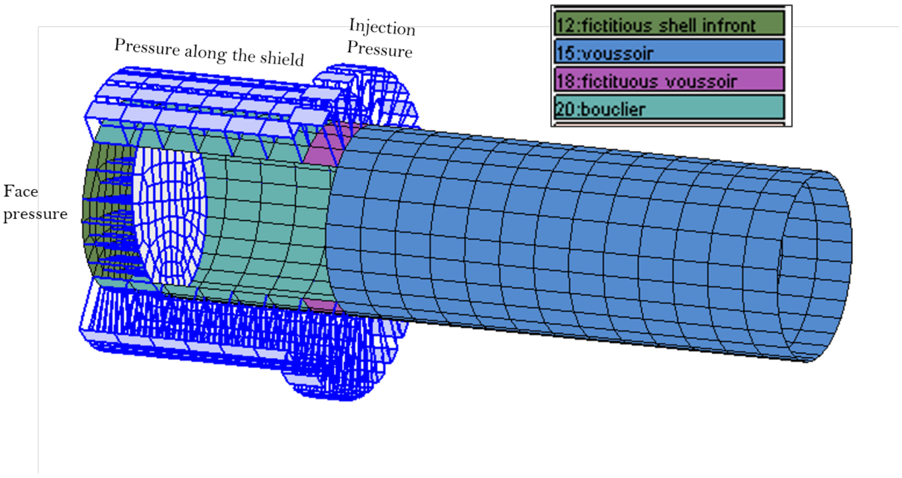

Figure 2.9: Pressure distribution around the TBM during the numerical simulation

For the Line 16 project, a 3D calculation was completed in about three days, so the use of the 2D FE model is strongly recommended.

2.5 Two dimensional simulation of TBM-construction

In this simulation, the tunnel construction is modeled using the plane strain assumption. Figure 2.10 shows the 2D model of the considered cross-section of the Paris Metro Line 16. As the cross-section is symmetrical, only half of the entire tunnel is modeled. The mesh is constituted of 2700 nodes with 2 degrees of freedom (except for the nodes along the boundaries allowed to move only vertically), and 2700 quadratic elements. The model is blocked horizontally on both the left and the right sides. The bottom of the model is fixed horizontally and vertically, and the upper boundary is set free. Different methods have been studied in the literature that simulate the three-dimensional effect of a TBM in a two-dimensional approach. Karakus (2007) summarized and compared these methods to the measurements done on the Heathrow Express tunnel in London. According to his results, the best approach to simulate the tunnel-induced settlement is the explicit approach of the convergence-confinement method. In explicit convergence-confinement method, the TBM-construction tunnel can be divided into two principal phases; the excavation and lining construction phase.

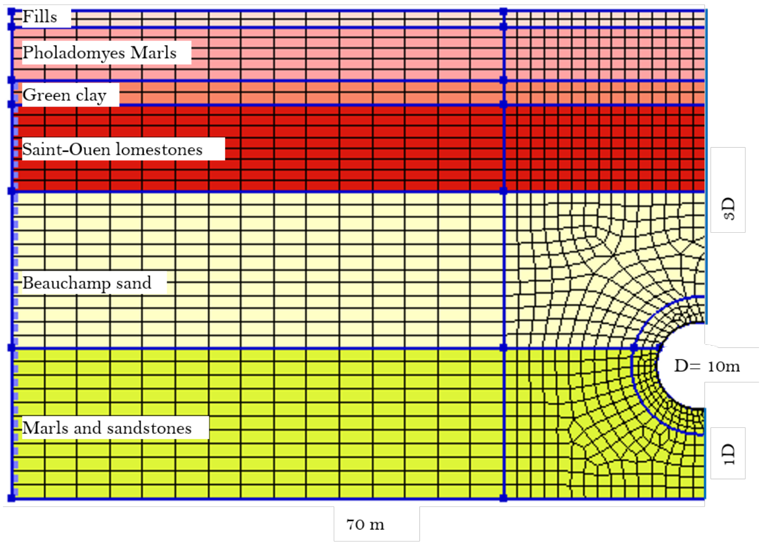

Figure 2.10: General view of the 2D numerical model

2.5.1 Excavation phase simulation and fictitious pressure application

According to this method, the excavation is modeled in 2D by applying a stress reduction coefficient called confinement loss and a 2D fictitious pressure simultaneously.

The confinement loss was originally developed for conventionally excavated tunnels mentioned by Sulem et al. (1987), Panet et al. (2001), and Vlachopoulos and Diederichs (2009). The initial work to determine the confinement loss was carried out in an isotropic medium at great depth.

Aristaghes and Autuori (2001) studied the evolution of the confinement loss at three points of the tunnel - crown, side, and invert - in an anisotropic medium with a relative depth of three times the tunnel radius. Figure 2.11 represents the evolution of the confinement loss rate as a function of the front position. According to Aristaghes and Autuori, the confinement loss is not homogeneous along the tunnel diameter and increases faster at the invert than at the crown or the sides. As demonstrated by Panet and Guenot (1983) and Bernaud and Rousset (1992) , the confinement loss λ is a function of the tunnel geometry and the distance of the considered section to the tunnel face, with λ varying between 0 and 1. A value of 0 means no influence by the tunneling process on stress release (no stress release), while a value of 1 means that the stress is completely released. Generally, the linings are installed at a distance greater than twice the TBM radius. In this thesis, in accordance with Panet and Guenot (1983) and Bernaud and Rousset (1992), a value of 0.9 to simulate the confinement loss of the soil is assumed.

For the pressurized tunnel, the progression of the TBM and the installation of the lining require the application of different pressures by the TBM. These include, among others, the confinement pressure by the excavation chamber, the injection pressure to fill the gap between the soil and the lining with grout, and sometimes the pressure around the shield. In 2D simulation, these pressures are reduced into a single fictitious pressure.

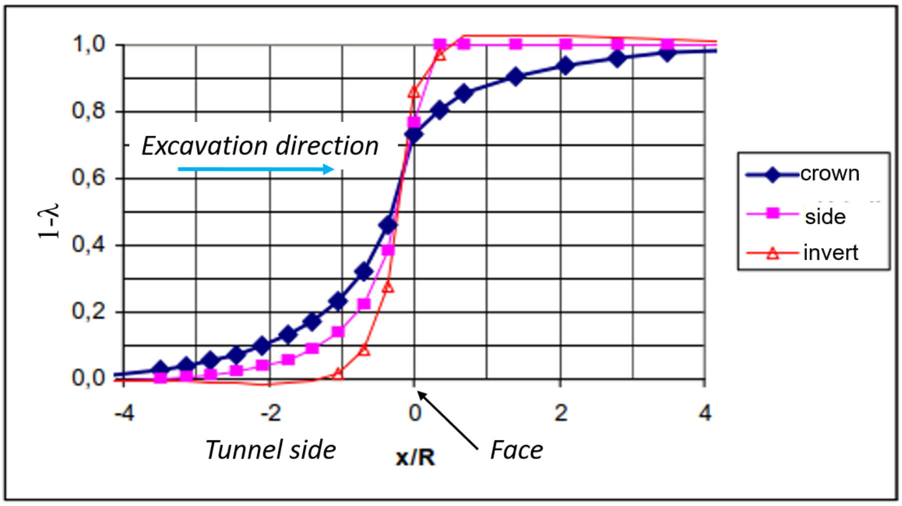

Figure 2.11: Evolution of the confinement loss at the crown, the side, and the invert (Aristaghes and Autuori, 2001)

The 2D FE simulation of the tunnel construction starts with the initialization of the geostatic stress under gravity loads and the lateral earth pressure. Then follows the excavation procedure where the confinement loss is applied to the excavated soil. the fictitious pressure is finally applied before installing the lining ring. In this chapter, the fictitious pressure is calibrated to fit the 2D settlement with the 3D one.

, such as described in the procedure above, is finally applied to simulate the 3D real pressures applied by the TBM before installing the lining rings.

2.5.2 Lining ring construction phase simulation

Concrete linings are simulated using a 35 cm thick beam element with an elastic stiffness of 13.5 GPa. The lining ring is installed, and the residual stress is completely released at the end of the procedure.

2.6 Soil behavior simulation

For a successful FE simulation, it is essential to better simulate soil behavior. The accuracy of FE analysis is essential and depends on the adequacy of the soil model to describe soil behavior. Simple linear constitutive models cannot fully reproduce the complex behaviors of soils, in particular, the nonlinear stress-strain relationship. The nonlinear elastoplastic constitutive models can describe complex behaviors of soils and can consider the variation of soil stiffness in the small-strains range. In this thesis, the Hardening Soil with Small Strain constitutive Model (HSSM) (Schanz et al., 2019) is adopted.

2.6.1 Background of small strain stiffness model

According to Skels and Bondars (2017) the back-calculated stiffnesses from observations of soil deformations are often greater than those used for geotechnical design. It has been demonstrated that only for very small shear strains ($< 10^{-6}$), soil can be described as linearly elastic, exhibiting fully recoverable behavior. Figure 2.12 illustrates the reduction of the shear modulus with the shear strain evolution. Three zones can be observed: the very small strains ($\gamma_s < 10^{-6}$), the small strains ($10^{-6} < \gamma_s < 10^{-3}$), and the larger strains ($\gamma_s > 10^{-3}$).

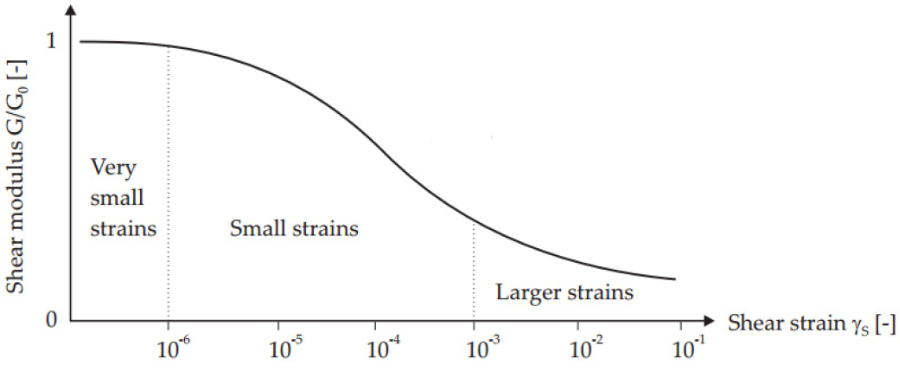

Figure 2.12: Characteristic stiffness-strain behavior, in logarithmic scale (Mair et al., 1993)

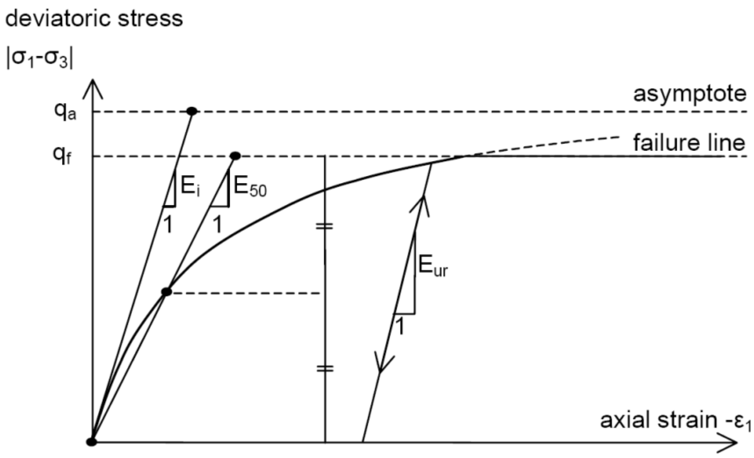

Figure 2.13: Hyperbolic stress-strain relation in primary loading for standard drained triaxial test (Schanz et al., 2019)

As shown in figure 2.13, the formulation of the Hardening-Soil model can be a hyperbolic relationship between the axial strain ϵ_1, and the deviatoric stress q, in primary triaxial loading (see equation 2.6.1 valid for $q < q_f$). When subjected to primary deviatoric loading, soil shows a decreasing stiffness and simultaneously, irreversible plastic strains develop (Likitlersuang et al., 2013). Schanz et al. (2019) presents more details concerning the HSSM (see also appendix A).

$$\epsilon_1 = \frac{q_a}{2E_{50}} \frac{q}{q_a - q} \tag{2.6.1}$$

The ultimate deviatoric stress q_f and the quantity q_a in this equation are defined as:

$$q_f = \frac{6 \cdot \sin\phi_p}{3 - \sin\phi_p}(p + c \cdot cot\phi_p) \tag{2.6.2}$$

$$q_a = \frac{q_f}{R_f} \tag{2.6.3}$$

The failure criterion of the HSSM is based on the one of the Mohr-Coulomb as presented in Equation 2.6.2. When $q = q_f$, the failure criterion is satisfied, and the perfectly plastic yielding occurs. The ratio between q_f and q_a is given by the failure ratio R_f (a value of 0.9 is usually assumed). The HSSM has 4 different stiffnesses (the unload-reload elastic stiffness E_{ur}, the secant stiffness in standard drained triaxial test E_{50}, the tangent stiffness for primary odometer loading E_{oed}, and the stiffness for very small strain E_0)

Table 2.2: Soil parameters used in the FE model

Layer	$\gamma[\frac{kN}{m^3}]$	C'[kPa]	$\phi'[°]$	$\psi'[°]$	$E_{50} = E_{oed}$[MPa]	E_{ur}[MPa]	E_0[MPa]
Fills (R)	19	0	28	0	14	28	56
Pholadomyes Marls (MPH)	19	5	34	4	48	96	384
Green clay(SV)	19.5	10	34	4	60	120	480
Saint-Ouen limestone (SO)	18	20	33	3	85	170	680
Beauchamp sand (SB)	21	10	33	3	174	348	1392
Marls and sandstones (MC)	20	25	35	5	300	600	2400

2.6.2 Soil parameter determination

Identification of the soil parameters requires the use of advanced laboratory devices and a large number of $in - situ$ and laboratory tests, which are not always available. Due to the lack of tests, according to Janin et al. (2015), Zhao et al. (2015), Zhang et al. (2018) and, Miliziano and de Lillis (2019), relationships can be assumed among the soil parameters following the requirement of Obrzud and Truty (2010).

Table 2.2 presents the soil parameters used in the numerical model. These parameters come from calibrations and are proposed for the purpose of the present study. In this table, the cohesion, friction, and dilatancy angles constitute the failure criterion.

In order to determine the 2D fictitious pressure knowing the 3D pressures, a set of 3D and 2D simulations are conducted. The idea of these analyses is to fit the 2D FE settlement to the 3D one in order to obtain the corresponding 2D fictitious pressure.

2.7 Numerical results and interpretations

Twenty 3D numerical simulations were conducted while varying the face pressure, the pressure around the shield and the grouting pressure to study their influence on the maximum settlement. Note that the pressure around the shield is always assumed to be equal to the hydrostatic pressure. So, varying the shield pressure also means a variation in the water level. Table 2.3 summarizes the model configurations and the numerical results. From model 1 to model 7, the face pressure varies from 230 kPa to 500 kPa at the crown with an increment of 19 kPa/m while the shield and injection pressures remain constant. From model 8 to model 11, the face pressure and the shield pressure are constant, but the injection pressure varies from 230 kPa to 400 kPa with an increment of 14 kPa/m. Finally, from model 12 to model 20, the face pressure and the injection pressure remain constant, and the water level varies; consequently, P_{min} also varies. The idea here is to study the influence of the pressure around the shield (the water level) on the settlement. Figure 2.14 presents the influence of the TBM pressures on the maximum settlement. According to this figure, the TBM pressures have different influences on the maximum settlement, as shown here below:

- Concerning the influence of the face pressure, it can be observed that, when the front is stabilized, the additional pressure $P_{add} = P_{front} - P_{min}$ does not influence the settlement. This conclusion was confirmed by Aristaghes and Autuori (2001) and Chortis et al. (2014). Aristaghes and Autuori (2001) explained that when excavating in a cohesive soil, the face pressure can only counterbalance the inflow of the water. According to Chortis et al. (2014), for stable tunnel faces, the effect of the front support pressure is negligible. Fixing the face pressure equal to the hydrostatic pressure is sufficient to ensure stability. The additional pressure has only a marginal effect.

- Concerning the grouting pressure, the settlement decreases with the pressure increase. Kasper and Meschke (2006) confirmed this conclusion; they highlighted the influence of the grouting pressure on the surface settlement. In the analysis, the grouting pressure varies from 230 kPa to 400 kPa, generating a settlement between 3.5 mm and 4.55 mm.

- Based on the initial assumption presented in section 2.4 (the pressure around the shield is equal to the hydrostatic pressure), the water table variation induces a variation of the shield pressure. It can be observed from the Figure.2.14 that decreasing the water table tends to increase the surface settlement. This can be explained by the fact that the effective stress of the soil increases with the decrease of the water table, and the pressure necessary to ensure the front stability is lower when the water table decreases.

The analysis of the 3D pressures influence on the settlement shows that the pressure around the shield is the most relevant. The injection pressure also has an influence on the settlement, although it is smaller compared to the pressure around the shield. On the other hand, when the tunnel face is stabilized, the face pressure influence can be neglected.

2.7.1 2D fictitious pressure determination

For each 3D modeling, 2D simulations are conducted in order to determine the 2D fictitious pressure that allows fitting the settlement obtained from the 3D simulation. Table 2.3 also presents the fictitious pressure that gives the same maximum settlement obtained from the corresponding 3D model. According to this table, there is a limited impact of the face pressure on the settlement, and it can be concluded that the additional pressure P_{add} does not influence the 2D fictitious pressure.

Figure 2.15 shows the evolution of settlements with fictitious pressure. In this figure, two curves can be identified. The first one corresponds to the configurations where the injection pressure and the face pressure have been varied. In these 2D and 3D models, the water level is constant. The

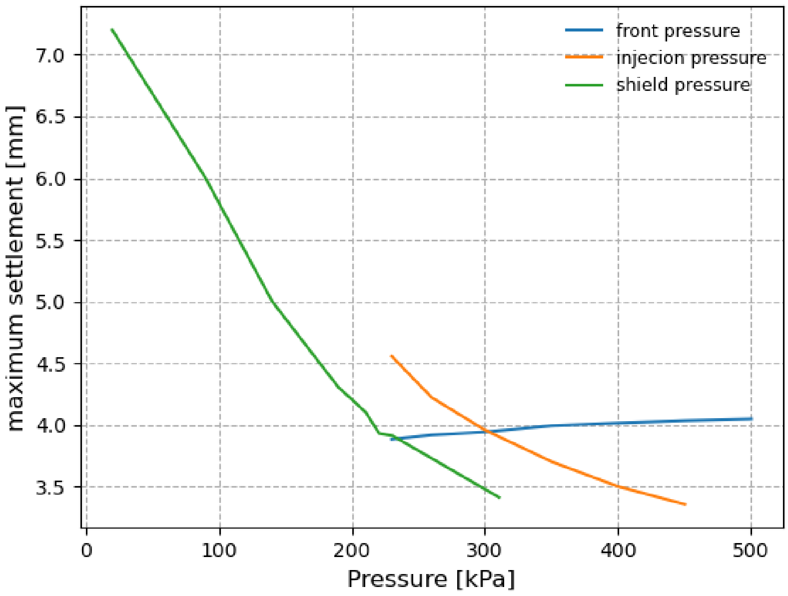

Figure 2.14: TBM pressures influence on the maximum settlement

second curve is characterized by a variation in the water level. The 2D models are calibrated on the 3D models with varying the water table level.

Concerning the models with the constant water table, the fictitious pressure varies with the injection pressure. In Table 2.3, from model 8 to model 11, a variation of 170 kPa on the injection pressure corresponds to a variation of 12 kPa on the 2D fictive pressure.

Concerning the models with the variable water table, the fictitious pressure varies with the pressure around the shield. In Table 2.3, from model 13 to model 20, with the variation of the water table from 39 NGF to 17 NGF, i.e. a variation of 220 kPa of the shield pressure, the fictitious pressure varies by 180 kPa.

Figure 2.16 presents the influence of shield pressure (P_{min}) and the injection pressure (P_{inj}) on the 2D fictitious pressure. According to this figure, two conclusions can be deduced. It is important to mention that these conclusions are only valid in the present study:

- A linear relationship can be assumed between the fictitious and injection pressure. An increase of 100 kPa of the injection pressure induces an increase of 7 kPa on the fictitious pressure.
- The shield pressure also shows a linear relationship to 2D fictitious pressure. An increase of 100 kPa of the shield pressure induces an increase of 82 kPa on the fictitious pressure.

It is important to mention that in the 2D method with an explicit approach, the fictitious pressure

Table 2.3: 2D fictitious pressure at the crown determination from the 3D pressures at the crown

Model	face pressure [kPa]	Water level [NGF]	Water pressure [kPa]	Grouting pressure [kPa]	Maximum settlement [mm]	2D pressure [kPa]
Model 1	230	30.6	227	300	3.88	207
Model 2	260	30.6	227	300	3.91	207
Model 3	300	30.6	227	300	3.94	207
Model 4	350	30.6	227	300	3.99	206
Model 5	400	30.6	227	300	4.01	206
Model 6	450	30.6	227	300	4.03	206
Model 7	500	30.6	227	300	4.04	206
Model 8	300	30.6	227	230	4.55	202
Model 9	300	30.6	227	260	4.22	204
Model 10	300	30.6	227	350	3.7	211
Model 11	300	30.6	227	400	3.5	214
Model 12	300	30.6	227	500	3.35	221
Model 13	300	39	311	300	3.41	277
Model 14	300	31	231	300	3.91	212
Model 15	300	30	220	300	3.93	204
Model 16	300	29	210	300	4.1	195
Model 17	300	28	200	300	4.2	187
Model 18	300	27	190	300	4.3	178
Model 19	300	22	140	300	5	137
Model 20	300	17	90	300	6	96

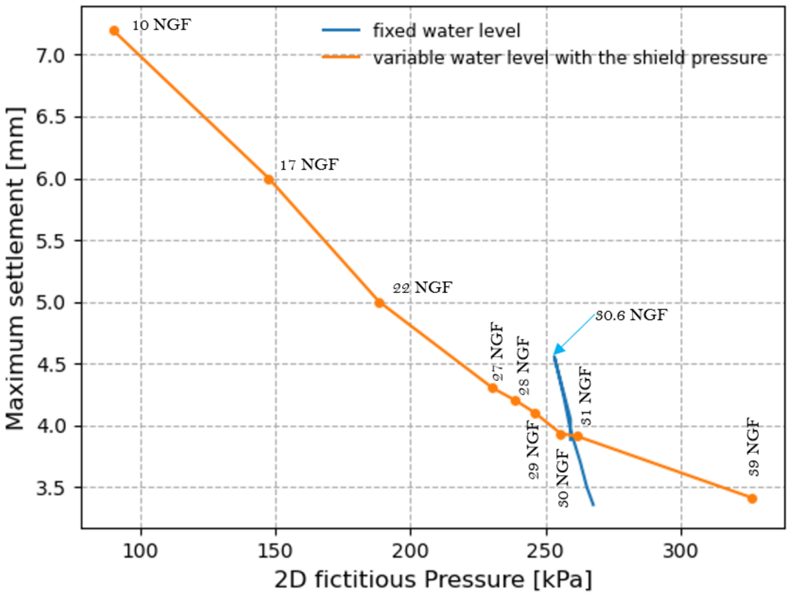

Figure 2.15: 2D fictitious pressure (at the axis) influence on the maximum settlement

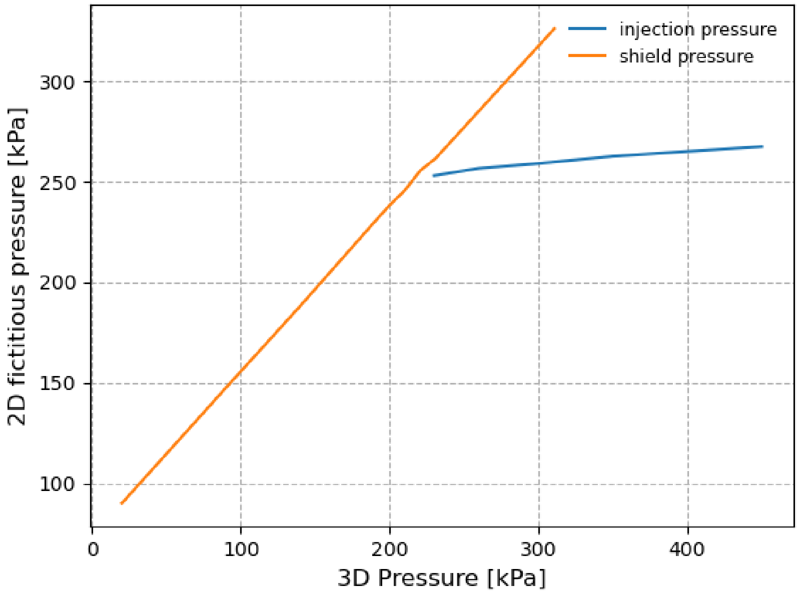

Figure 2.16: TBM pressures influence on the maximum settlement

depends on the value of the confinement loss λ. In Paris Metro Line 16 of the Grand Paris Express, the fictitious pressure determination mainly depends on P_{min}. As soon as the tunnel face is stabilized by the P_{min}, any additional pressure P_{add} has a marginal effect on the fictitious pressure. In this sense, the fictitious pressure is influenced by the shield pressure P_{min} and the injection pressure P_{inj}. Equation 2.7.1 presents the deduced formulation that links the fictitious pressure to the TBM pressures.

$$P_{fict} = 0.82P_{min} + 0.07P_{inj} \tag{2.7.1}$$

2.8 Conclusion

In this chapter, the real process of tunnel construction has been explained based on the TBM construction of the Paris Metro Line 16. During the construction of this metro line, two configurations of pressure distribution in the excavation chamber have been observed: the first configuration corresponds to the case in which the pressure at the crown is equal to the hydrostatic pressure and the second case corresponds to the pressure at the crown higher than the hydrostatic pressure.

Based on the first case, 3D modeling has been proposed to better simulate the process. However, this approach is limited due to the cost of calculation time (3 days of calculation for one model). The 2D explicit approach of the convergence-confinement method has been proposed to solve this limitation (almost 2 minutes of calculation for one model). This approach requires the application of a confinement loss and a fictitious pressure to represent the stress release and the pressures applied by the TBM, respectively.

Developing a formulation to obtain the fictitious pressure from the 3D TBM pressures required 3D simulations where the pressure at the face, the water table, and the mortar injection pressure varied. Considering a confinement loss of 0.9, 2D simulations were conducted to fit the results of the 3D simulations. Assuming the hydrostatic pressure around the shield, the fictitious pressure depends on the shield pressure and the injection pressure (P_{fict}=$0.82P_{min}$+$0.07P_{inj}$).

The formulation proposed in this chapter is based on the fact that the hydrostatic pressure is applied around the shield. Sometimes, in reality, the face pressure is higher than the hydrostatic pressure, and this may influence the shield pressure. In these cases, the proposed formulation that allows determining the fictitious pressure from the TBM pressures has to be improved.

Despite current progress in the FE simulation, a gap still remains between the FE result and the measurements (Gilleron and Bourgeois, 2018; Gilleron et al., 2021). This difference can be due to several factors such as the boundary conditions of the numerical models, the error related to the sensors measurements, and also the errors related to the soil parameters determination. When this difference is due to the soil parameters, it is essential to determine the optimum values that allow a better fitting of the FE result and the measurements.

Chapter 3

Analysis of the settlement trough induced by tunnel construction

Contents

3.1 Introduction

The use of TBM has made it possible to reduce the damage to nearby structures and infrastructures significantly. Despite the recent progress with this technology, the risks of damage to the structures in the vicinity of the tunnel persist. Numerical approaches are generally used to predict soil response to TBM construction (i.e. the surface settlement) to take corrective measures. To succeed in numerical simulations, the soil profile needs to be well represented. Presently, engineers simulate the soil with homogeneous layers with carefully chosen parameters. However, in geotechnical engineering, soil properties vary from point to point, even in so-called homogeneous soil layers. The variability in measured properties comes from different sources. The inherent variability (also known as soil heterogeneity), errors in measurement, and transformation errors can be listed as the primary sources of geotechnical uncertainties. In tunneling, the soil heterogeneity can influence the soil response to a tunnel excavated with Tunnel Boring Machine (TBM). Soil heterogeneity can be considered as a spatial variability model with the random field theory Miranda (2011). Few works are mentioned in the literature concerning the consideration of soil heterogeneity, among which the work of Miranda (2011); Xiao et al. (2017); Huang et al. (2017); Hamrouni et al. (2022) can be listed.

Among the numerical simulations, the finite element method (FEM) is becoming increasingly important in engineering practice. The three-dimensional (3D) modeling allows to represent the excavation phenomenon better as well as the application of pressures by the TBM (Galli et al., 2004; Yeo et al., 2009; Do et al., 2014). With this approach, it is possible to analyze the variation of the soil stress state during the TBM progress and to evaluate the settlement trough. However, this method is not always optimal due to its high cost in calculation time and the data required to construct the model are not always available. Hence, this approach is sometimes simplified by the two-dimensional (2D) one when the final results are concerned. This simplification procedure has already been explained in chapter 2 with the determination of the 2D fictitious pressure that accounts for the 3D TBM pressures and the adoption of a confinement loss to simulate the stress release due to the convergence of the tunnel. In the literature, the 2D simulation approach is generally used to evaluate the final settlement trough (Demagh et al., 2009; Janin et al., 2017). However, Gilleron et al. (2021) also used the 2D approach to prove that, despite the ability of the FE simulation to predict the tunnel-induced surface settlement, there is still a gap between the FE result and the field measurements. This difference may be explained by the boundary conditions, the heterogeneity of the soil conditions, the error in the field measurement and/or the lack of knowledge of the soil parameters. In this work, the uncertainties in the soil parameter are assumed to be the cause of this difference. Thanks to the work of Gaspar et al. (2014), El Kahi et al. (2020) and Noubissi et al. (2020), the problem can be solved with back analysis.

Uncertainties on soil parameters may seriously affect the TBM-induced surface settlement.

Thus, for a stratified soil layer, the soil parameters can have different influences on the surface settlement. Knowing this influence can guide the engineers on which parameters to focus for better prediction. To evaluate this influence, sensitivity analysis is generally a good tool (Tarantola et al., 2006; Tarantola and Mara, 2017). In section 3.2, the sensitivity analysis and the back analysis are performed on the TBM-induced settlement. These analyses are summarized in a paper that was submitted to the tunneling underground space and technology journal by the author of this thesis. Figure 3.1 presents the procedure followed to conduct the analyses based on the homogeneous stratified layers. This procedure can be summarized in three steps:

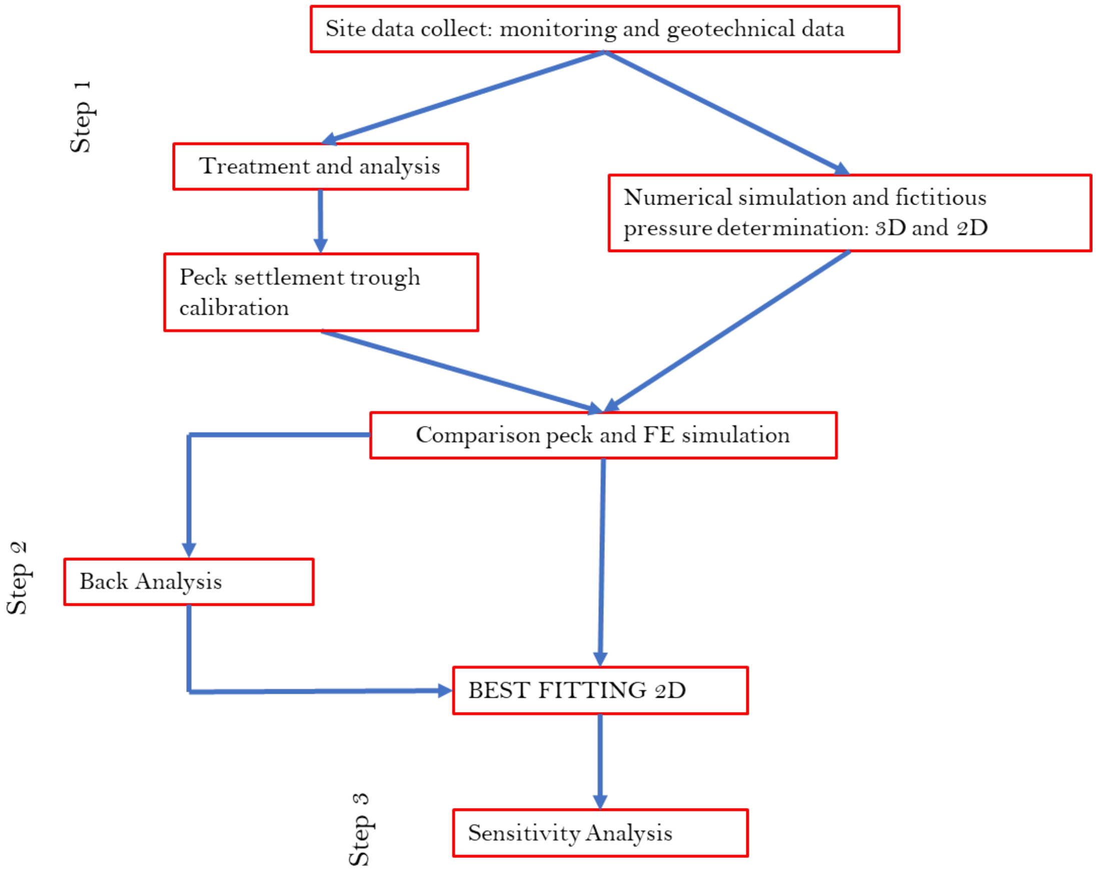

Figure 3.1: TBM induced settlement analysis chart

- Step 1: Collection and processing of the monitoring measurements; the transverse trough is calibrated by the Peck Gaussian curve (this phase is not developed in this thesis)
- Step 2: Development of an optimized back analysis method with the goal of determining the optimal set of parameters that gives the best fitting curve between the FE result and the measurement.

- Step3: The global sensitivity analysis which allows a good understanding of the influence of the soil parameters on TBM-induced surface settlement

As already mentioned, currently, for determining the final (stabilized) value of the surface settlement, 2D simulations are able to substitute 3D simulations. In this work, 2D simulations are also used to predict 3D simulation results for different phases of the TBM excavation. In order to calibrate the 3D FE model response with the 2D simulation, section 3.3 of this chapter presents the evolution of the settlement and the stresses obtained with the 3D simulations. Then, 2D simulations are conducted to fit the 3D settlement at different steps of excavation in order to compare the 2D stress field to the 3D one.

According to Miranda (2011) is possible to explicitly consider and quantify the spatial variability of soil on the tunnel-induced surface settlement. In this work, in addition to 2D finite element methods, the random field theory is finally developed in section 3.4 to study the effect of the spatial variability of soil on the TBM-induced surface settlement. The soil stiffness is considered as the only variable parameter and the application is conducted on the Paris Metro Line 12 extension.

3.2 An Optimized methodology of back-analysis and sensitivity analysis for the settlement evaluation: Case study on the TBM-extension of Line 12 in Paris area[1]

3.2.1 Introduction

The increased densification of urban areas has placed transportation system improvement high on the political agenda. Among existing solutions, tunneling appears as one of the most ingenious. Over the years, construction techniques of tunnels have increased and modernized. The mechanized process with a tunnel boring machine (TBM) has substituted the conventional excavation process for long tunnel alignment.

Excavations of tunnels in urban area can cause damage to structures/infrastructures near the tunnels (Kontogianni and Stiros, 2020). Three approaches - empirical, analytical, and numerical - are generally used to predict the soil response (Lu and Liu, 2008; Zamora Hernández et al., 2019; Huo et al., 2019; Aygar and Gokceoglu, 2021). The Finite Element Method (FEM) is the most sophisticated approach for Numerical simulations as demonstrated by Mollon et al. (2013), Do et al. (2014), Galli et al. (2004) Yeo et al. (2009), and Janin (2017). Despite the ability of the FEM to predict soil displacement due to tunnel excavation, however, a gap remains between field measurements and Finite Element (FE) results. This gap might be caused by boundary conditions, errors in measurements, heterogeneities of soil conditions, or/and lack of knowledge of soil behavior.

The use of models based on the nonlinear elastoplasticity theory to represent the nonlinear behavior of soil is always suitable since they represent a rational mechanical process (Pande and Pietruszczak, 1986). One of the challenges in using the FEM is the identification the soil parameters. Janin et al. (2017) conducted the back-analysis on the extension of the Paris Metro Line 11 to calibrate the geotechnical parameters that give the best agreement with the measurements. Demagh et al. (2009) worked on tunnel constructions in three different urban areas to fit the field measurements: Line D of the Metro network in Lyon, Line B of the Metro network in Toulouse, and the Yangtze River Tunnel in Shanghai. The authors of each study concluded that the FE settlement trough is larger than the measured one, even though the maximum value of the settlement can be calibrated accordingly. A consequence of having a larger settlement trough is the underestimated differential settlement. This is a non-conservative approach concerning the safety of structures/infrastructures. To overcome this limitation, Gilleron et al. (2021) proposed

---

[1] This paper is currently under review in the tunneling and underground space technology journal

a new constitutive model that considers the anisotropy of the soil. This approach has a restricted field of application to shallow tunnels excavated in normally consolidated and cohesionless soil. It also requires a certain number of simulations to calibrate certain parameters of the model. Moreover, this constitutive model is not implemented in current geotechnical software. However, some nonlinear elastoplastic constitutive models such as the Hardening Soil with Small Strain Model (HSSM) (Benz et al., 2009) have been used in the literature to simulate the soil behavior (Schanz et al., 2019; Likitlersuang et al., 2013).

Uncertainties on soil parameters can affect its response to excavation. When uncertainties are related to a multi-layer profile, the soil layers can have different influences on the FE result. A good understanding of this behavior can be addressed through a global sensitivity analysis as demonstrated in Gaspar et al. (2014), Noubissi et al. (2020), and El Kahi et al. (2020). Sensitivity analysis assesses the impact of individual input parameters or sets of input parameters on the response of the model. Tarantola and Mara (2017) indicated that such information is essential to point out the subset of inputs on which engineers should concentrate their efforts in future works to obtain more accurate and relevant predictions.

By performing the calculations with the FE code Zsoil V18.05 (Truty et al., 2020) and using the HSSM to simulate the soil behavior, this paper has two main goals. The first one is to evaluate the influence of each soil stiffness on the surface settlement trough via global sensitivity analysis. The second one is to fit the real cross-section surface settlement trough induced during the TBM-tunnel construction of the Paris Metro Line 12. Concerning the second goal, two approaches are developed: the back analysis conducted with the most influential parameters obtained from the sensitivity analysis and the back analysis conducted with all the soil stiffnesses. The two obtained settlement curves are then compared to highlight the advantage of working with the most influential parameter. Finally, the back analysis results obtained with all the stiffnesses are applied to another cross-section to compare the FE settlement curve width to the real settlement one for validation.

3.2.2 Back analysis procedure

The success of a back-analysis depends on the algorithm used to calibrate the measurements. This section presents the different optimization algorithms and explains the procedure followed to conduct the back analysis.
Back analysis problems are often solved using an approach that is based on an iterative procedure. A constrained nonlinear optimization technique was performed by minimizing a regression loss function ($\mathcal{L}(\theta_g)$) or a weighted objective function ($S(\theta_g)$) that assesses the discrepancy between

measurement/experimental and modeled behavior. θ_g denotes the vector of parameters of the FE model. There are two main types of optimization algorithms (Espada and Lamas, 2017):

- The classical algorithms use the first and/or second derivatives of the objective function. These algorithms also use specific constraints to guide the search process and are based on deterministic transition rules for selecting the next set of points in the sequence.
- The non-traditional algorithms have been receiving more attention recently. These algorithms use stochastic search methods and do not require the derivatives of the objective function.

The type of objective function determines the choice of the algorithm. When the objective function is smooth-shaped, the classical algorithm presents higher performance compared to the non-traditional algorithm. The drawback of the classical algorithm is that it can converge to a local minimum. The non-traditional algorithms may be able to obtain a global minimum but they are often time-consuming and require a large number of iterations. However, the optimization toolboxes with a large package of minimization algorithms are now available to strongly compute local and global minima searches.

This paper applies a non-traditional algorithm implemented in Python. This algorithm requires some parameters such as the function to be minimized, the bounds of the variables, and the initialization type of the population. This section implements a back-analysis procedure to identify the stiffness of the multilayer soil profile. Using the FEM results requires:

- The field measurements of the settlement trough as an input data;
- The 2D FEM simulating the tunnel construction and providing the surface settlement trough;
- An objective (discrepancy or error) function, that evaluates the difference between the FEM result and the field measurements;
- A suitable optimization algorithm that minimizes the objection function.

Figure 3.2 presents the different steps that constitute the back-analysis procedure.

3.2.2.1 Field measurements and project overview

During the excavation, the TBM encountered a multilayer geological configuration as shown in figure 3.3. In this paper, the analyses are conducted on the green cross section.

Sensors have been installed at the ground surface to record the soil movement during the tunnel extension. Figure 3.4 presents the plan view of the tunnel alignment with the position

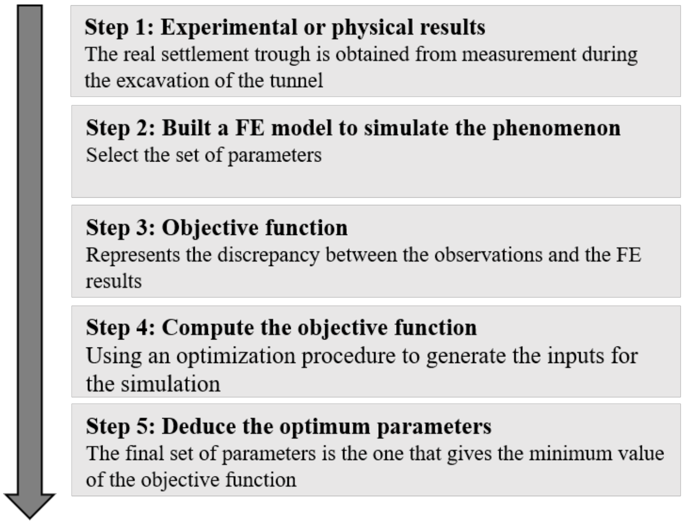

Step 1: Experimental or physical results
The real settlement trough is obtained from measurement during the excavation of the tunnel

Step 2: Built a FE model to simulate the phenomenon
Select the set of parameters

Step 3: Objective function
Represents the discrepancy between the observations and the FE results

Step 4: Compute the objective function
Using an optimization procedure to generate the inputs for the simulation

Step 5: Deduce the optimum parameters
The final set of parameters is the one that gives the minimum value of the objective function

Figure 3.2: Flow chart of the back-analysis procedure

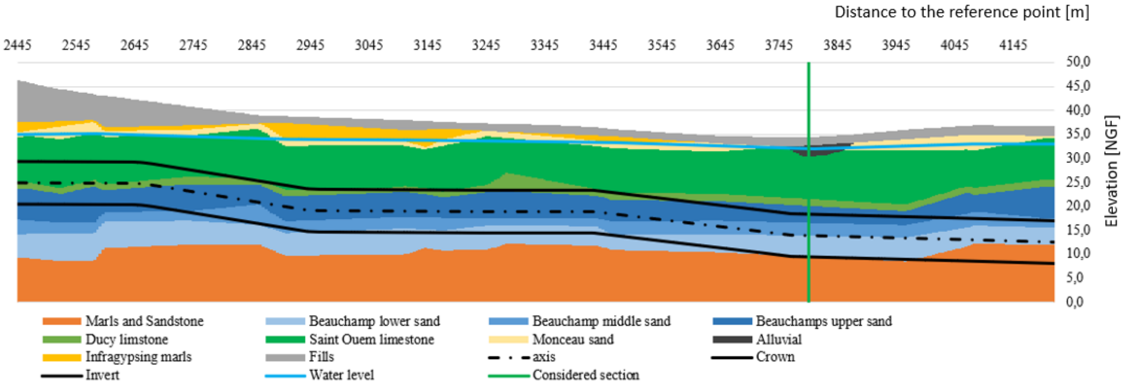

Figure 3.3: Geotechnical profile of the extension of the Metro line 12

of the sensors. The reference point is at the beginning of the first extension of the line (which is not presented in this figure). Figure 3.5 represents the normalized vertical displacement of sensor 2_3819. The sensor is located at the ground surface at 4220 m to the reference point, along the tunnel axis, and close to the receiving shaft. Before the passage of the cutter head in a given section, the settlement progression is slow; less than 10% of the final settlement. During the passage of the TBM, the settlement increases significantly and reaches 70%-80% of its final value. After the passage of the tail shield, the rate of displacement becomes slow again, and the settlement stabilizes. This response of the soil to the excavation process by a TBM had been described in the literature, and Zhang et al. (2019) named it the Pearl curve.

The Pearl curve shows the evolution of the settlement regarding the TBM advance. The stabilized value of the Pearl curve corresponds to the final value of the settlement. It is possible

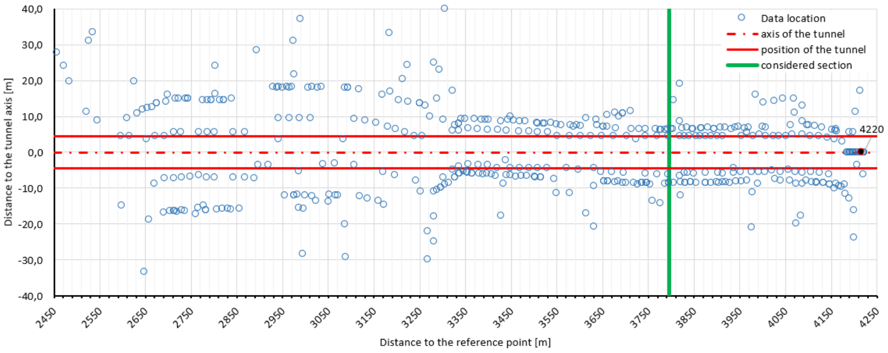

Figure 3.4: Top view of the position of sensors and considered section

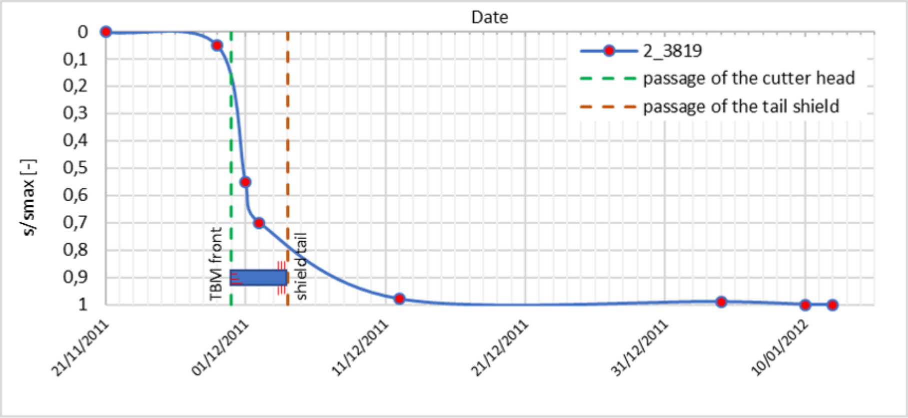

Figure 3.5: Vertical displacement evolution in time recorded by the sensor 2_3819; Time of crossing the respective section = 4 days

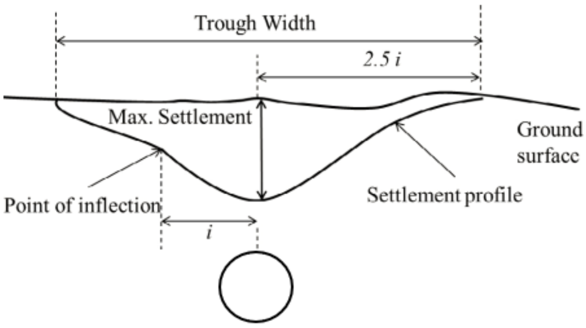

Figure 3.6: Schematic of the surface settlement induced by tunnel excavation

to obtain the whole settlement curve of a monitored cross-section to the tunnel path. For a greenfield configuration, the settlement profile induced by the tunnel excavation can be described by a Gaussian curve Peck (1969). This curve is characterized by two parameters, the maximum settlement at the tunnel axis (s_{max}) and the inflection point (i) as presented in figure 3.6 and in equation 3.2.1, where x represents the transversal distance to the tunnel axis.

$$s = s_{max} \exp(\frac{-x^2}{2i^2}) \tag{3.2.1}$$

3.2.2.2 Finite Element Method (FEM)

There are two approaches to conduct a tunnel excavation simulation with FEM. The 3 Dimensional (3D) is the more sophisticated one since the 3D excavation effects and the TBM pressures are correctly simulated, but it needs generally more parameters and sometimes powerful computers with a large amount of storage capacity to run the calculation and store the results. This method can also be very costly and time-consuming. Due to its rapidness and simplicity, the 2D approach is the most widely used for tunneling projects (Bernaud and Rousset, 1992; Lee et al., 1999; Dias, 2011; Do et al., 2014).

Two-dimensional (2D) Finite Element simulation

The 2D FE methods are adopted and the simulation steps are presented in this section. Karakus (2007) summarized and compared the different methodologies for a bi-dimensional simulation of tunnel construction. The convergence confinement method (Panet and Guenot, 1983), the stiffness reduction method (Swoboda, 1979), the disk calculation method (Schikora and Ostermeier, 1988), the hypothetical modulus of elasticity soft lining method (Powell et al., 1996), the gap volume (Rowe and Kack, 1983) and the volume loss method (Addenbrooke and Potts, 2001) can be listed. Karakus (2007) concluded that the best choice of the technique to fit the measurements is the convergence-confinement with the lining modeled with beam elements. The application of the convergence-confinement method by adopting the 2D FE model can be an efficient alternative to simulate the 3D effect of the excavation. Aristaghes and Autuori (2001) succeeded in applying the explicit convergence-confinement method for the case of a pressurized TBM. The application of this method requires the definition of two parameters known as the confinement loss and the 2D fictitious pressure.

Figure 3.7 shows half of the 2D mesh used for the FE simulation due to the symmetry of the model. This numerical model is a plane strain analysis type. The mesh is constituted by 3250 quadratic elements and 3350 nodes with 2 degrees of freedom except for the nodes along the boundaries. The model is 50 m wide and 34.4 m high to avoid boundary effects. The model is blocked in the horizontal direction on both the left and right sides. The bottom of the model is fixed horizontally and vertically, and the upper boundary is set free. The tunnel lining is modeled using the beam element with 3 degrees of freedom. The explicit approach of the convergence confinement method described by Aristaghes and Autuori (2001) is adopted to conduct the 2D

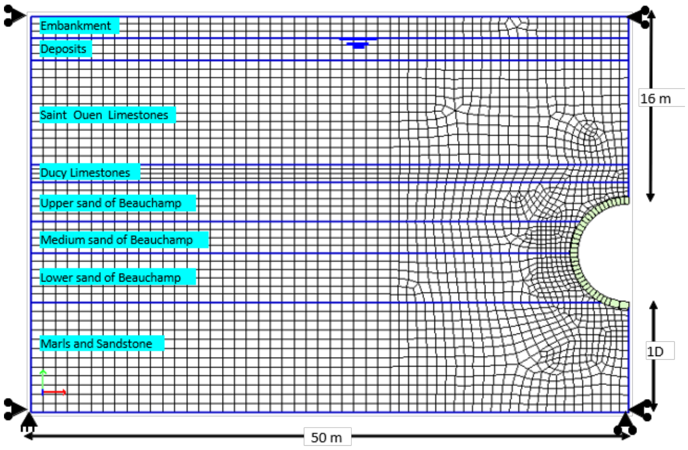

Figure 3.7: General view of the 2D numerical model

FE simulation. Two steps can describe the procedure as follows.

1) The Excavation procedure

The excavation of the tunnel is modeled by the application of the global confinement loss λ. Bernaud and Rousset (1992), Panet and Guenot (1983) and, Panet et al. (2001) proposed the value of λ as a function of the tunnel geometry and the distance of the considered section to the face for traditional excavation. In this paper a value of 0.9 is assumed according to Panet and Guenot (1983) and Aristaghes and Autuori (2001) to simulate the confinement loss of the soil due to the excavation.

2) Concrete lining segments construction

Concrete linings are simulated with 40 cm beam elements with an elastic stiffness of 13.5 GPa. The gap between the lining and the surrounding soil is filled with mortar by applying the injection pressure. The pressure is then removed with the hardening of the mortar. This phenomenon is considered in the 2D simulation by the application of a 2D pressure along the excavated area before the installation of the linings. The applied 2D fictitious pressure is calibrated to obtain the same surface settlement trough as the 3D model.

Soil parameter and constitutive model

Pressuremeter tests were conducted to obtain the soil parameters. According to Olivier (2006), it is possible to obtain the stiffness of soil from the Menard's modulus E_m as presented in equation 3.2.2.

$$E = k\frac{E_m}{\alpha} \tag{3.2.2}$$

Some constitutive models are used in the literature to simulate the soil behavior for the TBM-induced surface settlement. Shahin et al. (2019) explained that in some instances, using an elastic model to simulate the soil behavior can predict the surface settlement trough that occurs from the tunnel construction. However, with this constitutive model, the analysis does not consider various features of the soil, including plastic behavior. Gilleron et al. (2016) and Janin et al. (2015) adopted the nonlinear elastoplastic models, such as the hardening soil constitutive model (HSM) (Schanz et al., 2019) to calibrate the geotechnical model on the measurements. According to Schanz et al. (2019), the HSM constitutive model is used to simulate the behavior of both soft and stiff soils. The model requires three stiffnesses (the unload-reload elastic stiffness E_{ur}, the secant stiffness in standard drained triaxial test E_{50}, and the tangent stiffness for primary oedometer loading E_{oed}) and the plastic parameters (the cohesion c', the frictional angle ϕ' and, the dilatancy angle ψ') to describe the soil behavior. Zhao et al. (2015) and Zhang et al. (2018) improved their prediction by adopting the enhanced version of the HSM known as the Hardening Soil with Small Strain Model (HSSM) (Benz et al., 2009). The HSSM is able to handle the strong stiffness variation with increasing shear strain amplitudes and the nonlinear elastic stress-strain relationship in the domain of small strains. The stiffness at very small strain E_0 and the deviatoric strain at 70% of the initial shear modulus are the two additional parameters compared to the HSM. Generally, due to the lack of $in-situ$ and laboratory tests, correlations are adopted between the stiffnesses and the Menard's modulus.

For their predictions, Zhang et al. (2018) and Zhao et al. (2015) used the HSSM with the following correlation between the stiffnesses; $E_{ur} = 3E_{50}$, $E_0 = 6E_{50}$ and $E_{oed} = E_{50}$. In this work, different assumptions are proposed on the correlation factors between the stiffnesses i.e $E_{ur} = 2E_{50}$, $E_0 = 8E_{50}$ and $E_{oed} = E_{50}$ because better result are obtained with them. Triaxial consolidation and drained tests are conducted to illustrate the behavior of the two samples simulated using the HSSM with the previous correlations. Figure 3.8 presents the evolution of the stiffness curves. In this figure, the evolution of the two curves is the same till an axial deformation of 10^{-5}. After that value, the slope of the proposed sample decreases slower than the one that is generally used. According to these curves, the proposed correlation makes the sample stiffer than what is generally used. Table 3.1 presents the soil parameters used in the FE simulations.

3.2.2.3 The objective function

The goal of the objective function is to evaluate the discrepancy between the numerical results and the field measurements. From a settlement trough, one can deduce the maximum settlement and the volume loss that represent the measurements. In the 2D result, the volume loss is the area between the settlement trough and the x-axis. According to Attewell (1977) the volume loss can be calculated from equation 3.2.3. Two errors can be distinguished as presented in figure 3.9:

$$V_{loss} = \sqrt{2\pi} S_{max} i \tag{3.2.3}$$

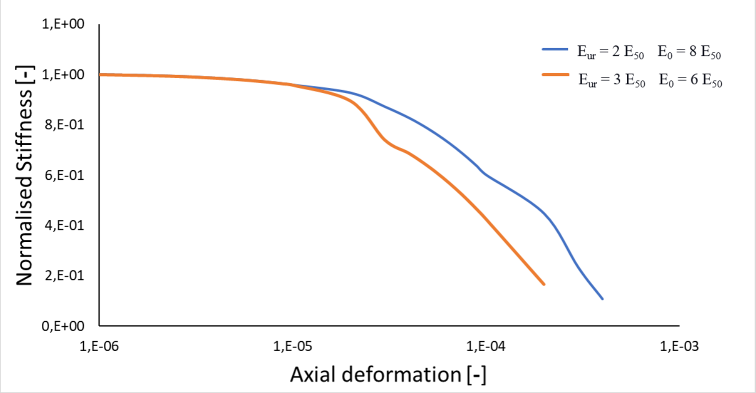

Figure 3.8: Comparison of the two sample behaviors

Table 3.1: Pressuremeter results and laboratory test results

Layers		γ $[kN.m^{-3}]$	E_m $[MPa]$	α $[-]$	E_{50} $[MPa]$	C' $[kPa]$	ϕ' $[°]$
Fill	R	20	8.5	0.5	25	0	25
Alluvial	AL	20	4	0.5	12	0	20
Monceau sand	SM	21	20	0.5	25	20	25
Saint-Ouen Limestone	CSO	19	12	0.5	35	0	25
Ducy Limestone	CD	19	6.5	0.5	20	0	25
Beauchamp upper sand	SB sup	21	38	0.33	170	0	30
Beauchamp middle sand	SB med	20	28	0.5	80	60	15
Beauchamp lower sand	SB inf	21	35	0.33	150	0	30
Marls and sandstones	MC	21	48	0.5	140	30	30

- The maximum settlement error S^{err}_{max} is presented in equation 3.2.4; this is the absolute ratio between the maximum settlement of the FE result (S^{FE}_{max}) and the maximum settlement of the measurements (S^{mes}_{max}).

$$S^{err}_{max} = |\frac{S^{FE}_{max}}{S^{mes}_{max}}| \tag{3.2.4}$$

- The volume loss error V^{err}_{loss} is presented in equation 3.2.5; The volume loss error is the square of the difference between the volume loss of the FE result V^{FE}_{loss} and the volume loss of the field measurements V^{mes}_{loss} results normalized by the volume loss of the field measurements.

$$V^{err}_{loss} = (\frac{V^{FE}_{loss} - V^{mes}_{loss}}{V^{mes}_{loss}})^2 \tag{3.2.5}$$

When the FE maximum settlement is lower than the measured maximum settlement, it can be possible that both curves give the same volume loss. This is a case to be avoided because the FE settlement curve will then be larger than the measured one as presented in figure 3.10. In this paper, the objective/loss function ($\mathcal{L}(\theta_g)$) is a conditional function, and its value depends on the value of the maximum settlement error. The vector (θ_g) represents the vector formed by the stiffness E_{50} of the soil layers.

- If the maximum settlement error is lower than 1, the objective function is set to a high value and it is not taken into account.
- Otherwise, the objective function is set to $\mathcal{L}(\theta_g) = V_{loss}^{err}$

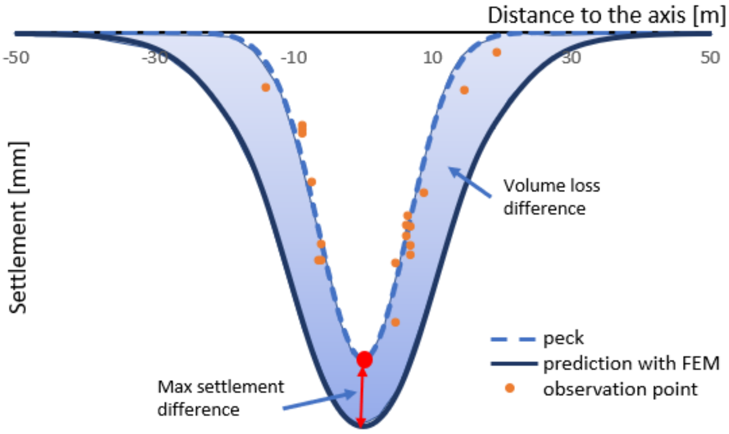

Figure 3.9: Maximum settlement error and volume loss error representation

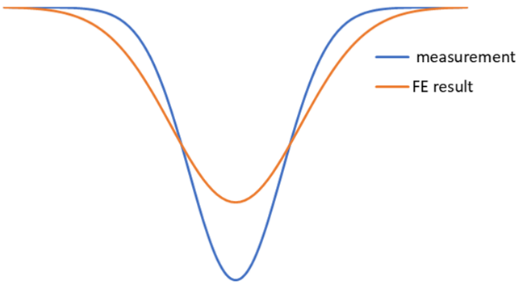

Figure 3.10: Situation to avoid; the S_{max} of the FE result is lower than the S_{max} of the measurement

3.2.3 Global Sensitivity analysis: Fourier Amplitude Sensitivity Test

Several methods exist to conduct a sensitivity analysis. Among them, the Fourier Amplitude Sensitivity Test (FAST) is highly useful (Tarantola et al., 2006; Tarantola and Mara, 2017). This technique gives the possibility to find the two types of sensitivity indices; the first-order sensitivity index measures the marginal effect of one input and the total sensitivity index, considers the first-order index and the interaction effect between the parameters.

Based on the Sobol indices, the influence of the input parameters on the response of a model can be quantified (Sobol, 1993). The analysis of the variance decomposition helps in determining the Sobol indices. The variance-based sensitivity has the goal of evaluating how the variance of an input or a group of input parameters influences the variance of the output of a model. It is always possible to decompose a square-integrable function y as a sum of elementary functions (Hoeffding, 1948). Under certain conditions, this decomposition is unique (Sobol, 1993). The variance of the output y can then be written as equation 3.2.6:

$$Var(y) = \sum_{i=1}^{p} D_i(y) + \sum_{i<j}^{p} D_{ij}(y) + ... + D_{12...P}(y) \tag{3.2.6}$$

Where $D_i(y) = Var[E(y|x_i)]$, $D_{i,j}(y) = Var[E(y|x_i x_j)] - D_i(y) - D_j(y)$ and so on for higher-order interactions. In this equation, E represents the expectation. Then, the Sobol indices can be defined as the ratio of the elementary variance over the total variance as presented by equation 3.2.7:

$$S_i = \frac{D_i(y)}{Var(y)}, S_{i,j} = \frac{D_{i,j}(y)}{Var(y)}, ... \tag{3.2.7}$$

3.2.3.1 The First Order Sensitivity index

The general method of the Fourier Amplitude Sensitivity Test (FAST) was first introduced by Cukier et al. (1975). Its principle relies on the fact that a model can be expanded into a Fourier series. Combining the Fourier series with specific frequencies for stochastic parameters, the Fourier coefficients can be used to estimate the partial variance of individual input parameters of the model (Tarantola et al., 2006). The essential task for computing the sensitivity index is the choice of the appropriate frequencies for the input parameters. The set of frequencies is chosen to avoid interferences between higher harmonics (Tarantola et al., 2006). Tarantola et al. (2006) developed an algorithm for the determination of the first-order sensitivity indices. The input parameters are generated through Monte Carlo simulation and follow a periodic curve that explores all the space. The output of the code is evaluated, the Fourier coefficients are computed, and the first-order sensitivities are deduced. Equation 3.2.8 presents the minimum number of simulations to conduct.

$$N_s = 2 \cdot M \cdot \omega_{max} + 1 \tag{3.2.8}$$

In this equation, M is the interference order and depends on the nonlinearity of the model (generally 4 but can go up to 10) and w the set of frequencies. However, these methods are expensive in terms of the number of model calculations with the increasing number of input parameters (Iooss and Lemaître, 2015). To overcome this limitation, Tarantola et al. (2006) coupled FAST with a Random Balanced Design (RBD) to obtain the first-order sensitivity indices.

For the RBD FAST, the input space is explored using the same frequency w. The set of input parameters is randomly generated for a certain number n of calculations, and the way of randomization is saved. The model is then evaluated at each point. The outputs are re-ordered according to the randomization that first affected the input parameters. The Fourier transformation is then computed for each re-ordered output. The highest harmonics of the frequencies (w, $2w$..., Mw) are used to obtain the first-order sensitivity indices. Knowing the first-order sensitivity is not enough to conclude its participation in the response of a model (Tarantola et al., 2006), the total order sensitivity indices also have to be carried out.

3.2.3.2 The Total Order sensitivity with Extended FAST

The Extension of the FAST (EFAST) algorithm based on the Sobol method has the advantage of computing the total order sensitivity indices. These indices take into account the interference among inputs. In this procedure, a high value of frequency w_{max} is set to generate the input of interest, while the other values remain small and do not need to be free in interference (Tarantola and Mara, 2017). The total number of computations is denoted by N. The highest harmonics at the frequencies $(w_{max}, w_{max+1}, , N/2)$ are used to obtain the total sensitivity indices.

3.2.4 Analysis of the results

In this section, the result of the sensitivity analysis is first presented. After that, the back analysis is conducted on the most influential parameters among the soil stiffnesses and on all the soil stiffnesses. The 2 obtained best-fitting curves are then compared to highlight the benefit of working only with the most influential parameters.

3.2.4.1 Global sensitivity analysis results

In this section, the influence of the soil stiffnesses variability on the settlement trough is studied. Given some uncertainties, it is possible to determine the influence of the parameters on the settlement trough through sensitivity analysis. This analysis is an aid to the decision-making since engineers can be warned which parameter to focus on for the geotechnical investigations and risk management.

As already mentioned, the HSSM is used to simulate the soil behavior. Since the variability of the $in-situ$ parameters is not available, for the sake of simplicity, the input parameters follow a uniform distribution with a coefficient of variation (CV) of 30% as shown in Table 3.2.

Table 3.2: Values of parameters used for sensitivity analysis

Layers		E_{50}	
		Mean$[MPa]$	CV
Fill	R	25	0.3
Alluvial	AL	12	0.3
Saint-Ouen Limestone	CSO	35	0.3
Ducy Limestone	CD	20	0.3
Beauchamp upper sand	SB sup	170	0.3
Beauchamp middle sand	SB med	80	0.3
Beauchamp lower sand	SB inf	150	0.3
Marls and sandstones	MC	140	0.3

The RBD-FAST and EFAST methods allowed the determination of the first-order (FOS) and total (TS) sensitivity indices of the input parameters on the settlement trough respectively. Figure 3.11 shows the results of the sensitivity analysis on the maximum settlement and on the inflection point. For the two results, the FOS and the TS are almost the same. This implies that in the FE code (black box) the interaction between the input parameters can be neglected.

Concerning the maximum settlement, the stiffness of the Saint Ouen limestone (CSO) is the most influential with a sensitivity index of about 42% followed by the upper sand of Beauchamp (SB sup) with a sensitivity index of 40%. Medium sand of Beauchamp (SB med) and the Ducy limestone (CD) have a sensitivity index of about 5%. Fixing a threshold at 5%, the stiffness of fills (RB), alluvions (AL), lower sand of Beauchamp (SB inf), and calcareous marlstone (MC) are not influential on the maximum settlement.

For the inflection point, the stiffness of the Saint Ouen limestone (CSO) is the most influential with a sensitivity index of about 45% followed by the upper sand of Beauchamp (SB sup) with a sensitivity index of 30%. The lower sand of Beauchamp (SB inf) with a sensitivity index of 18% is also an influential layer for the inflection point. A value of 5% of the threshold allows us to conclude that the fills (RB), the alluvions (AL), the Ducy limestone (CD), the medium sand of Beauchamp (SB med), and the calcareous marlstone (MC) are not influential layers.

In both cases (maximum settlement and inflection), the Saint Ouen limestone (CSO) is the most influential layer. This can be explained by its higher thickness and its position with regard to the tunnel. The calcareous marlstone (MC) is not influential because it is located below the tunnel section and has no influence on the response of the model. Concerning the fills and the alluvions, they are not influential, perhaps because of their weak thickness and their position relative to the tunnel.

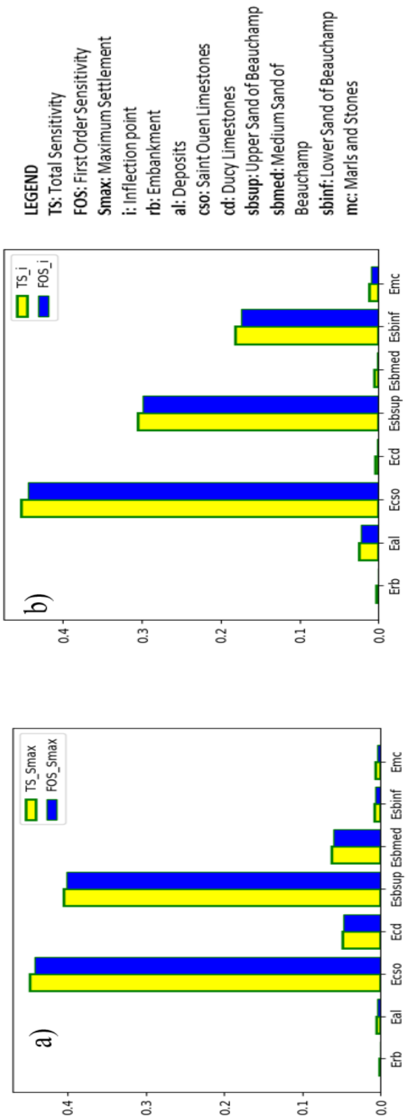

Figure 3.11: Sensitivity analysis considering E50 on (a) the maximum settlement and (b) the inflection point

3.2.4.2 Optimization result and interpretation

The Python package known as the optimized differential evolution function is used for the calculation of the objective function. The optimum value of the parameters (E_{50} of the 8 layers) that gives good agreement between the FE result and the field measurements is obtained at the end of the optimization process. Two types of simulations are conducted to illustrate the effect of the ratio between stiffnesses; the first simulation is done assuming as Zhao et al. (2015) and Zhang et al. (2018) that, $E_{ur} = 3E_{50}$, $E_0 = 6E_{50}$ while the back analysis is conducted with $E_{ur} = 2E_{50}$, $E_0 = 8E_{50}$.

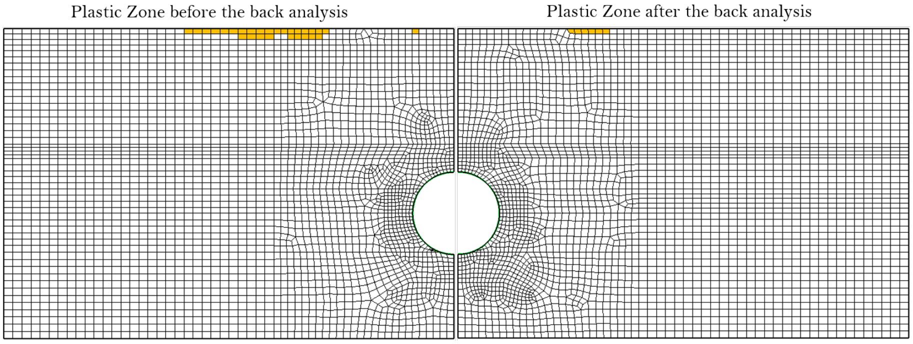

Figure 3.12: Plastic zone in the model before and after the back analysis

Table 3.3: Soil stiffnesses evolution; Back Analysis conducted on the most influential stiffnesses

Layers		Initial E_{50} $[MPa]$	Final E_{50} $[MPa]$	$\frac{E_{50final}}{E_{50initial}}$ [-]
Saint-Ouen Limestone	CSO	35	27	0.8
Beauchamp upper sand	SB sup	170	149	0.9
Beauchamp lower sand	SB inf	150	152	1.01

Figure 3.12 presents the plastic zones of the model before and after the back analysis. It is important to note that there is no plastic zone around the excavation and inside the model except for some elements at the surface. This result confirms that the plastic behavior is not mobilized since the back analysis is conducted by varying only the stiffnesses. As explained by Leca and New (2007) the settlement trough at the surface is divided into a compression part and an extension part creating a shear zone at the inflection point. An element of soil in the fill layer reaches the plasticity faster in the initial model than in the final model with the same deformation because it has a greater stiffness. For this reason, the plastic zone of the initial model is larger than the one of the model after the back analysis.

As already mentioned in this section, the first back analysis is conducted on the most influential stiffnesses. Two hundred and eighty (280) iterations were conducted to obtain the best fitting curve. Figure 3.13 presents the comparison between the surface settlement trough using Zhao et al. (2015) and Zhang et al. (2018) assumption, the surface settlement trough before and after the back Analysis procedure and the measurements. The measurements are fitted with the Gaussian peck curve. According to this figure, before the back analysis, the maximum value of the FE curve is lower than the one of the field measurements and the curve width is larger. On the contrary, after the back analysis, the maximum settlement and the curve width are well fitted. Table 3.3 compares the initial values and the optimized (final) values of the stiffness E_{50} of the most influential parameter i.e Saint-Ouen Limestone, Beauchamp upper sand and Beauchamp lower sand obtained from the back analysis. According to this table, the value of the stiffness

Table 3.4: Soil stiffnesses evolution; Back Analysis conducted on all the soil stiffenesses

Layers		Initial E_{50} $[MPa]$	Final E_{50} $[MPa]$	$\frac{E_{50final}}{E_{50initial}}$ [-]
Fills	R	25	10	0.4
Alluvial	AL	12	5	0.42
Saint-Ouen Limestone	CSO	35	40	1.14
Ducy Limestone	CD	20	39	2
Beauchamp upper sand	SB sup	170	60	0.36
Beauchamp middle sand	SB med	80	100	1.13
Beauchamp lower sand	SB inf	150	60	0.36
Marls and sandstones	MC	140	120	0.86

decreases after the back analysis.

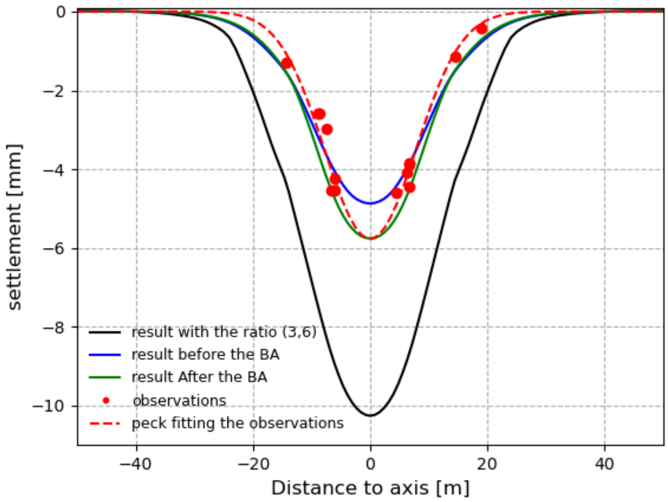

Figure 3.13: Fitted measurements calibration through the back-analysis result

The second back analysis is conducted on all the soil stiffnesses to evaluate how evolves the best fitting curve. Almost one thousand iterations were conducted to obtain the best fitting curve. Table 3.4 compares the initial values and the optimized (final) values of the stiffness E50 obtained from the back analysis. For some layers, the stiffness decreases while it increases for others. Figure 3.14 compares the back analysis result conducted on all the soil stiffnesses and the back analysis conducted on the three most influential variables. According to this figure, the two settlement curves fit well the field measurements. Even though the back analysis conducted on all the parameters fits better the width of the settlement trough there is not a big difference between the two curves.

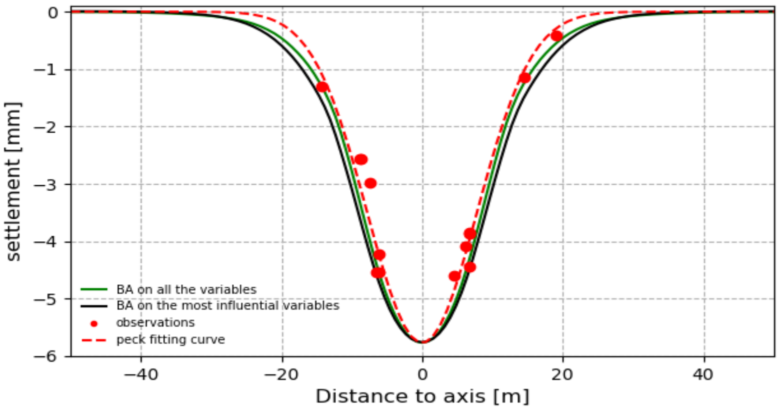

Figure 3.14: Comparison between the BA result conducted with the most influential parameters and the BA conducted with all the parameters

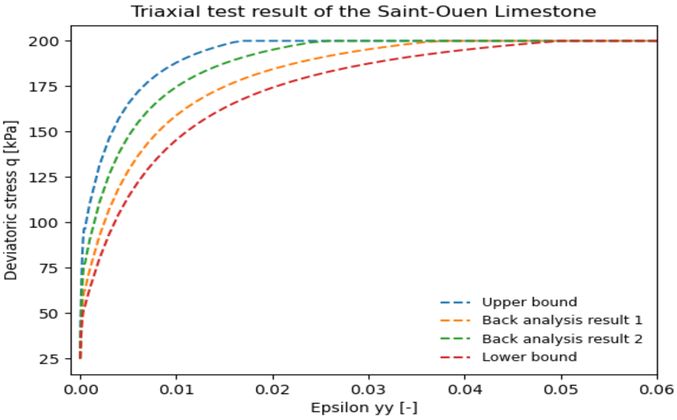

Figure 3.15: Triaxial test results comparing the Saint Ouen limestone behavior obtained after back analysis with the most influential parameters (back analysis result 1) and after back analysis with all the parameters back analysis result 2)

In order to understand the behavior of the soil in using these two back analysis results, several triaxial tests are conducted on the most influential soil layer according to the sensitivity analysis result i.e the Saint-Ouen limestone. Figure 3.15 presents the comparison of the Saint-Ouen limestone behavior obtained after back analysis with the most influential parameters (back analysis result 1) and after back analysis with all the parameters (back analysis result 2). This figure also presents the Saint-Ouen limestone curve behavior bounds obtained with a CV of 30%. The area located between these two curves represents the possible behavior of the soil. According to this figure, the behavior obtained using the 3 most influential parameters for the back analysis is softer than the behavior obtained using all the parameters.

The advantage of conducting back analysis on the most influential parameters has been presented in this section. However, in the following of this work, the back analysis result obtained with all the parameters is adopted. In order to understand how evolves the stress in the models (before and after the back analysis procedure using the adjusted modulus), a comparison is done between the mean principal stress p and the deviatoric stress $\sqrt{j_2}$ distribution of the two models (before the back analysis and after the back analysis). These stresses come from the decomposition of the main stresses tensor (the formulations are explained in chapter 5). Figure 3.16 and figure 3.17 present respectively the difference of the deviatoric stress ($\sqrt{j_2}_{final} - \sqrt{j_2}_{initial}$) and the difference of the average principal stress ($p_{final} - p_{initial}$) between the final model and the initial model of the back analysis. The deviatoric stress $\sqrt{j_2}$ and the mean principle p stress in the model at the tunnel crown are smaller after the back analysis procedure than before the back analysis. According to this result, the layer located at the tunnel crown (the Beauchamp upper sand) must be softer after the back analysis than before the back analysis to obtain the same settlement as the measurements. This result is in agreement with the parameters presented in table 3.4.

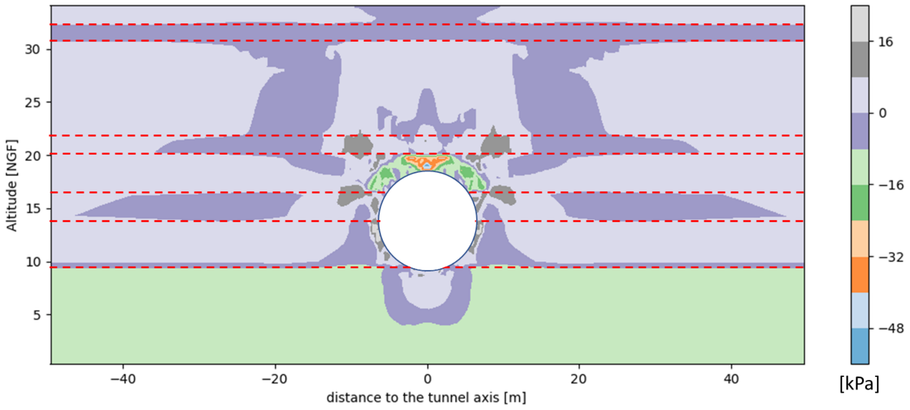

Figure 3.16: Difference of the final model and the initial back-analysis one in terms of the deviatoric stress: A negative value means that the $\sqrt{j_2}$ after the BA is lower than the $\sqrt{j_2}$ before the BA.

In order to validate the back analysis result, the parameters that come from the procedure are used to conduct a FE simulation at a second cross-section (4000 m to reference point). At this cross-section, the water table is at 32.7 NGF and the tunnel axis is located at 13.3 NGF. This section is constituted by an additional layer (the Monceau sand) whose parameters were not optimized. These latter are taken from table 3.1 following the proposed correlation coefficient among the stiffness of the HSSM i.e $E_{ur} = 2E_{50}$, $E_0 = 8E_{50}$. This 2 m thickness layer is located between the Fills and the Saint-Ouen limestones and there is no more alluvial. Figure 3.18 presents the FE settlement trough and the measurement fitted with the Gaussian Peck formulation. The

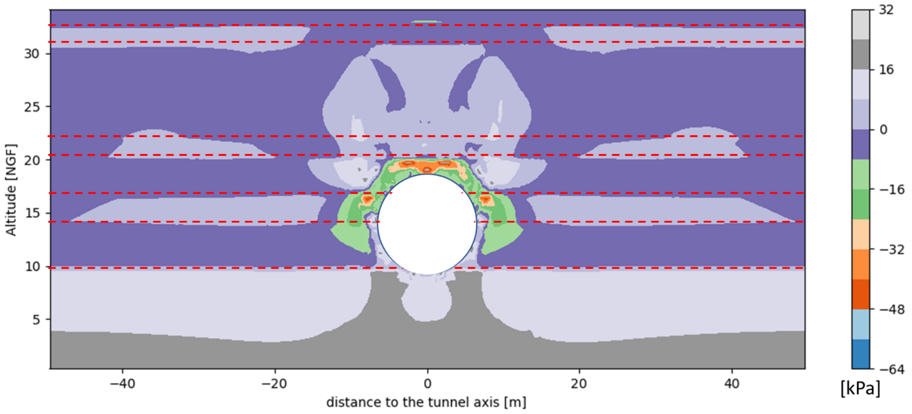

Figure 3.17: Average stress (p) difference between the final and the initial model of the back analysis : A negative value means that the p after the BA is lower than the p before the BA with p a positive value.

two curves are very close so, the back analysis parameters can be validated.

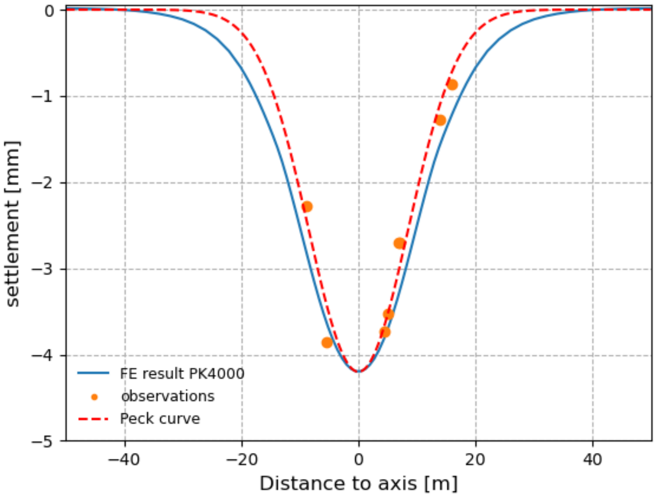

Figure 3.18: Numerical result and field measurement at the second section (4000 m to the referent point)

3.2.5 Conclusion

In this work, global sensitivity analysis and an optimized back analysis are applied on the Paris Metro Line 12 extension. the global sensitivity analysis is conducted to evaluate the influence of the soil parameter on the surface settlement trough due to the uncertainties on the soil parameters. The sensitivity analysis highlights the influential layers on the settlement trough. The results of this analysis show that the relative position of the layer to the tunnel crown and the thickness of the layers play an essential role in the sensitivity analysis results.

After that, a back analysis is conducted with the most influential parameters. An objective function measuring the gap between the FE result and the real settlement trough is developed. The non-traditional algorithm of a Python package known as the optimized differential evolution function is used to calculate the objective function by searching for the optimum value of the stiffnesses of the multilayer soil profile. The surface settlement trough that comes from the back-analysis procedure is better than the one commonly proposed in the literature regarding the width of the curve. Another back analysis is also conducted with all the soil stiffnesses and the 2 best fitting curves (with the most influential parameters and with all the soil parameters) are compared. According to these results, conducting the analysis with the most influential parameters is less time-consuming but the result is not very accurate. The back-analysis parameters (considering all the soil layers) are used to conduct a FE simulation on a second cross-section of the Line 12 tunnel path and the settlement trough obtained is very close to the measurements.

The analyses presented in this work were conducted using the 2D FE method. Although this method has some advantages as explained in this work, it does not accurately represent the soil response during TBM construction because this procedure is actually a 3D problem. In the next section, the 3D simulation of the Paris metro line 12 will be conducted and the different steps of excavation will be calibrated with 2D FE simulation. The goal of this analysis is to evaluate the possibility of representing the 3D excavation steps with 2D simulations.

3.3 3D analysis of the TBM-induced settlement

3.3.1 3D Finite Element simulation

Figure 3.19 shows the general view of the numerical model. The symmetry of the model allows the reduction of its size. The mesh is constituted of 94000 cubic elements with eight nodes. At the vertical faces, no horizontal displacement is allowed, while the lower boundary is fixed both vertically and horizontally. Tunnel construction is a step-by-step procedure and it can be divided into two phases, the excavation phase and the lining ring installation phase.

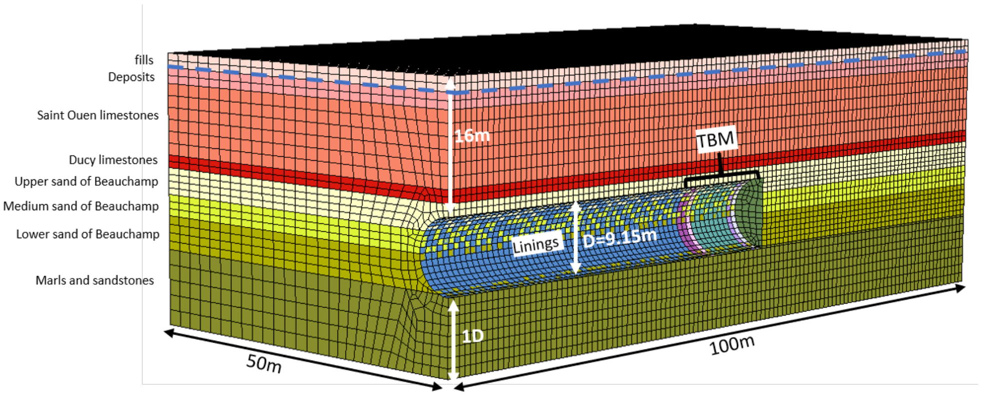

Figure 3.19: General view of the 3D numerical model

- The excavation phase is simulated by the deactivation of soil elements at the tunnel face during the progression of the TBM. The first lining ring is installed at the same time as the first excavation to limit the soil deformations. At each excavation step, the confinement pressure is applied at the front to ensure the stability of the tunnel face. This pressure is larger than the pore water pressure at the face (136 kPa at the crown). Due to the over-excavation of the cutting wheel and the connection between the void around the shield and the excavation chamber, the face pressure influences the pressure distribution around the shield. In this thesis, the shield pressure is calibrated to fit the field measurement and a total value of 150 kPa is applied around the shield.
- At the shield tail, reinforced concrete linings are installed, and the annular gap with surrounding soil is filled with mortar. To simulate this phenomenon, a value of 266 kPa is applied at the shield tail.

The lining segments are modeled as a continuous cylindrical shell, with the width and the thickness equal to 1 m and 40 cm, respectively. The deformation modulus of the lining concrete is assumed to be 13.5 GPa. The weight of the TBM equipment is neglected as demonstrated by

Kasper and Meschke (2006), and the linings are installed 12 m behind the tunnel face.
Figure 3.20 presents the settlement map at the end of the calculation phases. It can be observed that the beginning of the model is influenced by the boundary conditions. The transversal settlement trough can be obtained at a section located in the middle of the model where the settlement is stabilized. In this section, the evolution of the settlement at the surface and at the crown is studied, and the evolution of the vertical total stress at the crown.

Figure 3.21 depicts the normalized settlement of the point located at the ground surface and at the crown along the axis of the tunnel. Both curves are S-shaped. At the crown, the soil begins to settle when the TBM is located at 1 diameter of the section. 10% of the settlement occurs before the cutting wheel passes. When the tunnel boring machine passes, the settlement curve drops and reaches 90% of its maximum value before the lining ring is installed. During the construction of the lining ring, the ground rises due to the injection of mortar before stabilizing. At the surface, the soil response is different. At 2 time diameters of the section, the effect of the excavation starts and the soil begins to settle. This settlement progressively evolves and reaches almost 10% when the TBM is at 1 diameter to the section, then almost 40% when the cutting wheel passes. After the passage of the TBM the settlements are 85% of the maximum value. The settlement profile continues to evolve and starts to stabilize at 1 diameter after the passage of the TBM tail.
From these analyses two conclusions can be highlighted; the settlements evolve from the tunnel crow to the soil surface. This evolution is a delayed process. The injection pressure affects the equilibrium of the soil at the crown and sometimes these effects do not reach the soil surface.

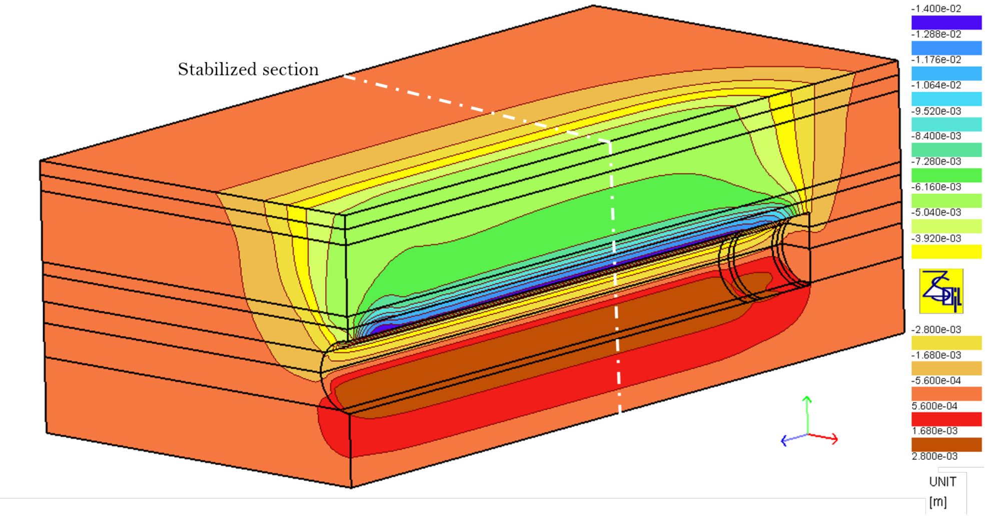

Figure 3.20: 3D settlement map

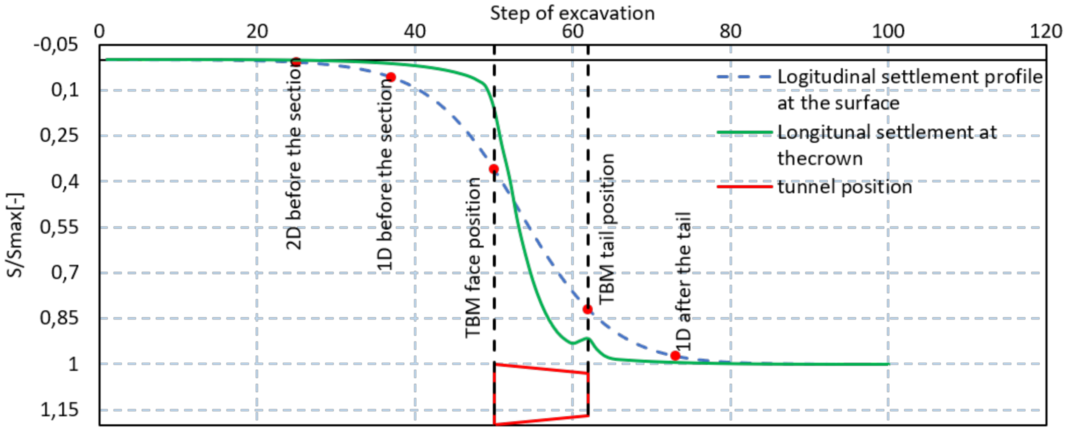

Figure 3.21: Longitudinal settlement trough evolution at the ground surface and at the crown

3.3.2 3D excavation steps calibration using the 2D simulation approach

Two main characteristics of the soil response to TBM-excavation can be reproduced by the 3D approach. The convergence of the soil surrounding the excavation which is not uniform around the tunnel and the $in-situ$ stress state of the soil which is modified by the TBM progress. In this section, the 2D FE method is used to reproduce the 3D response of the soil to the excavation at some progression steps of the TBM by modifying the fictitious pressure in order to fit the 3D settlement trough at the studied section. The positions of the TBM that have been chosen are 2 diameters before the studied section, 1 diameter before the studied section, at the studied section, 1 diameter behind the studied section, and 2 diameters behind the studied section.

Figure 3.22 shows the evolution of the total vertical stresses of the 3D model and the corresponding 2D model at the crown as a function of the TBM position. Concerning the 3D model, when the tunnel is twice the diameter far from the studied section, it has no influence on the stress state. With the advance of the TBM, the pressure of the excavation chamber increases the stresses by about 15%. When passing the TBM at the studied cross-section, the over-excavation around the shield creates a stress relief and this latter reaches 50% of the initial value. During the application of the injection pressure, the stress increases up to 80% and then decreases again before stabilizing around 60%. The evolution of the stresses at the crown of the 2D model is different from the one of the 3D model and has a S shape. The 2D model is not calculated for the configuration where the TBM is located at 2 diameters before the section because the settlements are almost zero. At 1 diameter to the section, the resulting stress at the crown from the studied confinement loss and the application of the fictitious pressure is 90% of the initial stress. When the cutting wheel is located at the studied section, it decreases to 70%. As the TBM tail crosses the section, the total vertical stress is almost stabilized at 60%.

Figure 3.23 presents the comparison of the total vertical stress map ($\sigma_{v3D} - \sigma_{v2D}$) between

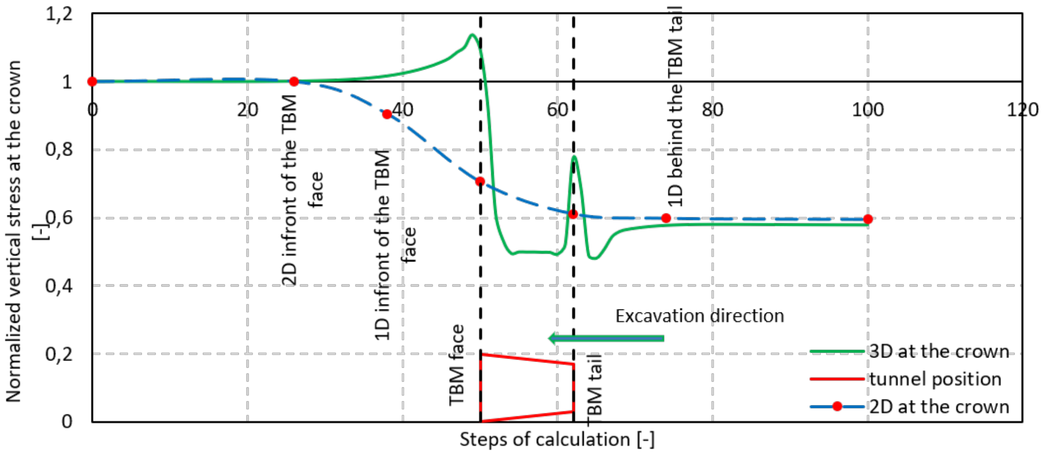

Figure 3.22: Total vertical stress evolution at the crown comparison 3D vs 2D.

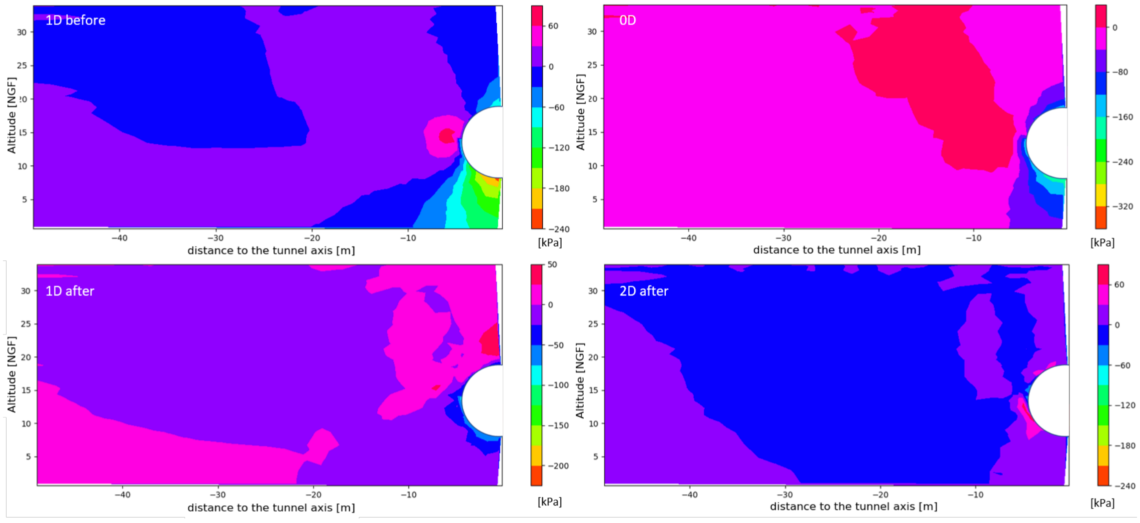

Figure 3.23: Total vertical stress comparison ($\sigma_{v3D} - \sigma_{v2D}$)

the 3D model and the corresponding 2D model for different positions; the TBM head located at 1 diameter to the studied section, the TBM head located at the studied section, the TBM head located at 1 diameter behind the studied section, and the TBM head located 2 diameters behind the section. As the stress is negatively oriented, a negative value of $\sigma_{v3D} - \sigma_{v2D}$ means greater stress in the 3D model than in the 2D model.

- 1 diameter before the studied section; the stresses at the crown, at the surface and at the

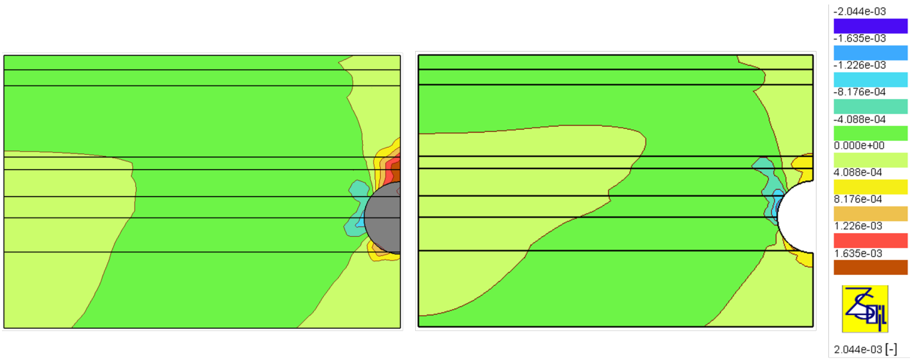

Figure 3.24: Deviatoric strain evolution field comparison 3D (on the left) vs 2D (on the right).

invert are greater in the 3D model than in the 2D model while the stresses at the tunnel side are lower in the 3D model.

- The TBM head located at the studied section; the stresses at the crown, at the surface and at the invert of the tunnel are greater in the 3D model. At the tunnel side, and going towards the surface, the 2D stresses are greater than the 3D stresses.
- 1 diameter behind the studied section; the 2D stresses are greater at the crown in the 2D model than in the 3D model while they are lower at the invert in the 2D model than in the 3D model.
- 2 diameters behind the studied section; all around the tunnel, the stresses are globally similar in 2D and 3D models except at some zones at the tunnel side.

Figure 3.24 presents the strain maps at the end of the excavation of the 3D model and the 2D model respectively. Positive values of the strain mean an extension of the soil element while negative values mean a compression. It can be observed that the soil elements located above the crown extend more in the 3D model than in the 2D model while the elements on the side compress more in the 2D model than in the 3D model.
From these previous analyses, although the results of the 3D and 2D settlement trough can be the same, the 2D FE simulation is not able to reproduce the evolution of the stress state and the strain state inside the soil mass. This conclusion highlights the 3D effects of the three-dimensional model that can not be represented with a bi-dimensional model.

In these previous sections, the homogeneous and stratified soil model was used to conduct the optimized back analysis procedure, the sensitivity analysis and the stress evolution analysis. However, as already mentioned, in geotechnical engineering, soil properties vary from point to point due to different sources. According to Miranda (2011); Xiao et al. (2017); Huang et al. (2017);

Hamrouni et al. (2022) this soil variability influences the soil response to tunnel excavation. In the next section, the soil heterogeneity effect on the TBM-induced surface settlement is analysed using the 2D FE method.

3.4 Soil heterogeneity simulated with random field theory

As already mentioned in this chapter, the gap between the FE result and the measurement may be caused by the heterogeneity of soils which is generally not taken into account in FE simulations. In this section, the heterogeneity of soil is considered in FE simulation and its influence on TBM-induced surface settlement is studied.

The soil heterogeneity is modeled with a discrete random field. Modeling the soil heterogeneity requires the generation of different soil properties. A random field expresses at a time the natural stochastic variability and the lack of knowledge that exist on the spatial repartition of the natural medium properties as explained by Houmadi (2011). In this section, the natural variability of soil is simulated with random field theory. For every soil layer, sub-layers are added with different behavior to account for the variability. Figure 3.25 presents the different steps to generate a spatially variable model. It consists of a coupling between the Python program and the Zsoil calculation program. The random field is generated using a specific algorithm developed in the python program with a specific mesh. The Zsoil Finite Element (FE) program is used to generate the FE model with a different mesh and with different material types. One of the problems to be solved by using such a method is to join the two different meshes (the one of the random field and the one of the FE model). Thus, another algorithm is developed in the Python program to couple the random field with the model generated from Zsoil to obtain the spatially variable model.

Generally in some projects, there is not enough information concerning the uncertainties on soil parameters. For this reason, the spatial variability models generated in this thesis are constituted of three different soil models. These soil models are characterized by different stiffness divided into three zones as further explained in section 3.4.2. The application of this methodology is conducted on the Paris Metro Line 12 extension profile to analyze the effect of the spatially variable model on the TBM-induced surface settlement trough.

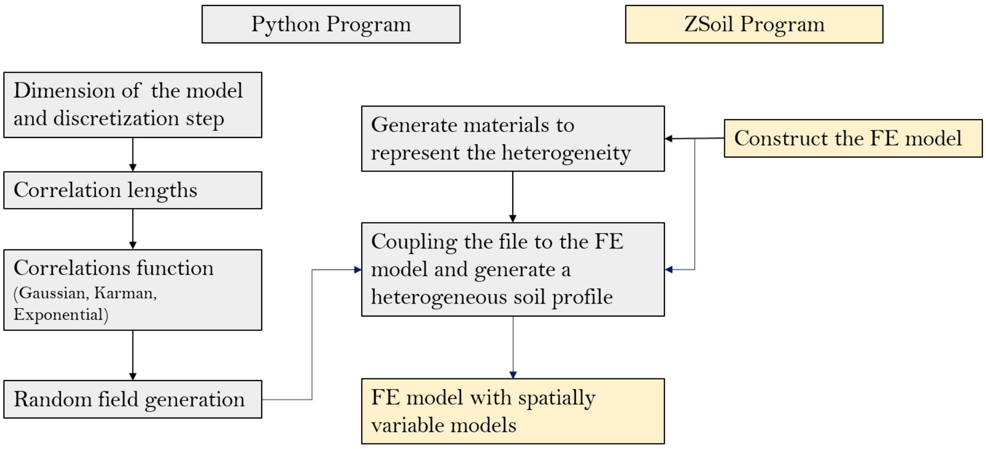

Figure 3.25: Spatially variable model generation steps

3.4.1 Two-dimensional random field generation methodology

Generating a random field depends on the statistical distribution of the correlation function. In the literature, the Gaussian distribution, the Exponential distribution and the Von Karman distribution can be listed (Houmadi, 2011; Hamrouni et al., 2022). The correlation function g depends on the vertical and horizontal correlation length i.e maximum distance where the soil parameters are correlated from Mahadevan and Haldar (1991), the mesh and the model dimension. Let's suppose;
a_x: as the horizontal correlation length (along the x axis)
a_y: as the vertical correlation length (along the y axis)
The correlation function g can be expressed as (Mai and Beroza, 2002):

- Gaussian distribution

$$g(x,y) = \exp(-(\frac{x^2}{a_x^2} + \frac{y^2}{a_y^2})) \tag{3.4.1}$$

- Exponential distribution

$$g(x,y) = \exp(-\sqrt{(\frac{x^2}{a_x^2} + \frac{y^2}{a_y^2})}) \tag{3.4.2}$$

- Von Karman distribution

$$ra = \sqrt{(\frac{x^2}{a_x^2} + \frac{y^2}{a_y^2})} \tag{3.4.3}$$

$$g(x,y) = 2^{(1-H)} \cdot ra^H \cdot \frac{JV(ra,H)}{\gamma(H)} \tag{3.4.4}$$

The g function of the Von Karman is more complex because it requires other functions as; JV: the Bessel function
H: the Hurst exponential is in $[0, 0.5]$. for $H = 0.5$, the Von Karman correlation function is identical to the Exponential function (Mai and Beroza, 2002).
γ: the gamma function

To generate a two-dimensional random field, a rectangular FE model geometry is discretized into nl*nw elements to create the mesh as presented in Figure 3.26. nl is constant (1000) and represents the number of elements along the $x-$axis and nw is variable (depending on the height of the model) the number of elements along the $y-$axis. The discretization size ds in both directions is chosen to be the same. To each element, a value of the generated random field is assigned.

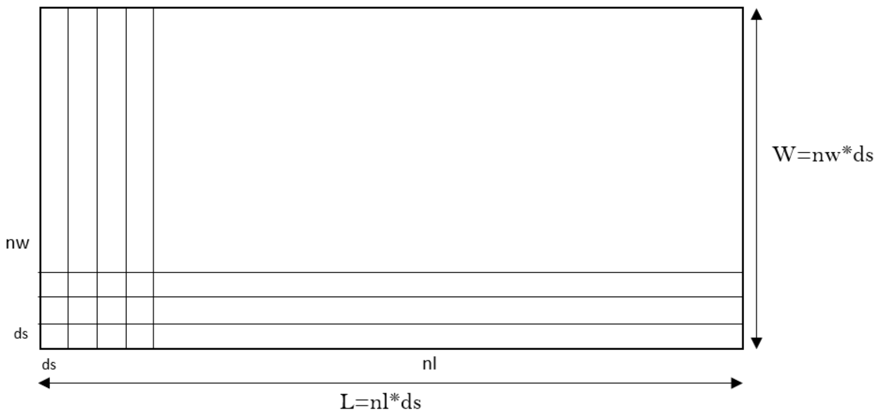

Figure 3.26: Soil mesh discretization to generate a random field

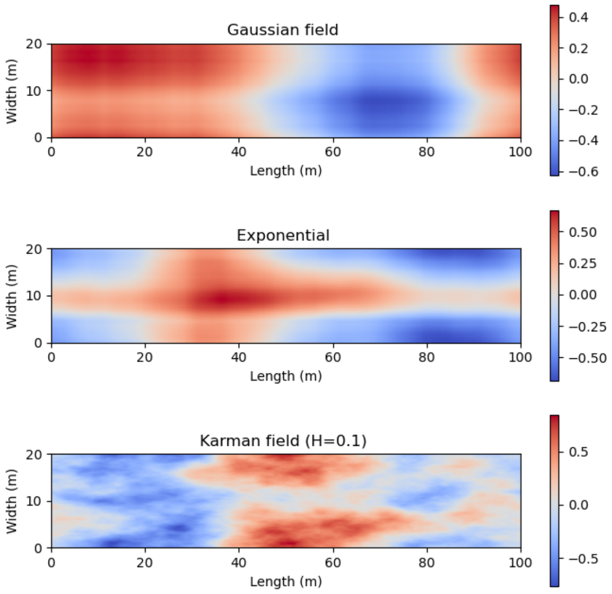

Figure 3.27: Example of random field generated with Gaussian, Exponential and Karman field correlation function

Figure 3.27 represents an example of the random fields generated with the three correlation functions. The length of the model is L=100 m, the height is W=20 m, and the discretization step both horizontal and vertical is ds=0.1 m. By assumption, the Von Karman field is generated with a value of 0.1 for the Hurst exponent. According to this figure 3.27, the random field generated with the Gaussian distribution is smoother than the random field generated with the exponential distribution which is also smoother than the random field generated with the Von Karman distribution.

3.4.2 Random field transformation in soil parameters

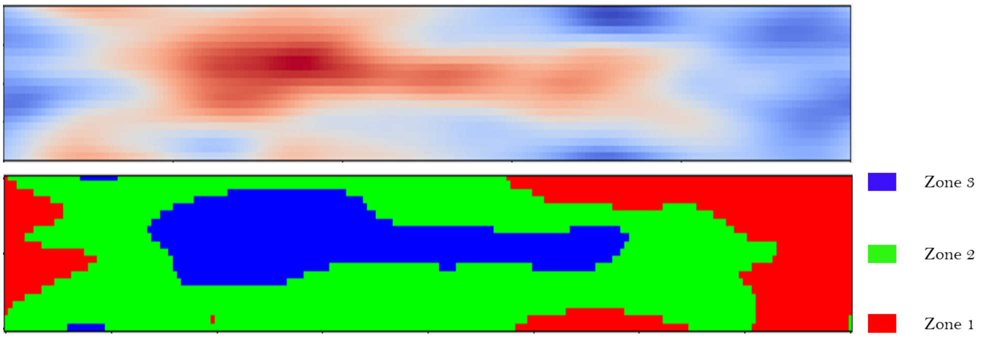

Figure 3.28: Transformation of a random field in a heterogeneous soil with three types of properties i.e the soil stiffness

Usually, the generation of soil model (i.e the soil stiffness) is conducted with Monte Carlo simulation following a certain probability density function. However, in the Paris Metro extension Line 12, the information on the probability density functions of the soil parameters is not available even though the corresponding mean and the standard deviation are provided. In order to generate a heterogeneous media with a fixed number of parameters, the generated random field has to be discontinuous. For simplification reasons, in this thesis, each soil layer is subdivided into 3 sub-layers. These sub-layers are characterized by different soil stiffnesses. The assumed values of the stiffnesses are; the mean (μ), the mean minus the standard deviation ($\mu - \sigma$) and the mean plus the standard deviation ($\mu + \sigma$). Following this division, the random field is split into three zones according to the limits of its values as presented in figure 3.28. Let's note a the minimum value of the generated random field and b the maximum value of the generated field. An example of a and b bounds are presented in figure 3.27. The three zones can be distinguished :

- zone 1 for values belonging to $[a; \frac{2}{3}a + \frac{1}{3}b[$
- zone 2 for values belonging to $[\frac{2}{3}a + \frac{1}{3}b; \frac{1}{3}a + \frac{2}{3}b[$
- zone 3 for values belonging to $[\frac{1}{3}a + \frac{2}{3}b; b]$

To construct a random variable model, the FE model and the generated random field must have the same dimensions but the mesh dimension can be different. To each element of the model is assigned the value of the corresponding zone in the random field. In the literature, three methods exist to assign the random field to the FE model. The Mid-Point or nodal point method, the

Table 3.5: Values of parameters used to generate the spatially variable profile

Layers		E_{50} Mean$[MPa]$	Std$[MPa]$	thickness [m]	C' $[kPa]$	ϕ' [°]
Fills	R	25	17	1.8	0	25
Alluvial	AL	12	6	2	0	20
Saint-Ouen Limestone	CSO	35	16	9	0	25
Ducy Limestone	CD	19	9	1.6	0	25
Beauchamp upper sand	SB sup	168	44	3.4	0	30
Beauchamp middle sand	SB med	82	30	2.7	60	15
Beauchamp lower sand	SB inf	154	44	4.3	0	30
Marls and sandstones	MC	141	41	9.6	30	30

discretization by value and the discretization by series development (the series expansion methods, the optimal linear estimation and the Karhumen-Loeve) method can be listed (Houmadi, 2011; Hamrouni et al., 2022). In this thesis, the Mid-Point method is chosen to link the FE model to the random field due to its simplicity.

3.4.3 2D spatially variable model and effect on the surface settlement trough

In this thesis, the correlation function characterized by the Gaussian distribution is used to generate the random field. The horizontal correlation length is 50m according to Houmadi (2011) and the vertical correlation length is assumed to be 0.8 times the height of the layer. Figure 3.29 presents an example of a spatially variable model of the Metro line 12 profile in the Paris area.The layers are generated with different random fields. The model is 100 m wide and the tunnel cover is 16 m. The tunnel is located below the water table and the lower boundary of the model is located at a diameter below the tunnel invert section 3.2.2.2 presents more information about the model description. The tunnel is excavated in a multi layer profile and the parameters are presented in table 3.5. In this table, the mean and the standard deviation of the soil stiffnesses are presented.

3.4.3.1 2D simulation and effect of the mesh size on model

Based on the spatially variable model, three bi-dimensional FE models are developed to study the influence of the mesh size on the surface settlement trough by comparing the settlement trough result. The calculation times of the models are also compared. Each mesh is symmetrical with respect to the tunnel axis. As already mentioned, the uncertainties are considered only on the soil

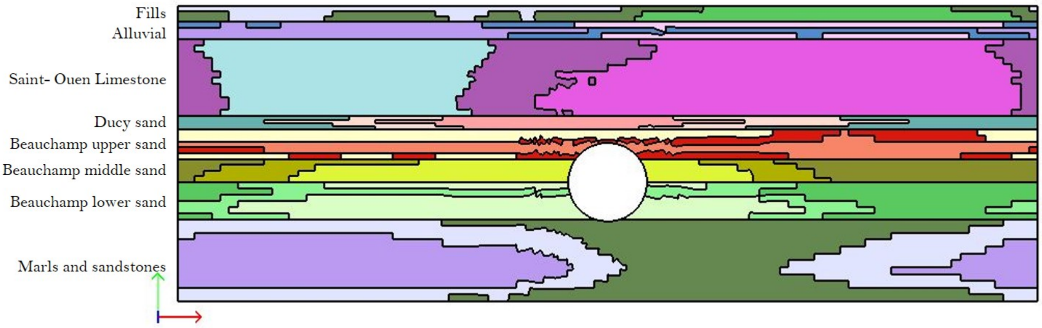

Figure 3.29: An example of the spatial variability of a Paris Metro line 12 profile; consideration of the stiffness

stiffnesses. For each sublayer, the soil stiffnesses are randomly assigned among the mean (μ), the mean minus the standard deviation ($\mu-\sigma$) and the mean plus the standard deviation ($\mu+\sigma$). The value of the standard deviation is different from the one presented in the previous section of this chapter. as already mentioned, table 3.5 presents the value of the considered standard deviation. Figure 3.30 shows half of the mesh size of the FE models. These FE models are calculated with ZSoil program.

- The coarse mesh is constituted by 1800 quadratic elements and 1900 nodes with 2 degrees of freedom at each nodes except for the nodes along the boundaries. The coarse model is calculated in 1 minute.
- The optimized mesh is constituted by 2500 quadratic elements and 2600 nodes and is calculated in 2 minutes.
- The fine mesh is constituted by 6500 quadratic elements and 6700 nodes and is calculated in 4 minutes.

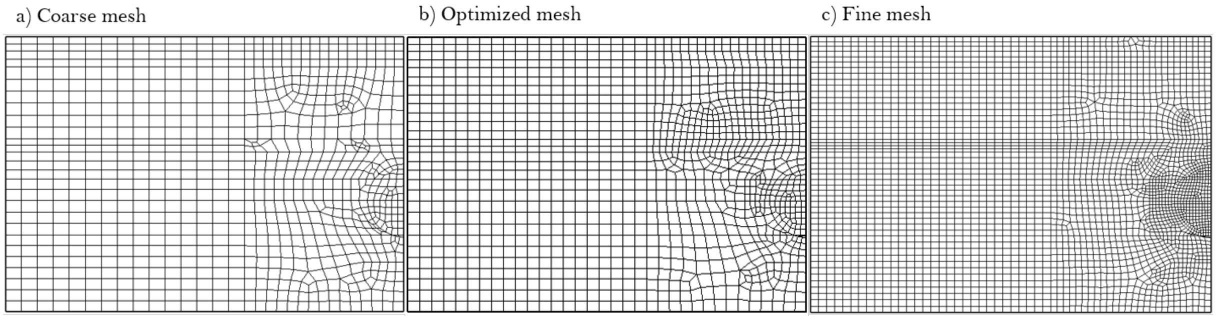

Figure 3.30: Comparison between the three different meshes

The convergence confinement method with the explicit approach developed by Aristaghes and Autuori (2001) and described in chapter 2 is adopted for the 2D numerical simulations. This approach needs two parameters; confinement loss and fictitious pressure. The confinement loss is used to simulate the stress release due to the excavation process and a value of 0.9 is assumed. Concerning the fictitious pressure, it is calibrated on the face pressure, the injection pressure and eventually the pressure around the shield using a homogeneous stratified model as demonstrated in chapter 2 section 2.6.2. Regarding the constitutive model of the soil, the Hardening Soil with Small Strain Model is used to represent the soil behavior following the hypotheses of chapter 2 i.e $E_{ur} = 2E_{50}$, $E_0 = 8E_{50}$ and $E_{oed} = E_{50}$ for the deformation moduli and the cohesion c', the frictional angle ϕ' and, the dilatancy angle ψ' for the plastic parameters.

Figure 3.31 presents the settlement trough result of the 3 models characterized by the 3 different meshes of the spatially variable model. It can be observed that the settlement trough is not symmetric to the tunnel axis due to the asymmetry of the soil model. The curves follow the same profile and the soil starts to settle at almost 30 m distance from the tunnel axis. The width of the settlement troughs is the same in the three cases even though the maximum settlements are different. Assuming that the settlement trough of the fine mesh is the reference, there is an error of 10% regarding the coarse model and 2% regarding the optimal model concerning the maximum value. Supposing the same response for a different model, even though the fine mesh provides a better result, in order to save some calculation time, the optimal mesh is adopted for 2D FE simulations in this thesis.

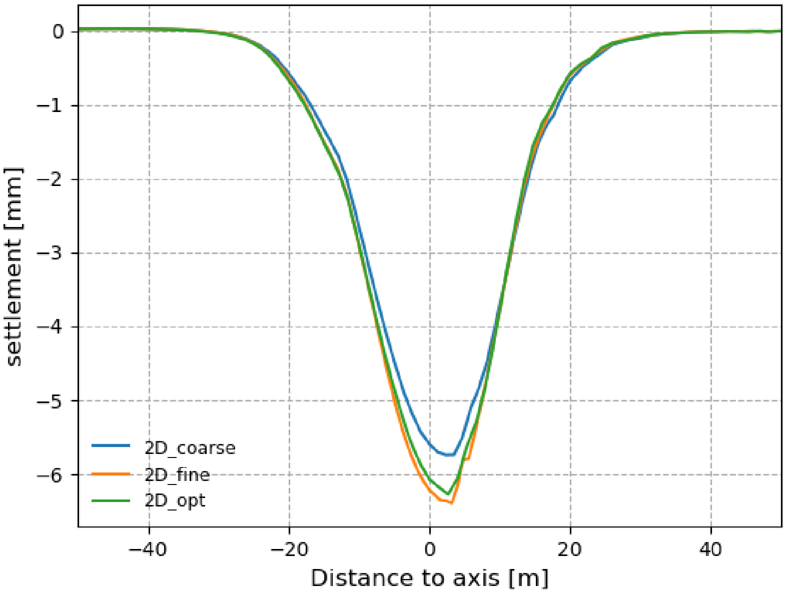

Figure 3.31: Surface settlement trough comparison with different mesh types

3.4.3.2 Effect of the spatial variability of the soil on the surface settlement trough

A total of 300 models are developed with 300 different random fields and calculated to study the influence of spatial variability on the surface settlement curve. From one model to another, the soil configuration and the soil stiffness are different. Figure 3.32 depicts the set of settlement troughs resulting from the simulations. It can be clearly seen that all these curves have a Gaussian shape as indicated by Peck (1969), but they are not always symmetrical with respect to the tunnel axis. In all the cases, the maximum settlement is close to the tunnel axis. Its value varies between 3 mm and 8.5 mm. By analyzing the 300 simulations, Figure 3.33 presents the distribution of the maximum settlement and the corresponding probability of exceedance (1- CDF cumulative density function). The latter is the probability to obtain the maximum settlement greater than a certain value. From this figure, the mean of the maximum settlement is 5.71mm, the standard deviation is 0.88mm, and the coefficient of variation is 15%. This figure also presents the maximum settlement of the field measurement and the back analysis result presented in section 3.2 (5.7 mm) which are very close to the mean result of the 300 models. Concerning the CDF, a maximum settlement larger than 5.7 mm can be obtained with a probability of 50%.

To study the influence of the spatial variability of the stiffness on the width of the settlement trough, each settlement curve is fitted with a symmetrical Gaussian curve to the axis of the tunnel following the least-squares method. It is therefore possible to determine the inflection point that characterizes the width of the settlement curve. Figure 3.34 shows the histogram of

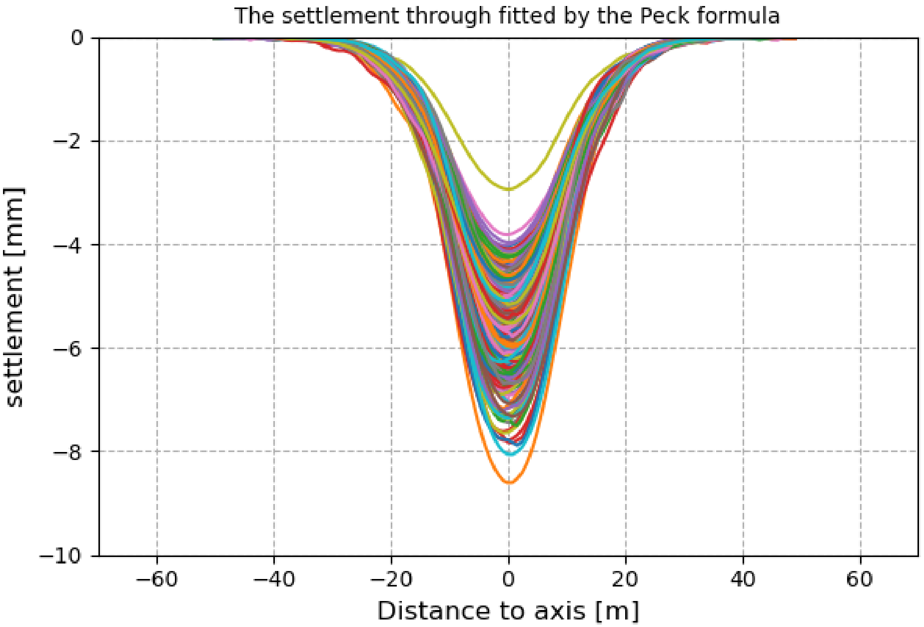

Figure 3.32: Surface settlement trough resulting from different heterogeneity configurations

the inflection point and the probability of exceedance. The inflection point is located between 8.25m and 10.5m from the axis of the tunnel with a mean value of 9.3 m, a standard deviation of 0.34m, and a coefficient of variation of 3%. This figure also presents the settlement width of the field measurement and of the back analysis result conducted with all the soil stiffnesses presented in section 3.2. According to this result, all the settlement curves obtained with spatially variable models are wider than the one of the field measurement. Concerning the result of the back analysis, the settlement width (9,6 m) is greater than the mean of the spatial variability one. From the coeficient of variation, it can be concluded that, the spatial variability of the stiffness influences the maximum settlement more than the inflection point. Concerning the CDF, a greater value of the inflection point can be obtained with a probability of 20% .

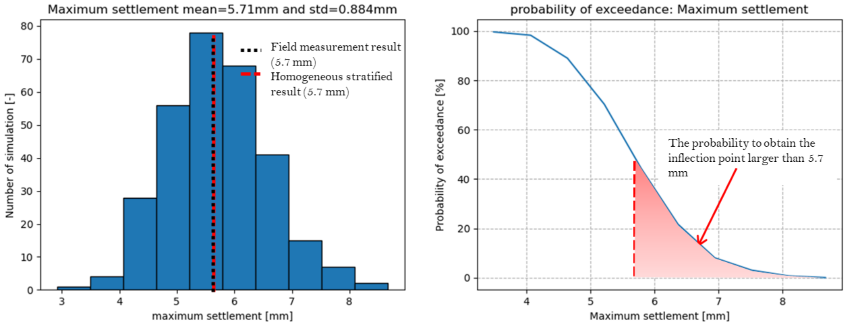

Figure 3.33: Histogram of the maximum settlement and cumulative distribution function

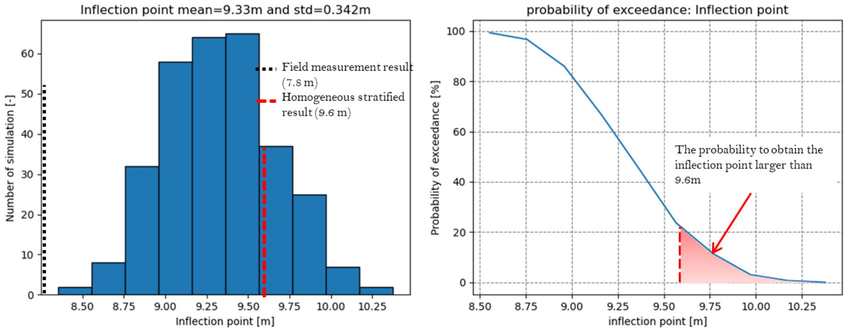

Figure 3.34: Histogram of the inflection point

In this section, the consideration of soil heterogeneity in predicting the TBM-induced surface settlement was first conducted using random field theory. Then, based on a Paris Metro Line 12 extension profile, the influence of the spatial variability of the soils on the surface settlement trough was studied. From this analysis, the settlement troughs obtained reveal to have Gaussian shapes, but they are not always symmetrical with respect to the tunnel axis. In addition, the maximum settlement is more influenced by the spatial variability of the soils than the inflection point which represents the width of the settlement curve.

3.5 Conclusion

In this chapter, several analyses were conducted to improve the FE simulations and to better understand the soil response to TBM excavation. As demonstrated by Janin et al. (2017), Demagh et al. (2013) and, Gilleron et al. (2021) despite the improvements in numerical simulation, there is still a gap between the numerical settlement trough and the field measurements settlement trough. With the 2D FE simulation and based on the extension of the Paris Metro Line 12, an optimized back analysis method was developed to determine the optimal set of parameters that offers the best agreement between the measurements and the FE results. Subsequently, a global sensitivity analysis was conducted to study the influence of soil parameters on the maximum settlement and the inflection point. This latter shows that the relative position of the layer to the tunnel crown and the thickness of the layers play an essential role in the sensitivity analysis results.

2D model being a simplified approach of the 3D one, a 3D simulation and some 2D FE simulations were also conducted to analyze the soil response to tunneling. The 3D simulation was conducted to study the evolution of both the longitudinal settlement curve at the surface and the stresses at the tunnel crown. The longitudinal settlement troughs at the crown and at the surface have the same profile and the values depend on the TBM location. Following the 3D model progression steps, 2D models were conducted to calibrate the transversal settlement curve obtained at different TBM locations. After that, the evolution of the stresses and strains in the ground with the 3D model and the 2D model is compared. This comparison showed that the vertical stress field before the stabilization of the settlement is globally greater in the 3D model than in the 2D models. After the settlement stabilization, the stresses in both models are almost the same except at the tunnel sides. Similarly, concerning the strains, the soil elements located at the crown extend more in the 3D model than in the 2D model while the elements located at the tunnel sides compress more. In all these previous analyses, the soil is represented by a homogeneous stratified layer. However, in reality, due to the natural formation process of soils, they are heterogeneous. The last part of this chapter considered the heterogeneity of soils in FE simulation.

Random field theory was used to simulate the heterogeneous character of soils. By coupling this method with the 2D FE method, 2D spatial variability models were also developed to study the effect of soil heterogeneity (soil stiffness) on the TBM-induced settlement. According to the results of the analyses carried out on a profile of the Paris Metro Line 12 extension in Paris, the settlement troughs all have a Gaussian shape but are not always symmetrical with respect to the axis. In addition, the maximum settlement is more influenced by the effect of variability of the parameters than the width of the settlement curve. Futher analyses using the Heterogeneous approach to simulated the soil behavior will be presented in chapter 5.

Uncertainties of soil parameters using homogeneous and stratified soil profiles or heterogeneous soil profiles influence the TBM-induced settlement. The determination of these influences requires a large number of numerical simulations which is a time-consuming process. Nowadays, simplified models such as meta models based on Machine Learning approach are developed to complete and even replace the numerical methods Koseoglu Balta et al. (2021), Feinberg and Langtangen (2015), Armaghani et al. (2017), Rajabi et al. (2017), Ninic et al. (2021), Mahdevari et al. (2014), Yagiz and Karahan (2015), and Javad and Narges (2010) . This approach will be discussed in the next chapter.

Chapter 4

TBM-induced surface settlement prediction with Machine Learning tools

Contents

4.1 Introduction

The excavation rate and the soil disturbance control are the main advantages of using a Tunnel Boring Machine (TBM) to construct tunnels. Despite these benefits, soil deformation sometimes affects the safety of buildings in the vicinity of the tunnel. As already explained in chapter3, the heterogeneity of soils can be considered in FE simulation either implicitly with uncertainties on soil parameters or explicitly with spatially variable models. Studying the soil response to tunnel excavation by considering the soil heterogeneity requires some numerical simulations, which can be time-consuming with increasing the number of simulations. Thanks to models built with the Machine Learning approach (meta-models), it is possible to consider a large number of simulations to study the soil response to TBM-excavation in a very short time.

In civil engineering problems in general and tunneling in particular, different machine learning algorithms are used to construct meta-models: The non-supervised algorithms and the supervised algorithms (Laskov et al., 2005; Sathya and Abraham, 2013). The non-supervised algorithms learn patterns from untagged data, whereas the supervised algorithms must be trained, validated and tested with different databases before being used. The validation of a model is done with different metrics that are further explained in section 4.4 (the correlation coefficient R between -1 and 1, the determination coefficient R^2 between 0 and 1, the root mean square error RMSE among them can be listed). The construction of a model based on a supervised learning algorithm required the partitioning of data into two sets called the input and the output sets. In meta-modeling, the input parameters do not always have the same influence on the output parameters. It can happen in some cases that, by neglecting the less influential parameters, there is no or minimal effect on the prediction.

Among the existing non-supervised algorithms, the clustering algorithms such as the k-means algorithm (Adams, 2018) and the K-Nearest Neighbor algorithm (Huang et al., 2020) can be listed. Concerning the supervised algorithms, the Artificial Neural Network ANN (Mohammadi et al., 2015; Chen et al., 2019; Ocak and Seker, 2013), the Adaptive Neuro-Fuzzy Inference System (Ahangari et al., 2015), the convolutional neural network (Zhang et al., 2021a) and the Random Forest (Kohestani et al., 2017) among others can also be listed. Concerning the use of meta-model in tunneling, Liu et al. (2020) utilized the TBM driving parameters (the penetration rate of the TBM, the torque of the TBM cutter head, the thrust of the TBM cutter head, and the revolution per minute) to predict rock mass parameters (uniaxial compressive strength, brittleness index, the distance between plane of weakness, and the orientation of discontinuities). They determined the relationship between the TBM driving parameters and the rock mass parameters by applying a hybrid algorithm that integrates the back propagation neural network with simulated annealing. Zhang et al. (2021a) used the convolutional neural network to predict the tunnel deformation in spatially variable soil. The proposed method successfully identified the pattern between random field input and the safety factor of tunnel deformation output. This chapter studies the use of meta-models for predicting the TBM-induced settlement. Other authors have already focused on predicting Tunnel-induced settlement. For example, Mohammadi et al. (2015) used the ANN to investigate the maximum surface settlement of the Niayesh subway tunnel, excavated with the New Austrian Tunnelling Method (NATM). In contrast, Ghiasi and Koushki (2020) applied the multilayer perceptron (MLP) ANN to predict the TBM-induced surface settlement. The depth-to-diameter ratio (H/D), the soil cohesion, the internal friction angle, and the permeability coefficient were considered as input parameters. Suwansawat and Einstein (2006) applied the ANN to an Earth Balanced pressure (EBP) shield tunnel to predict the surface settlement of the Bangkok MRTA project. Santos and Celestino (2008) used the ANN to predict the surface settlement of a double-track shotcrete-supported tunnel excavated through the Sao Paulo sedimentary basin. their work reveals a weak performance of the simple ANN model because they provided a low value of the determination coefficient R^2. According to Wang et al. (2020), the thorough investigation of the application of simple ANNs in tunnel engineering is still insufficient because the predictions are sometimes very different from the targets. Consequently, the value of the performance indices they provide (R^2 and R, for example) are small.

Generally, from a database, different set of samples are used to train and validate the model; for example, Aydin et al. (2019) used 90% of the samples for training and 10% for validation. To increase the value of the performance indices, a large number of training data is sometimes required. However, obtaining a sufficient amount of data is a great challenge and time-consuming (for numerical data) or expensive (for field measurements). In a context of small amounts of data, the traditional use of database construction techniques offers very approximate results. In order to improve these results, the K-means algorithm is adopted with data where the input parameters and output parameters are considered in the same database, and grouped in clusters. Then, data is extracted from these clusters to build the metamodel. Following this methodology and considering the heterogeneity character of the soil, this chapter firstly proposes a coupling the ANN to the k-means algorithm based on two-dimensional (2D) FE simulation. The proposed methodology is applied to the Paris Metro Line 12 extension following the 2 mentioned approaches (spatial variability model and homogeneous stratified with uncertainties on the soil parameters) that consider the soil heterogeneity with the ZSoil FE calculation program. The non-linear soil deformation moduli of all the layers are considered as the input parameter since according to Nour et al. (2002) and Baecher and Christian (2005a), they are more affected by the uncertainties than the friction angle and the cohesion. To find the most influential parameters on the predictions and better understand the relationship between input and output parameters, techniques such as the Sensitivity Analysis (SA) that is already explained in chapter 3, the Principal Component Analysis (PCA) and the classical correlation method are studied in this chapter. Predicting the

TBM-induced surface settlement with the proposed technique can be affected by uncertainties due to some reasons related to the architecture of the meta-model and the non-exhaustive number of input/output patterns (see section 4.5.3 for further explanations). These uncertainties are totally different from the one explained in chapter 3 which were related to soil parameters. The bootstrap approach is finally proposed in this thesis to quantify these uncertainties.

4.2 Database construction

This section explains the database construction procedures for the 2 cases mentioned above; the Homogeneous stratified layer model with uncertainties on the soil parameters and the spatial variability model. For these cases, the soil is simulated with the nonlinear elastoplasticity model Hardening Soil with Small Strain Model (HSSM) (Schanz et al., 2019). As explained in chapter 2, the HSSM is characterized by 4 different stiffnesses (the unload-reload elastic stiffness E_{ur}, the secant stiffness in standard drained triaxial test E_{50}, the tangent stiffness for primary odometer loading E_{oed}, and the stiffness for very small strain E_0) in addition to the plastic parameters (the friction angle, the dilatancy angle and the cohesion). In these analyses, only the secant stiffness E_{50} of the eight layers (so 8 inputs) are considered as input parameters. As explained in chapter 3, there is no plasticity after the excavation with these input parameters. Concerning the soil model, the relationships explained in chapter 2 are also considered among the different stiffnesses. The output parameters, they are formed by the maximum value (S_{max}) and the inflection point (i).

4.2.1 Database for homogeneous stratified layers with uncertainties

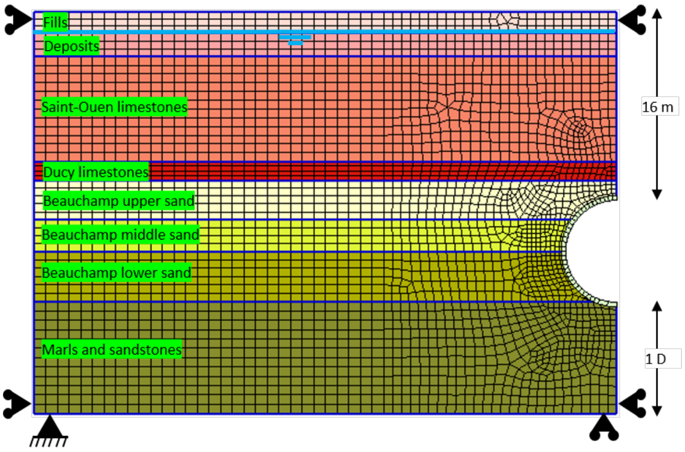

Figure 4.1: General view of the 2D numerical model

Figure 4.1 presents the 2D model of the Paris Metro Line 12 extension excavated in a homogeneous stratified layered. For a simplification reason, Monte Carlo simulation is used to generate the input parameters following a uniform distribution with a coefficient of variation (CV) of 30% as shown in table 4.1.These parameters are the same presented in section 3.2.4.1 of chapter 3.

Table 4.1: Used parameters with the homogeneous stratified layer

Layers		E_{50}	
		μ[MPa]	CV[1]
Fill	RB	10	0.3
Alluvial	AL	5	0.3
Saint-Ouen Limestone	CSO	40	0.3
Ducy Limestone	CD	39	0.3
Beauchamp upper sand	SB sup	60	0.3
Beauchamp middle sand	SB med	100	0.3
Beauchamp lower sand	SB inf	60	0.3
Marls and sandstones	MC	120	0.3

4.2.2 Database for spatial variability models

Different random fields are generated to construct the FE models concerning the spatial variability models. These models are distinguished from each other by the configuration of the sub-layers. Each soil layer is constituted of three sub-layers which are characterized by the soil stiffness; either the mean (μ), the mean minus the standard deviation ($\mu - \sigma$) and the mean plus the standard deviation ($\mu + \sigma$). Table 4.2 presents the parameters used to generate the spatial variability models. These parameters are the same presented in section 3.4 of chapter 3. According to the sensitivity analysis presented in chapter 3, the Saint Ouen limestones, the Beauchamp upper sand and the Beauchamp lower sand were revealed to be the most influential because of either their relative position to the tunnel or their thickness. Due to the larger thickness of the Saint-Ouen limestone compared to the other layers, more points are considered for this layer. The stiffnesses of the soil layers located at the tunnel invert and below the tunnel are not considered as the input parameter because the sensitivity result obtained in chapter 3 shows that their influence on the maximum settlement and inflection point is negligible. For these reasons, the input database is constituted of (18 discrete data); the stiffness of the sub-layers above the tunnel, the stiffness of the Saint Ouen limestone located at 6 m to the tunnel axis and the stiffness of the soil around the upper part of the excavation as shown in figure 4.2.

4.3 Machine Learning algorithms

4.3.1 K-Means Algorithm

The k-means algorithm is a partitioning technique used to form a small number of clusters from many observations. Given a dataset of n data points x_1, x_2, ..., x_n such that each data point is in R^d and the points $\{m_j\}$ $(j = 1, 2, , k)$ being the cluster centroids. The problem in equation 4.3.1

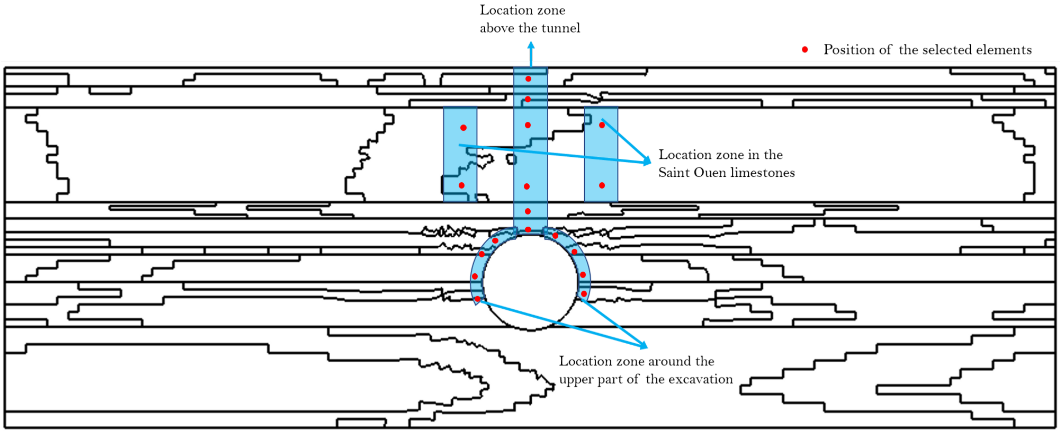

Figure 4.2: Location zone of interest for the construction of the meta model

Table 4.2: Values of parameters used to generate the spatially variable profile

Layers		E_{50}	
		μ[MPa]	σ[MPa]
Fills	RB	25	17
Alluvial	AL	12	6
Saint-Ouen Limestone	CSO	35	16
Ducy Limestone	CD	19	9
Beauchamp upper sand	SB sup	168	44
Beauchamp middle sand	SB med	82	30
Beauchamp lower sand	SB inf	154	44
Marls and sandstones	MC	141	41

is to find k cluster centroids, such that the average squared Euclidean distance d^2 (mean squared error, MSE) between a data point (x_i) and its nearest cluster centroid (m_j) is minimized (Adams, 2018; Fahim et al., 2006).

$$d_{min} = \frac{1}{n}\sum_{i=1}^{n}[min_j d^2(x_i, m_j)] \tag{4.3.1}$$

The k-means algorithm can be thought of as a gradient descent procedure, which begins at some starting cluster centroids, and iteratively updates these centroids to minimize equation 4.3.1. The k-means always converges to a local minimum. The particular local minimum found depends on the starting cluster centroids. The following steps present the procedure to perform a k-means algorithm (Fahim et al., 2006).

- step 1: determine the number of clusters to group data and the database to cluster as input values

- step 2: initialize the first k clusters by taking the first k instances or random sampling of k elements
- step 3: calculate the arithmetic means of each cluster formed in the dataset
- step 4: each record is assigned to the nearest clusters using a measure of distance (e.g. Euclidean distance)
- step 5: k-means re-assigns each record in the dataset to the most similar cluster and re-calculates the arithmetic mean of all the clusters in the dataset.

4.3.2 Artificial Neural Network

Given a set of input/output data examples (patterns), $D = \{(X_n, Y), n = 1..., N\}$ where X_n is a vector of input variables (with $X_n = \{x_{1,n}, x_{2,n} \ ..., x_{j,n} \ ..., x_{M,n}\}$ and M the dimension of the vector X_n) and Y the output target, it is possible to estimate a nonlinear relationship between the vector of input variables and the output target. Thus, it can be assumed that Y is related to the input vector X_n by an unknown nonlinear deterministic function $g(X_n)$ (FE method for instance) corrupted by a Gaussian white noise $\epsilon(X_n)$ as shown by the equation 4.3.2 (Bishop, 1995).

$$Y = g(X_n) + \epsilon(X_n); \qquad \epsilon(X_n) \sim N(0, \sigma_\epsilon^2(X_n)) \tag{4.3.2}$$

In this thesis, the ANN is proposed to reproduce the nonlinear relation between the inputs vector X_n and the output target Y. According to Braspenning et al. (1995), Abraham (2005) and Ghiasi and Koushki (2020) , ANN contains three parts: an input layer, one or several hidden layers and an output layer. Each layer contains neurons that perform different tasks. In the input layer, neurons are responsible for collecting and transmitting input data to hidden layers. At hidden layers, neurons receive data from the input layer through encoded values, called weights. The procedure of calculation and processing are performed in hidden layers with different learning methods and algorithms that can be applied. Finally, the results from the hidden layers are returned in the output layer through a transfer function. Figure 4.3 summarizes the different tasks followed by the ANN algorithm. As explained by Ferrario et al. (2017), the objective of the regression task by ANN is to estimate Y through a regression function $h(X_n, w)$ that depends on the set of ANN parameters w as explained in equation 4.3.4. The determination of the regression function h for an ANN with one hidden layer is presented in equation 4.3.3.

$$h(X_n, w) = f(\sum_{j=1}^{m}(w_j + \theta_j))f(\sum_{i=1}^{n}(w_{ij} + \theta_i)) \tag{4.3.3}$$

$$y = h(X_n, w) + e \tag{4.3.4}$$

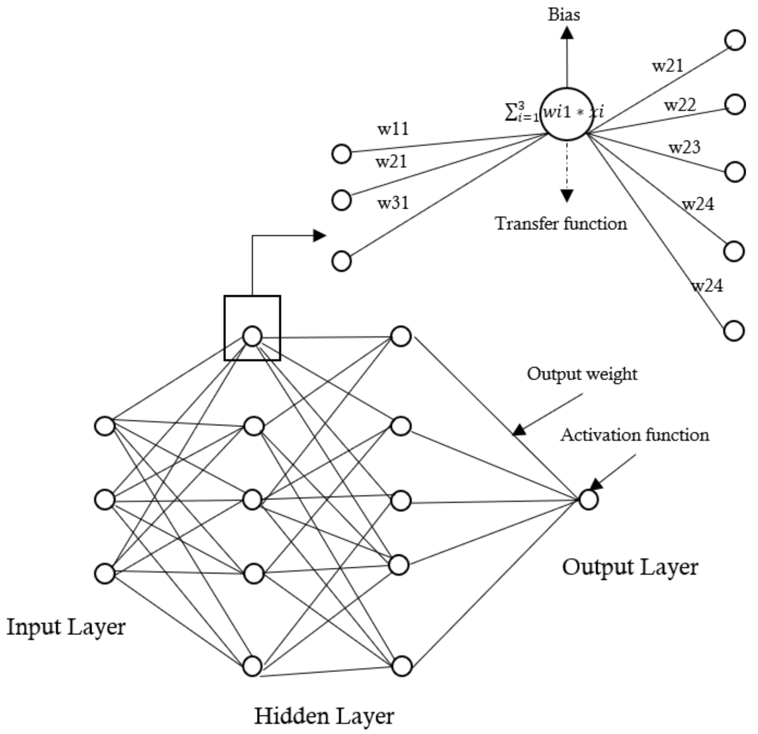

Figure 4.3: The optimal architecture of the ANN (Abraham, 2005)

In this equation, w_{ij} are the connection weights between input and hidden neurons, w_j are the connection weights between hidden and output neurons, θ is the bias and f an activation function used to transform the input values and transfer them to the next layer. A training procedure establishes the relation between the input and output, adjusting the connection weights w to minimise the error e between output target g and the result of the expression $h(X_n, w)$ for several patterns m. Using a gradient descent method, the connection weights w_i are updated as presented in equation 4.3.5 where γ is a learning rate. The learning rate is a hyperparameter that controls how much to change the model in response to the estimated error each time the model weights are updated.

$$w_{is} = w_{is-1} + \Delta w \qquad \Delta = \gamma \frac{\delta e}{\delta w} \qquad e = (Y - h(X_n, w))^2 \tag{4.3.5}$$

As already mentioned, three main steps, including training, validation, and testing, constitute the steps to follow to succeed in an ANN prediction. During the training step, the algorithm is applied to update the weights and minimize the error between the output target and the predictions. As explained by Avunduk et al. (2014), the validation step is the criterion for stopping the training step. According to Wang et al. (2020), in most cases, the training and the testing steps are carried out because an appropriate model can be chosen through previous experience. The training procedure is performed in several iteration steps is, and the weights w are updated for

Table 4.3: Main performance function of a trained ANN model

Function	Range	Optimal value
Mean absolute error (MAE)	$[0, +\infty[$	0
Mean absolute percentage error (MAPE)	$[0, +\infty[$	0
Mean squared error (MSE)	$[0, +\infty[$	0
Root mean square error (RMSE)	$[0, +\infty[$	0
Relative root mean square error (RRMSE)	$[0, +\infty[$	0
Relative absolute error (RAE)	$[0\%, 100\%]$	0
Root relative square error (RRSE)	$[0\%, 100\%]$	0
Correlation coefficient (R)	$[-1, 1]$	-1, 1
Determination coefficient (R^2)	$[0, 1]$	1
Variance accounted for (VAF)	$[0\%, 100\%]$	100%

all connections between input-hidden, hidden-hidden, and hidden-output neurons. The quality of the training phase depends on both the network architecture (number of hidden layers and hidden neurons) and learning parameters (number of iteration steps and learning rate γ). The performance of a trained ANN model is based on certain indicators. Table 4.3 summarizes some main performance metrics. This thesis uses the determination coefficient presented in equation 4.3.6 to validate the model. In this equation, n is the total number of data points, Y_i is the target point, $\hat{Y}_i$ is the estimator of Y_i and $\bar{Y}$ is the mean value of the data points Y_i.

$$R^2 = \frac{\sum_{i=1}^{n}(\hat{Y}_i - \bar{Y})^2}{\sum_{i=1}^{n}(Y_i - \bar{Y})^2} \tag{4.3.6}$$

4.4 The proposed technique methodology and application

As already mentioned, increasing the value of the performance indices of meta-models sometimes requires a large number of training data. However, obtaining sufficient data is a great challenge, time-consuming and/or expensive. In this thesis, a technique is proposed based on the coupling of unsupervised learning (k-means) and supervised learning (ANN). With the k-means algorithm, the data are grouped in clusters containing input and output data with similar behavior. The higher the cluster number, the better the division between the data and the more expensive the calculation time. The optimum number of clusters is selected from the minimum value of the average distance between the clusters centroids and the data points. In this thesis, the average distance is called the error and it is present as a decreasing curve with the number of clusters. Figure 4.4 presents an example of the error between the cluster centroids and the data points (as explained in equation 4.3.1) evolution according to the number of clusters. The optimal number of clusters takes into account both the precision (the error d_{min}) and the calculation time (not present in the figure). After determining the optimal number of clusters, a certain amount of data points are selected from each cluster for training and testing the meta-model constructed with the ANN. Figure 4.5 presents the steps of the proposed technique used to build the Meta model.

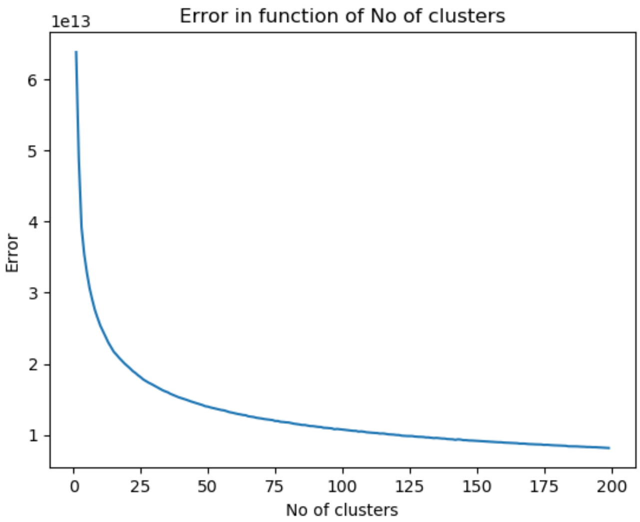

Figure 4.4: Evolution of the error (d_{min}) in function of the number of clusters

- step 1; the data base is created from 2D FE simulation.
- step 2; with the k-means, the original data base is clustered and partitioned in some data points for training and others observations for testing.
- step 3; the meta model is constructed and the hyperparameters are calibrated to optimize the results.

In this chapter, meta-models are developed using the 2D FE simulations based on the two approaches presented in chapter 3 i.e the homogeneous soil profile with uncertainties on the soil parameters and the spatial variability models. The k-means and the multilayer perceptron ANN functions of the scikit learn package of python programming language are used to construct the meta-models. Several parameters characterize the multilayer perceptron ANN functions, but in this chapter, the most relevant ones are presented (for more information, see the work of Hackeling (2017)). In each case, two meta-models are constructed; one for the maximum settlement and one for the inflection point.

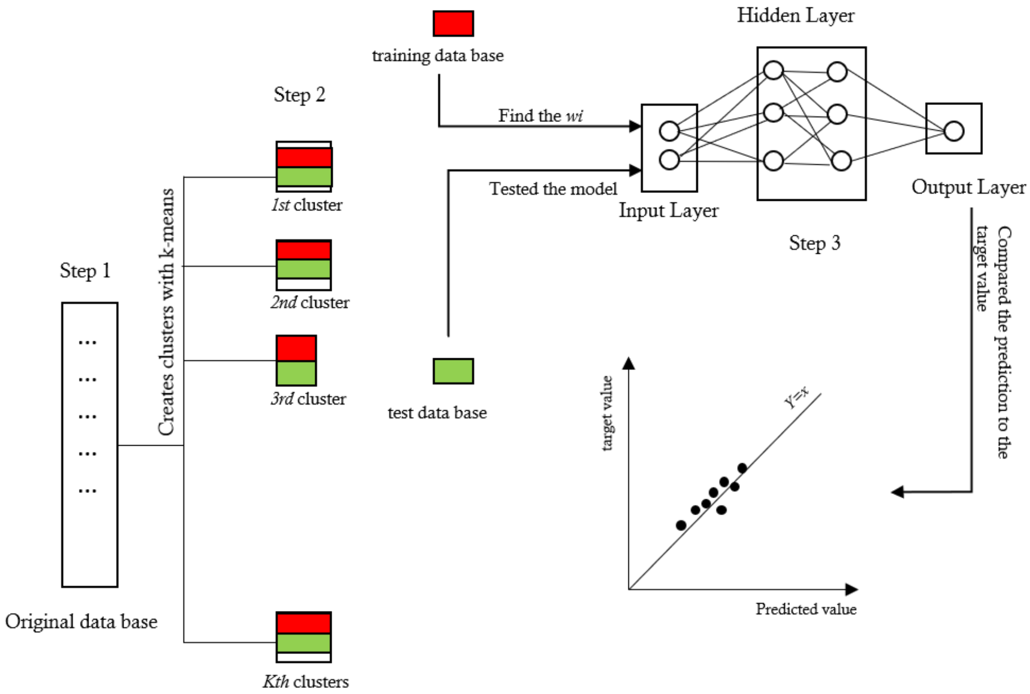

Figure 4.5: Proposed technique of coupling k-means with ANN

4.4.1 Meta model constructed on homogeneous stratified layer model

As already mentioned, for the homogeneous stratified soil, eight input parameters (the secant stiffnesses E_{50} of the layers) are used to sample 300 values with the Monte Carlo simulation following a uniform distribution for each of the input parameters. These inputs are then used to generate and calculate the 300 FE models. Figure 4.6 compares the distribution of the input parameters and the probability density function of the maximum settlement and the inflection point. According to this figure, different behaviors can be highlighted;

- The maximum settlement decreases with the increase of the deformation modulus of the Saint-Ouen limestones (E_{50}_cso) and the Beauchamp upper sand (E_{50}_sbs). This behavior reveals some correlations between the amplitude of the settlement and the modulus of the latter layers as demonstrated in chapter 3.

- The inflection point increases with the increase of the deformation modulus of the Saint-Ouen limestones (E_{50}_cso) and the Beauchamp upper sand (E_{50}_sbs) and the decrease of the deformation modulus of the Beauchamp lower sand (E_{50}_sbi).

- The maximum settlement increases with the decrease of the inflection point. This behavior reveals some correlations between the width of the settlement and the modulus of the latter layers as demonstrated in chapter 3.

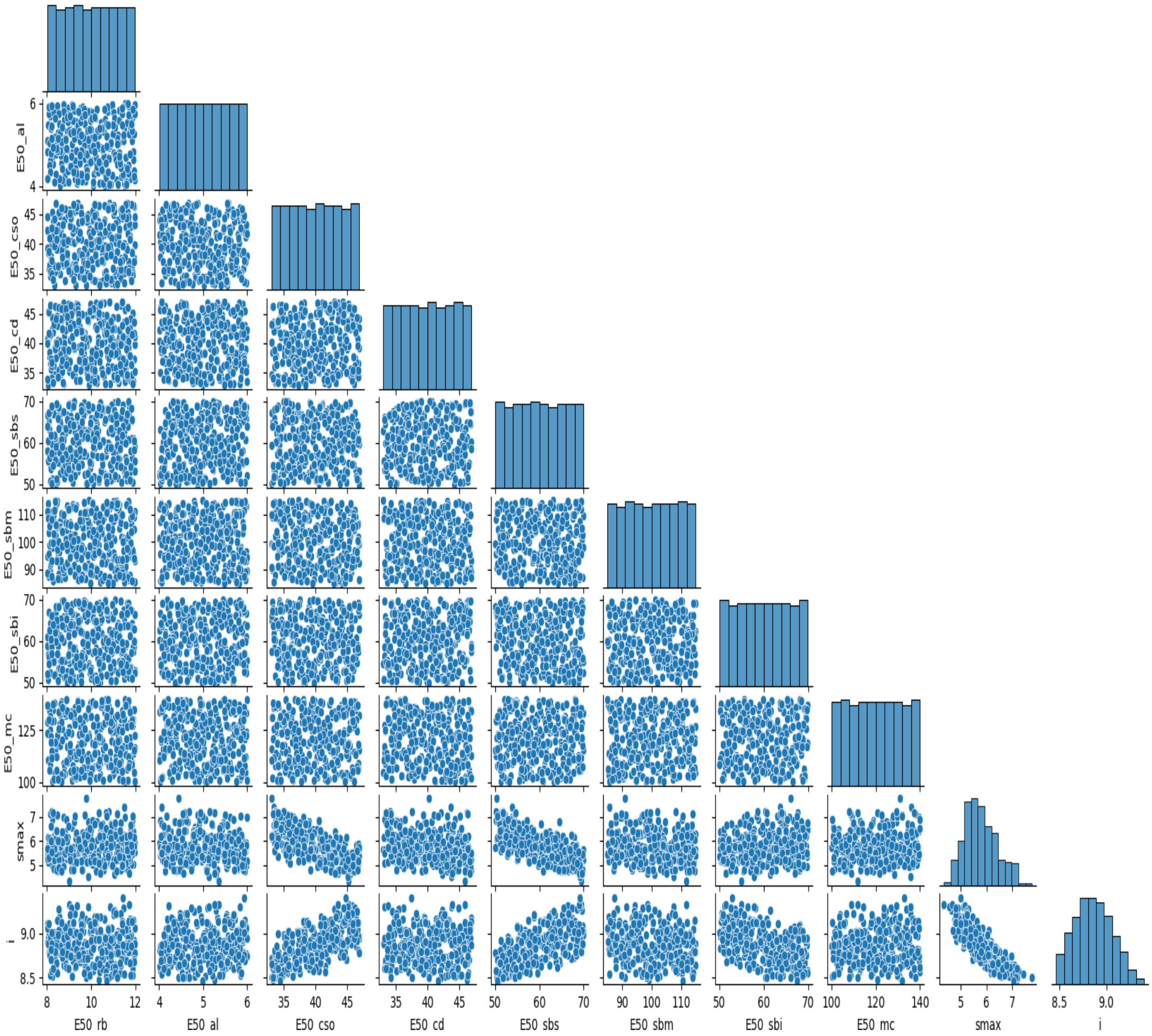

Figure 4.6: Uniform distribution of the input parameters and probability density function of the maximum settlement and the inflection point

Concerning the construction of the meta-models, table 4.4 presents the hyper parameters of the multilayer perceptron ANN function. These parameters were chosen iteratively by changing their values by hand. After dividing the database into clusters, 2 data points are selected in each cluster to train the model and 1 data point is selected for the validation. Figure 4.7 presents the determination coefficient R^2 between the predicted values and the FE result of the maximum settlement and the inflection point as a function of the number of clusters (from 10 to 25 clusters). The determination coefficient increases with the number of clusters and reaches a maximum of 97% for the maximum settlement and 95% for the inflection point.

Table 4.4: parameter used to construct the meta model in the homogeneous stratified case

Parameters	Object/value (S_{max})	Object/value (i)
Activation function	identity	identity
Solver	lbfgs	lbfgs
number of hidden layers	2	2
number of neurons	(10,4)	(15, 4)

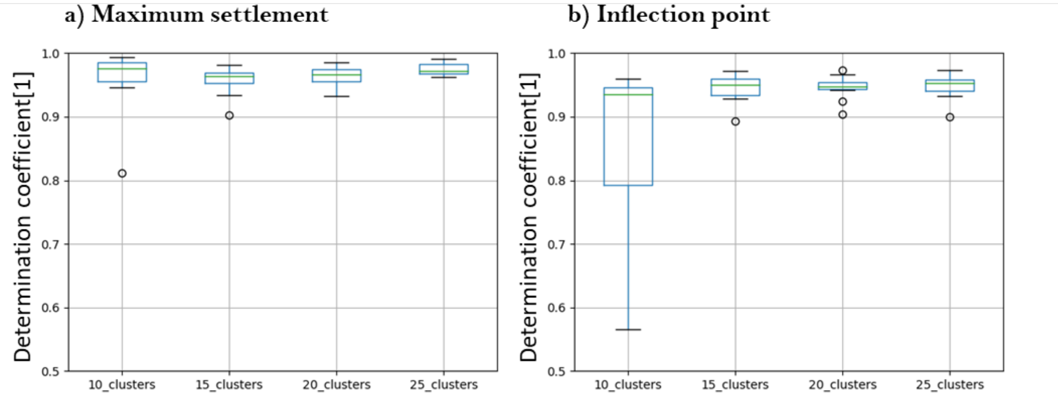

Figure 4.7: Determination coefficient of the meta model constructed with the full database for the stratified layer

For each of the selected clusters, a comparison is conducted between the FE results (10_FE for example for 10 clusters) and the predictions with the meta-models (10_Pred for example for 10 clusters). Figures 4.8 and 4.9 present the results of the maximum settlement and the inflection point respectively. The result are compared by couple (number of clusters_FE vs number of cluster_Pred for the settlement amplitude and the settlement trough width). Concerning the maximum settlement, with the increasing number of clusters, the mean of the predictions is closer to the mean value of the FE result. However, this conclusion is not valid for the inflection point. In both cases, the prediction results match the FE results very well and the dispersions of the outputs are almost the same. Using the meta-model constructed with 25 clusters, the predicted results and the FE results using the input data for testing are plotted on the same figure 4.10. The line with the equation $y = x$ represents the line where the predictions coincide with the FE results. It is observed that the predictions perfectly fit the FE results for both the maximum settlement and the inflection point.

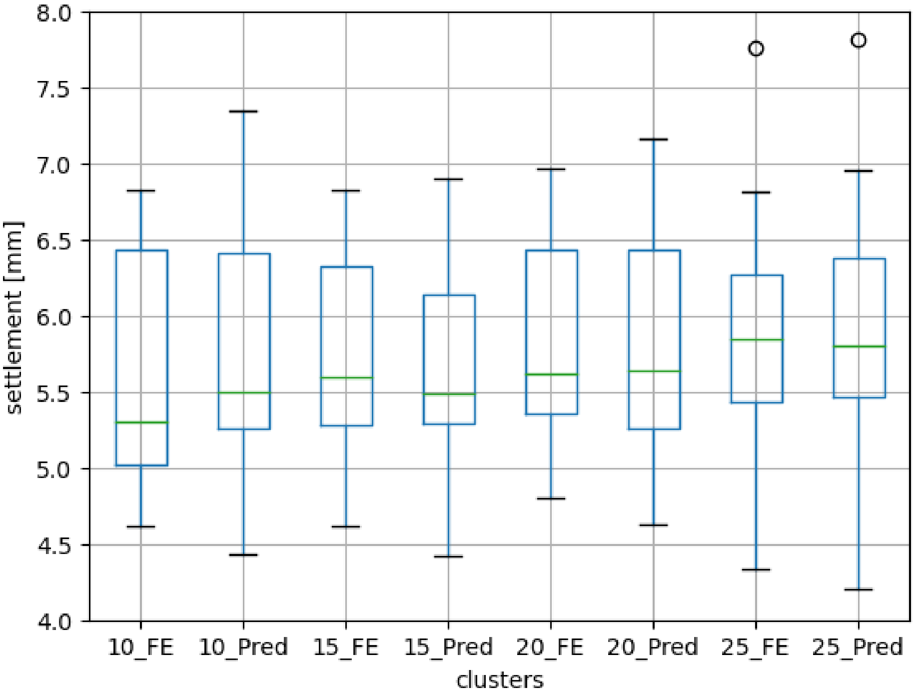

Figure 4.8: Maximum settlement box plot of the FE results (FE) and the predictions (Pred) for the stratified homogeneous layers according to a selected number of clusters

4.4.2 Meta model constructed with spatial variability model

As already explained in section 4.2 a model differs from another by the spatial repartition of the sublayer that comes from a random field. In order to consider this random generation of layers, several zones are selected using specific points in the models. Figure 4.2 presented the position of the 18 elements selected as input parameters for the meta-models construction. Each layer can have three possible values of deformation modulus E_{50} i.e. the mean (μ), the mean minus the standard deviation ($\mu - \sigma$) and the mean plus the standard deviation ($\mu + \sigma$). A total of 1000 2D simulations were carried out to construct the database following the proposed methodology.

Table 4.5: parameter used to construct the meta model in the spatial variability case

Parameters	Object/value (S_{max})	Object/value (i)
Activation function	identity	identity
Solver	lbfgs	lbfgs
number of hidden layers	2	2
number of neurons	(50,30)	(50, 4)

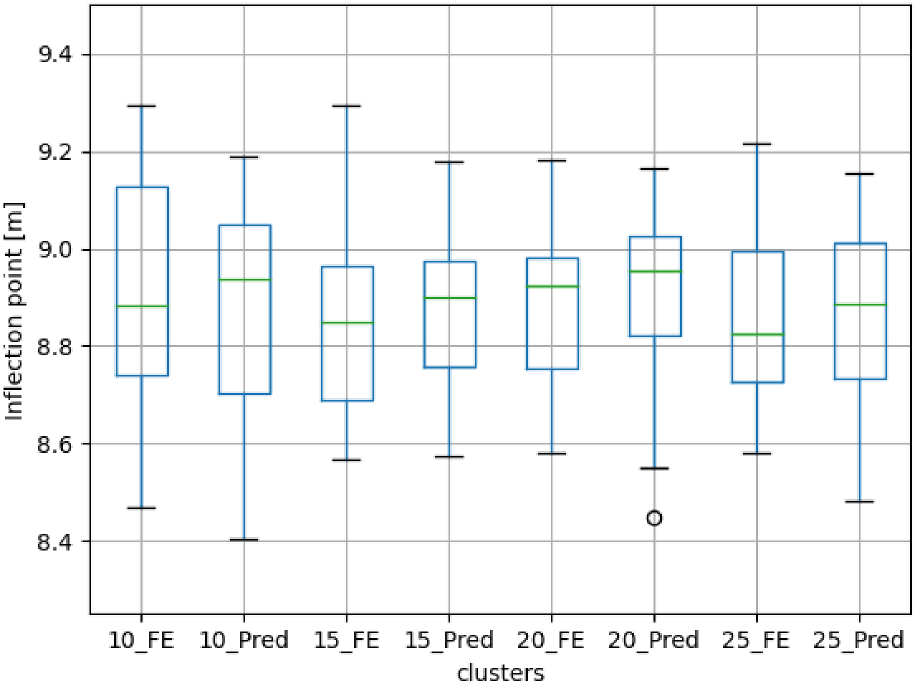

Figure 4.9: Inflection point box plot of the FE results (FE) vs the predictions (Pred) for the stratified homogeneous layers according to a selected number of clusters

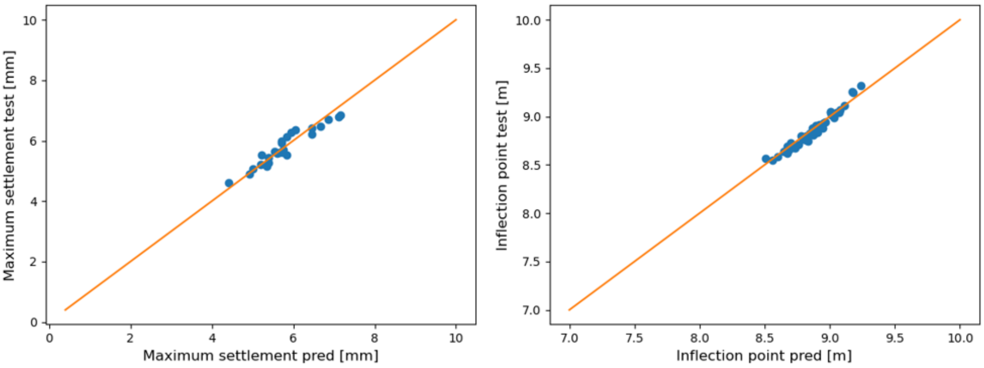

Figure 4.10: Meta model predictions vs FE results for the stratified homogeneous layers with 25 clusters

After dividing the database into clusters, 19 data points are selected in each cluster to train the model and 1 data point is selected for the validation. In this part, the number of training data is increased to improve the training. Table 4.5 presents the hyper parameters of the multilayer perceptron ANN function. These parameters were also chosen iteratively by changing their values by hand. The value of the hyper parameters that gives the highest R^2 was selected. Figure 4.11 presents the determination coefficient R^2 between the predicted values and the FE result of the maximum settlement and the inflection point as a function of the number of clusters (from 5 to 20 clusters). The determination coefficient increases with the number of clusters and reaches a maximum of 75% for the maximum settlement and 70% for the inflection point. For each selected number of clusters, a comparison is conducted between the FE results (5_FE for example) and the predictions with the meta-models (5_Pred for example). Figures 4.12 and 4.13 present the box plot results of the maximum settlement and the inflection point respectively. The results are compared by couple (number of clusters_FE vs number of cluster_Pred for the settlement amplitude and the settlement trough width). Concerning the maximum settlement, the mean of the predictions is closer to the mean value of the FE results and the dispersions of the FE results are different from the prediction one. For the inflection point, the mean value of the predictions are different from the one of the FE results and the dispersion of the results are different too. Using the meta-model constructed with 20 clusters, the predicted results and the FE results using the input data for testing are plotted on the same figure 4.14. 10 iterations are done in every cluster to construct these boxplots. this is why we have 4 different values of the determination coefficient. From this figure, even though the predictions follow the trend of the FE result, it is observed that the model predicts better the maximum settlement than the inflection point. These results confirmed that the meta model is not very performant.

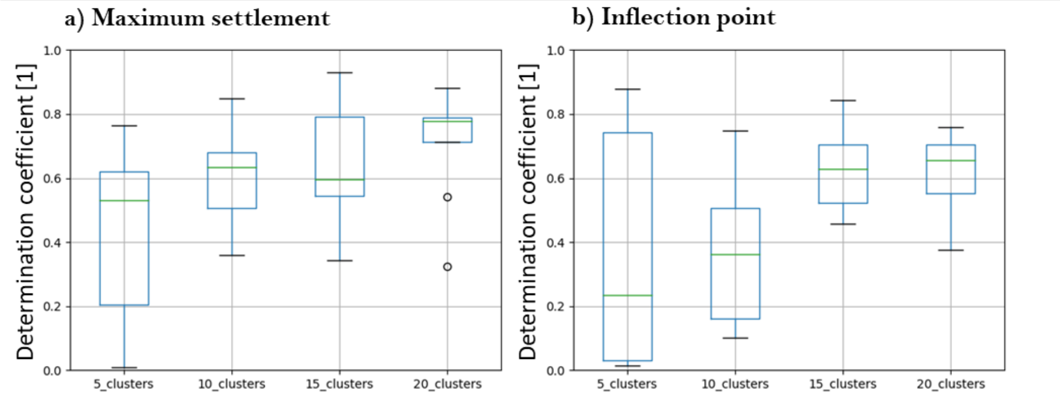

Figure 4.11: Determination coefficient of the meta model constructed with the spatial variability models

In this section, the proposed approach for constructing the meta-model has been used to predict the TBM-induced surface settlements. The results of 2D FE simulations provide the database. Two cases have been studied; the soil modeled as a stratified layer with uncertainties

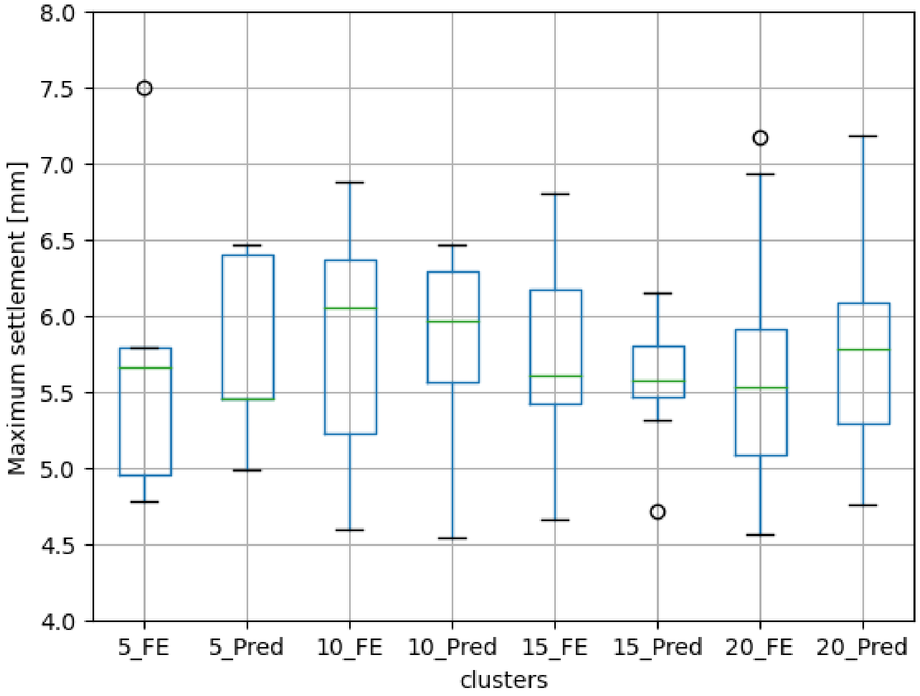

Figure 4.12: Maximum settlement box plot of the FE results (FE) and the predictions (Pred) for the spatial variability model according to a selected number of clusters

on the soil parameters and the spatial variability model. Using FE stratified models results has allowed obtaining excellent results for both the maximum settlement and the inflection point. Concerning the data from the spatial variability models, the results of the meta-modeling are not very good and deserve to be improved. For example the number of input parameters can be increased. Among the eight input parameters of the meta-model developed with the FE results of the stratified layers model, it can happen that all the parameters do not have the same influence on the outputs. In this case, it could be essential to understand the relationships between the input parameters and the output parameters. In the next section, some methods are firstly proposed to find the most relevant input parameters. Then, the number of input parameters will be reduced, and a new meta-model will be constructed based on the remains input parameters.

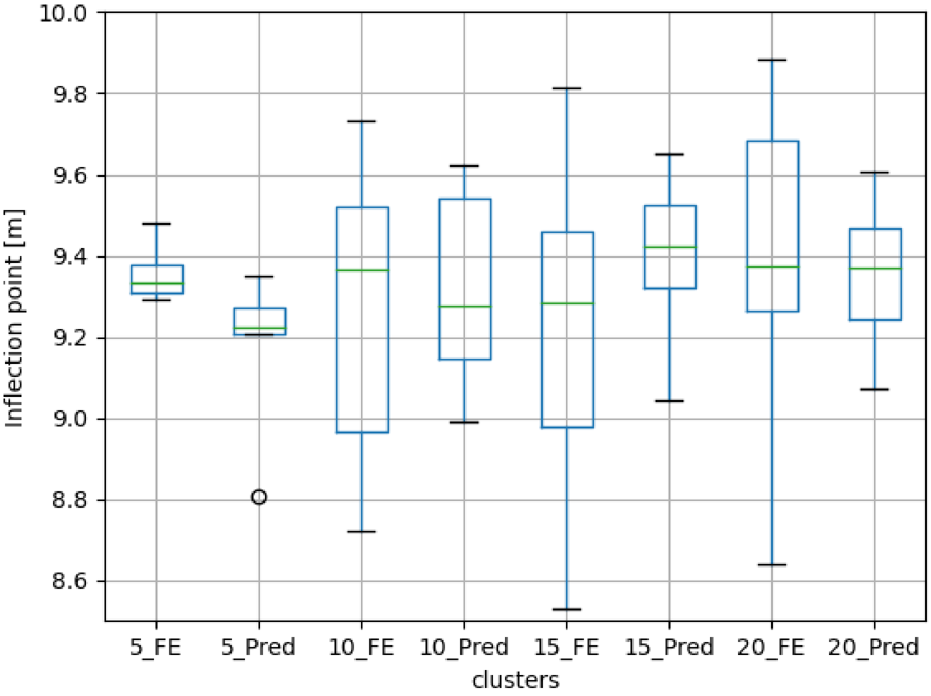

Figure 4.13: Inflection point box plot of the FE results (FE) and the predictions for the spatial variability model (Pred) according to a selected number of clusters

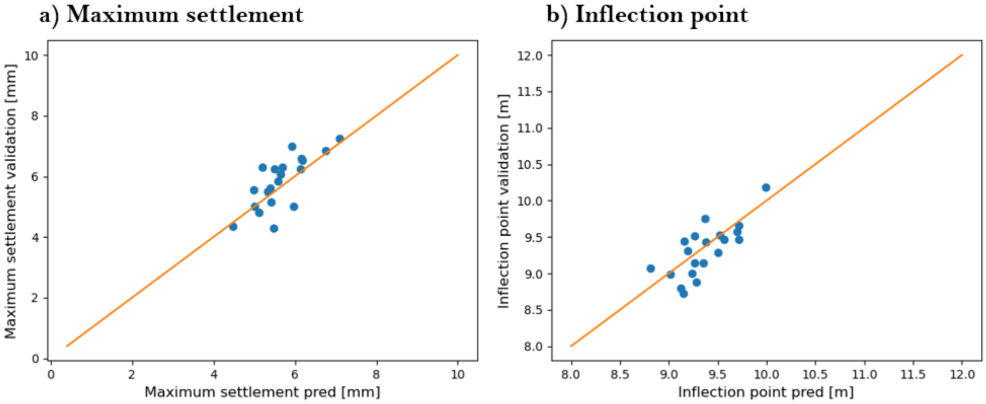

Figure 4.14: Meta model predictions vs FE results for the spatial variability model

4.5 Reduction of the input parameters and construction of a new meta model

4.5.1 Reduction of the input parameters

The objective of this study is to reduce the number of input parameters so that the remaining parameters explain some meaningful properties of the original data of the stratified layer model. Three methods are conducted to find the relevant parameters that most influence the maximum settlement and the inflection point; the sensitivity analysis, the Principal Component Analysis (PCA) and the classical correlation coefficient.

4.5.1.1 Sensitivity analysis

Chapter 3.1 of this thesis presents the methodology and the sensitivity analysis results. In this section, only the main results are presented. As already mentioned in the previous chapter, two main indices are required to quantify the influence of the input parameters on the settlement (maximum settlement and inflection point): the first order sensitivity (FOS) index and the total sensitivity (TS) index. The FOS index measures the marginal effect of one input parameter, whereas the TS index considers the FOS index and the interaction effect between the parameters. According to the results that are recalled in figure 4.15, for the maximum settlement, the stiffness E_{50} of the Saint Ouen limestone (CSO) is the most influential, with a sensitivity index of about 42% followed by the one of the upper sand of Beauchamp (SB sup) with a sensitivity index of 40%. The rest of the parameters can be considered negligible. Concerning the inflection point, the stiffness E_{50} of the Saint Ouen limestone is the most influential with a sensitivity index of about 45% followed by the one of the upper sand of Beauchamp with a sensitivity index of 30% and the one of the lower sand of Beauchamp with a sensitivity index of 18%.

4.5.1.2 Classical correlation coefficient for linear relationships among the parameters

The analysis by the correlation coefficient is a simplified approach that consists in determining the correlation coefficient between the input parameters and the output parameters. A positive correlation coefficient value means that an increase in the input variable leads to an increase in the output variable. A 0 value of the correlation coefficient means that the input variable and the output variable are not correlated, while a value of 1 or -1 implies that they are perfectly correlated.

The classical correlation method is conducted on the database to find the correlation between the input and output parameters. Figure 4.16 depicts the correlation between the stiffness of the multi-layer profile and a) the maximum settlement and b) the inflection point. From this

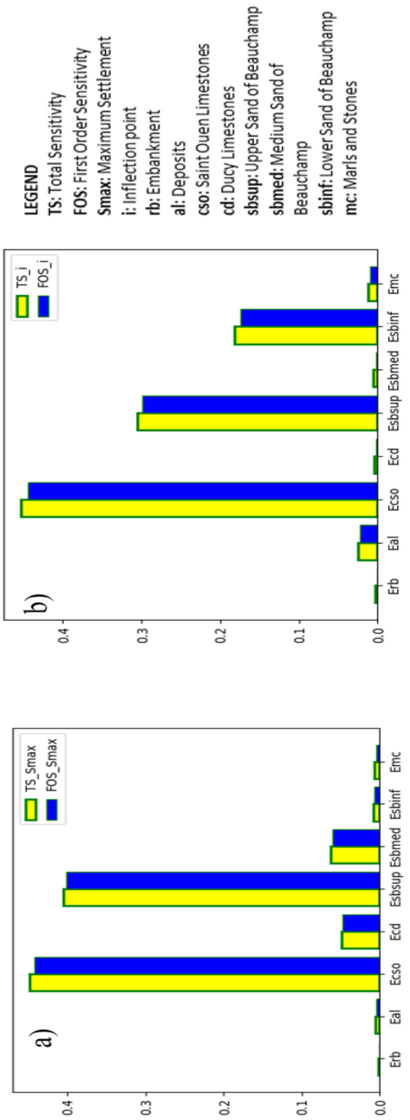

Figure 4.15: Sensitivity analysis considering E50 on (a) the maximum settlement and (b) the inflection point

figure, the Saint-Ouen limestones, the Beauchamp upper sand and the Beauchamp lower sand are correlated with the maximum settlement and the inflection point. This result completes the one obtained by the sensitivity analysis because it provides the sign of the correlation. For example, concerning the Beauchamp lower sand, its stiffness is negatively correlated with the inflection point. This means that the increase of this value creates a reduction of the inflection point.

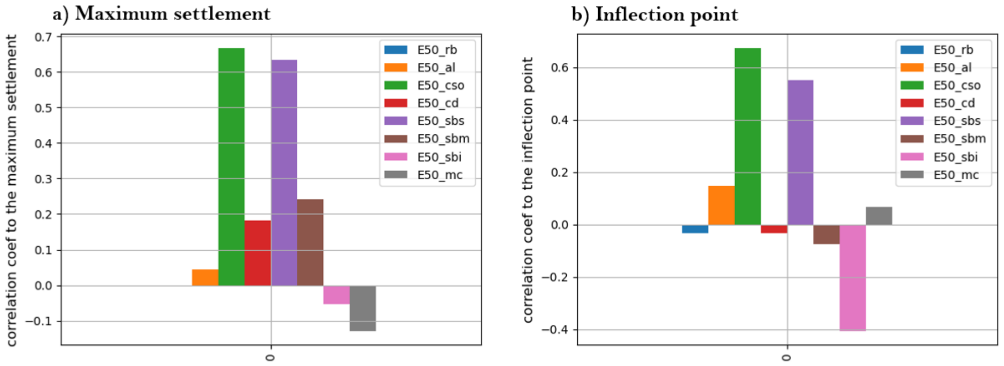

Figure 4.16: Correlation coefficient between the layer stiffness and a) the maximum settlement and b) the inflection point

4.5.1.3 Principal Component Analysis

Principal Component Analysis (PCA) is an unsupervised learning algorithm used to reduce the dimension of data in machine learning. The new features or the output of PCA are the principal components. The number of these principal components is either equal to or less than the original features present in the dataset. Some properties of these principal components are given below:

- The principal component must be the linear combination of the original features.
- These components are orthogonal among them.
- The importance of each component decreases with the rank of the principal component.

This importance is explained by the eigenvalues or the variance ratio which represent the weight of the principal component. According to Abdi and Williams (2010) in order to exploit the linear relationship between the results without a lot of information losses, the two first principal components must account for at least 70% on the overall data description.

PCA is conducted on the database formed by the eight input parameters and the two outputs (the amplitude of the settlement trough and inflection point). The two outputs are deduced from the settlement trough obtained from every simulation. The ratio of the eigenvalues and the cumulative curve of the principal components are represented by the Pareto chart in figure 4.17. According to this figure, all the principal components have almost the same importance (the variance ratio is around 10%) except the first principal component, whose variance is around 30%. For this reason, this analysis is focused on the first principal component. The contribution of the variables to the principal components is explained in figure 4.18. Concerning the first principal component, it is constituted by the variance of the maximum settlement (58%), the inflection (58%), the

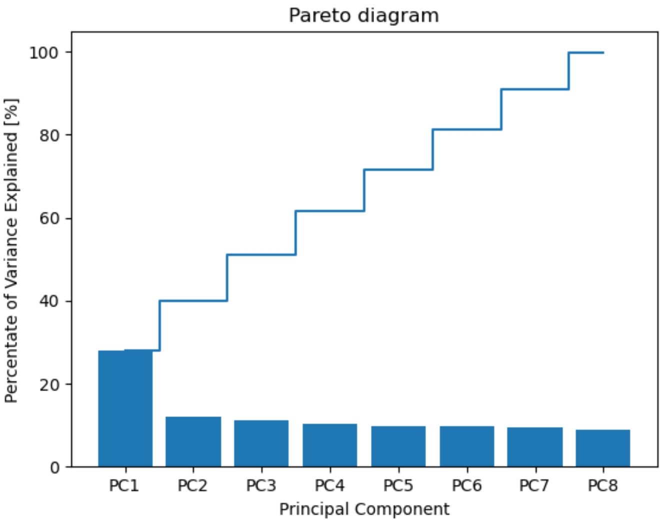

Figure 4.17: Principle component analysis eigenvalues representation

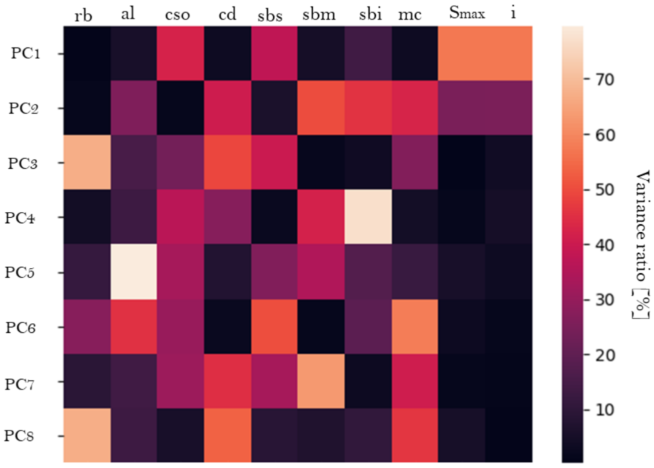

Figure 4.18: Contribution of the variables on the principal components

stiffness of the Saint Ouen limestones (43%), the stiffness of the upper sand of Beauchamp (38%) and the stiffness of the lower sand of Beauchamp (13%). This result makes it possible to explain the linear relationship between the data with these variables. To explain the relationship between these previous variables, the correlation circle formed by the two first principal components is used in figure 4.19. According to this figure, the stiffness of the Saint Ouen limestones and the stiffness of the upper sand of Beauchamp are a little bit correlated to the maximum settlement and the inflection. In contrast, the lower sand of Beauchamp is not correlated to the maximum

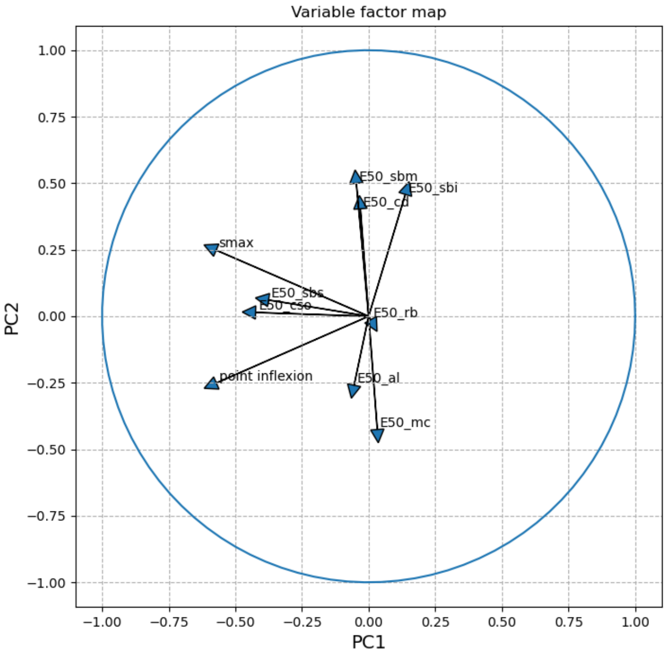

Figure 4.19: Correlation circle formed by the two main principal components

settlement but a little bit to the inflection point (for more application of the PCA see appendix B)

Between the three approaches used to determine the most relevant parameters on the output parameters (maximum settlement and the inflection point), the sensitivity analysis and the classical correlation coefficient give quite the same result. The latter can be explained by the Saint Ouen limestones, the upper sand of Beauchamp and the lower sand of Beauchamp influences. A weak linear relation is pointed out concerning the PCA between these variables and the output parameters.

4.5.2 New meta model constructed with the reduced database

According to the reduction of the number of input parameters, the original database with eight inputs can be reduced to a database of 3 inputs. In this subsection, 2 new meta-models are constructed using this reduced database. The first one is constructed to predict the maximum settlement while the second one is constructed to predict the inflection point. The hyper-parameters used for these meta models are the same as for the meta-model with the original database. Figure 4.20 presents the determination coefficient between the prediction and the FE result as a function of the number of clusters for the maximum settlement and the inflection point. The determination

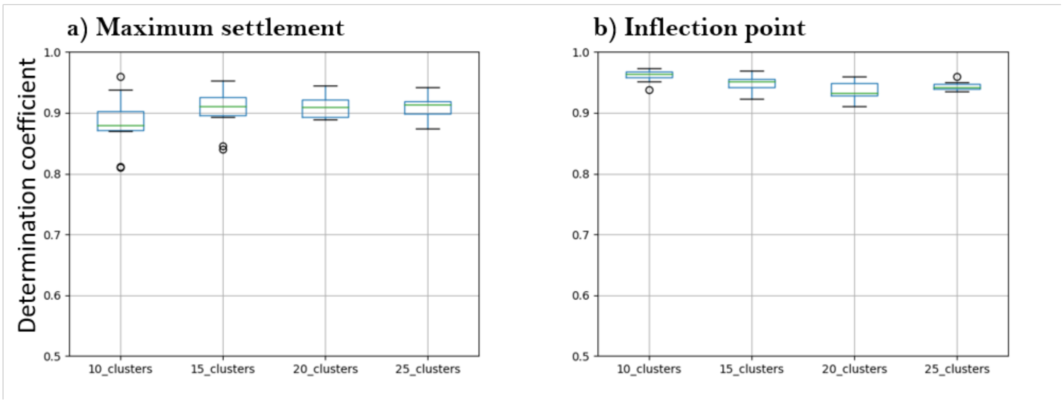

Figure 4.20: Determination coefficient of the meta model constructed with the reduced database

coefficient reduces from 97% to 90% for the maximum settlement while it remains constant around 94% for the inflection point.
The decrease of the determination coefficient value concerning the maximum settlement is due to the fact that in the meta model construction, the stiffness of the Beauchamp middle sand and the Ducy limestones were not considered. Even though according to figure 4.16 these parameters have a non-negligible influence on the maximum settlement. Concerning the inflection point, Beauchamp lower sand, Beauchamp upper sand and Saint-Ouen limestones are enough to completely explain the behavior between the inputs and the outputs.

The prediction of data using meta-models developed with regression algorithms like the ANN can be affected by uncertainties due to the random procedure of generating the weights that link the neurons. In this study, bootstrap is proposed to quantify these uncertainties in predicting the maximum settlement and the inflection.

4.5.3 Uncertainties estimation on the prediction

According to Ferrario et al. (2017), the prediction of a quantity with models like ANN can be affected by uncertainties due to different reasons:

- The training data set D_{train} cannot be exhaustive due to the limited number of input/output patterns that do not cover all the input space. Consequently, different training sets can give rise to different sets of weights w and then, to different sets of regression functions.
- The choice of the network architecture can be inappropriate. The number of hidden neurons plays a role in the model's efficiency.
- The global minimum may not be achieved: the minimization algorithm may get stuck in a local minimum, and/or the training may be stopped before reaching the minimum.

Thus, due to the uncertainties, for given model input parameters X_n, the model output Y can vary within a range of possible values characterized by a mean and a coefficient of variation. Bootstrapping gives the possibility to quantify the uncertainty of meta-models by estimating the interval of confidence of the quantity $h(X_n, w) - Y$. This method is able to quantify model uncertainties by considering a set of ANNs built on different data sets that are sampled with replacement (bootstrapped) from the original one (Zio, 2006). From each bootstrap data set, a bootstrapped regression model is built and the model output of interest is computed. Different bootstrap data sets give rise to a distribution of regression functions and so to a probability density function of the model output. Thus, the uncertainty of the estimated quantities provided by the ANNs can be quantified. An advantage of the method is that it provides confidence intervals for a given model output, without making any assumptions. As explained by Ferrario et al. (2017), the operative steps to quantify the uncertainties of the ANN model are detailed in the following steps:

- Step 1; divide the entire available data set of N input/output patterns into training and test data sets.
- Step 2; generate B bootstrap training data sets, $D_{train,b}, b = 1, ..., B$, by sampling with replacement from the original training data set D_{train}. Each set $D_{train,b}$, is composed by the same number N_{train} of the original training data set. Due to the sampling with replacement some of the input/output patterns in D_{train} can appear more than once in $D_{train,b}$, whereas some may not appear at all.
- Step 3; build the bootstrapped regression models $h_b(X_n, w_b), b = 1, ..., B$, on the basis of the training data sets $D_{train,b}$, generated at the previous step 2.
- Step 4; use the regression models of step 3 to compute the estimated $h_{Boot,b}(X_n), b = 1, ..., B$ of the model output $h(X_n)$ on the new data set $D_{test} = \{(X_n, h(X_n), n = 1, ..., N_{test}\}$. This way, N_{test} bootstrap-based empirical PDFs for the quantity $g(X_n)$ are produced. In correspondence of a new input X_n the bootstrap estimation $\mu(h_{Boot,b})$ is the average of the regression functions $h_{Boot,b}(X_n), b = 1, ..., B$ as shown in equation 4.5.1 and the bootstrap variance $\sigma^2_{Boot}(X_n)$ in equation 4.5.2

$$\mu(h_{Boot,b}) = \frac{\sum_{b=1}^{B} h_{Boot,b}(X_n)}{B} \tag{4.5.1}$$

$$\sigma^2_{Boot}(X_n) = \frac{\sum_{b=1}^{B} [h_{Boot,b}(X_n) - \mu(h_{Boot,b})]^2}{B-1} \tag{4.5.2}$$

To illustrate the bootstrap method, its application is conducted on the prediction of the maximum settlement and the inflection using the reduced database. This method is used here with

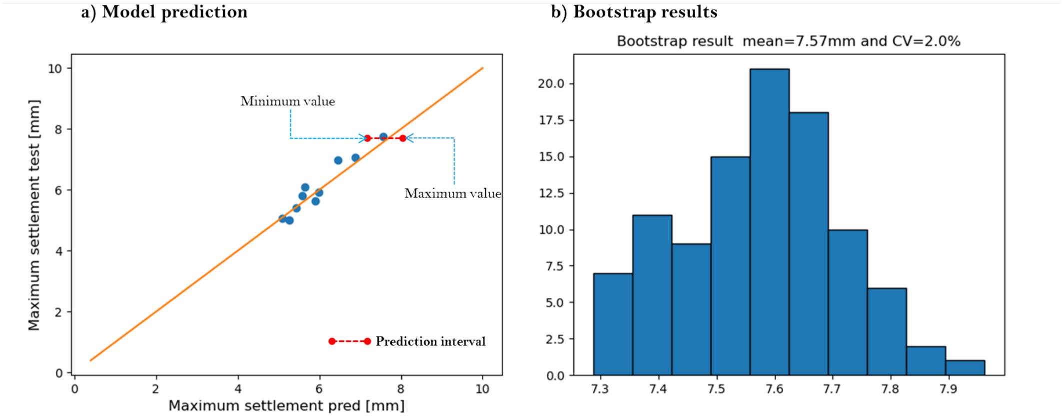
a) Model prediction

b) Bootstrap results

Figure 4.21: Uncertainty quantification on the maximum settlement due to the ANN model; a) the model prediction and b) the bootstrap results

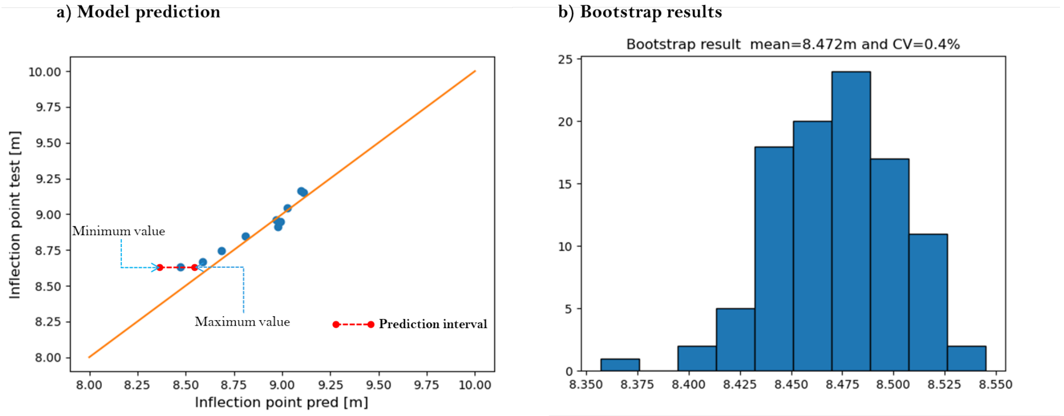
a) Model prediction

b) Bootstrap results

Figure 4.22: Uncertainty quantification on the inflection point due to the ANN model; a) the model prediction and b) the bootstrap results

a fixed network architecture i.e. the number of hidden neurons. It is possible to quantify the uncertainties on all the prediction points by computing the mean and the coefficient of variation. In this study, only one observation point is selected among 10 to illustrate the results. Figure 4.21a and figure 4.22a highlight the prediction interval (minimum and the maximum value) of the selected point for the maximum settlement and the inflection point respectively. Figure 4.21b and figure 4.22b represent the histogram of the predicted value of the maximum settlement and the inflection point respectively. According to these figures, the maximum settlement is more affected by the uncertainties (2% of the coefficient of variation) than the inflection point (0.4% of the coefficient of variation).

4.6 Conclusion

In this chapter, a new method of coupling an unsupervised learning algorithm (k-means) with a supervised learning algorithm (ANN) is proposed for meta-models construction in order to predict the TBM-induced surface settlement. Two approaches are considered to construct the database with 2D FE simulations. These databases are formed by the secant stiffness E_{50} of the soil layers as input parameters and the maximum settlement and the inflection point as the output parameters. 8 variables constituted the input parameters for the stratified layer model and 18 variables formed the input parameters for the spatial variability model. The predictions using the database constructed with homogeneous stratified layers give very good results (97% of the determination coefficient for the maximum settlement and 95% for the inflection point) compared to the prediction using the database constructed with the spatial variability model (75% of the determination coefficient for the maximum settlement and 70% for the inflection point).

Based on the stratified layers and the model reduction result, the number of input parameters on the database is reduced by considering only the parameters that mostly influence the maximum settlement and the inflection point i.e Bauchamp upper sand, Saint-Ouen limestones and Beauchamp lower sand. Other meta-models are also developed using the reduced database to predict the maximum settlement and the inflection point. The determination coefficient of the maximum settlement was reduced to 90% while the one of the inflection point remained almost constant (94%). Due to some reasons that have been already explained, the prediction with a regression model such as the ANN is affected by some uncertainties. With the bootstrap method, the uncertainties of the meta-models have been quantified, and the inflection point appears to be less affected than the maximum settlement.

In a heterogeneous soil profile, it is generally difficult to determine the spatial distribution of the soil parameter due to the lack of $in-situ$ tests. In the case of TBM construction, these limitations can seriously affect the safety of structures and infrastructures in the vicinity of the tunnel. In the next chapter, the consideration of the soil heterogeneity effect on the TBM-induced building damage will be studied.

Chapter 5

Soil heterogeneity effect on the TBM-induced settlement

Contents

5.1 Introduction

Tunnelings in urban areas are excavated at shallow depths and in the heterogeneous soil profile, TBM-induced building damages have to be carefully studied. To prevent damage scenarios, prediction methods are usually adopted. As it has already been shown, the numerical simulation with the three-dimensional (3D) Finite Element simulation appears to be the best approach to evaluate the TBM-induced building damages since it allows a better representation of the TBM pressures and excavation and gives reliable results (high fidelity result). But, this approach can be time-consuming when several simulations are conducted. Thanks to the methodology that has already been explained in chapter 2, the 2D approach gives the possibility to save some calculation time. On the contrary, two major problems appear with the use of this method: Firstly, the calibration of the 2D fictitious pressure used in the convergence-confinement method that accounts for the 3D pressures. This fictitious pressure is not reliable since it has been carried out with homogeneous and stratified soil models. Secondly, the results from 2D simulations are not always reliable (Low fidelity results) due to the simplification in the reduced models. However, it is possible to determine reliable data from low-fidelity data with machine learning approaches based on a multi-fidelity approach (Kampolis and Giannakoglou, 2008; Li and Jia, 2020).

In literature, some authors demonstrated that soil heterogeneity can be implicitly considered with probabilistic approaches in geotechnical problems (Baecher and Christian, 2005b; Phoon and Kulhawy, 1999, 1996; Griffiths and Fenton, 2007; Whitman, 1984). It was in this mind that Franco et al. (2019) studied a rational and efficient probabilistic framework on the extension of Line 5 of the Sao Paulo Metro to address the uncertainties of geotechnical properties of soil and stratigraphic profiles in tunneling-induced building damage assessment. Mollon et al. (2013) implemented the collocation-based stochastic response surface method based on hypothetical cases to provide a comprehensive approach for evaluating settlement and horizontal displacement uncertainties. On the other hand, Some authors tried to consider explicitly the heterogeneity of soils in analyses. El Gonnouni et al. (2005) used the random field theory and information from the borehole logs made along a tunnel path to estimate the mean values for the layer positions and their corresponding variances by employing the geostatistical kriging method. They proposed an approach for estimating the ground settlement and lateral displacement due to tunneling that considers the spatial variability of the longitudinal ground profile.

Concerning the improvement of predictions with machine learning approaches, in the literature, some authors presented different approaches to improve the prediction of meta models with a smaller amount of high fidelity (HF) data. Nabian et al. (2021) tried to solve this issue via an importance sampling strategy. Recently, some researchers also tried to utilize data with low fidelity (LF), such as 2D numerical simulation results, to replenish the lack of HF data (Kampolis and Giannakoglou, 2008). By introducing the LF data into the database for model training, the issue of lacking enough training samples would be relieved. However, due to the low accuracy of LF data, the corresponding model's accuracy and generalization ability could be affected. To enhance the model built from different fidelity levels of data, Kennedy and O Hagan (2000) carried out an autoregression (AR) Co-kriging scheme based on a Gaussian process model to promote the accuracy of low-fidelity data through the cross-correlation between high- and low fidelity data. Raissi and Karniadakis (2016) combined the AR Co-kriging scheme with forward neural networks and proposed a deep multi-fidelity (MF) Gaussian process model, which could solve nonlinear regression problems. Li and Jia (2020), Meng and Karniadakis (2020), and Zhang et al. (2021b) also tried to improve the MF approach by combining different Machine Learning approaches.

In this chapter, 3D and 2D simulations of the Paris Metro Line12 extension are conducted with heterogeneous soil profiles to determine the value of the fictitious pressure that allows to fit the 2D settlement trough to the 3D one. Then, based on the 2D approach, the TBM-induced building damage is assessed, and the effect of the building location and the TBM pressure are studied. Finally, with some 3D FE (HF data) simulations and 2D FE simulations (LF data), the methodology proposed in chapter 4 is applied in addition to the MF approach to determine the building damages from the 2D results.

5.2 Heterogeneity of soil modeled as spatial variability model

In Chapter 3, the fictitious pressure used for the 2D spatial variability models was calibrated on stratified homogeneous soils. The study of the influence of the mesh size on the settlement trough showed that the use of a fine mesh gives slightly larger settlements than the coarse mesh with a higher calculation time. The objective of this section is to examine the validity of using calibrated fictitious pressure on heterogeneous soil profiles. For this purpose, 3D and 2D models with spatial variability on the soil stiffness are developed with the same random fields in order to determine the fictitious pressure that allows to calibrate the settlements obtained with a 3D model. The coarse mesh is adopted for the models.

5.2.1 Three-dimensional approach of spatial variability model

The 3D models are developed by taking into account the 2D plane spatial variability that is well explained in chapter 3 by extruding along the z axis. As already mentioned, developing a spatial variability model requires the generation of random fields and their transformations into soil layers. Figure 5.1 presents an example of a 3D spatial variability model configuration in which soil layer is divided into three sub-layers by considering the different values of the soil stiffness: the mean

(μ), the mean minus the standard deviation ($\mu - \sigma$) and the mean plus the standard deviation ($\mu + \sigma$).

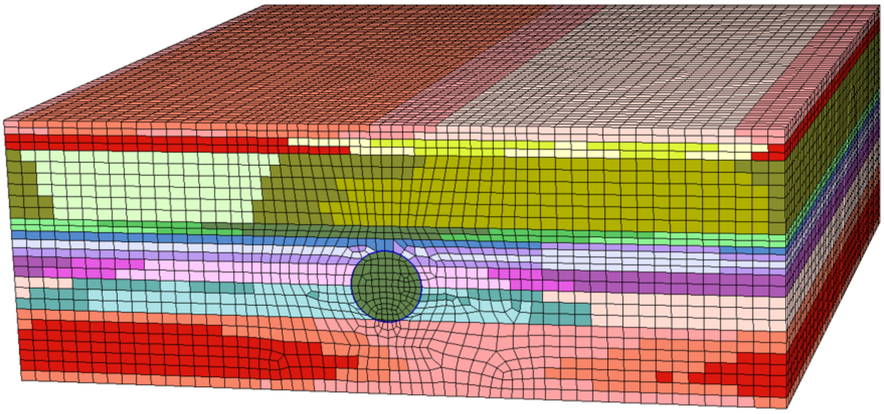

Figure 5.1: An example of a 3D heterogeneous model

The methodology to conduct 3D and 2D FE simulations have already been explained in chapter 2 section 2.4 and in chapter 3 sectionmodeldescription with a homogeneous stratified layer profile. Concerning the 3D simulation, the tunnel construction is a step-by-step procedure. The excavation is simulated by eliminating of the soil element while applying a face pressure to maintain the face stability and prevent inflow. During the progression of the TBM, pressure is applied along the shield, and also the grout injection behind the liner to install the linings at the shield tail as presented in chapter 2. At the end of the calculation steps, the settlement is stabilized in the middle of the model. For the 2D simulation, the convergence confinement method with the explicit approach is adopted with a confinement loss of 0.9. The fictitious pressure that accounts for the 3D real pressures has already been calibrated.

5.2.2 Three-dimensional and two-dimensional Finite Element comparison

In this section, the fictitious pressure calibrated in chapter 3 using the homogeneous stratified soil layer is first used to conduct the 2D FE simulation. The goal of this section is to compare the 3D and 2D FE settlement troughs in order to confirm whether the fictitious pressure is also valid with heterogeneous soil.

A series of twenty 3D and 2D FE simulations are conducted to evaluate the maximum settlement. The 2D models are developed with the same spatial repartition of the soil parameters as the 3D ones. Figure 5.2 presents the result of the 3D simulations and the corresponding 2D simulations. In this figure, the line $y = x$ represents the trend where the 3D result equals the 2D one. The points represent the couple formed by the 2D and corresponding 3D results. According to this figure, the 3D results are higher than the corresponding 2D results consequently, the value of the fictitious pressure is not valid for the heterogeneous model. However, the points formed by the 2D and 3D results follow a linear trend. So, according to this figure, apart from the spatial variability, another phenomenon is involved in the response of the models. To better understand this phenomenon, the 2D fictitious pressure used in the simulations is adjusted to fit the 3D results before analyzing the 3D, and 2D stresses evolution.

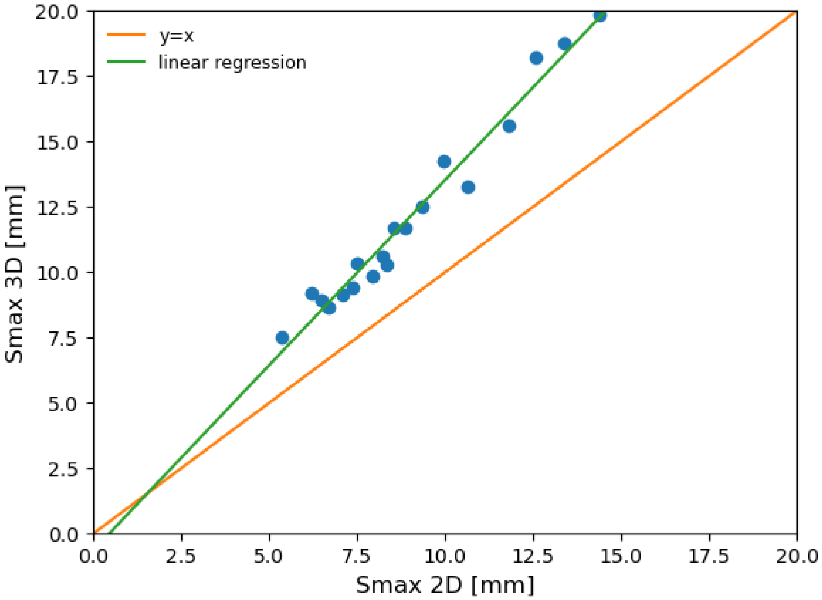

Figure 5.2: 3D results and the corresponding 2D result of the heterogeneous soil profile

For each configuration, the fictitious pressure that allows to fit the 2D spatially variable model results to their corresponding 3D spatially variable models is calibrated. Figure 5.3 shows the result of the 3D and 2D maximum settlement after calibration. As it can be seen on this figure, the 3D and the 2D results perfectly coincide.

Assuming that the 3D results and the 2D fictitious pressure calibrated from the stratified homogeneous model are the right solutions, there is a relation between the pressure variation and the maximum settlement. In this study, the difference between the original 2D fictitious pressure calibrated on the homogeneous stratified layer and the adjusted 2D fictitious pressure is assumed to be related to the variation of the injection pressure in the 3D model. Thus, to analyze this variation effect, the variation rate in the maximum settlement and in the injection pressure are compared. The maximum settlement error is assumed to be the ratio between the 2D result (using the initial fictitious pressure) and the 3D result. The injection pressure error is supposed to be

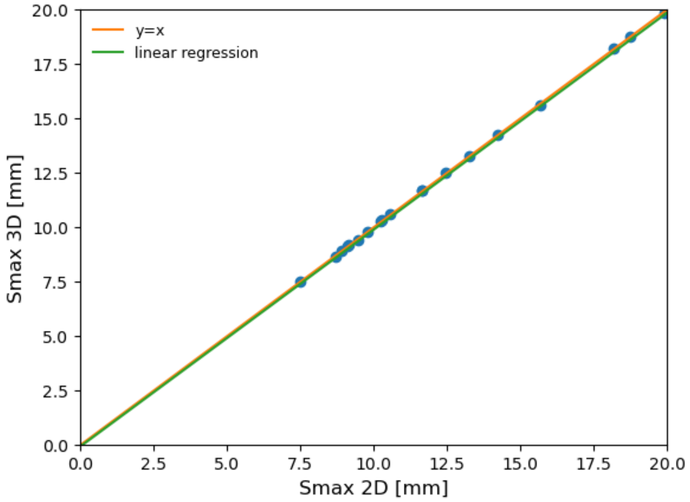

Figure 5.3: 3D results and the corresponding 2D result with the modified fictitious pressure

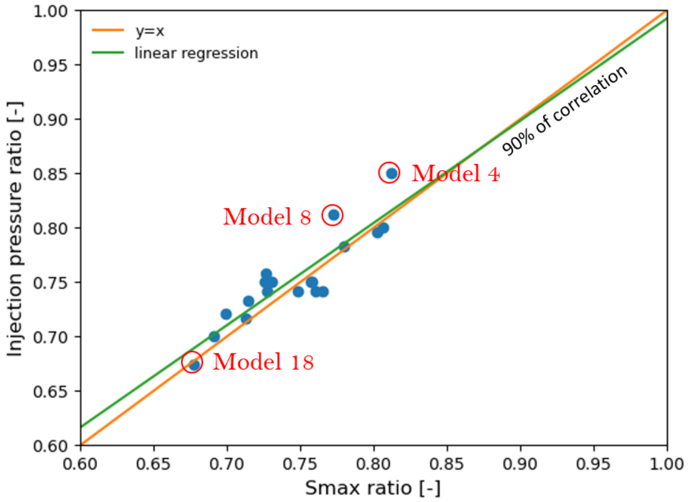

Figure 5.4: Comparison between the maximum settlement ratio and the injection pressure ratio

the ratio between the injection pressure of the spatially variable model (coming from the adjusted 2D fictitious pressure) and the injection pressure of the homogeneous stratified model. Figure 5.4 presents the maximum settlement error and the injection pressure error results. According to this figure, the maximum settlement ratio and the injection pressure ratio are correlated with a correlation coefficient of 0.90. In this figure, it can also be seen that a variation of the pressure does not have the same effect on the maximum settlement for all models.

To better understand these effects, three models are considered for further investigation, i.e. models 4, 8 and 18 as presented in figure 5.4. These investigations are the analysis of the displacement field and the stress evolution of the models.

5.2.2.1 3D and 2D settlement field analysis

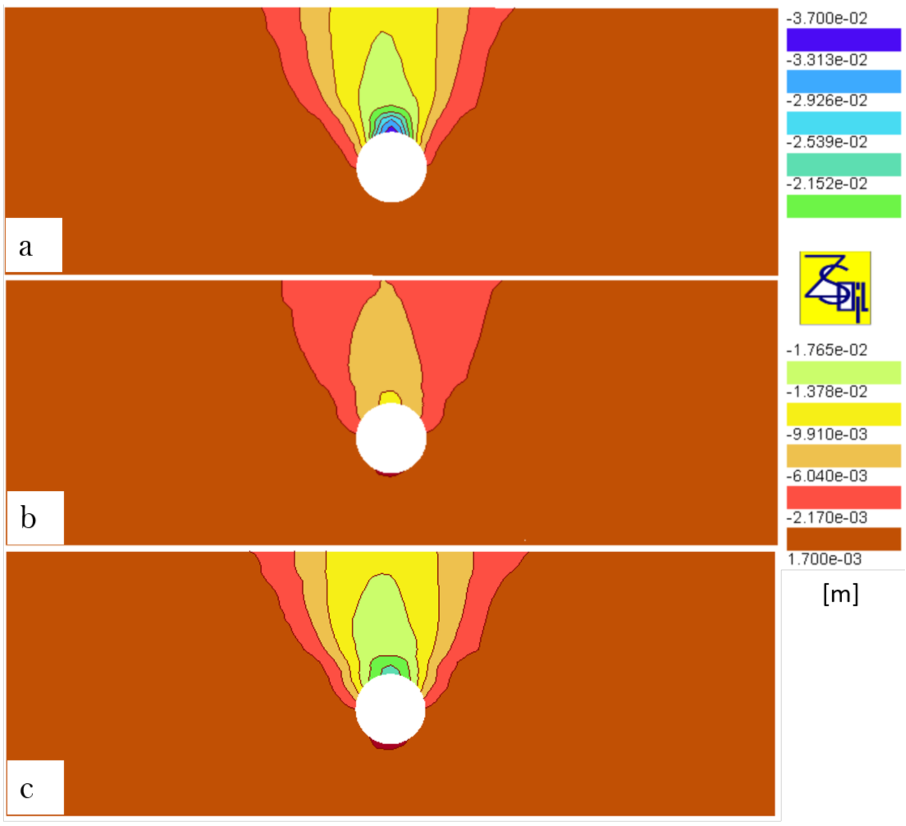

Figure 5.5: Settlement field in the soil mass for a) The 3D spatially variable soil profile, b) The corresponding 2D model simulated with the fictitious pressure calibrated on the homogeneous stratified model and, c) The corresponding 2D model simulated with the new fictitious pressure (calibrated pressure that allows to fit the 2D settlement to 3D one with the spatial variability model)

Figure 5.5a shows the settlement field of a 3D spatially variable model at a cross-section in which the settlements are stabilized. Figure 5.5b shows the 2D settlement field of the corresponding model calculated with the original fictitious pressure (pressure calibrated with the homogeneous stratified layer). Figure 5.5c shows the 2D settlement field of the spatially variable model with the adjusted fictitious pressure. Although the maximum surface settlement in figure 5.5a and figure 5.5c are equal, the settlement maps inside the soil mass are different. At the tunnel crown, the soil mass more converges in the 3D model than in the 2D model (figure 5.5c). At the tunnel invert, the uplift is more significant in the 2D model than in the 3D model. These results can be due to the third-dimensional effect not considered in the 2D model. Assuming the plane strain hypothesis, the deformation of the element in the third dimension is not considered. To better understand this effect, some analyses of soil element stresses located at the crown of the tunnel are conducted in the next section.

5.2.2.2 3D and 2D stress state analysis

As the excavation proceeds, the stress tensor $\begin{bmatrix} \sigma_{xx} & \sigma_{xy} & \sigma_{xz} \\ \sigma_{yx} & \sigma_{yy} & \sigma_{yz} \\ \sigma_{zx} & \sigma_{zy} & \sigma_{zz} \end{bmatrix}$ that characterizes a soil element evolves. Since the stress tensor is a real symmetric matrix, it can be written as a diagonal matrix consisting of its principal stresses: $\begin{bmatrix} \sigma_1 & 0 & 0 \\ 0 & \sigma_2 & 0 \\ 0 & 0 & \sigma_3 \end{bmatrix}$. The principal stresses σ_1, σ_2, σ_3 allow to determine the invariants of the tensor (as presented in equations 5.2.1,5.2.2 and,5.2.3), i.e. the characteristic quantities which do not depend on the chosen basis.

$$I_1 = \sigma_1 + \sigma_2 + \sigma_3 \tag{5.2.1}$$

$$I_2 = \sigma_1\sigma_2 + \sigma_3\sigma_2 + \sigma_3\sigma_1 \tag{5.2.2}$$

$$I_3 = \sigma_1\sigma_2\sigma_3 \tag{5.2.3}$$

Let note $p = \frac{I_1}{3}$ the isostatic stress. The stress tensor can be decomposed into a sum of two tensors: the deviator $\begin{bmatrix} s_{xx} & s_{xy} & s_{xz} \\ s_{yx} & s_{yy} & s_{yz} \\ s_{zx} & s_{zy} & s_{zz} \end{bmatrix}$ and the isostatic pressure $\begin{bmatrix} p & 0 & 0 \\ 0 & p & 0 \\ 0 & 0 & p \end{bmatrix}$. The deviator has the same principal directions as the stress tensor, and can therefore be written as $\begin{bmatrix} s_1 & 0 & 0 \\ 0 & s_2 & 0 \\ 0 & 0 & s_3 \end{bmatrix}$. One can define the invariant of this tensor as presented in equations.5.2.4, 5.2.5 and, 5.2.6.

$$J_1 = s_1 + s_2 + s_3 = 0 \tag{5.2.4}$$

$$J_2 = -s_1s_2 - s_3s_2 - s_3s_1 = \frac{1}{3}I_1^2 - I_2 \tag{5.2.5}$$

$$J_3 = s_1s_2s_3 = \frac{2}{27}I_1^3 - \frac{1}{3}I_1I_2 + I_3 \tag{5.2.6}$$

Concerning the three models that have been selected to study the evolution of stresses at the crown, the soil element at the crown of model 4 is characterized by a value of E_{50} equal to 168 kPa, the one of model 8 is characterized by a value of E_{50} equal to 123 kPa and the one of model 18 is characterized by a value of E_{50} of 212 kPa. Figure 5.6 shows the evolution of the deviatoric stress in the 3D model.

At calculation step 0, the stresses are initialized in the soil mass and a slight stress difference between the three models is observed. To quantify the difference, the variation rate in initial stresses is computed as $\frac{J_{2max}-J_{2min}}{J_{2max}}$. Between model 4 and model 18, the error on the deviatoric stress is 7%. Between model 4 and model 8, this error is 9%.
With the TBM progression, the deviatoric stresses decreased until 15 m (1.5 times the diameter, corresponding to step 25) to the section in which the settlement stabilized. From 1.5 times the diameter to the excavation of the section, the stresses increase due to the face pressure and the arch effect that develops at the TBM face. During the front excavation, the stresses drop dramatically (from steps 34 to 35). While the TBM crosses the section, the settlement remains almost constant (from step 35 to step 41). During the installation of the lining segments, the effect of the injection pressure to fill the mortar increases the stresses before their stabilization (from step 41 to step 43). At the end of the procedure, the final value of the stresses is lower than the initial one.

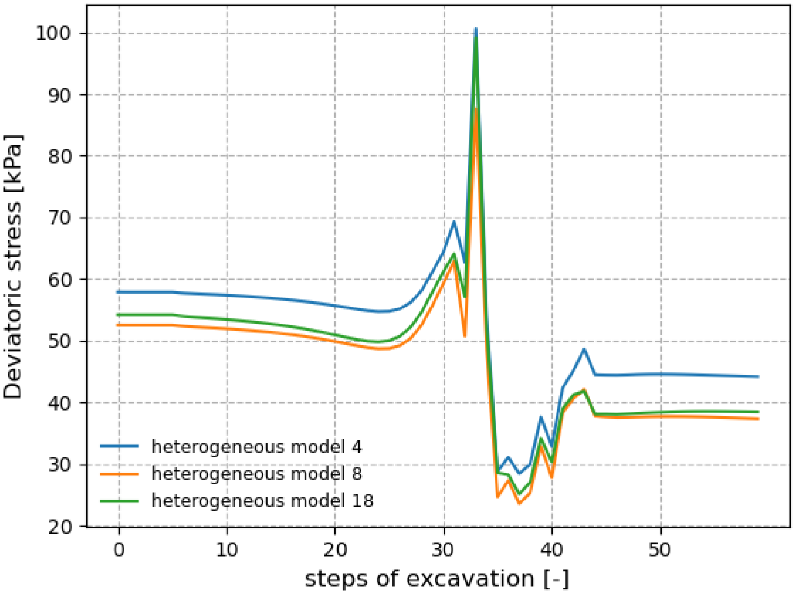

Figure 5.6: Deviatoric stress path evolution in the 3D models

Concerning the 2D simulation stress analysis, figure 5.7 shows the evolution of the deviatoric stress. In this figure, two cases can be distinguished; the solid curves for the models in which the fictitious pressure is calibrated on the homogeneous stratified model (initial case) and the dashed curves for the models in which the fictitious pressure has been adjusted to fit the 3D maximum settlement (calibrated case). As it has already been explained, the simulation procedure of a TBM excavation is mainly divided into 3 phases: the initialization of the stresses, the excavation and the construction of the lining segments. The stresses are the same from the initialisation to the excavation phase in both cases. Between model 4 and model 18, the error in the deviatoric stress is 5%. Between model 4 and model 8, this error is 13%.

During the excavation phase, the stress evolution is different in the two cases.

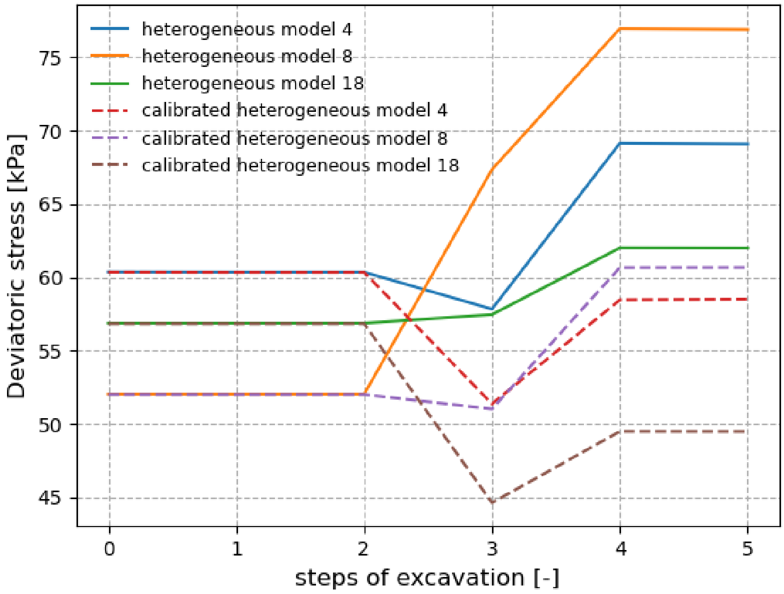

Figure 5.7: Deviatoric stress path evolution in the 2D models

- For the initial case: the soil element at the crown in model 4 is stiffer than the soil element at the crown in model 18 and softer than the one in model 8. Applying the confinement loss to simulate the excavation and the fictitious pressure increases the deviatoric stresses in models 8 and 18, unlike in model 4.
- For the case after calibration: the stresses decrease during excavation. This reduction is more significant in model 18 than in model 4 and in model 8.

In the lining segment construction phase, the application of the fictitious pressure creates an increase in the stresses. The final deviatoric stress of models 18 and 4 is lower than the initial stresses as the 3D result, while the final deviatoric stress of model 8 is higher than the initial one. Figure.5.8 shows the deviatoric stress maps of the 3D model, the initial 2D model and the calibrated 2D model at the end of the excavation.

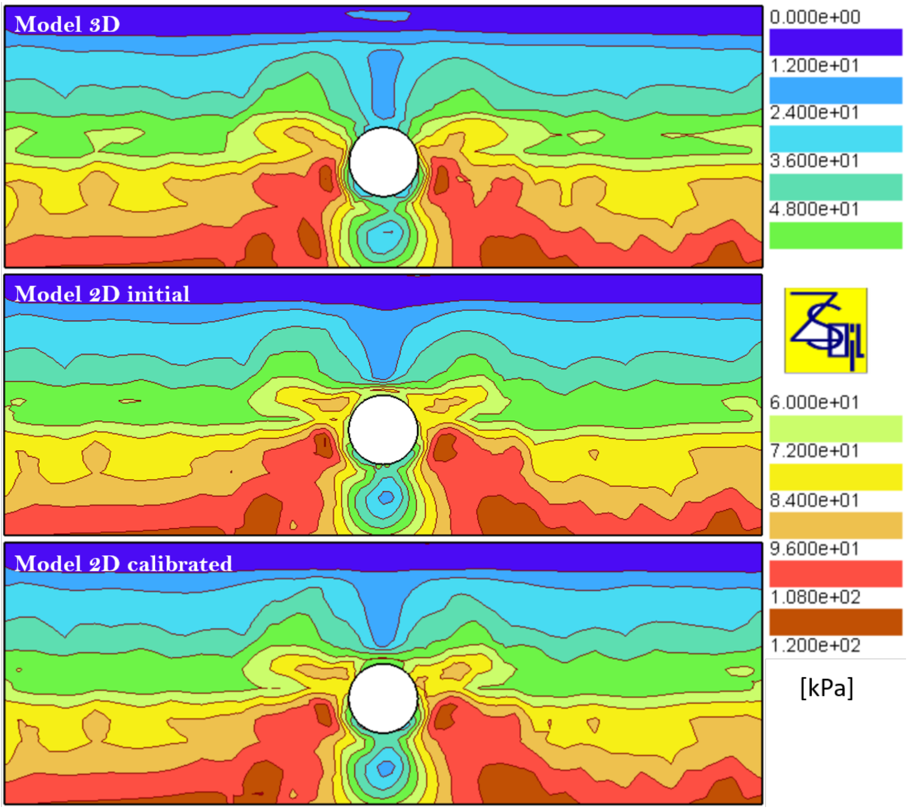

Figure 5.8: Principal deviatoric stress distribution in the soil mass

The stress variation between the 3D and the initial 2D model is similar to the one between the 3D and the calibrated 2D model. Figure 5.9 shows the logarithm of the difference in the deviatoric stress variation (final state minus the initial stress state) between the 2D models and the 3D model. This comparison is conducted between the 2D adjusted model and the 3D model (figure 5.9a) and between the initial 2D model and the adjusted 2D model (figure 5.9b). In these figures, the green area represents the area in which the 3D deviatoric stresses are higher than the 2D deviatoric stresses, and the blue area represents the areas in which the 3D stresses are lower than the 2D stresses.

In figure 5.9a, it can be noticed that at the final equilibrium state, the deviatoric stress variation is higher at the crown in the 2D model than in the 3D model. One would expect higher displacements in the 2D crown than in the 3D model but, this is actually not the case. This behavior is explained by the effect of the third component, which cannot be represented in the 2D

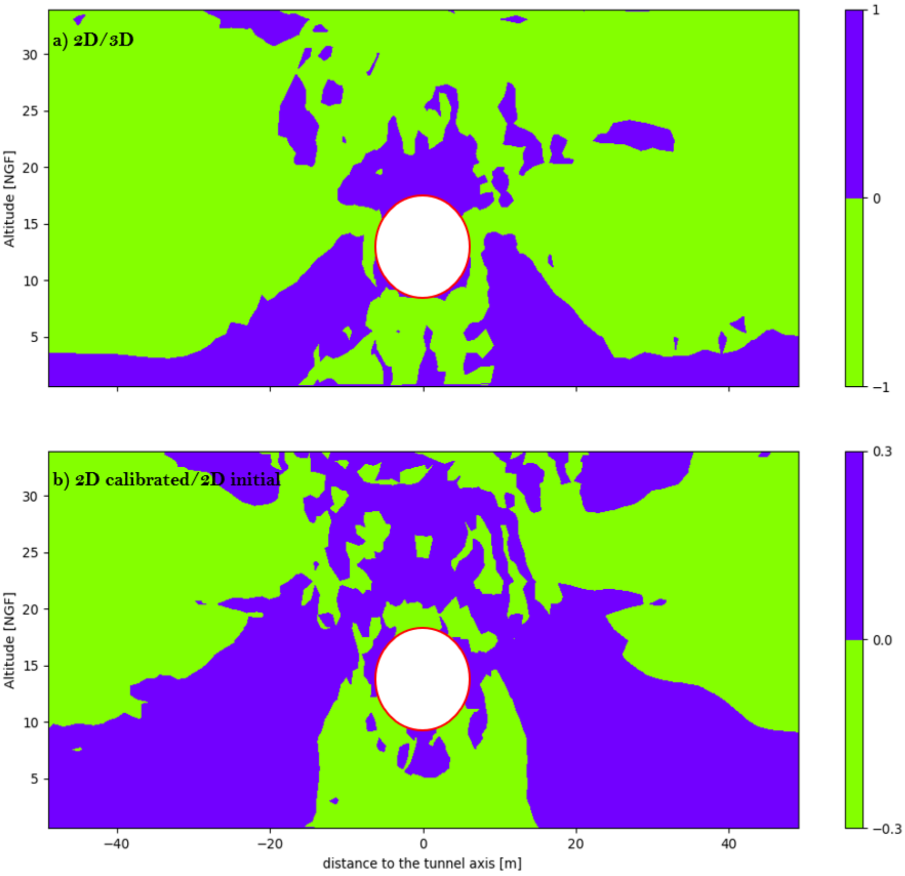

Figure 5.9: Deviatoric stresses comparison between; a) The 2D adjusted model and the 3D model ($\sqrt{j_2\_2D} - \sqrt{j_2\_3D}$) and b) the 2D adjusted model and the 2D initial model $\sqrt{j_2\_2Dadjusted} - \sqrt{j_2\_2Dinitial}$

approach. Over the tunnel crown, the 3D stresses are higher than the 2D stresses. The fictitious pressure is not the same in the initial 2D model and the calibrated 2D model. The fictitious pressure of the adjusted model is lower than the fictitious pressure of the initial model. Figure 5.9b compares the final steady-state stresses of the calibrated model and the initial model. It is not obvious to conclude on the stress variation because this latter is not uniform around the tunnel. However, we notice that, above the crown, the stress of the adjusted model is greater than that of the initial model.

In the first section of this chapter, the 3D simulation explained in the chapters 2 and 3 was used to study the effect of soil heterogeneity on the TBM-induced surface settlement. To solve the calculation problem of 3D simulations, 2D models (with the fictitious pressure calibrated in chapter 3) are conducted, and the results are compared with those of 3D simulations. The results revealed that the settlements obtained from 3D simulations are higher than those obtained with 2D simulations. To understand this difference, the initial 2D pressure (calibrated on a homogeneous stratified layer) was adjusted to fit the 3D results to study the evolution of stresses at the crown. The adjusted fictitious pressure appears to be lower than the initial fictitious pressure. According to the results of the stress analyses, the third-dimensional component that cannot be taken into account in 2D simulations is responsible for this difference.

Tunnel construction frequently occurs in urban areas where many buildings exist. As already mentioned, the tunneling process induces ground movements that come from the stress state modification. This ground displacement can damage the buildings and utilities near the tunnel. Tunneling-induced building damage can be affected by soil heterogeneity and the TBM pressures. In the next section, to study the effect of the soil heterogeneity and the TBM pressure on tunneling-induced building damage, 2D FE simulations are conducted even though this approach is not very reliable.

5.3 Soil heterogeneity and TBM pressure effect on the assessment of tunneling-induced building damage

In this section, soil heterogeneity is considered as spatial variability on the geotechnical parameter to assess the TBM-induced building damage. Two cases based on different TBM pressure configurations are conducted with the 2D FE approach. Although the 2D is not very reliable, this method is chosen in this section because it is quicker than the 3D FE simulation. To study these effects on building damages, the charts proposed by Burland (1995) and Son and Cording (2005) are used to evaluate and compare the damage levels.

5.3.1 TBM-induced building damage assessment

During a tunneling project, the excavation and the construction phases induce ground loss. According to Son and Cording (2005) it is possible to evaluate the building response in steps from the source of ground loss around the tunnel and understand their effect on the buildings. The pre-existing structures and the soil and structure stiffnesses can modify tunneling-induced free-field ground movements. As demonstrated by Burland (1995), estimating the building response that considers these soil-structure interactions may be significantly different from evaluating the building response that assumes to deform with a green field displacement. When subjected to self-weight, structures undergo vertical displacement predominantly, whereas structures subjected to tunneling are exposed to both settlement and horizontal displacement. Different authors developed interaction diagrams based on these deformations to assess building distortion and damage.

Son and Cording (2005) worked on the generalization of damage estimation criterion based on the state of strain at a point or an average strain across a building unit proposed by Boscardin and Cording (1989). Assuming that the structure is deformed by the angular distortion and the lateral strain, the proposed interaction diagram can be applied to any type of structure. The procedure to assess the angular and the lateral strain is described in figure 5.10.

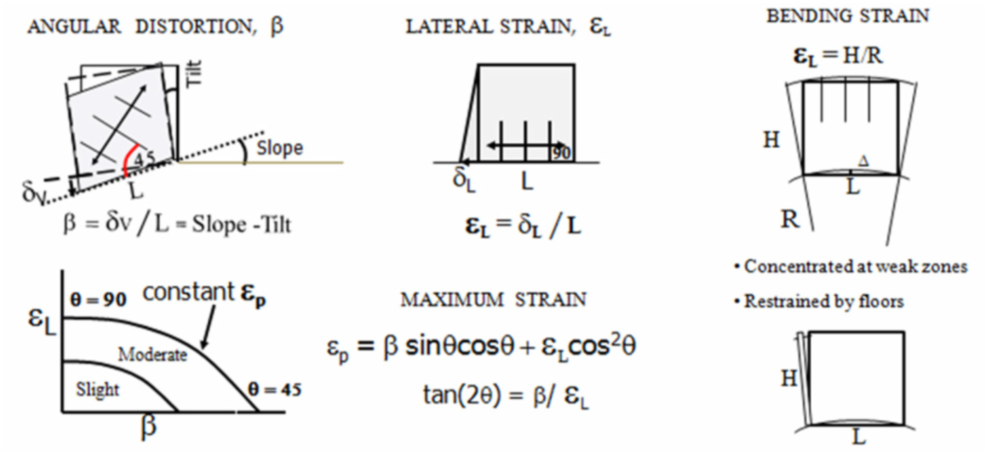

Figure 5.10: Angular distortion and lateral strain in a structural element due to ground movement (Son and Cording, 2005)

Burland (1995) neglected the characteristics of the structure and considered a deformation shape of the greenfield configuration to assess the building damage. According to his study, this approach is conservative as it assumes the building is infinitely flexible and follows the greenfield settlement trough. He proposed two criteria to assess the damage: the deflection ratio as presented in figure 5.11 and the lateral strain shown in figure 5.10. According to Burland et al. (1977) and Burland (1995), the damage category is based on the ease of repair of cracks. They summarized the categories of damages as follows:

- Category 0, very slight; the cracks are less than about 0.1 mm, they are classed as negligible and are visible on close inspection. They can easily be treated during normal decoration.

- Category 1, slight; the cracks width are between 1 and 5 mm. They are visible externally and some re-pointing may be required externally to ensure weathertightness. Doors and windows may stick slightly. The cracks can be easily filled and redecoration is probably required.

- Category 2, moderate; the width of the cracks is between 5 and 15 mm. They require some opening up and can be patched by a mason. Suitable linings can mask recurrent cracks. Repointing of external brickwork and possibly a small amount of brickwork to be replaced. Doors and windows stick, service pipes may fracture, and weather tightness is often impaired.

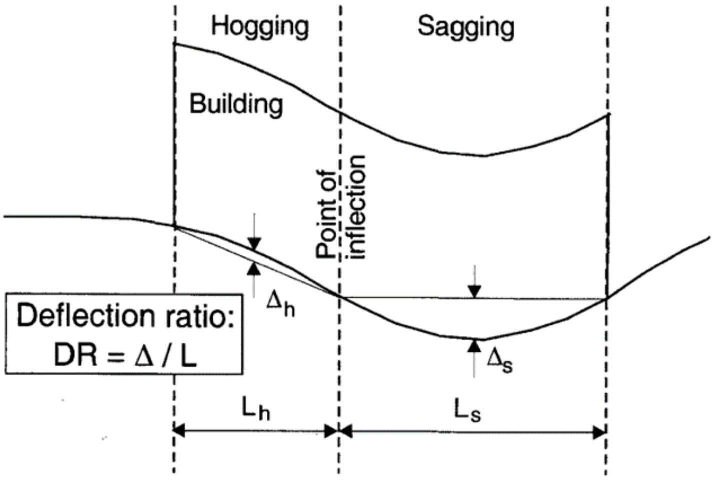

Figure 5.11: Building damage parameter: Definition of deflection ratio (Franzius et al., 2004)

- Category 3, severe; the width of the cracks is between 15 and 25 mm. Windows and door frames can be distorted. Floor sloping, walls leaning or bulging, some loose bearing in beams, and disrupted service pipes can appear. Extensive repair works in breaking outing out and replacing sections of walls, especially over doors and windows, are required.

- Category 4 and 5, very severe; the width of the cracks is usually larger than 25 mm. Beams lose their bearing capacity, walls lean badly and require shoring, windows are broken with distortion, and the danger of instability is visible. A significant repair job may require a partial or complete rebuilding of the structure.

Generally, this classification is simplified in aesthetic damage, for categories 0, 1, and 2 and severe damage, for categories 3, 4 and 5.

As it has been clearly explain in this section, the assessment of the building damages due to tunneling depends on the soil displacement. As demonstrated in chapter 3, soil displacement due to tunneling can be well estimated with FE simulations (Demagh et al., 2009; Do et al., 2014; Janin et al., 2017; Mollon et al., 2013). This chapter concluded that, if the 2D FE model is well calibrated, it is able to predict the TBM-induced soil displacement accordingly. However, despite the ease of application of the 2D FE model, it has also been demonstrated in section 5.2 of this chapter that the result of the 2D FE is not very reliable. In the next sections, the 2D simulations will be first conducted with the soil heterogeneity to assess the TBM-induced building damages. The multifidelity approach will be then adopted to enhance the building damage that comes from 2D FE simulation since these results are based on an approach that is not very reliable.

5.3.2 2D Finite Element simulation to assess soil displacement

The model used in this thesis is based on the approach proposed by Burland (1995) in which the building is considered as a weightless and flexible beam for conservative reasons. With these assumptions, the angular distortion developed by Son and Cording (2005) corresponds to the deflection ratio proposed by Burland (1995). The building considered in this analysis is inspired by the work of Son and Cording (2005) and is $B = 20$ m wide, and its axis is located at a distance x from the tunnel axis as presented in figure 5.12.

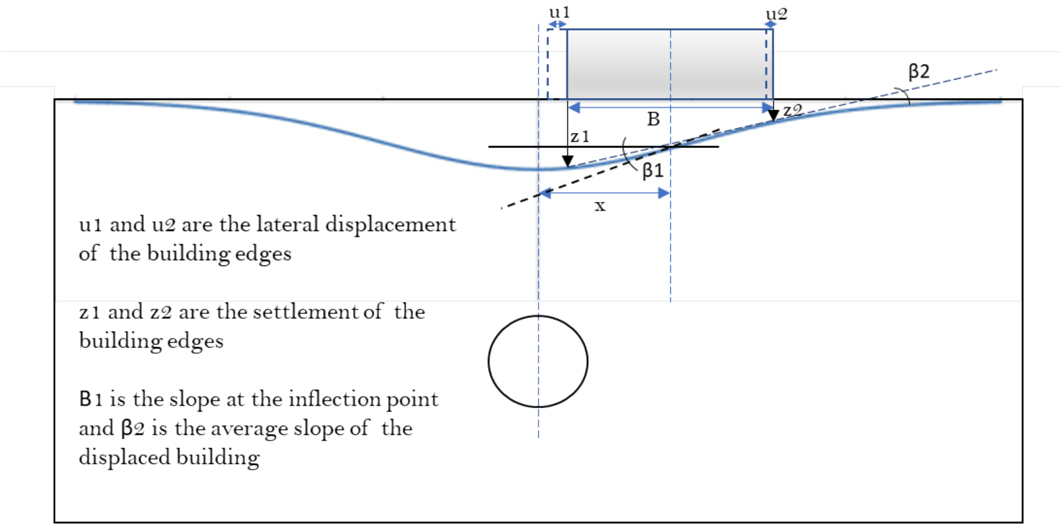

Figure 5.12: Geometry of the problem based on the work of Son and Cording (2005)

To study the effect of the TBM pressure and the spatial variability of the soils 300 models are developed with different heterogeneity soil configurations. Two fictitious pressure are considered in the analysis. For the first one, the simulations are conducted with a low 2D fictitious pressure (the pressure calibrated with heterogeneous soil profile in section 5.2) whereas a higher confinement pressure (the pressure calibrated in chapter 3 with the homogeneous soil profile) is considered for the second one. The settlement and horizontal displacement troughs are presented in figures 5.13 and 5.14 respectively. According to these figures, the settlement and the horizontal displacement obtained with higher pressure (case 2) is lower than the one obtained with lower pressure.

5.3.3 Finite Element simulation to assess building damage

Burland (1995) proposed to consider the deflection ratio of building as the average slope affecting the building stability after the tunnel construction. However, according to figure 5.12, the average building slope can sometimes be lower than the slope at a certain point of the settlement trough. For this reason, we propose in this thesis to assess the building deflection ratio or the angular

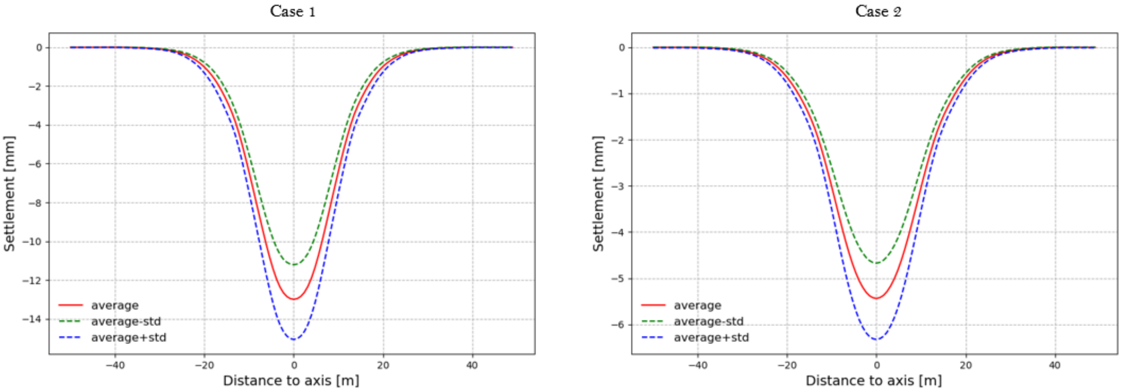

Figure 5.13: Statistical result of the settlement trough; Case 1: spatial variable models calculated with a lower confinement pressure, and case 2: spatial variable models calculated with a higher confinement pressure

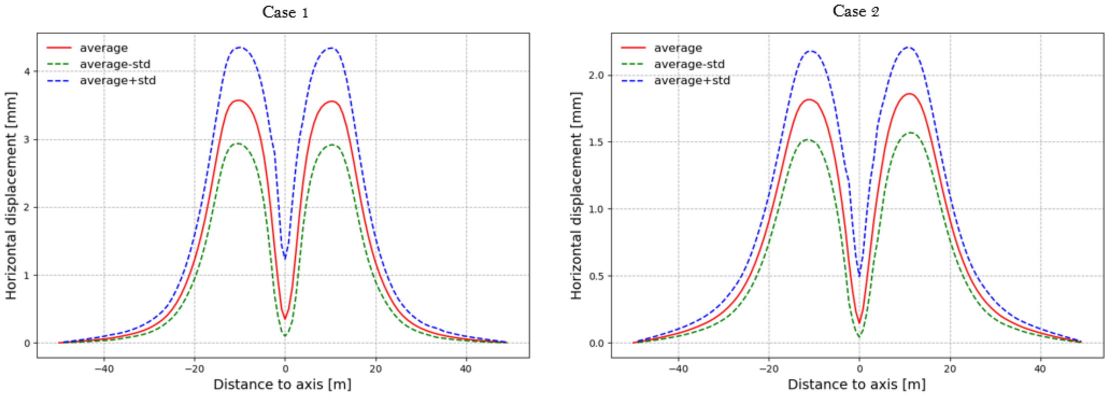

Figure 5.14: Statistical result of the lateral displacement trough; Case 1: spatial variable models calculated with a lower confinement pressure, and case 2: spatial variable models calculated with a higher confinement pressure

distortion as the maximum of the slopes at every point of the building. In order to determine this slope, the derivative $\frac{\delta s(x)}{\delta x}$ of the settlement curve with respect to x is computed, with $s(x)$ being the settlement trough and x the distance to the tunnel axis. Similarly, the lateral deflection of the building is considered to be the maximum value of the elongations at every point of the building. The elongation of the building is considered to be the derivative of the lateral displacement curve $\frac{\delta l(x)}{\delta x}$ with $l(x)$ the lateral displacement trough and x the distance to the tunnel axis.

In order to study the influence of the building position on damage assessment, the building is located at a distance x to the tunnel axis. Due to the asymmetry of the settlement trough with heterogeneous soil profiles, the two sides of the tunnel are considered in the analyses to compute the deflection ratio and the angular distorsion that affects the building. The distance x is taken in the set {0D,1D,2D,3D,4D} with D the diameter of the tunnel. The charts proposed by Burland (1995) and Son and Cording (2005) are used to assess the damage category of each of the building configuration. Figure 5.15 and figure 5.16 present the damage categories of the two cases using the Burland (1995) chart and the Son and Cording (2005) chart respectively.

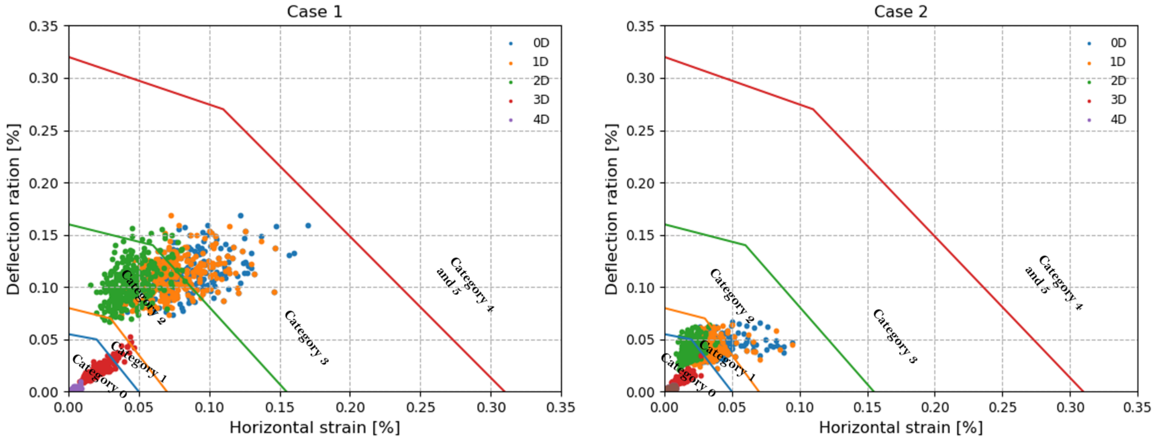

Figure 5.15: Damage categories assessed using the chart of Burland (1995) : Case 1; spatial variable models calculated with a lower confinement pressure, and case 2; spatial variable models calculated with a higher confinement pressure

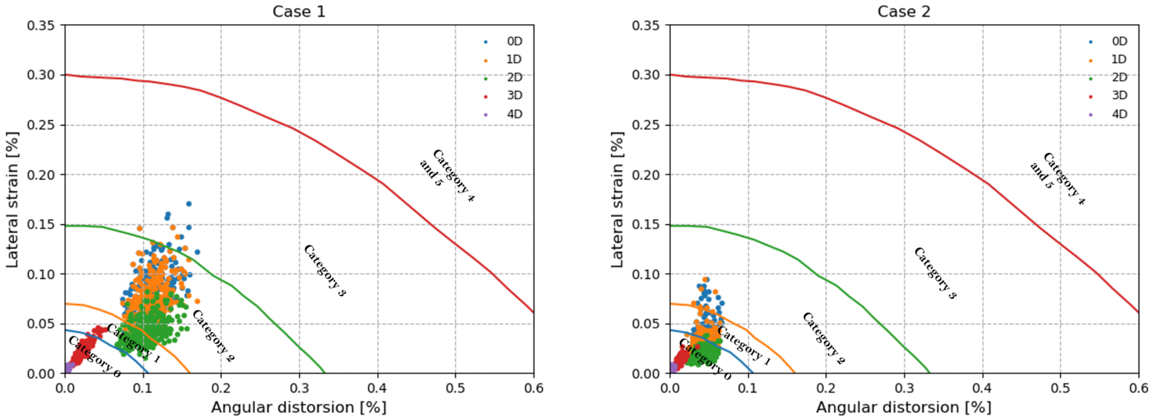

Figure 5.16: Damage categories assessed using the chart of Son and Cording (2005) : Case 1; spatial variable models calculated with a lower confinement pressure, and case 2; spatial variable models calculated with a higher confinement pressure

According to figure 5.15 and figure 5.16 the location of the building to the tunnel has a significant effect on the damage categories. The damage level decreases with the increase of the distance between the building and the tunnel. The confinement pressure also has a significant influence on the building damage. Using higher pressure tends to reduce the building damages. The results also highlight that with the chart of Burland (1995) the building is more conservative than the chart of Son and Cording (2005). When the building is located at 0, 1 or 2 times the tunnel diameter from the tunnel axis, several models provide severe damage.

As the damage level is the combination of the angular distortion or the deflection ratio and the lateral strain, we also study in this thesis the probability of exceedance of various levels of the angular distortion and the lateral strain for the two studied cases in figure 5.17 and figure 5.18 respectively. According to figure 5.17, the probability of exceedance when the building is located at 0, 1, and 2 times the diameter from the tunnel axis are almost the same. This can be explained by the fact that for the three configurations, the inflection point is located close to the building. Concerning the lateral strain, the probability curves can be well distinguished in the two cases. In summary, the probability of exceedance at a certain level decreases with the increase in distance between the building and the tunnel.

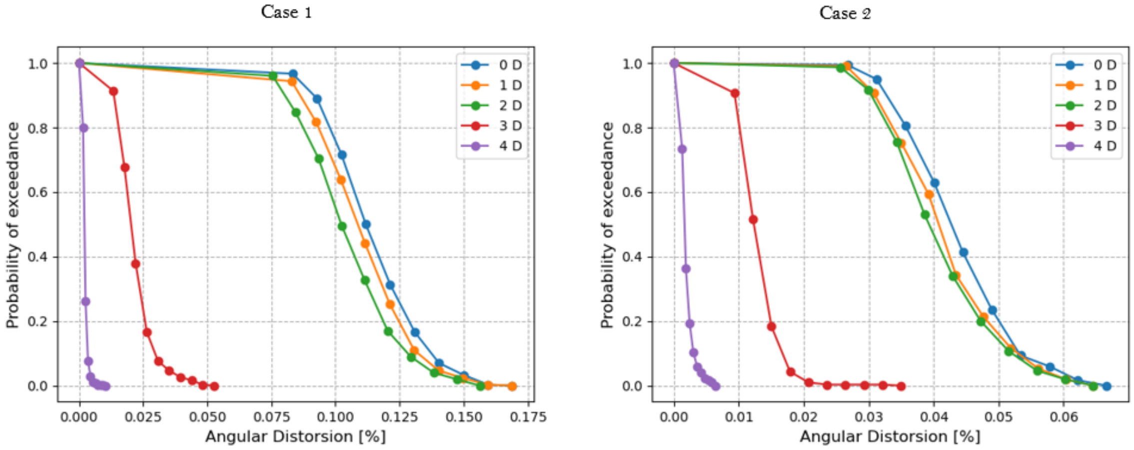

Figure 5.17: Probability of exceedance at various levels of the angular distortion; Case 1: spatial variable models calculated with a lower confinement pressure, and case 2: spatial variable models calculated with a higher confinement pressure

As it has already been explained, although it is possible to save some calculation time using the 2D simulation in analysis, this approach remains time-consuming when many simulations are required. For this reason, in chapter 4 the procedure to construct a meta-model based on 2D FE simulation data was explained to substitute the FE simulations. In section 5.2 of this chapter, it has been demonstrated that the approaches based on the 2D FE simulations are unreliable since they provide Low Fidelity (LF) data. However, it is very time-consuming to conduct a lot of 3D simulations to obtain High Fidelity (HF) data and determine the real effect of the TBM-induced building damages. Thanks to the Multi-fidelity approach (Li and Jia, 2020; Zhang et al., 2021b; Chen and Feng, 2022), the meta-model constructed with the LF data can be enhanced with some

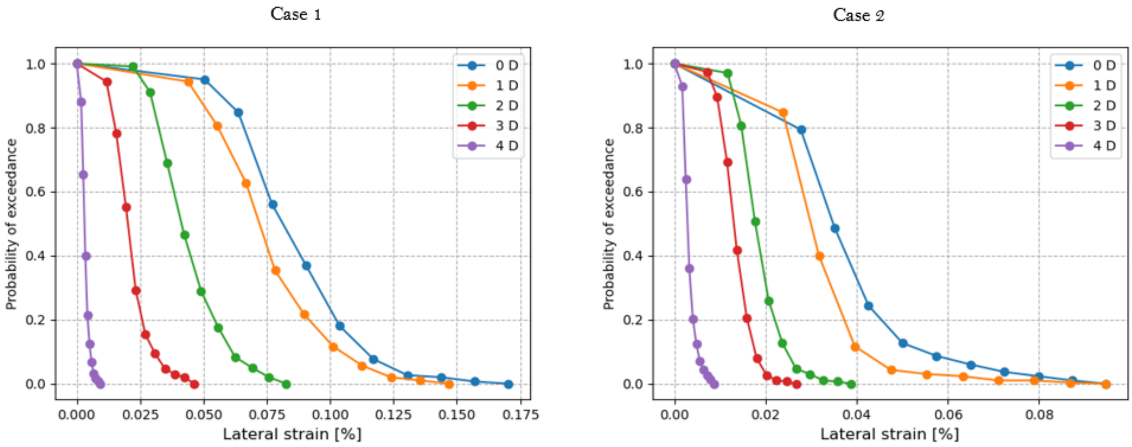

Figure 5.18: Probability of exceedance at various levels of the lateral strain; Case 1: spatial variable models calculated with a lower confinement pressure, and case 2: spatial variable models calculated with a higher confinement pressure

HF data points to better predict the TBM-induced building damage.

5.4 Multifidelity approach to enhance predictions

5.4.1 Multifidelity approach methodology

The multifidelity approach proposed in this thesis is illustrated on data with two distinct levels of fidelity; The LF 2D data denoted by (x_L, y_L), and the HF 3D data denoted by (x_H, y_H). The procedure used in this thesis was proposed by Chen and Feng (2022) and is explained in the following steps:

- *Step* 1; Establishing low-fidelity prediction model M_{LL} to fit x_L, y_L
- *Step* 2; Obtaining low-fidelity predicting result at high-fidelity points, $y_{HL} = M_{LL}(x_H)$
- *Step* 3; Forming expended input vector $x_H^e = [x_H, y_{HL}]$
- *Step* 4; Establishing correlation model $M_{LH}(x^e)$ to fit x_H^e to y_H
- *Step* 5; Obtaining enhanced prediction result at low-fidelity points $y_{LH} = M_{LH}(x_L^e)$
- *Step* 6; Enhanced multifidelity data $x_M = [x_L; x_H]$, $y_M = [y_{LH}; y_H]$
- *Step* 7; Establishing multifidelity prediction model $M_M F$ to fit x_M to y_M

After predicting data with the multi-fidelity approach, a validation analysis is necessary to determine the accuracy of the model. During this analysis, the prediction result is compared to 3D high-fidelity data through a confusion matrix that measures the performance of the model.

Generally, the confusion matrix reports how the model classifies and compares the different fault categories with respect to their actual classifications (Khalil, 2021). The matrix row represents the actual (or observed) class under test and the classification (or prediction) of that particular class is represented under the matrix column. M[i][j] gives the number of times that observation of class i was assigned to the prediction j. The diagonal represents the correct classifications. Three metrics are usually used to evaluate or compare predictions from a confusion matrix: Accuracy, Precision and Recall. Figure 5.19 presents the confusion matrix of a 2-class classification problem.

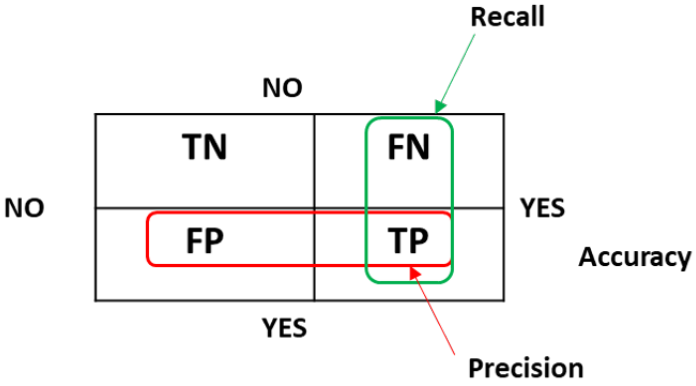

Figure 5.19: Summary of the confusion matrix and its classification

Depending on each study for the meaning of the terms “positive” and “negative”, in the following study, the term “positive” means that a data is under a certain threshold (i.e. a damage level), whereas “negative” designates the opposite. Hence, four pieces of data can be presented:

- True Negative (TN): A sample is negative and was predicted as negative.
- False Negative (FN): A sample is positive but was predicted as negative. FN is sometimes known as Type I Error.
- False Positive (FP): A sample is actually negative but was predicted as positive. FP is also known as Type II Error.
- True Positive (TP): A sample is actually positive and was predicted as positive.

The first metric obtained from the above pieces of data is the *Accuracy*. It indicates how close to reality the prediction is. It is calculated as:

$$Accuracy = \frac{TN + TP}{TN + TP + FN + FP} \tag{5.4.1}$$

The *Recall* focuses on the data that were correctly identified (i.e. how many predictions are correct). It should be close to 1 (or 100%) in the ideal case.

$$Recall = \frac{TP}{TP + FN} \tag{5.4.2}$$

The *Precision* focuses on the data that are positives. It indicates from all the positive classes, how many are actually positive.

$$Precision = \frac{TP}{TP + FP} \tag{5.4.3}$$

Therefore, a successful prediction means high Accuracy and Recall, whereas a high Precision is not always critical.

5.4.2 Application of a multi-fidelity approach for the TBM-induced building damage

Reliable meta-models are built with HF data such as field-collected data and advanced 3D numerical models. However, the high-fidelity data are sometimes hard to obtain and only available in a limited quantity. Meanwhile, the low-fidelity data like 2D FE results are in large amounts, but their accuracy is relatively poor and is not suitable for establishing models. According to Chen and Feng (2022), Aydin et al. (2019), and Guo et al. (2022), it is possible to enhance the reliability of meta-models constructed with LF data with the multi-fidelity approach (the bi-fidelity since only two degrees of fidelity are involved in this study) to better predict real phenomena. This approach is proposed for the TBM-induced building damage assessment in this section.

5.4.2.1 Data used in the multi-fidelity approach

As already mentioned, in civil engineering in general and tunneling in particular, the HF data usually possess high accuracy, but their total available number is usually small, which is not enough for fitting a reasonable model. In contrast, the low-fidelity data are in large amounts and have low accuracy. To apply this procedure to TBM-induced building damage, the HF data (x_H, y_H) and the LF data (x_L, y_L) are derived from the 3D spatial variability models and the 2D spatial variability models respectively. For the HF data, a series of twenty 3D simulations are conducted to construct the database, while 300 2D simulations are carried out for the LF data.

The building used in this analysis is 20 m wide and located above the tunnel. This building is simplified into a beam without stiffness. The damage level is determined from both the charts of Burland (1995) and Son and Cording (2005). The horizontal strain and the deflection ratio come from the derivative of the lateral displacement curve and the settlement curve, respectively and constitute the outputs of the models. Concerning the input data of the model, they correspond to the stiffness of the soil at the position presented in chapter 4 (a total of 18 input parameters). The coupling between ANN and the k-means is used to construct the 2 LF prediction models to predict the two outputs (horizontal strain and deflection ratio).

5.4.2.2 Result, interpretation, and discussion

Step 1: The low fidelity (LF) prediction result.

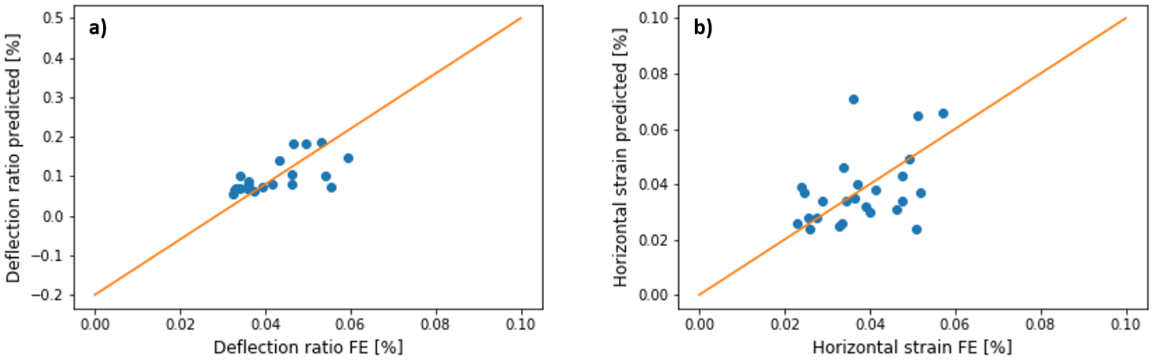

Figure 5.20: Comparison between 2D FE and LF prediction result: a) Deflection ratio and b) Horizontal strain

The coupling between the ANN and the k-means is adopted to construct the prediction model (M_{LL}) of the LF data to fit (x_L, y_L) with x_L the LF input data and y_L the LF output data. The data are grouped into 25 clusters, and 3 data are taken in each cluster to train the model. For the model validation, 1 data is selected and tested in each cluster. Figure 5.20a and Figure 5.20b present the comparison between the 2D FE results and the prediction results with the LF model of the deflection ratio and the horizontal strain, respectively. According to this figure, the prediction of the deflection ratio is overestimated, while the predicted values of the horizontal strain are in agreement with the FE result.

Step 2 *and* 3: Predicting HF data with LF model.

The LF models are used to predict the HF data ($y_{HL} = M_{LL}(x_H)$) with (x_H) the inputs of the HF data and y_{HL} the predicted value (deflection ratio and horizontal strain). The results of this prediction are used to enhance the original 2D FE data base to form an expended data set

($x^e_H = [x_H, y_{HL}]$).

Steps 4: Correlation between the LF prediction and the HF data.

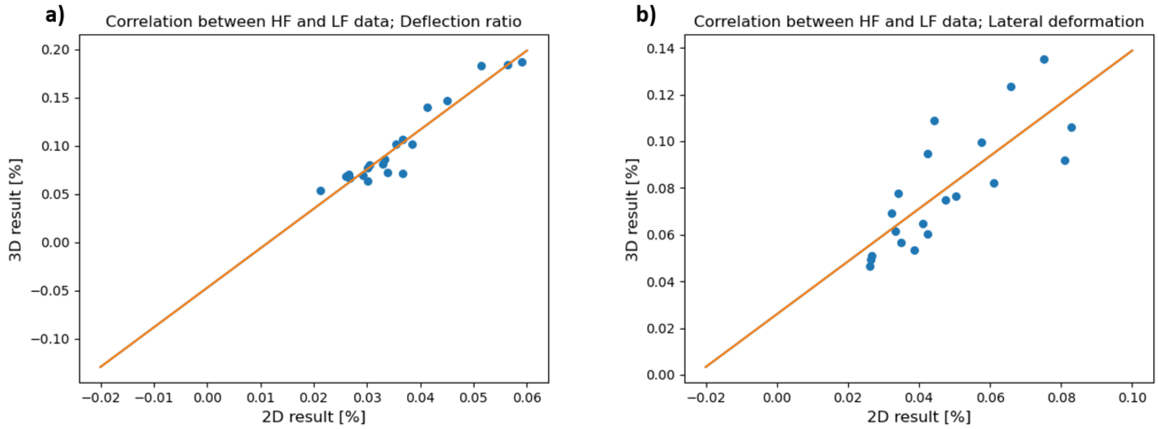

Figure 5.21: Hypothesis on the correlation between the LF prediction and the HF data : a) Deflection ratio and b) Horizontal strain

To obtain the correlation (M_{LH}) between the LF data and the HF data, the HF input data are used to conduct 2D FE simulations. The simulation results in deflection ratio and the horizontal strain are plotted in figure 5.21a and figure 5.21b, respectively. According to these figures, a linear correlation can be assumed among the data for a simplification reason.

steps 5, 6, *and* 7: The correlation model is used to enhance the expended data (y_{LH} =

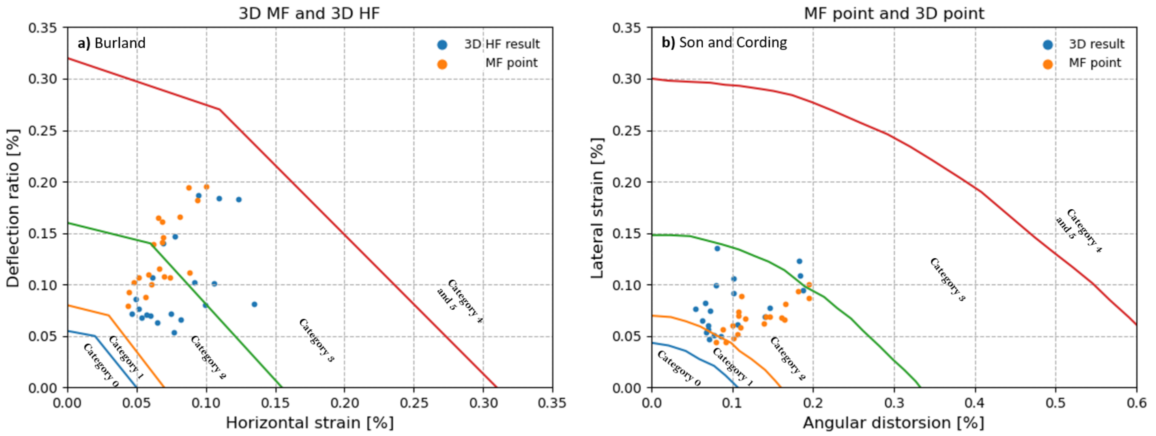

Figure 5.22: MF prediction of the TBM-induced building damage using : a) From Burland (1995) chart and b)From Son and Cording (2005) chart

$M_{LH}(x_L^e)$). From the result of this prediction, a combined database is formed ($x_M = [x_L; x_H]$ and $y_M = [y_{LH}; y_H]$) and a multi-fidelity prediction model (M_{MF}) is established to fit x_M to y_M. The charts proposed by Burland (1995) and Son and Cording (2005) are used to plot and compare the damage level of the 3D high fidelity (HF) points and the multi-fidelity (MF) points. The result is presented in Figure 5.22. According to this result, the MF points are in agreement with the 3D points. The chart proposed by Burland (1995) gives more critical damage levels. Supposing that the limit between category two and category 3 is the threshold, using the chart proposed by Burland (1995), the MF model gives more critical points than the 3D simulation (10 points against 8). Concerning the chart proposed by Son and Cording (2005), the 3D simulation gives more critical points compared to the MF point (2 against 1).

To compare the prediction of the damage level with the two different charts, the accuracy, the recall, and the precision of the correlation matrix are analyzed. Figure 5.23 presents the confusion matrices from the Burland chart and the Cording chart. The correlation matrices metrics are presented in table 5.1. In addition to the recall, the precision and the accuracy, the F-score ($\frac{2*Recall*Precision}{Recall+Precisison}$) is computed to compare the results of the two charts. According to this results, the multi-fidelity approach predicting the TBM-induced building damage is better when the chart of Son and Cording (2005) is adopted (92% against 90%).

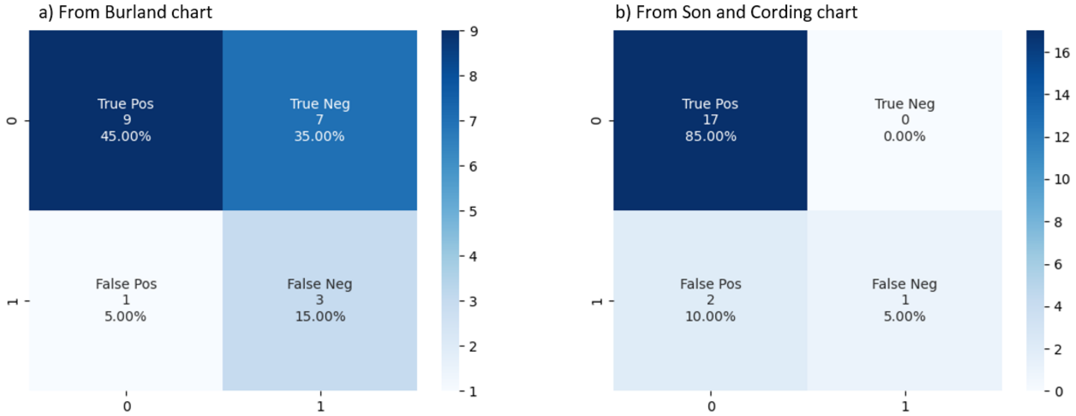

Figure 5.23: Confusion matrices results : a) From Burland (1995) chart and b)From Son and Cording (2005) chart

5.5 Conclusion

In this chapter, the effect of the heterogeneity of soil, the TBM pressure and the location of the building effect on the TBM-induced building damages are firstly studied with the 2D FE simulations. The soil heterogeneity is accounted for by the spatial variability of the soil parameters.

Table 5.1: Correlation matrices parameters

Chart	Recall [%]	Precision [%]	Accuracy [%]	F-Score [%]
Burland (1995)	75	90	80	82
Son and Cording (2005)	94	90	85	92

Several simulations were conducted to study the influence of heterogeneity on soil displacements. From this latter, the damage level of the building was assessed by considering different cases: to study the effect of the TBM pressure, a lower 2D fictitious pressure and higher 2D fictitious pressure were applied to the numerical simulation. Concerning the effect of the building position, different building locations were considered in the analyses. As a result of this study, the TBM pressure and the building location play a significant role in the TBM-induced building damage as the damage level decreases with the increase of the TBM pressure and/or the distance to the tunnel axis.

As already demonstrated in this thesis, the 2D FE simulation may provide unreliable results due to the simplified approaches concerning the TBM pressure and the model dimension. On the contrary, with the 3D FE simulations, it is possible to obtain more reliable results but with a significant amount of calculation time. Then, to compare the 3D FE result to the 2D FE result by considering the heterogeneity of soils, some 3D simulations and 2D simulations have been conducted to analyze the settlement field and stress evolution. The two results appeared different due to the third dimension and the arch effect that are not considered in the 2D simulation.

The TBM-induced soil displacement has been demonstrated to be the main cause of the building damage. For this reason, it is possible to determine the damage level from both the settlement and the horizontal displacement. 2D FE is used in this thesis to assess the TBM-induced building damage, although this approach does not provide reliable results. In order to enhance this result, and by taking advantage of meta-models constructed from machine learning approaches as explained in chapter 4, this thesis finally presented the multi-fidelity approach based on the 2D and the 3D FE data. The developed models are used to predict the TBM-induced building damage with two different charts. At the end, reliable predictions are produced since the correlation matrix indices provided good results.

General conclusion and perspectives

The construction of tunnels in urban areas causes some ground movements that may have detrimental effects on the surrounding structures and infrastructures. Despite the recent advances in the use of mechanized excavation techniques, the ground deformations and movements induced by this process are still required to be more understood. It is why TRACTEBEL and Centrale-Supelec, with the agreement of the National Association for Research and Technology (ANRT in french), have set up this thesis.

One of the main objectives of this thesis, entitled ”pressurized tunnels behavior in urban areas”, was to propose a numerical simulation methodology (3D and 2D approaches) using finite elements method for predicting the TBM-induced surface settlement trough. This thesis also aimed to improve the practice and methods in the design phases to better consider the heterogeneous character of the soils and to study its influence on the TBM-induced soil displacement and building damage assessment.

In order to achieve these objectives, this thesis dealt with the following points:

- Adopting a constitutive model that better represents the soil behavior in order to improve the settlement amplitude and width obtained by the FE results.
- Determining a formulation to obtain the 3D pressures from the fictitious pressure for a TBM tunnel construction.
- Developing a meta-model for the determination of the surface settlement trough induced by TBM tunneling.
- Studying the influence of the spatial variability of soils on the TBM-induced soil displacement and building damage.

To fulfill all these objectives, this thesis was divided into 5 chapters:

Chapter 1 presented the state of art done on TBM tunneling. In particular, this chapter discussed:

- The criteria for choosing the type of TBM.

- The stress state and the strain state evolution of the soil during a TBM-excavation.
- Existing methods for predicting the soil movements in general and settlement in particular due to tunneling.
- Studies on the consideration of soil heterogeneity and uncertainties on its parameters.
- The use of meta models in tunneling.

The objective of chapter 2 was to find a formulation for the determination of the 2D fictitious pressure in order to simplify the 3D modeling by a 2D modeling with the explicit approach of the convergence confinement method. To achieve this objective, the following aspects were studied:

- The method of construction by pressurized TBM was carefully studied in order to be able to simulate better the physical phenomenon. The application was conducted on the construction of the Paris Metro Line 16 in France.
- Subsequently, a methodology for 3D modeling of tunneling with a TBM was presented. This modeling was revealed to be the most adapted thanks to the possibility of considering a set of complex phenomena that occurred during the excavation. However, it has a drawback time consuming (for example it required 3 days to complete a calculation).
- In order to govern the time consuming, a 2D modeling methodology based on the convergence confinement method with the explicit approach was proposed. This approach required the use of a confinement loss of 0.9 to represent the stress release due to the excavation and a 2D fictitious pressure to represent all the pressures applied in the 3D model. 3D and 2D simulations were conducted in order to propose a formulation to determine the fictitious pressure. It was shown that the fictitious pressure is influenced by the pressure around the shield and the injection pressure (P_{inj}) but much less by the pressure of the excavation chamber. In summary, assuming a self-stabilizing front in which the minimum stability pressure (P_{min}) i.e the hydrostatic pressure is applied, the fictitious pressure can be obtained from this equation : P_{fict}=$0.82P_{min}$+$0.07P_{inj}$.
- The Hardening Soil with Small Strain Model (HSSM) was used to simulate the soil behavior. This constitutive model has the particularity that the stiffness evolves with the strain even for very small values of strain. The HSSM requires 4 different stiffnesses (the unload-reload elastic stiffness E_{ur}, the secant stiffness in standard drained triaxial test E_{50}, the tangent stiffness for primary odometer loading E_{oed}, and the stiffness for very small strain E_0) and the deviatoric strain at 70% of the initial shear modulus (a value of 10^{-4} was assumed). In this thesis, the correlations ($E_{ur} = 2E_{50}$, $E_0 = 8E_{50}$, $E_{oed} = E_{50}$) allowed to obtain the FE settlement amplitude and width very close to the measurements. These correlations are in agreement with the requirements proposed by Obrzud and Truty (2010).

Due to the natural formation process of soils, they are heterogeneous media. In current practice, soils are modeled as homogeneous layers with sometimes uncertainties on the parameters to consider the heterogeneity. These aspects are studied in chapter 3.

- Firstly, a homogeneous stratified layer approach is explained in a paper submitted to the journal Tunneling and Underground Space Technology. In this paper, an optimized back analysis procedure has been proposed to determine the adequate set of parameters to obtain the FE settlement trough that well-fitted the measurements. Subsequently, a global sensitivity analysis procedure was also proposed to quantify the influence of the parameters on the maximum settlement and the inflection point. Two main objectives are followed in this paper: Firstly, when applying at the beginning of tunnel excavation, the back analysis procedure allows to determine the optimal value of the parameters for further FE calculations. Secondly, with the global sensitivity analysis, it is possible to determine the most influential parameters of the settlement induced by tunnel excavation. This analysis could able the engineers to identify the geological risky layer for which the investigation is required.

- Secondly, with the 3D modeling of the stratified layer profile, the effect of the TBM advancement on the settlement trough and the simulation of this effect are compared to the 2D result. This study allowed us to highlight the effect of the third dimension which cannot be represented in a 2D modeling. In summary, it is possible to represent with a 2D modeling the initial and final state of the excavation process, but not the intermediate steps.

- Finally, 2D spatially variable models were conducted using the random field theory to assess the TBM-induced surface settlement trough. The first observation was that the settlement trough is not always symmetrical to the tunnel axis. Statistical analysis allows us to conclude that the spatial variability influences the maximum settlement (the coefficient of variation of 15%) more than the inflection point (the coefficient of variation of 3%).

Quantifying uncertainties using numerical methods requires a large number of simulations, which makes the process time-consuming. Chapter 4 proposed the use of a meta-model developed thanks to artificial intelligence techniques to save calculation time. The developed meta model was based on the coupling between k-means algorithm and artificial neural networks. The method was applied to the Paris Metro Line 12 extension.

- The proposed method was firstly applied with FE element simulation of the heterogeneity of soil to predict the surface settlement trough. Two meta-models were developed to determine TBM-induced surface settlement trough (the maximum settlement and the inflection point). The determination coefficient of 75% for the maximum settlement and 70% for the inflection point was obtained.

- Using a database constructed with FE simulations of stratified layer, this chapter also developed meta models to predict the TBM-induced surface settlement. A value of 97% for the maximum settlement and 95% for the inflection point was obtained.

- For the homogeneous stratified approach, the initial database was reduced by determining the influence of the input parameters (the stiffnesses of the soil layers) on the output parameters (maximum settlement and inflection point) using the correlation coefficients. The reduced basis was used to determine the new meta models. A coefficient of determination of 90% was obtained for the settlement and 94% for the inflection point.

In the last chapter of this thesis, the effect of TBM pressures and building location on TBM-induced building damages is studied.

- 2D simulations were conducted to assess the influence of the pressure, the soil heterogeneity, and the building location on the TBM-induced building damage. Two different charts proposed by Burland (1995) and Son and Cording (2005) were used to assess the building vulnerability. According to the results, the safety of a building for a TBM-construction depends on its distance to the tunnel and to the TBM pressures.

- 3D spatially variable models were also conducted with the consideration of the spatial variability in a plane. By comparing the 2D results to the 3D results, there was a necessity to adjust the fictitious pressure in order to obtain the same settlement. This result highlighted the influence on the 3rd dimension that can not be taken into account in the 2D model.

- Considering the 3D results and the 2D results, the multi-fidelity approach was applied in addition to meta-models constructed with the proposed method of chapter 4 to better predict the building damage level using the charts of Burland (1995) and Son and Cording (2005).

The work presented in this thesis has some limitations that would be interesting to study in future theses.

- The proposed formulation for the determination of the fictitious pressure is based on certain assumptions; the tunnel is located below the water table and the excavation chamber pressure is equal to the hydrostatic pressure. It would be important to study the influence of these assumptions in order to generalize the formulation relating the 2D fictitious pressure to the TBM pressures.

- The 3D approach adopted in this thesis is based on the projection of a 2D cross-section in the longitudinal direction of the tunnel. However, in the real situation, the soil layers are not always parallel and the tunnel has a sloping profile along the longitudinal axis. Another perspective of this work is to integrate these different aspects in 3D modeling in order to predict a settlement trough for a wide range of applications.

- The 3D approach for spatial variability proposed in this thesis is based only on the assumption of the plane variability. In the following work, it will be important to consider the variability along the longitudinal direction of the tunnel.

- One of the objectives of this thesis was to develop meta-models capable of predicting the TBM-induced surface settlement trough. Two types of meta-models were developed; a meta-model which takes into account uncertainties in soil parameters and a meta-model which takes into account the spatial variability of the models. The latter presents a small but acceptable coefficient of determination. However, this approach needs to be improved in order to better predict TBM-induced settlement by considering the heterogeneity of soils.

Synthèse en français

La construction de tunnels dans les zones urbaines provoque des mouvements de terrain qui peuvent avoir des effets graves sur les structures et les infrastructures environnantes. Malgré les récents progrès dans l'utilisation des techniques d'excavation mécanisées, les déformations et mouvements du sol induits par ce mécanisme doivent être mieux étudiées. C'est dans cette optique que TRACTEBEL et CentraleSupelec, avec l'accord de l'Association Nationale de la Recherche et de la Technologie (ANRT), ont mis en pied ce projet de thèse.

L'un des objectifs principaux de cette thèse, intitulée "comportement des tunnels pressurisés en milieu urbain", était de proposer une méthodologie de simulation numérique (approches 3D et 2D) utilisant la méthode des éléments finis pour prédire la cuvette de tassement en surface induit par le creusment au tunnelier. Cette thèse avait également pour but d'améliorer les pratiques et les méthodes dans les phases de conception afin de mieux prendre en compte le caractère hétérogène des sols et d'étudier son influence sur le déplacement des sols induit par le creusement de tunnel au tunnelier et l'évaluation des dommages aux bâtiments.

Afin d'atteindre ces objectifs, cette thèse a traité les points suivants :

- Adopter la loi la plus appropriée pour représenter au mieux le comportement du sol afin d'améliorer l'amplitude et la largeur de la cuvette de tassement obtenues par les résultats FE.

- Détermination d'une formulation permettant d'obtenir les pressions 3D à partir de la pression fictive pour la construction d'un tunnel au tunnelier.

- Développer un méta-modèle pour la prédiction de la cuvette de tassement en surface induit par la construction d'un tunnel.

- Étude de l'influence de la variabilité spatiale des sols sur le déplacement du terrain et les dommages aux bâtiments induits par le creusement d'un tunnel.

Pour remplir tous ces objectifs, cette thèse a été divisée en 5 chapitres :

Le chapitre 1 a présenté l'état de l'art réalisé sur le creusement de tunnels au tunnelier. En particulier, ce chapitre a abordé :

- Les critères de choix du type de tunnelier.
- L'état de contrainte et l'évolution des déformations du sol pendant une excavation au tunnelier.
- Méthodes existantes pour prédire les mouvements du sol en général et les tassements en particulier dus au creusement d'un tunnel.
- Études sur la prise en compte de l'hétérogénéité du sol et des incertitudes sur ses paramètres.
- L'utilisation de méta-modèles dans la construction de tunnels.

L'objectif du chapitre 2 était de déterminer une formulation pour la détermination de la pression fictive 2D afin de simplifier la modélisation 3D par une modélisation 2D avec l'approche explicite de la méthode confinement-convergence. Pour atteindre cet objectif, les aspects suivants ont été étudiés :

- La méthode de construction par l'utilisation d'un tunnelierà front pressurisé a été soigneusement étudiée afin de pouvoir mieux simuler le phénomène physique. L'application a été menée sur la construction de la ligne 16 du métro Parisien en France.
- Par la suite, une méthodologie de modélisation 3D du creusement de tunnels avec un tunnelier a été présentée. Cette modélisation s'est révélée être la plus adaptée grâce à la possibilité de considérer un ensemble de phénomènes complexes qui se produit lors de l'excavation. Cependant, elle présente l'inconvénient d'être coûteuse en temps de calcul (par exemple, besoin de 3 jours pour réaliser un calcul).
- Afin de remédier à ce problème de temps de calcul important, une méthodologie de modélisation 2D basée sur l'approche explicite de la méthode de confinement-convergence a été proposée. Cette approche a nécessité l'utilisation d'un déconfinement de 0,9 pour représenter le relachement des contraintes due à l'excavation et une pression fictive 2D pour représenter toutes les pressions appliquées dans le modèle 3D. Des simulations 3D et 2D ont été réalisées afin de proposer une formulation pour déterminer la pression fictive. Il a été montré que la pression fictive est influencée par la pression autour du bouclier et la pression d'injection (P_{inj}) mais beaucoup moins par la pression de la chambre d'excavation. En résumé, en supposant un front auto-stabilisant où la pression minimale de stabilité (P_{min}) c'est-à-dire la pression hydrostatique est appliquée, la pression fictive peut être obtenue à partir de cette équation : P_{fict}=$0.82P_{min}$+$0.07P_{inj}$.
- La loi élastoplastique avec écrouissage et prise en compte des petites déformations (HSSM) a été utilisé pour simuler le comportement du sol. Ce modèle constitutif a la particularité

que le module évolue avec la déformation même pour de très petites valeurs de déformation. La loi HSSM requiert 4 modules différentes (la module élastique E_{ur}, le module sécant dans l'essai triaxial drainé standard E_{50}, le module tangent pour la charge odométrique primaire E_{oed}, et le module pour une très petite déformation E_0) et la déformation déviatorique à 70% du module de cisaillement initial (une valeur de 10^{-4} a été supposée). Dans cette thèse, les corrélations ($E_{ur} = 2E_{50}$, $E_0 = 8E_{50}$, $E_{oed} = E_{50}$) ont permis d'obtenir l'amplitude et la largeur de la cuvette de tassement aux EF très proches des mesures. Ces corrélations sont en accord avec les exigences proposées par Obrzud and Truty (2010).

En raison du processus naturel de formation des sols, ces derniers sont de nature hétérogènes. Dans la pratique, les sols sont modélisés comme des couches homogènes avec parfois des incertitudes sur les paramètres de sol permettant de prendre en compte ce charactère hétérogène. Ces aspects sont étudiés dans le chapitre 3.

- Tout d'abord, une approche par couches stratifiées homogènes est expliquée dans un article qui a été soumis à la revue Tunneling and Underground Space Technology. Dans cet article, une procédure de rétroanalyse optimisée a été proposée pour déterminer l'ensemble des paramètres adéquats afin d'obtenir le cuvettes de tassement EF qui correspond le mieux aux mesures. Par la suite, une procédure d'analyse de sensibilité globale a également été proposée pour quantifier l'influence des paramètres sur le tassement maximal et le point d'inflexion. Deux objectifs principaux sont étudiés dans cet article : Dans un premier temps, lorsqu'elle est appliquée au début de l'excavation du tunnel, la procédure de rétroanalyse permet de déterminer la valeur optimale des paramètres pour les calculs EF ultérieurs. Par la suite, avec l'analyse de sensibilité globale, il est possible de déterminer les paramètres les plus influents sur les tassements causés par l'excavation du tunnel. Cette analyse pourrait permettre aux ingénieurs d'identifier les couches de sol problématiques pour lesquelles plus d'investigations sont nécessaires.

- Ensuite, grâce à la modélisation 3D, l'effet de l'avancement du tunnelier sur l'apparition des tassements et la simulation de cet effet sont comparés au résultat 2D. Cette étude nous a permis de mettre en évidence l'effet de la troisième dimension qui ne peut être représenté dans une modélisation 2D. En résumé, il est possible de représenter avec une modélisation 2D l'état initial et final du processus d'excavation, mais pas les étapes intermédiaires.

- Enfin, des modèles 2D à variablilité spatiale ont été réalisés en utilisant la théorie des champs aléatoires pour évaluer la cuvette de tassement causée par le creusement du tunnel. La première remarque qui en découle est que le tassement n'est pas toujours symétrique à l'axe du tunnel. L'analyse statistique nous permet de conclure que la variabilité spatiale influence davantage le tassement maximal (coefficient de variation de 15%) que le point d'inflexion (coefficient de variation de 3%).

La quantification des incertitudes à l'aide de méthodes numériques nécessite un grand nombre de simulations, ce qui rend le processus coûteux en temps de calcul. Dans le chapitre 4 l'utilisation d'un méta-modèle développé grâce à des techniques d'intelligence artificielle pour gagner du temps de calcul a été proposé. Le méta-modèle développé a été basé sur le couplage entre l'algorithme k-means et les réseaux de neurones artificiels. La méthode a été appliquée à l'extension de la ligne 12 du métro parisien.

- La méthode proposée a premièrement été appliquée sur des modèles EF hétérogènes pour prédire la cuvette de tassement. Deux méta-modèles ont été développés pour déterminer la cuvette de tassement (le tassement maximum et le point d'inflexion). Le coefficient de détermination obtenu est de 75% pour le tassement maximal et de 70% pour le point d'inflexion.
- À l'aide d'une base de données construite à partir de simulations numérique de couches stratifiée, ce chapitre a également développé des méta-modèles pour prédire le tassement. Une valeur de 97% pour le tassement maximal et de 95% pour le point d'inflexion a été obtenue.
- Pour l'approche stratifiée homogène, la base de données initiale a été réduite en déterminant l'influence des paramètres d'entrée (les modules de déformation des couches de sol) sur les paramètres de sortie (tassement maximal et point d'inflexion) en utilisant les coefficients de corrélation. La base réduite a été utilisée pour déterminer des nouveaux méta-modèles. Un coefficient de détermination de 90% a été obtenu pour le tassement et de 94% pour le point d'inflexion.

Dans le dernier chapitre de cette thèse, l'effet des pressions du tunnelier et de a position des bâtiments sur les dommages causés par le creusement de tunnel est étudié.

- Des simulations en 2D ont été réalisées pour évaluer l'influence de la pression, de l'hétérogénéité du sol et de l'emplacement des bâtiments sur les dommages causés par le tunnelier. Deux tableaux différents proposés par Burland (1995) et Son and Cording (2005) ont été utilisés pour évaluer la vulnérabilité du bâtiment. D'après les résultats, la sécurité d'un bâtiment pour une construction au tunnelier dépend de sa distance par rapport au tunnel et aux pressions du tunnelier.
- Des modèles 3D à variabilité spatiale ont également été réalisés en tenant compte de la variabilité spatiale plane. En comparant les résultats 2D aux résultats 3D, il a été nécessaire d'ajuster la pression fictive afin d'obtenir le même tassement. Ce résultat a mis en évidence l'influence sur la 3ème dimension qui ne peut être prise en compte dans le modèle 2D.

- Considérant les résultats 3D et les résultats 2D, l'approche par multi-fidélité a été appliquée en plus des méta-modèles construits avec la méthode proposée dans le chapitre 4 pour mieux prédire le niveau de dommage du bâtiment en utilisant les abaques de Burland (1995) et Son and Cording (2005).

Le travail developpé dans cette thèse présente certaines limites qu'il serait intéressant d'étudier pour des futures thèses.

- La formulation proposée pour la détermination de la pression fictive est basée sur certaines hypothèses ; le tunnel est situé sous la nappe phréatique et la pression de la chambre d'excavation est égale à la pression hydrostatique. Il serait important d'étudier l'influence de ces hypothèses afin de généraliser la formulation reliant la pression fictive 2D aux pressions du tunnelier.

- L'approche 3D adoptée dans cette thèse est basée sur la projection d'une section transversale 2D dans la direction longitudinale du tunnel. Cependant, dans la situation réelle, les couches de sol ne sont pas toujours parallèles et le tunnel présente un profil en pente le long de l'axe longitudinal. Une autre perspective de ce travail est d'intégrer ces différents aspects dans la modélisation 3D afin de prédire les tassements pour une gamme d'applications plus étendue.

- L'approche 3D de la variabilité spatiale proposée dans cette thèse est basée uniquement sur l'hypothèse de la variabilité plane. Dans les prochains travaux, il sera important de considérer la variabilité le long de la direction longitudinale du tunnel.

- L'un des objectifs de cette thèse était de développer des méta-modèles capables de prédire les tassements de surface induit par le creusement. Deux types de méta-modèles ont été développés ; un méta-modèle qui prend en compte les incertitudes des paramètres du sol et un méta-modèle qui prend en compte la variabilité spatiale des modèles. Ce dernier présente un coefficient de détermination faible mais acceptable. Ainsi donc, cette approche doit être améliorée afin de mieux prédire les tassements induits par le creusement en considérant l'hétérogénéité des sols.

Bibliography

Abdi, H. and Williams, L. J. (2010). Principal component analysis. Wiley interdisciplinary reviews: computational statistics, 2(4):433–459.

Abraham, A. (2005). Artificial Neural Networks. John Wiley & Sons.

Adams, R. P. (2018). K-means clustering and related algorithms. Princeton University.

Addenbrooke, P. and Puzrin (1997). The influence of pre-failure soil stiffness on the numerical analysis of tunnel construction. Geotechnique, 47:693–712.

Addenbrooke, T. I. and Potts, D. M. (2001). Twin tunnel interaction: Surface and subsurface effects. Int. J. Geomech., 1(2):249–271.

Ahangari, K., Moeinossadat, S. R., and Behnia, D. (2015). Estimation of tunnelling-induced settlement by modern intelligent methods. Soils and Foundations, 55(4):737–748.

Aristaghes, P. and Autuori, P. (2001). Calcul des tunnels au tunnelier. Revue française de géotechnique, (97):31–40.

Armaghani, D. J., Mohamad, E. T., Narayanasamy, M. S., Narita, N., and Yagiz, S. (2017). Development of hybrid intelligent models for predicting tbm penetration rate in hard rock condition. Tunnelling and Underground Space Technology, 63:29–43.

Atkinson, J. and Potts, D. (1979). Subsidence above shallow tunnels in soft ground. Journal of the Geotechnical Engineering Division, ASCE GT4:307–325.

Attewell, P. (1977). Ground movements caused by tunnelling in soil. Conference on Large Ground Movements and Structures, pages 812–984.

Attewell, P. B., Yeates, J., and Selby, A. R. (1986). Soil movements induced by tunnelling and their effects on pipelines and structures. Methuen, Inc., New York, NY.

Avunduk, E., Tumac, D., and Atalay, A. (2014). Prediction of roadheader performance by artificial neural network. Tunnelling and Underground Space Technology, 44:3–9.

Aydin, R. C., Braeu, F. A., and Cyron, C. J. (2019). General multi-fidelity framework for training artificial neural networks with computational models. Frontiers in Materials, 6:61.

Aygar, E. B. and Gokceoglu, C. (2021). Analytical solutions and 3d numerical analyses of a shallow tunnel excavated in weak ground: a case from turkey. Geo-Engineering, 12(1):9.

Baecher, G. and Christian, J. (2005a). Reliability-based design in civil engineering.

Baecher, G. B. and Christian, J. T. (2005b). Reliability and statistics in geotechnical engineering.

Bauer, J. and Puła, W. (2000a). Reliability with respect to settlement limit-states of shallow foundations on linearly-deformable subsoil. Computers and Geotechnics, 26(3-4):281–308.

Bauer, J. and Puła, W. (2000b). Reliability with respect to settlement limit-states of shallow foundations on linearly-deformable subsoil. Computers and Geotechnics, 26(3-4):281–308.

Benz, T., Vermeer, P., and Schwab, R. (2009). A small-strain overlay model. International journal for numerical and analytical methods in geomechanics, 33(1):25–44.

Bernat, S. (1996). Modélisation du creusement d'un tunnel en terrain meuble. Qualification sur chantier experimental, PhD thesis, Ecole Centrale de Lyon.

Bernaud, D. and Rousset, G. (1992). La «nouvelle méthode implicite» pour l'étude du dimensionnement des tunnels. Revue française de Géotechnique, (60):5–26.

Berry, J. (1977). Nzr's kaimai tunnel nears completion on major cut-off. Railway Gazette International, 133(10).

Bishop, C. M. (1995). Neural networks for pattern recognition. Oxford University Press.

Bolle, A. (2000). Investigation and allowance for spatial variability. Revue française de la Géotechnique, 93:55–66.

Boscardin, M. D. and Cording, E. J. (1989). Building response to excavation-induced settlement. Journal of Geotechnical Engineering, 115(1):1–21.

Braspenning, P. J., Thuijsman, F., and Weijters, A. (1995). Artificial neural networks: an introduction to ANN theory and practice, volume 931. Springer Science & Business Media.

Broere, W. (2016). Urban underground space: Solving the problems of today's cities. Tunnelling and Underground Space Technology, 55:245–248.

Burland, J., Broms, J., and De Mello, V. (1977). Behavior of foundations and structures. soa report session 2. In Proceedings of the 9th International Conference SMFE, Tokyo, volume 2, pages 495–546.

Burland, J. B. (1995). Assessment of risk of damage to buildings due to tunnelling and excavations. In 1st International Conference on Earthquake Geotechnics.

Cao, Y., Li, J., Hao, J., and Yang, X. (2021). Application of constitutive model in simulation analysis of tunnel construction. Journal of Applied Science and Engineering, 24(5):791–797.

Carranza-Torres, C. and Fairhurst, C. (2000). Application of the convergence-confinement method of tunnel design to rock masses that satisfy the hoek-brown failure criterion. Tunnelling and underground space technology, 15(2):187–213.

Celestino, T., Gomes, R., and Bortolucci, A. (2000). Errors in ground distortions due to settlement trough adjustment. Tunnelling and underground space technology, 15(1):97–100.

Chapeau, C. (1991). Auscultation du sol pendant le creusement. Tunnels et ouvrages souterrains, (107):235–245.

Chapman, D., Metje, N., and Stärk, A. (2017). Introduction to tunnel construction. Crc Press, 2nd edition.

Chen, R.-P., Zhang, P., Kang, X., Zhong, Z.-Q., Liu, Y., and Wu, H.-N. (2019). Prediction of maximum surface settlement caused by earth pressure balance (EPB) shield tunneling with ANN methods. Soils and Foundations, 59(2):284–295.

Chen, S.-Z. and Feng, D.-C. (2022). Multifidelity approach for data-driven prediction models of structural behaviors with limited data. Computer-Aided Civil and Infrastructure Engineering, 37(12):1566–16581.

Cherubini, C., Giasi, C., and Rethati, L. (1993). The coefficients of variation of some geotechnical parameters. In Conference on probabilistic methods in geotechnical engineering, pages 179–183. CRC Press.

Chiasson, P., Lafleur, J., Soulie, M., and Law, K. T. (1995). Characterizing spatial variability of a clay by geostatistics. Canadian Geotechnical Journal, 32(1):1–10.

Chortis, F., Tzivakos, K., and Kavvadas, M. (2014). Investigation of the influence of face pressure on surface settlements in epb mechanized tunnelling.

Clough, G. and Schmidt, B. (1981). Design and performance of excavations and tunnels in soft clay. Soft clay engineering, ASCE GT4:569–634.

Corbetta, F., Bernaud, D., and Minh, D. N. (1991). Contribution à la méthode convergence-confinement par le principe de la similitude. Revue française de géotechnique, (54):5–11.

Cording, E., Hansmire, W., MacPherson, H., Lenzini, P., and Vonderohe, A. (1976). Displacements around tunnels in soil. volume 23.

Cukier, R., Schaibly, J., and Shuler, K. E. (1975). Study of the sensitivity of coupled reaction systems to uncertainties in rate coefficients. iii. analysis of the approximations. The Journal of Chemical Physics, 63(3):1140–1149.

De La Fuente, M., Taherzadeh, R., Sulem, J., Nguyen, X.-S., and Subrin, D. (2019). Applicability of the convergence-confinement method to full-face excavation of circular tunnels with stiff support system. Rock Mechanics and Rock Engineering, 52(7):2361–2376.

Demagh, R., Emeriault, F., and Kastner, R. (2009). Modélisation 3d du creusement de tunnel par tunnelier à front pressurisé–validation sur 3 cas d'études. In Proceedings of the 17ème Conférence de Mécanique des Sols et de Géotechnique (17ème ICSMGE), pages 5–9.

Demagh, R., Emeriault, F., and Kastner, R. (2013). Modélisation 3d du creusement de tunnel par tunnelier à front pressurisé dans les sols surconsolidés. Revue française de Géotechnique, (142):17–26.

Detournay, E. and Fairhurst, C. (1987). Two-dimensional elastoplastic analysis of a long, cylindrical cavity under non-hydrostatic loading. International Journal of Rock Mechanics and Mining Sciences, 24(4):197–211.

Dias, D. (2011). Convergence-confinement approach for designing tunnel face reinforcement by horizontal bolting. Tunnelling and Underground Space Technology, 26(4):517–523.

Division, S. A. P. (2019). Department of Economic and Social Affairs, volume 1. United Nations Publications.

Do, N.-A., Dias, D., Oreste, P., and Djeran-Maigre, I. (2014). Three-dimensional numerical simulation for mechanized tunnelling in soft ground: the influence of the joint pattern. Acta Geotech., 9(4):673–694.

Duncan, J. M. (2000). Factors of safety and reliability in geotechnical engineering. Journal of geotechnical and geoenvironmental engineering, 126(4):307–316.

Ejday, M. (2011). Optimisation Multi-Objectifs à base de Métamodèle pour les Procédés de Mise en Forme. PhD thesis, École Nationale Supérieure des Mines de Paris.

Ejezie, S. and Harrop-Williams, K. (1984). Probabilistic characterization of nigerian soils. Probabilistic characterization of soil properties: bridge between theory and practice/edited by David S. Bowles and Hon-Yim Ko.

El Gonnouni, M., Riou, Y., and Hicher, P. Y. (2005). Geostatistical method for analysing soil displacement from underground urban construction. Risk and Variability in Geotechnical Engineering, 55(2):171–182.

El Jirari, S. (2021). Modélisation numérique du processus de creusement pressurisé des tunnels. PhD thesis, Université de Lyon.

El Kahi, E., Deck, O., Khouri, M., Mehdizadeh, R., and Rahme, P. (2020). Simplified probabilistic evaluation of the variability of soil-structure interaction parameters on the elastic transmission of ground movements. Engineering Structures, 213:110554.

Espada, M. and Lamas, L. (2017). Back analysis procedure for identification of anisotropic elastic parameters of overcored rock specimens. Rock Mechanics and Rock Engineering, 50(3):513–527.

Fahim, A., Salem, A., Torkey, F. A., and Ramadan, M. (2006). An efficient enhanced k-means clustering algorithm. Journal of Zhejiang University-Science A, 7(10):1626–1633.

Feinberg, J. and Langtangen, H. P. (2015). Chaospy: An open source tool for designing methods of uncertainty quantification. Journal of Computational Science, 11:46–57.

Fenton, G. A. and Griffiths, D. (2003). Bearing-capacity prediction of spatially random c φ soils. Canadian geotechnical journal, 40(1):54–65.

Fenton G.A., G. D. (2005). Three-dimensional probabilistic foundation settlement. J. of Geotech. and Geoenv. Engrg, ASCE, 131:232–239.

Ferrario, E., Pedroni, N., Zio, E., and Lopez-Caballero, F. (2017). Bootstrapped artificial neural networks for the seismic analysis of structural systems. Structural Safety, 67:70–84.

Founta, V. (2018). Prediction of instability and ground movements during tunnel construction in non-homogenous conditions. PhD thesis, Massachusetts Institute of Technology.

Franco, V. H., de F.N. Gitirana, G., and de Assis, A. P. (2019). Probabilistic assessment of tunneling-induced building damage. Computers and Geotechnics, 113:1–15.

Franza, A. and Marshall, A. M. (2019). Empirical and semi-analytical methods for evaluating tunnelling-induced ground movements in sands. Tunnelling and Underground Space Technology, 88:47–62.

Franzius, J. N., Potts, D. M., Addenbrooke, T. I., and Burland, J. B. (2004). The influence of building weight on tunnelling-induced ground and building deformation. Soils and foundations, 44(1):25–38.

Fredlund, D. and Dahlman, A. (1972). Statistical geotechnical properties of glacial lake edmonton sediments. In Statistics and Probability in Civil Engineering, volume 5, pages 203–228. Oxford University Press: London.

Galli, G., Grimaldi, A., and Leonardi, A. (2004). Three-dimensional modelling of tunnel excavation and lining. Computers and Geotechnics, 31(3):171–183.

Gao, X., Shi, M., Song, X., Zhang, C., and Zhang, H. (2019). Recurrent neural networks for real-time prediction of TBM operating parameters. Automation in Construction, 98:225–235.

Gaspar, A., Lopez-Caballero, F., Modaressi-Farahmand-Razavi, A., and Gomes-Correia, A. (2014). Methodology for a probabilistic analysis of an rcc gravity dam construction. modelling of temperature, hydration degree and ageing degree fields. Engineering Structures, 65:99–110.

Ghiasi, V. and Koushki, M. (2020). Numerical and artificial neural network analyses of ground surface settlement of tunnel in saturated soil. Springer Nature Applied Sciences, 2(5):1–14.

Gilleron, N. and Bourgeois, E. (2018). Modéliser une cuvette de tassement au tunnelier réaliste a l'aide d'une loi de comportement adaptée. page 8.

Gilleron, N., Bourgeois, E., Chatellier, P., and Saïtta, A. (2021). An anisotropic model for the numerical analysis of tunneling-induced settlements in the paris area. Geotechnical and Geological Engineering, 39(4):3133–3146.

Gilleron, N., Bourgeois, E., and Saitta, A. (2016). Utilisation du hardening soil model dans l'étude du creusement de tunnels superficiels. In JNGG 2016-Journées Nationales de Géotechnique et de Géologie de l'Ingénieur, page 8.

Giroux, A., Chalivat, P., Cioci, V., Pouemi, P., Ziem, C., Pallu, B., Kreziak, C., Ferrari, M., et al. (2022). Grand paris express ligne 16-traitements de terrain pour la maîtrise de l'eau. In 11èmes journées nationales de géotechnique et de géologie de l'ingénieur.

Goff, J. A. and Jordan, T. H. (1988). Stochastic modeling of seafloor morphology: Inversion of sea beam data for second-order statistics. Journal of Geophysical Research: Solid Earth, 93(B11):13589–13608.

Gong, W., Juang, C. H., Martin II, J. R., Tang, H., Wang, Q., and Huang, H. (2018). Probabilistic analysis of tunnel longitudinal performance based upon conditional random field simulation of soil properties. Tunnelling and Underground Space Technology, 73:1–14.

González, C. and Sagaseta, C. (2001). Patterns of soil deformations around tunnels. application to the extension of madrid metro. Computers and Geotechnics, 28(6):445–468.

Grasso, P. and Pelizza, S. (1994). Metodologia per la previsione ed il controllo delle subsistenze. un'applicazione: la bretella di voltri. Gallerie e Grandi Opere Sotterranee, 43:12–25.

Griffiths, D. and Fenton, G. A. (2001). Bearing capacity of spatially random soil: the undrained clay prandtl problem revisited. J. Geotech, 51:351–359.

Griffiths, D., Fenton, G. A., and Manoharan, N. (2002). Bearing capacity of rough rigid strip footing on cohesive soil: Probabilistic study. J. Geotech. Geoenviron. Eng., 128:743–755.

Griffiths, D. V. and Fenton, G. A. (2007). Probabilistic methods in geotechnical engineering, volume 491. Springer Science & Business Media.

Guerra, F. (1973). On stochastic field theory. J. Phys. Colloques, 34:C1–95–C1–98.

Guglielmetti, V., Grasso, P., Mahtab, A., and Xu, S. (2008). Mechanized tunnelling in urban areas: design methodology and construction control. CRC Press.

Gunn (1993). The prediction of surface settlement profiles due to tunnelling, predictive soil mechanics. Proc. of the Wroth Memorial Symposium, pages 304–316.

Guo, M., Manzoni, A., Amendt, M., Conti, P., and Hesthaven, J. S. (2022). Multi-fidelity regression using artificial neural networks: efficient approximation of parameter-dependent output quantities. Computer methods in applied mechanics and engineering, 389:13.

Hackeling, G. (2017). Mastering Machine Learning with scikit-learn. Packt Publishing Ltd.

Hamrouni, A., Dias, D., and Guo, X. (2022). Behavior of shallow circular tunnels—impact of the soil spatial variability. Geosciences, 12(2):97.

Hamrouni, A., Sbartai, B., and Dias, D. (2021). Etude de l'influence de la variabilité spatiale sur la réponse d'ouvrages géotechniques. PhD thesis.

Harr, M. E. (1984). Reliability-based design in civil engineering, volume 20. Department of Civil Engineering, School of Engineering, North Carolina State.

Hashimoto, T., Nagaya, J., Konda, T., and Tamura, T. (2002). Observation of lining pressure due to shield tunneling. in proceedings of the 3rd international symposium on geotechnical aspects of underground construction in soft ground. pages 119–124.

Hemphill, G. B. (2012). Practical tunnel construction. John Wiley and Sons.

Hoeffding, W. (1948). A class of statistics with asymptotically normal distributions. Annals of Mathematics, 19:293–325.

Holliger, K. and Levander, A. R. (1992). A stochastic view of lower crustal fabric based on evidence from the ivrea zone. Geophysical Research Letters, 19(11):1153–1156.

Houmadi, Y. (2011). Prise en compte de la variabilité spatiale des paramètres géotechniques. PhD thesis, Thèse de doctorat, université de Tlemcen, p167.

Huang, H., Xiao, L., Zhang, D., and Zhang, J. (2017). Influence of spatial variability of soil young's modulus on tunnel convergence in soft soils. Engineering Geology, 228:357–370.

Huang, S., Qi, Q., Liu, J., and Liu, W. (2020). Tunnel surrounding rock stability prediction using improved knn algorithm. Journal of Vibroengineering, 22(7):1674–1691.

Huo, R., Zhou, P., Song, Z., Wang, J., Li, S., and Zhang, Y. (2019). Study on the settlement of large-span metro station's baseplate caused by the tunnels newly built beneath it. Advances in Mechanical Engineering, 11(2):168781401882516.

Iooss, B. and Lemaître, P. (2015). A Review on Global Sensitivity Analysis Methods, volume 59. Springer.

jacobsz, S. (2003). Tunnelling effects on piled foundations. volume 35, pages 28–31.

Janin, J., Dias, D., Emeriault, F., Kastner, R., Le Bissonnais, H., and Guilloux, A. (2015). Numerical back-analysis of the southern toulon tunnel measurements: A comparison of 3d and 2d approaches. Engineering Geology, 195:42–52.

Janin, J. P. (2012). Tunnels en milieu urbain: Prévisions des tassements avec prise en compte des effets des pré-soutènements (renforcement du front de taille et voûte-parapluie). PhD thesis, INSA de Lyon.

Janin, J.-P. (2017). Apports de la simulation numérique tridimensionnelle dans les études de tunnels. Revue Française de Géotechnique, (150):3.

Janin, J.-P., Renier, P., and Bissonnais, H. L. (2017). Méthode 3d simplifiée pour la prévision des tassements générés par le creusement d'un tunnel au tunnelier pressurisé. In Congrès International de l'AFTES, page 8.

Javad, G. and Narges, T. (2010). Application of artificial neural networks to the prediction of tunnel boring machine penetration rate. Mining Science and Technology (China), 20(5):727–733.

Javadi, M., Sayadi, S., Sharifzadeh, M., and Shahriar, K. (2020). Evaluation of soil constitutive model effects on numerical modeling of settlement induced by tunneling in urban area, case study of the amirkabir tunnel. Journal of Analytical and Numerical Methods in Mining Engineering, 10(24):119–136.

Kampolis, I. C. and Giannakoglou, K. C. (2008). A multilevel approach to single-and multiobjective aerodynamic optimization. Computer Methods in Applied Mechanics and Engineering, 197(33-40):2963–2975.

Karakus, M. (2007). Appraising the methods accounting for 3d tunnelling effects in 2d plane strain FE analysis. Tunnelling and Underground Space Technology, 22(1):47–56.

Kasper, T. and Meschke, G. (2006). On the influence of face pressure, grouting pressure and tbm design in soft ground tunnelling. 2nd Eastern European Tunnelling conference, 21(2):160–171.

Kennedy, M. C. and O Hagan, A. (2000). Predicting the output from a complex computer code when fast approximations are available. Biometrika, 87(1):13.

Khalil, C. (2021). Seismic analysis of a liquefiable soil foundation-embankment system: life cycle performance and mitigation. PhD thesis, université Paris-Saclay.

Kohestani, V., Bazarganlari, M., and Asgari Marnani, J. (2017). Prediction of maximum surface settlement caused by earth pressure balance shield tunneling using random forest. Journal of AI and Data Mining, 5(1):127–135.

Kontogianni, V. and Stiros, S. C. (2020). Ground loss and static soil–structure interaction during urban tunnel excavation: Evidence from the excavation of the athens metro. Infrastructures, 5(8):64.

Koseoglu Balta, G., Dikmen, I., and Birgonul, M. (2021). Bayesian network based decision support for predicting and mitigating delay risk in TBM tunnel projects. Automation in Construction, 129:103819.

Kulhawy, F. H. (1993). On the evaluation of static soil properties. In Stability and performance of slopes and embankments II, pages 95–115. ASCE.

Lacasse, S. and Nadim, F. (1996). Uncertainties in characterising soil properties. In Uncertainty in the geologic environment: From theory to practice, pages 49–75. ASCE.

Laskov, P., Düssel, P., Schäfer, C., and Rieck, K. (2005). Learning intrusion detection: Supervised or unsupervised? In Image Analysis and Processing–ICIAP 2005: 13th International Conference, Cagliari, Italy, September 6-8, 2005, Proceedings, volume 3617, pages 50–57. Springer.

Leblais, Y., Andre, D., Chapeau, C., Dubois, P., Gigan, J., Guillaume, J., Leca, E., Pantet, A., and Riondy, G. (1995). Tassements liés au creusement des ouvrages en souterrain. Tunnels et ouvrages souterrain, (132):379–386.

Leca, E. (1987). Mouvements occasionnés par le creusement d'un tunnel. In Rapport de recherche: Centre d'Enseignement et de recherche en mecanique des sols Noisy, page 20.

Leca, E. and New, B. (2007). Settlements induced by tunneling in soft ground. Tunnelling and Underground Space Technology, 22(2):119–149.

Lee, C.-J., Wu, B.-R., and Chiou, S.-Y. (1999). Soil movements around a tunnel in soft soils. Proceedings-national science council republic of China part a phisical science and engineering, 23:235–247.

Lee, I., White, W., and Ingles, O. (1983). Geotechnical Engineering, Copp Clark. Pitman.

Lee, K., Rowe, R. K., and Lo, K. (1992). Subsidence owing to tunnelling. i. estimating the gap parameter. Canadian geotechnical journal, 29(6):929–940.

Li, M. and Jia, G. (2020). Multifidelity gaussian process model integrating low-and high-fidelity data considering censoring. Journal of Structural Engineering, 146(3):3487–3502.

Likitlersuang, S., Teachavorasinskun, S., Surarak, C., Oh, E., and Balasubramaniam, A. (2013). Small strain stiffness and stiffness degradation curve of bangkok clays. Soils and Foundations, 53(4):498–509.

Liu, B., Wang, R., Zhao, G., Guo, X., Wang, Y., Li, J., and Wang, S. (2020). Prediction of rock mass parameters in the TBM tunnel based on BP neural network integrated simulated annealing algorithm. Tunnelling and Underground Space Technology, 95:103103.

Loganathan, N. (2011). An Innovative Method for Assessing Tunnelling-induced Risks to Adjacent Structures. PB 2009 William Barclay Parsons Fellowship. Parsons Brinckerhoff Incorporated.

Lombardi, M., Cardarilli, M., and Raspa, G. (2017). Spatial variability analysis of soil strength to slope stability assessment. Geomechanics and Engineering, 12(3):483–503.

Lu, Z. and Liu, G. (2008). Analysis of surface settlement due to the construction of a shield tunnel in soft clay in shanghai. In Geotechnical Aspects of Underground Construction in Soft Ground, pages 821–826. CRC Press.

Lumb, P. (1966). The variability of natural soils. Canadian geotechnical journal, 3(2):74–97.

Lumb, P. (1972). General report on strength and stability problems. In Fourth Asian Regional Conf Proc, volume 2.

Lunardi, P. and Bindi, R. (2004). The evolution of reinforcement of the advance core using fibre-glass elements. Gluckauf Forschungshefte, 65:91–100.

Mahadevan, S. and Haldar, A. (1991). Practical random field discretization in stochastic finite element analysis. Structural safety, 9(4):283–304.

Mahdevari, S., Shahriar, K., Yagiz, S., and Akbarpour Shirazi, M. (2014). A support vector regression model for predicting tunnel boring machine penetration rates. International Journal of Rock Mechanics and Mining Sciences, 72:214–229.

Mahmoodzadeh, A., Mohammadi, M., Ibrahim, H. H., Rashid, T. A., Aldalwie, A. H. M., Ali, H. F. H., and Daraei, A. (2021). Tunnel geomechanical parameters prediction using gaussian process regression. Machine Learning with Applications, 3:100020.

Mai, P. M. and Beroza, G. C. (2002). A spatial random field model to characterize complexity in earthquake slip. Journal of Geophysical Research: Solid Earth, 107(B11):ESE–10.

Mair, R., Taylor, R., and Bracegirdle, A. (1993). Subsurface settlement profiles above tunnels in clays. Geotechnique, 43(2):315–320.

Mair, R. J. and Taylor, R. (1999). Bored tunnelling in the urban environments. In Fourteenth International Conference on Soil Mechanics and Foundation Engineering. ProceedingsInternational Society for Soil Mechanics and Foundation Engineering, volume 4.

Marto, A., Abdullah, M. H., Makhtar, A. M., Sohaei, H., and Tan, C. S. (2015). Surface settlement induced by tunneling in greenfield condition through physical modelling. Jurnal Teknologi, 76(2).

Meng, X. and Karniadakis, G. E. (2020). A composite neural network that learns from multi-fidelity data: Application to function approximation and inverse pde problems. Journal of Computational Physics, 401:29.

Metwally, K. G. (2016). Numerical prediction of the tunnel deformation due to intersection with other tunnels. In Civil Engineering Department, Beni-Suef University, page 64.

Miliziano, S. and de Lillis, A. (2019). Predicted and observed settlements induced by the mechanized tunnel excavation of metro line c near s. giovanni station in rome. Tunnelling and Underground Space Technology, 86:236–246.

Miranda, L. (2011). The Influence of Geotechnical Variability in the Subsidence Caused by Urban Tunnel Excavation. PhD thesis, Laboratoire Nationale de l'Ingénierie Civil, Portugal.

Mohammadi, S. D., Naseri, F., and Alipoor, S. (2015). Development of artificial neural networks and multiple regression models for the NATM tunnelling-induced settlement in niayesh subway tunnel, tehran. Bull Eng Geol Environ, 74(3):827–843.

Mollon, G., Dias, D., and Soubra, A.-H. (2013). Probabilistic analyses of tunneling-induced ground movements. Acta Geotech., 8(2):181–199.

Morse, R. (1971). Importance of proper soil units for statistical analysis. In Proccedings of the 1st International Conference On applications of Statistics and Probability to Soil and Structural Engineering, Hong Kong.

Mousivand, M. and Maleki, M. (2018). Constitutive models and determining methods effects on application of convergence–confinement method in underground excavation. Geotechnical and Geological Engineering, 36(3):1707–1722.

Nabian, M. A., Gladstone, R. J., and Meidani, H. (2021). Efficient training of physics-informed neural networks via importance sampling. Computer-Aided Civil and Infrastructure Engineering, 36(8):962–977.

Ninic, J., Alsahly, A., Vonthron, A., Bui, H.-G., Koch, C., König, M., and Meschke, G. (2021). From digital models to numerical analysis for mechanised tunnelling: A fully automated design-through-analysis workflow. Tunnelling and Underground Space Technology, 107:103622.

Norgrove, W. and Attewell, P. (1984). Assessing the benefits of site investigation for tunnelling. Municipal Engineer, 1(2).

Norgrove, W. and PB, A. (1979). Site investigation procedures adopted for the northumbrian water authority's tyneside sewerage scheme, with special reference to settlement prediction when tunnelling through urban area. In International symposium of Tunnelling, pages 79–104.

Noubissi, C., Taherzadeh, R., Puel, G., and Lopez-Caballero, F. (2020). An optimized methodology of back analysis for tunneling in urban area: Application on the extension of line 12 in paris area. In Association Francaise des Travaux Souterrains, page 22.

Nour, A., Slimani, A., and Laouami, N. (2002). Foundation settlement statistics via finite element analysis. Computers and Geotechnics, 29(8):641–672.

Obrzud, R. F. and Truty, A. (2010). The Hardening Soil Model - A pratical guidebook.

Ocak, I. and Seker, S. E. (2013). Calculation of surface settlements caused by epbm tunneling using artificial neural network, svm, and gaussian processes. Environmental earth sciences, 70(3):1263–1276.

Okhulkova, T. (2015). Integration of uncertainty and definition of critical thresholds for CO2 storage risk assessment. PhD thesis, Université Paris-Saclay (ComUE).

Olivier, C. (2006). L'usage des modules de déformation en géotechnique. Revue française de géotechnique, (114):3–32.

O'Reilly, M. and New, B. (1983). Settlement above tunnels in the united kingdom—their magnitude and prediction. In International Journal of Rock Mechanics and Mining Sciences & Geomechanics Abstracts, volume 20, pages 173–181. Pergamon.

O'Reilly, M. P. and New, B. (1982). Settlements above tunnels in the united kingdom - their magnitudes and prediction. In International Journal of Rock Mechanics and Mining Sciences, pages 173–181.

Pande, G. and Pietruszczak, S. (1986). Symmetric tangential stiffness formulation for non-associated plasticity. Computers and Geotechnics, 2(2):89–99.

Panet, M. (1973). La stabilité des ouvrages souterrains soutènements et revetements. Number 28.

Panet, M. (1976). La mécanique des roches appliquée aux ouvrages de génie civil.

Panet, M., Givet, Guilloux, A., Duc, Piraud, J., and Wong (2001). The convergence–confinement method. AFTES–recommendations des Groupes de Travail.

Panet, M. and Guenot, A. (1983). Analysis of convergence behind the face of a tunnel: Tunnelling 82, proceedings of the 3rd international symposium. 20(1):A16.

Peck, R. (1969). Deep excavations and tunneling in soft ground. state of the art report. 7th International Conference on Soil Mechanics and Foundation Engineering, pages 225–290.

Phoon, K. K. and Kulhawy, F. H. (1996). On quantifying inherent soil variability. In Uncertainty in the Geologic Environment: from Theory to Practice, pages 326–340.

Phoon, K.-K. and Kulhawy, F. H. (1999). Evaluation of geotechnical property variability. Canadian Geotechnical Journal, 36(4):625–639.

Popescu, R. (1995). Stochastic variability of soil properties: data analysis, digital simulation, effects on system behavior. PhD thesis, Princeton University.

Poulos, H. G. (1974). Settlement analysis of structural foundation system. In Transport and Road Research Laboratory report.

Powell, D., Sigl, O., and Beveridge, J. (1996). Heathrow express-design and performance of platform tunnels at terminal 4. In International conference of Tunnelling, pages 565–593.

Raissi, M. and Karniadakis, G. (2016). Deep multi-fidelity Gaussian processes.

Rajabi, M., Rahmannejad, R., Rezaei, M., and Ganjalipour, K. (2017). Evaluation of the maximum horizontal displacement around the power station caverns using artificial neural network. Tunnelling and Underground Space Technology, 64:51–60.

Rankin, W. (1988). Ground movements resulting from urban tunnelling: predictions and effects. Geological Society, London, Engineering Geology Special Publications, 5(1):79–92.

Rowe and Kack (1983). A theoretical examination of the settlements induced by tunnelling: Four case histories. Canadian Geotechnical Journal, 20(2):299–314.

Sagaseta, C. (1987). Analysis of undrained soil deformation due to ground loss. Geotechnique, 37(3):301–320.

Santos, O. J. and Celestino, T. B. (2008). Artificial neural networks analysis of são paulo subway tunnel settlement data. Tunnelling and Underground Space Technology, 23(5):481–491.

Sathya, R. and Abraham, A. (2013). Comparison of supervised and unsupervised learning algorithms for pattern classification. International Journal of Advanced Research in Artificial Intelligence, 2(2):34–38.

Schanz, T., Vermeer, P., and Bonnier, P. G. (2019). The hardening soil model: formulation and verification. In Beyond 2000 in computational geotechnics, pages 281–296. Routledge.

Schikora, K. and Ostermeier, B. (1988). Two-dimensional calculation model in tunnelling. verification by measurement result and by spatial calculation. Proceedings of the 6th International Conference on Numerical Methods in Geomechanics, 1:1499–1503.

Shahin, H. M., Nakai, T., and Okuno, T. (2019). Numerical study on 3d effect and practical design in shield tunneling. Underground Space, 4(3):201–209.

Simpson, A. and Jovicis (1993). The influence of anisotropy on calculations of ground settlements above tunnels. Proc. of International Symposium on Geotechnical Aspects of the Underground Construction in Soft Ground, pages 511–514.

Skels, P. and Bondars, K. (2017). Applicability of small strain stiffness parameters for pile settlement calculation. Procedia Engineering, 172:999–1006.

Sobol, I. M. (1993). Sensitivity analysis for non-linear mathematical models. Mathematical modelling and computational experiment, 1:407–414.

Soga, K., Laver, R. G., and Li, Z. (2017). Long-term tunnel behaviour and ground movements after tunnelling in clayey soils. Underground Space, 2(3):149–167.

Son, M. and Cording, E. J. (2005). Estimation of building damage due to excavation-induced ground movements. Journal of geotechnical and geoenvironmental engineering, 131(2):162–177.

Soulie, M., Montes, P., and Silvestri, V. (1990). Modelling spatial variability of soil parameters. Canadian Geotechnical Journal, 27(5):617–630.

Sulem, J., Panet, M., and Guenot, A. (1987). An analytical solution for time-dependent displacements in a circular tunnel. International journal of rock mechanics and mining sciences, 24(3):155–164.

Suwansawat, S. and Einstein, H. H. (2006). Artificial neural networks for predicting the maximum surface settlement caused by EPB shield tunneling. Tunnelling and Underground Space Technology, 21(2):133–150.

Swoboda, G. (1979). Finite element method of the new austrian tunnelling method (natm). Proceedings of the 3rd international conference of Numerical Methods in Geomechanics, 2:581–586.

Tarantola, S., Gatelli, D., and Mara, T. (2006). Random balance designs for the estimation of first order global sensitivity indices. Reliability Engineering & System Safety, 91(6):717–727.

Tarantola, S. and Mara, T. A. (2017). Variance-based sensitivity indices of computer models with inputs: the fourier amplitude sensitivity test. Int. J. UncertaintyQuantification, 7(6):511–523.

Truty, A., Zimmermann, T., Podleś, K., and Obrzud, R. (2020). User manual zsoil. PC v2020. Soil, Rock and Structural Mechanics in dry or partially saturated media (1985-2020). Elmepress International.

Until, E. (2013). World population prospects: The 2012 revision. United Nations Department of Economic and Social Affairs.

Vahdatirad, M. J., Ghodrat, H., Firouzianbandpey, S., and Barari, A. (2010). Analysis of an underground structure settlement risk due to tunneling: A case study from tabriz, iran. Songklanakarin Journal of Science and Technology, 32(2):145–152.

Vakili, K., Lavasan, A., Schanz, T., and Datcheva, M. (2014). The influence of the soil constitutive model on the numerical assessment of mechanized tunneling. In Numerical Methods in Geotechnical Engineering contains the proceedings of the 8th European Conference on Numerical Methods in Geotechnical Engineering (NUMGE 2014), Delft, The Netherlands, pages 18–20.

Vanmarcke, E. H. (1977). Probabilistic modeling of soil profiles. Journal of the geotechnical engineering division, 103(11):1227–1246.

Vanmarcke, E. H. (1983). Random fields: Analysis and synthesis. Cambridge.

Verruijt, A. (1997). A complex variable solution for a deforming circular tunnel in an elastic half-plane. International Journal for Numerical and Analytical Methods in Geomechanics, 21(2):77–89.

Vlachopoulos, N. and Diederichs (2009). Improved longitudinal displacement profiles for convergence confinement analysis of deep tunnels. Rock mechanics and rock engineering, 42(2):131–146.

Vorster, T., Klar, A., Soga, K., and Mair, R. (2005). Estimating the effects of tunneling on existing pipelines. Journal of Geotechnical and Geoenvironmental Engineering, 131(11):1399–1410.

Wang, X., Lu, H., Wei, X., Wei, G., Behbahani, S. S., and Iseley, T. (2020). Application of artificial neural network in tunnel engineering: A systematic review. IEEE Access, 8:119527–119543.

Whitman, R. V. (1984). Evaluating calculated risk in geotechnical engineering. Journal of Geotechnical Engineering, 110(2):143–188.

Wolff, T. F. (1996). Probabilistic slope stability in theory and practice. In Uncertainty in the geologic environment: From theory to practice, pages 419–433. ASCE.

Xiao, L., Huang, H., and Zhang, J. (2017). Effect of soil spatial variability on ground settlement induced by shield tunnelling. In Geo-Risk 2017, pages 330–339.

Yagiz, S. and Karahan, H. (2015). Application of various optimization techniques and comparison of their performances for predicting TBM penetration rate in rock mass. International Journal of Rock Mechanics and Mining Sciences, 80:308–315.

Yeo, C., Lee, F., Tan, S., Hasegawa, O., Suzuki, H., and Shinji, M. (2009). Three dimensional numerical modelling of a new austrian tunneling method tunnel. International Journal of Japanese Committee of Rock Mechanics, 5(1):33–38.

Zamora Hernández, Y., Durand Farfán, A., and Pacheco de Assis, A. (2019). Three-dimensional analysis of excavation face stability of shallow tunnels. Tunnelling and Underground Space Technology, 92:103062.

Zhang, J., Phoon, K. K., Zhang, D., Huang, H., and Tang, C. (2021a). Deep learning-based evaluation of factor of safety with confidence interval for tunnel deformation in spatially variable soil. Journal of Rock Mechanics and Geotechnical Engineering, 13(6):1358–1367.

Zhang, Q., Wu, K., Cui, S., Yu, Y., Zhang, Z., and Zhao, J. (2019). Surface settlement induced by subway tunnel construction based on modified peck formula. Geotech Geol Eng, 37(4):2823–2835.

Zhang, R., Zhang, W., and Goh, A. T. C. (2018). Numerical investigation of pile responses caused by adjacent braced excavation in soft clays. International Journal of Geotechnical Engineering, pages 1–15.

Zhang, X., Xie, F., Ji, T., Zhu, Z., and Zheng, Y. (2021b). Multi-fidelity deep neural network surrogate model for aerodynamic shape optimization. Computer Methods in Applied Mechanics and Engineering, 373:25.

Zhao, C., Lavasan, A. A., Barciaga, T., Zarev, V., Datcheva, M., and Schanz, T. (2015). Model validation and calibration via back analysis for mechanized tunnel simulations – the western scheldt tunnel case. Computers and Geotechnics, 69:601–614.

Zheng, G., Du, Y., Cheng, X., Diao, Y., Deng, X., and Wang, F. (2017). Characteristics and prediction methods for tunnel deformations induced by excavations. Geomechanics and Engineering, 12(3):361–397.

Zheng, Y., Zhang, Q., and Zhao, J. (2016). Challenges and opportunities of using tunnel boring machines in mining. Tunnelling and Underground Space Technology, 57:287–299.

Zio, E. (2006). A study of the bootstrap method for estimating the accuracy of artificial neural networks in predicting nuclear transient processes. Ieee Transactions on Nuclear Science, 53(3):1460–1478.

Appendices

Appendix A

Numerical simulation of TBM excavation and model simplification

Hardening Soil with Small Strain Model

Governing equations of the HS-Small model

The governing equation of the HSSM is presented here. A complete list of model parameters can be also found the following table.

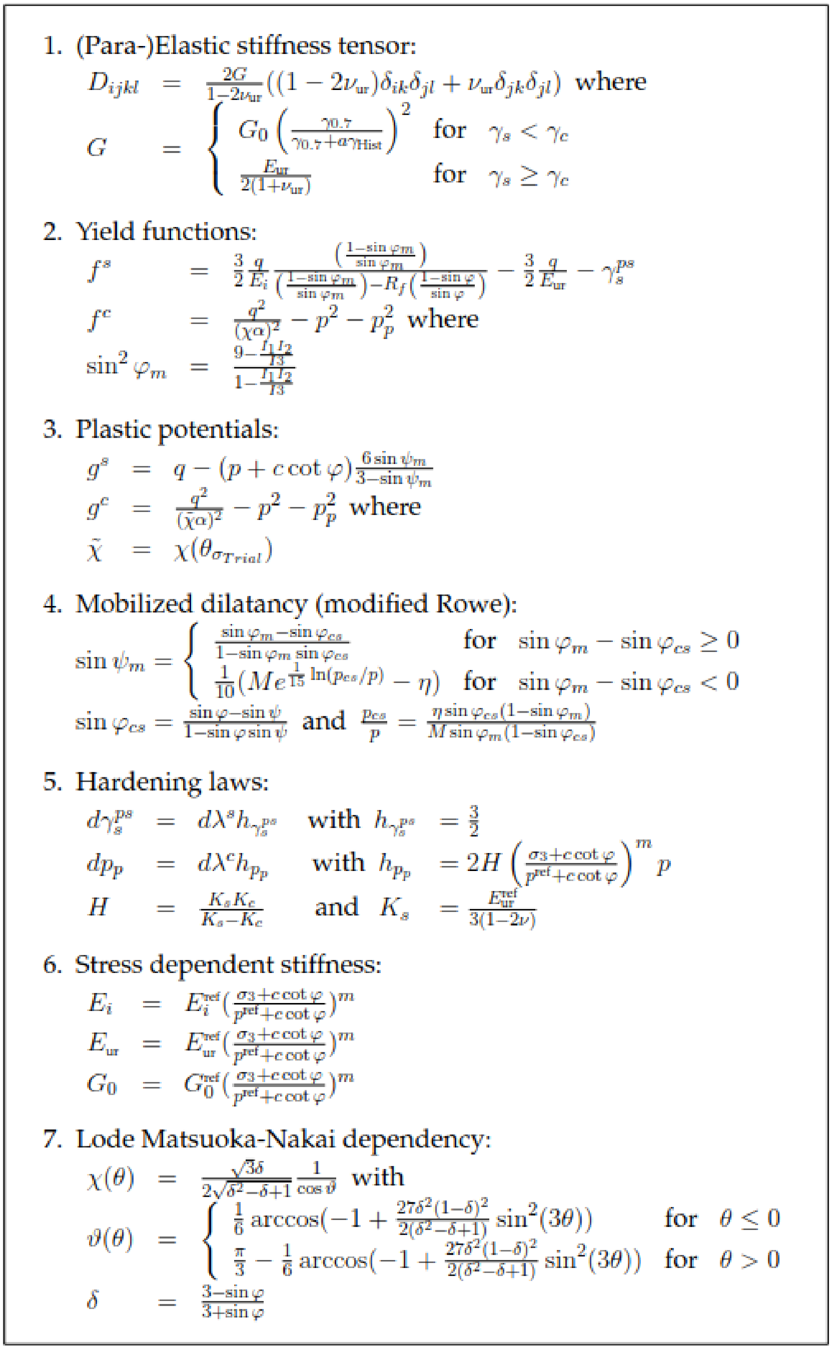

1. (Para-)Elastic stiffness tensor:

$$\begin{aligned} D_{ijkl} &= \frac{2G}{1-2\nu_{\text{ur}}}((1-2\nu_{\text{ur}})\delta_{ik}\delta_{jl} + \nu_{\text{ur}}\delta_{jk}\delta_{jl}) \text{ where} \\ G &= \begin{cases} G_0 \left(\frac{\gamma_{0.7}}{\gamma_{0.7}+a\gamma_{\text{Hist}}}\right)^2 & \text{for} \quad \gamma_s < \gamma_c \\ \frac{E_{\text{ur}}}{2(1+\nu_{\text{ur}})} & \text{for} \quad \gamma_s \geq \gamma_c \end{cases} \end{aligned}$$

2. Yield functions:

$$\begin{aligned} f^s &= \frac{3}{2}\frac{q}{E_i}\frac{\left(\frac{1-\sin\varphi_m}{\sin\varphi_m}\right)}{\left(\frac{1-\sin\varphi_m}{\sin\varphi_m}\right)-R_f\left(\frac{1-\sin\varphi}{\sin\varphi}\right)} - \frac{3}{2}\frac{q}{E_{\text{ur}}} - \gamma_s^{ps} \\ f^c &= \frac{q^2}{(\chi\alpha)^2} - p^2 - p_p^2 \text{ where} \\ \sin^2\varphi_m &= \frac{9-\frac{I_1 I_2}{I_3}}{1-\frac{I_1 I_2}{I_3}} \end{aligned}$$

3. Plastic potentials:

$$\begin{aligned} g^s &= q - (p + c\cot\varphi)\frac{6\sin\psi_m}{3-\sin\psi_m} \\ g^c &= \frac{q^2}{(\chi\alpha)^2} - p^2 - p_p^2 \text{ where} \\ \tilde{\chi} &= \chi(\theta_{\sigma_{Trial}}) \end{aligned}$$

4. Mobilized dilatancy (modified Rowe):

$$\begin{aligned} \sin\psi_m &= \begin{cases} \frac{\sin\varphi_m - \sin\varphi_{cs}}{1-\sin\varphi_m\sin\varphi_{cs}} & \text{for} \quad \sin\varphi_m - \sin\varphi_{cs} \geq 0 \\ \frac{1}{10}(Me^{\frac{1}{15}\ln(p_{cs}/p)} - \eta) & \text{for} \quad \sin\varphi_m - \sin\varphi_{cs} < 0 \end{cases} \\ \sin\varphi_{cs} &= \frac{\sin\varphi - \sin\psi}{1-\sin\varphi\sin\psi} \text{ and } \frac{p_{cs}}{p} = \frac{\eta\sin\varphi_{cs}(1-\sin\varphi_m)}{M\sin\varphi_m(1-\sin\varphi_{cs})} \end{aligned}$$

5. Hardening laws:

$$\begin{aligned} d\gamma_s^{ps} &= d\lambda^s h_{\gamma_s^{ps}} & \text{with } h_{\gamma_s^{ps}} &= \frac{3}{2} \\ dp_p &= d\lambda^c h_{p_p} & \text{with } h_{p_p} &= 2H\left(\frac{\sigma_3 + c\cot\varphi}{p^{\text{ref}} + c\cot\varphi}\right)^m p \\ H &= \frac{K_s K_c}{K_s - K_c} & \text{and } K_s &= \frac{E_{\text{ur}}^{\text{ref}}}{3(1-2\nu)} \end{aligned}$$

6. Stress dependent stiffness:

$$\begin{aligned} E_i &= E_i^{\text{ref}}\left(\frac{\sigma_3 + c\cot\varphi}{p^{\text{ref}} + c\cot\varphi}\right)^m \\ E_{\text{ur}} &= E_{\text{ur}}^{\text{ref}}\left(\frac{\sigma_3 + c\cot\varphi}{p^{\text{ref}} + c\cot\varphi}\right)^m \\ G_0 &= G_0^{\text{ref}}\left(\frac{\sigma_3 + c\cot\varphi}{p^{\text{ref}} + c\cot\varphi}\right)^m \end{aligned}$$

7. Lode Matsuoka-Nakai dependency:

$$\begin{aligned} \chi(\theta) &= \frac{\sqrt{3}\delta}{2\sqrt{\delta^2-\delta+1}}\frac{1}{\cos\vartheta} \text{ with} \\ \vartheta(\theta) &= \begin{cases} \frac{1}{6}\arccos(-1 + \frac{27\delta^2(1-\delta)^2}{2(\delta^2-\delta+1)}\sin^2(3\theta)) & \text{for} \quad \theta \leq 0 \\ \frac{\pi}{3} - \frac{1}{6}\arccos(-1 + \frac{27\delta^2(1-\delta)^2}{2(\delta^2-\delta+1)}\sin^2(3\theta)) & \text{for} \quad \theta > 0 \end{cases} \\ \delta &= \frac{3-\sin\varphi}{3+\sin\varphi} \end{aligned}$$

Symbole	**Definition**
D_{ijkl}	isotropic paraelasticity tensor

E_{ur}, G_{ur}	Unload reload stiffness and shear stiffness
G_0	Shear modulus
ν_{ur}	Poisson's ratio
γ_c	shear strain where tangent stiffness is reduced to the unloading-reloading stiffness
γ^{ps}	plastic deviatoric strain
p_p	pre-consolidation stress
K_c	the bulk stiffness in primary loading
K_s	the bulk stiffness in unloading-reloading
H	model parameter
χ	Lode Matsuoka-Nakai criterion
f^c	cap-type yield surface
f^s	cone-type yield function

Parameters for the HS and the HS-Small models

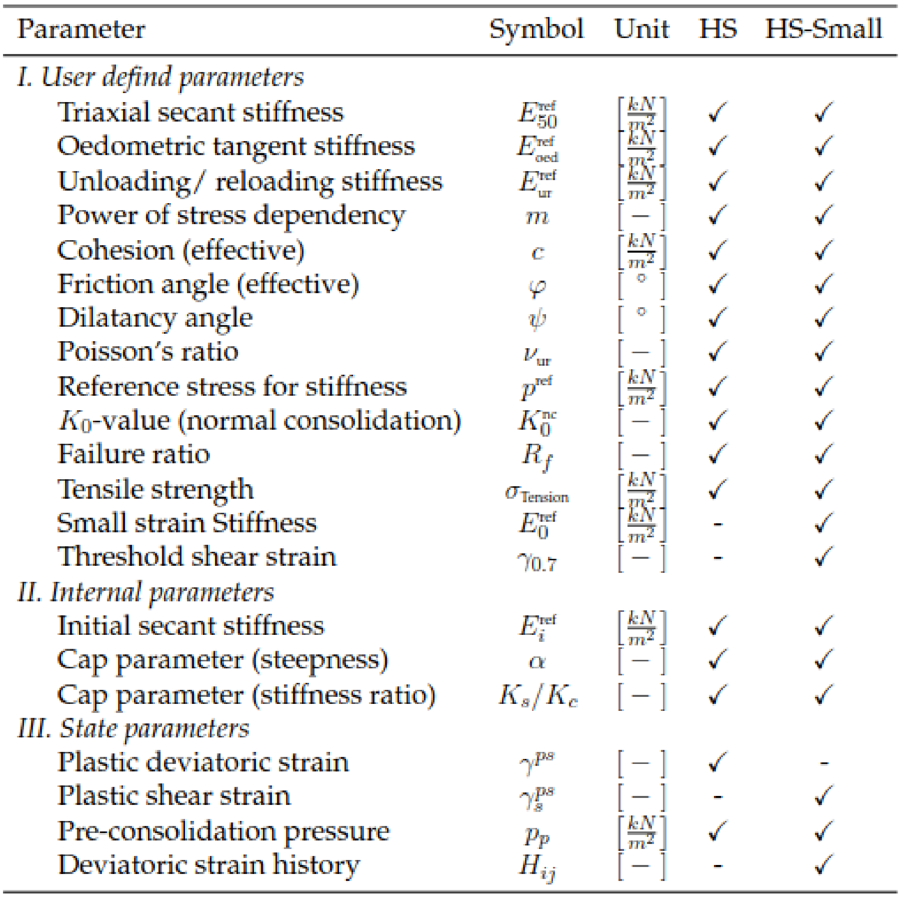

Parameter	Symbol	Unit	HS	HS-Small
I. User defind parameters				
Triaxial secant stiffness	E_{50}^{ref}	$\left[\frac{kN}{m^2}\right]$	✓	✓
Oedometric tangent stiffness	$E_{\text{oed}}^{\text{ref}}$	$\left[\frac{kN}{m^2}\right]$	✓	✓
Unloading/ reloading stiffness	$E_{\text{ur}}^{\text{ref}}$	$\left[\frac{kN}{m^2}\right]$	✓	✓
Power of stress dependency	m	$[-]$	✓	✓
Cohesion (effective)	c	$\left[\frac{kN}{m^2}\right]$	✓	✓
Friction angle (effective)	φ	$[^\circ]$	✓	✓
Dilatancy angle	ψ	$[^\circ]$	✓	✓
Poisson's ratio	ν_{ur}	$[-]$	✓	✓
Reference stress for stiffness	p^{ref}	$\left[\frac{kN}{m^2}\right]$	✓	✓
K_0-value (normal consolidation)	K_0^{nc}	$[-]$	✓	✓
Failure ratio	R_f	$[-]$	✓	✓
Tensile strength	σ_{Tension}	$\left[\frac{kN}{m^2}\right]$	✓	✓
Small strain Stiffness	E_0^{ref}	$\left[\frac{kN}{m^2}\right]$	-	✓
Threshold shear strain	$\gamma_{0.7}$	$[-]$	-	✓
II. Internal parameters				
Initial secant stiffness	E_i^{ref}	$\left[\frac{kN}{m^2}\right]$	✓	✓
Cap parameter (steepness)	α	$[-]$	✓	✓
Cap parameter (stiffness ratio)	K_s/K_c	$[-]$	✓	✓
III. State parameters				
Plastic deviatoric strain	γ^{ps}	$[-]$	✓	-
Plastic shear strain	γ_s^{ps}	$[-]$	-	✓
Pre-consolidation pressure	p_p	$\left[\frac{kN}{m^2}\right]$	✓	✓
Deviatoric strain history	H_{ij}	$[-]$	-	✓

Appendix B

Principal Component Analysis for predicting the TBM-induced surface settlement field: Application on the Paris Metro Line 16

This appendix studies the relationship between several soil parameters and the surface settlement trough of the first zone of the Paris Metro Line 16 to predict the surface settlement field. The Principal Component Analysis is used with the 2D Finite Element simulations to determine the correlation between the variables (layer thicknesses, tunnel position, TBM pressure, tunnel axis, and water level) and the settlement trough (maximum settlement and inflection point). The global analysis of the tunnel path indicates that the tunnel cover, the TBM pressure, the maximum settlement and the inflection are correlated. From these parameters, the surface settlement field is predicted with the coupling between the K-news and Artificial Neural Network. Then, a series of 2D FE analyses is performed along the tunnel alignment to study the effect of the soil layers modulus on the TBM-induced surface settlement.

Data generation with 2D Finite Element simulations

As shown in figure B.1, along the tunnel path, 14 cross-section profiles have been defined to construct the database with the 2D Finite Element (FE) simulations using the ZSoil calculation program. The cross-profiles differ in the soil stratificationl, the water level, the layer thicknesses, the tunnel axis position, and the TBM pressure. The convergence confinement method explained in chapters 2 and 3 is used to conduct the 2D simulation. The 2D fictitious pressures at the cross-sections are determined from the methodology explained in chapter 2 that takes into account the front pressure, the pressure along the shield and the injection pressure. It has been demonstrated in

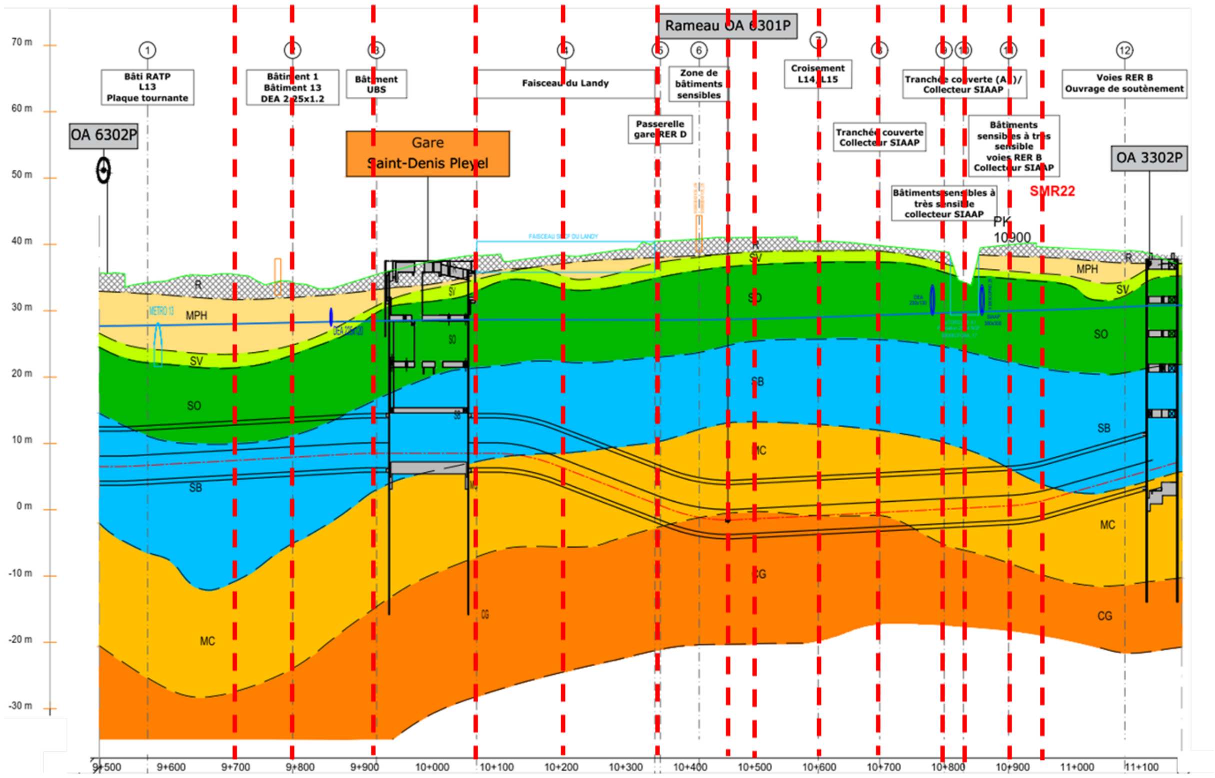

Figure B.1: Determination of the cross-section profile along the first zone of the Paris Metro Line 16

this thesis that when the tunnel front is stabilized, the extra front pressure beyond the stabilized one has a marginal effect on the settlement. Moreover, the minimum pressure to ensure the stability of the front is the water pressure and the front pressure slightly influences the 2D fictitious pressure. In this study, the water pressure is assumed along the shield. For all these reasons, the 2D fictitious pressure is governed by the injection pressure. Table B.1 presents the 2D fictitious pressure used for the FE simulation at all the cross-section profiles. These profiles are formed by stratified soil layer with the parameters following an uniform distribution as presented in Table B.2. In this table, C' and ϕ' represent the cohesion and the friction angle respectively. Em_{Mean} and Em_{std} are the mean and the standard deviation of the Menard modulus that comes from the pressuremeter test. The Hardening Soil with Small Strain Model is used to simulate the soil behavior. This constitutive model and the different correlations have been explained in this these:

- $E_{oed} = \frac{k*E_m}{\alpha}$ E_m is the Menard's modulus, k is a constant and E_{oed} the tangent stiffness for primary oedometer loading.

- $E_{50} = E_{oed}$ E_{50} is the secant stiffness in standard drained triaxial test.

- $E_{ur} = 2 * E_{50}$ E_{ur} is the unload-reload elastic stiffness.

Table B.1: Typical profiles used to construct the data set

Section name	PM	Tunnel cover [m]	Water level [NGF]	2D Pressure at the crown [kPa]
SMR22	10977	31.6	30.6	260
section 2	10900	33.5	30.6	279
section 3	10830	28.1	30.1	272
section 4	10800	32.9	30	270
section 5	10700	34.3	29.7	272
section 6	10600	35.5	29.4	274
section 7	10500	36.6	29.1	275
section 8	10450	36.7	29	285
section 9	10300	30.5	28.7	237
section 10	10200	25.9	28.7	205
section 11	10100	24	28.8	190
section 12	9900	20.5	28.6	184
section 13	9800	20.2	28.3	188
section 14	9700	22.1	28.1	192

Table B.2: Statistical distribution of the pressurimeter modulus

Layers	alpha	Em_{Mean} [MPa]	Em_{std} [MPa]	C' [kPa]	ϕ' ϕ'[°]
Fills (R)	0.5	7	2.5	0	28
Pholadomynes Marls (MPH)	0.5	24	10	5	34
Green clay(SV)	0.5	30	23	10	34
Saint-Ouen limestone (SO)	0.33	28	25	20	33
Beauchamp sand (SB)	0.5	87	85	10	33
Marls and sandstones (MC)	0.33	176	166	25	35

- $E_0 = 8 * E_{50}$ E_0 is the stiffness at very small strain.

Principal Component Analysis application

The Principal Component Analysis (PCA) is used in this study to analyze the correlation between model variables and the settlement trough. This PCA methodology has already been explained in chapter 4 and in this appendix. Thus the application of this method is carried out in this appendix.

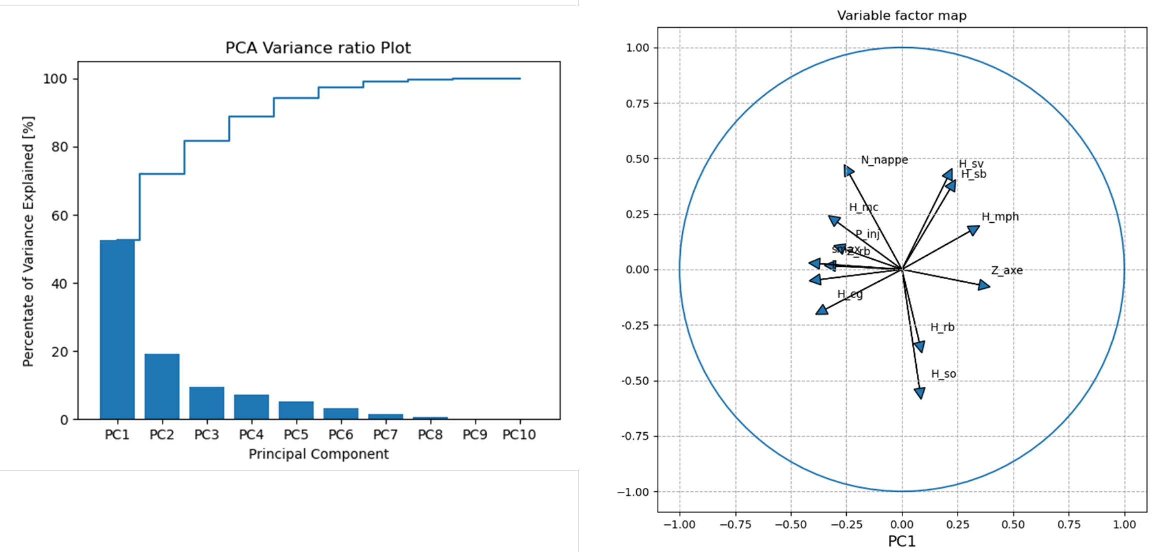

Figure B.2: The pareto diagram representing the variance of the principal components and the correlation circle formed by the two principal components of the global analysis of LINE 16

Global analysis of the Paris Metro Line 16 with the PCA and prediction of the settlement field

The database in this analysis is constituted by the FE simulations of the 14 cross-section profiles. The mean value of the soil stiffness is used to conduct the calculations. The input parameter of the database is formed by the soil layer thicknesses, the TBM pressure, the natural soil level, and the water level while the outputs of the model are the maximum settlement and the inflection point. Figure B.2 presents the 'variance explained' of the principal components and the correlation circle formed by the two first principal components. The 'variance explained' and its cumulative are presented on the Pareto diagram. According to this figure, the two principal components participate for more than 70% of the variance explained. According to Abdi and Williams (2010) these two components can be used to explain the linear relationship among the data. Two variables are correlated when they follow the same direction in the correlation circle. As presented in the correlation circle, the natural soil level (Z__rb), the maximum settlement (Smax) and the tunnel axis (Z__axe) are strongly correlated. Thus the maximum settlement (Smax), is correlated to (Z__rb - Z__axe) which is the tunnel cover. According to this figure, the TBM pressure (P__inj) and the tunnel axis (Z__axe) are also correlated. Concerning the inflection point (i), there is a slightly linear correlation between the maximum settlement (Smax) and the natural soil level (Z__rb). Based on these results, meta-models will be developed to predict the maximum settlement and the inflection point along the tunnel path to recover the 3D settlement profile.

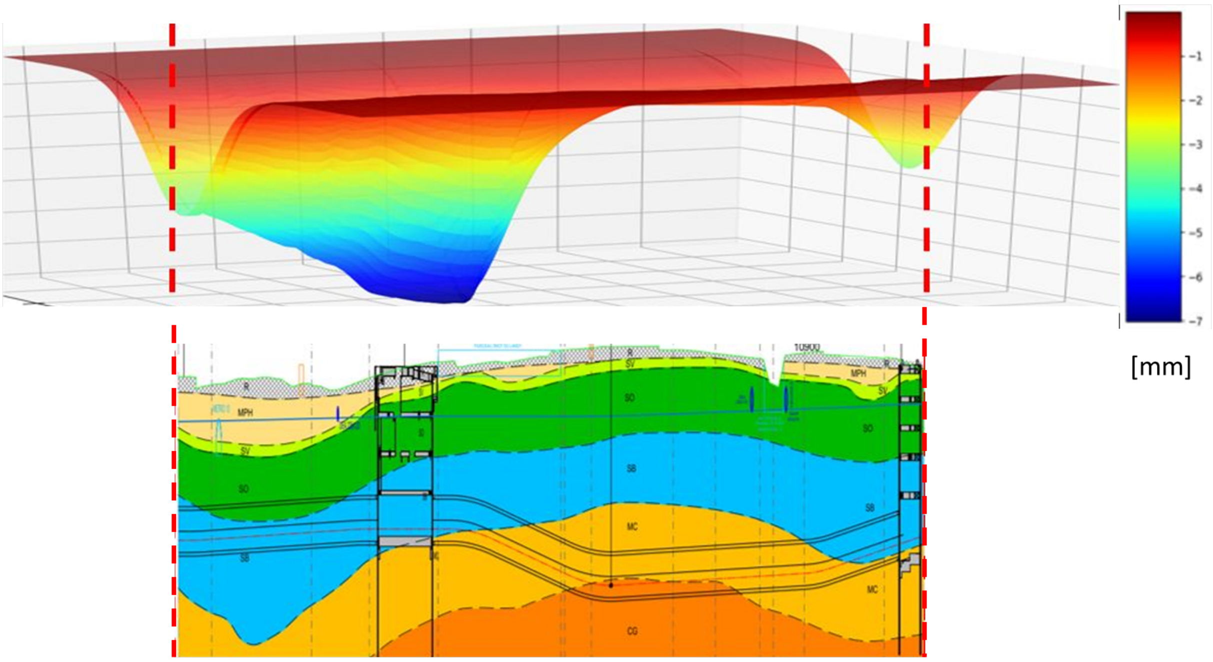

Figure B.3: TBM-induced surface settlement field predicted with the proposed meta model

In chapter 4, the methodology of constructing meta models with coupling the K-means and the ANN is studied. The tunnel axis (Z_axe), the TBM pressure (P_inj) and the natural soil level (Z_rb) are the input parameters while the maximum settlement (Smax) and the inflection point (i) formed the output parameters. The database is formed by the 14 cross-section profiles 2D FE simulations. 10 data points are used to train the model and the remaining 4 are used for testing. In this appendix, only the result of the surface settlement field is presented in figure B.3. According to this figure, the settlement amplitude decreases with the increase of the tunnel cover and varied from 1mm to 7mm.

PCA on the cross-section profiles

In this section, the PCA is conducted at each cross-section profile to determine the linear relation between the soil parameters and the settlement trough (Smax and i). The database is constituted by the 2D FE simulations with different soil stiffness that follows a uniform distribution as shown in table B.2. The stiffnesses are generated with the Monte Carlo simulation following the Latin hypercube sampling. Figure B.4 combines the results of the 'variance explained' of the principal components and the correlation circle of the 2 first principal components. According to this figure, the parameters that are correlated to the maximum settlement and the inflection point are summarized here below:

- SMR22 at PM 10977: The 2 principal components represent almost 50% of the 'variance explained'. The stiffness E50_SB (Beauchamp sand) showed a linear correlation with the maximum settlement whereas, the inflection point is slightly correlated to the stiffness E50_SO of the Saint Ouen limestone.

- PM 10900: The 2 principal components represent almost 60% of the 'variance explained'. The inflection point is slightly correlated to the stiffness E50_SO of the Saint Ouen limestone.
- PM 10830, PM 10800, PM 10700, PM 10600, PM 10500, PM 10450: The 2 principal components represent almost 60% of the 'variance explained'. No feature is strongly correlated to neither the maximum settlement nor the inflection point and these parameters are completely uncorrelated.
- PM 10300: The 2 principal components represent almost 55% of the 'variance explained'. E50_SO of the Saint Ouen limestone is correlated to the inflection point.
- PM 10200: The 2 principal components represent almost 60% of the 'variance explained'. E50_SO of the Saint Ouen limestone and E50_SB of the Beauchamp sand are correlated to the maximum settlement.
- PM 10100: The 2 principal components represent almost 60% of the 'variance explained'. There is a slight correlation between the maximum settlement and the inflection point.
- PM 9900: The 2 principal components represent almost 60% of the 'variance explained'. E50_SO of the Saint Ouen limestone is correlated to the maximum settlement and the inflection point.
- PM 9800: The 2 principal components represent almost 60% of the 'variance explained'. E50_SO of the Saint Ouen limestone is correlated to the maximum settlement.
- PM 9700: The 2 principal components represent almost 60% of the 'variance explained'. E50_SO of the Saint Ouen limestone the maximum settlement and the inflection point are correlated. The inflection point is oriented in the opposite direction compared to E50_SO and smax.

From the result of this study, it can be concluded that, when the soil parameters are constant along the tunnel path, the settlement trough is mostly influenced by the TBM pressure, and by the tunnel cover. When the uncertainties on the soil parameters are included, the influence of these latter on the settlement parameter (smax and i) depend on the tunnel cover. This influence can be identified when the tunnel cover reduces. In this study, at shallow depths, the stiffness of the Saint Ouen limestones most influence the settlement perhaps because of its thickness and its position close to the tunnel crown.

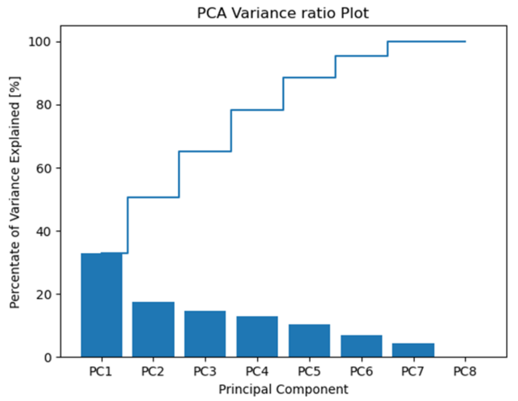
PCA Variance ratio Plot
Percentage of Variance Explained [%]
100
80
60
40
20
0
PC1
PC2
PC3
PC4
PC5
PC6
PC7
PC8
Principal Component

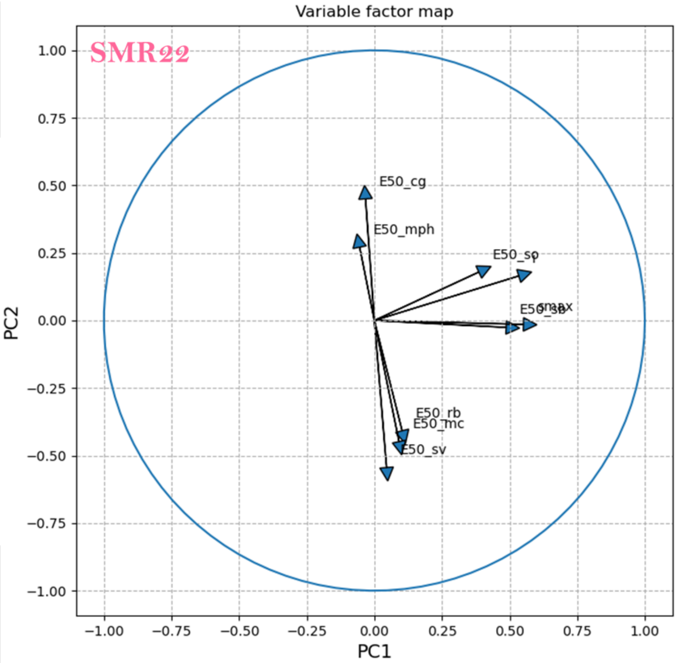
Variable factor map
SMR22
E50_cg
E50_mph
E50_sp
E50_sb
smax
E50_rb
E50_mc
E50_sv
PC2
PC1
1.00
0.75
0.50
0.25
0.00
−0.25
−0.50
−0.75
−1.00
−1.00
−0.75
−0.50
−0.25
0.00
0.25
0.50
0.75
1.00

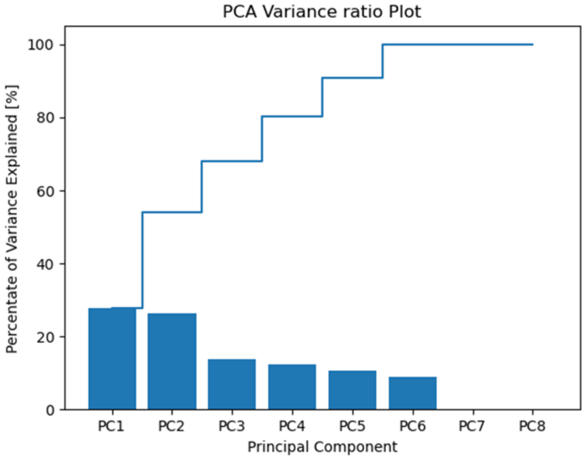
PCA Variance ratio Plot
Percentage of Variance Explained [%]
100
80
60
40
20
0
PC1
PC2
PC3
PC4
PC5
PC6
PC7
PC8
Principal Component

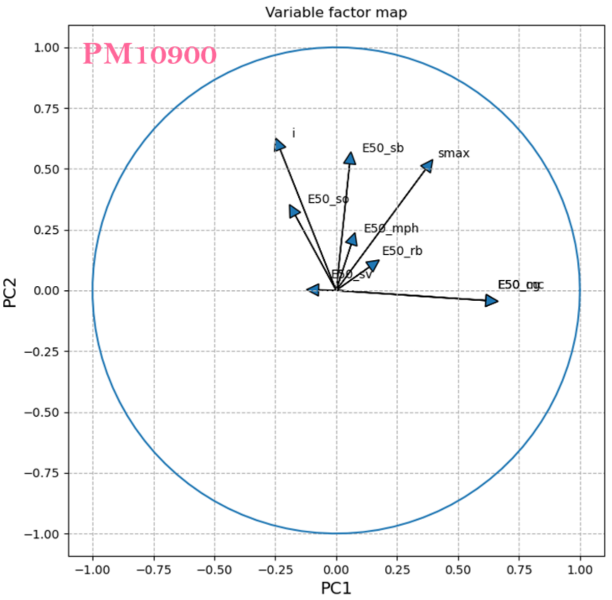
Variable factor map
PM10900
i
E50_sb
smax
E50_so
E50_mph
E50_rb
E50_sv
E50_cg
E50_mc
PC2
PC1
1.00
0.75
0.50
0.25
0.00
−0.25
−0.50
−0.75
−1.00
−1.00
−0.75
−0.50
−0.25
0.00
0.25
0.50
0.75
1.00

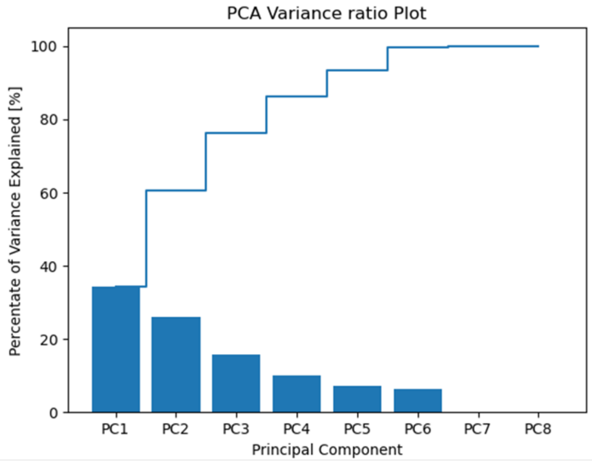
PCA Variance ratio Plot
Percentage of Variance Explained [%]
100
80
60
40
20
0
PC1
PC2
PC3
PC4
PC5
PC6
PC7
PC8
Principal Component

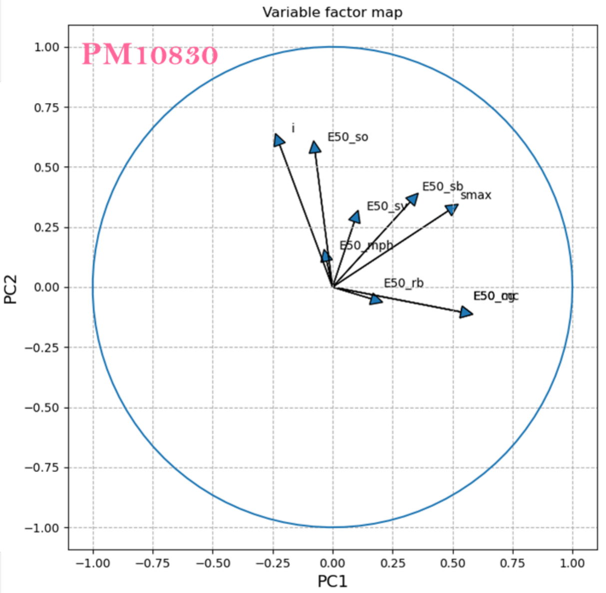
Variable factor map
PM10830
i
E50_so
E50_sb
smax
E50_sv
E50_mph
E50_rb
E50_cg
E50_mc
PC2
PC1
1.00
0.75
0.50
0.25
0.00
−0.25
−0.50
−0.75
−1.00
−1.00
−0.75
−0.50
−0.25
0.00
0.25
0.50
0.75
1.00

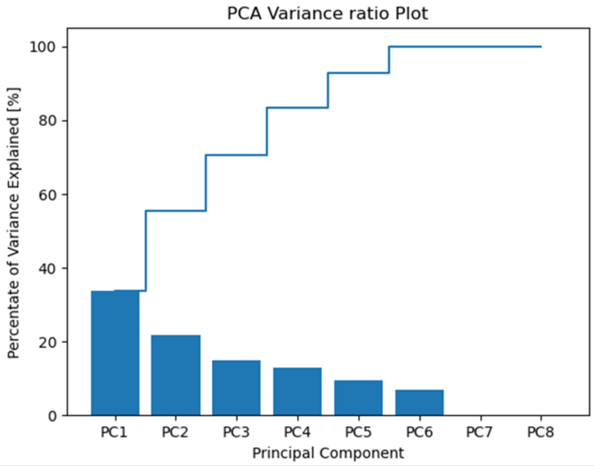
PCA Variance ratio Plot
Percentate of Variance Explained [%]
0
20
40
60
80
100
PC1
PC2
PC3
PC4
PC5
PC6
PC7
PC8
Principal Component

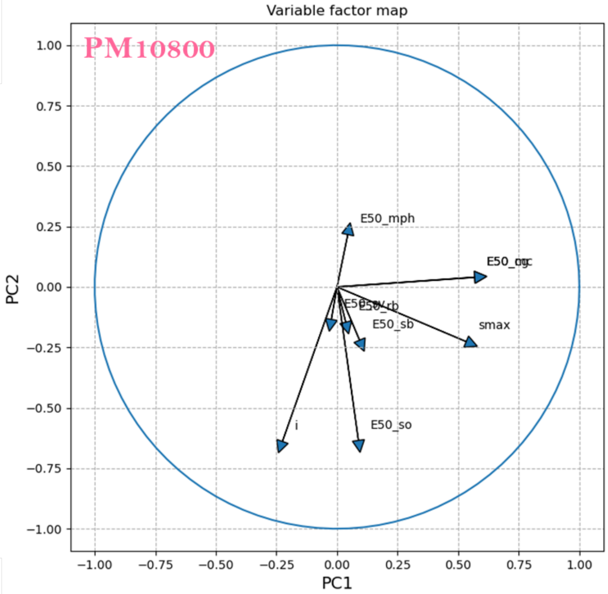
Variable factor map
PM10800
E50_mph
E50_ocg
E50_sv
E50_rb
E50_sb
smax
i
E50_so
PC1
PC2
−1.00
−0.75
−0.50
−0.25
0.00
0.25
0.50
0.75
1.00

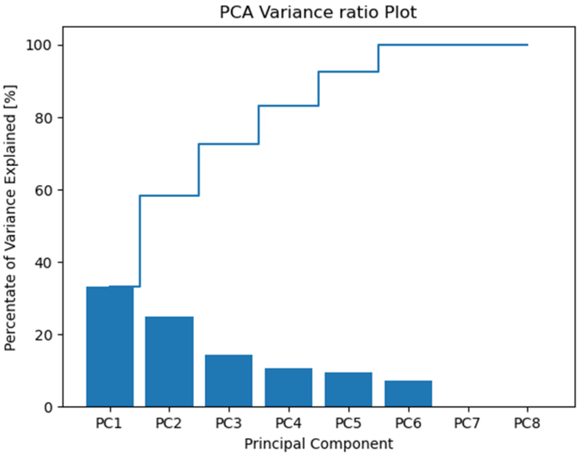
PCA Variance ratio Plot
Percentate of Variance Explained [%]
0
20
40
60
80
100
PC1
PC2
PC3
PC4
PC5
PC6
PC7
PC8
Principal Component

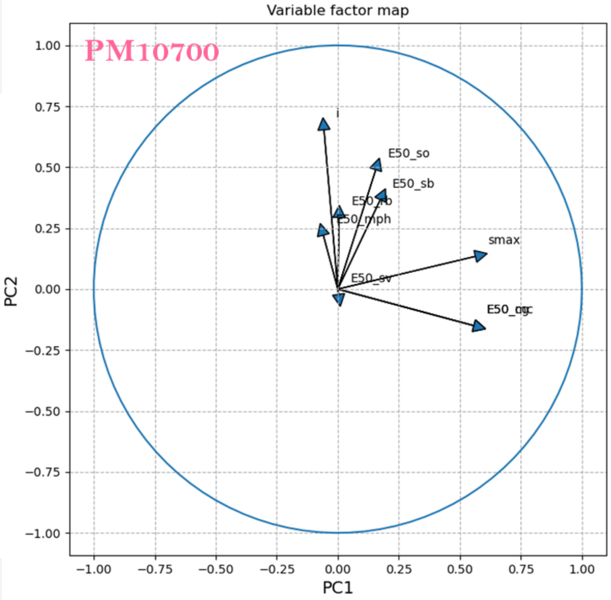
Variable factor map
PM10700
i
E50_so
E50_sb
E50_rb
E50_mph
smax
E50_sv
E50_ocg
PC1
PC2
−1.00
−0.75
−0.50
−0.25
0.00
0.25
0.50
0.75
1.00

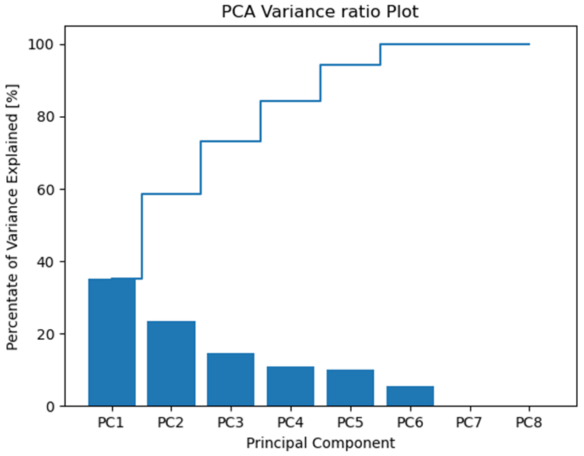
PCA Variance ratio Plot
Percentate of Variance Explained [%]
0
20
40
60
80
100
PC1
PC2
PC3
PC4
PC5
PC6
PC7
PC8
Principal Component

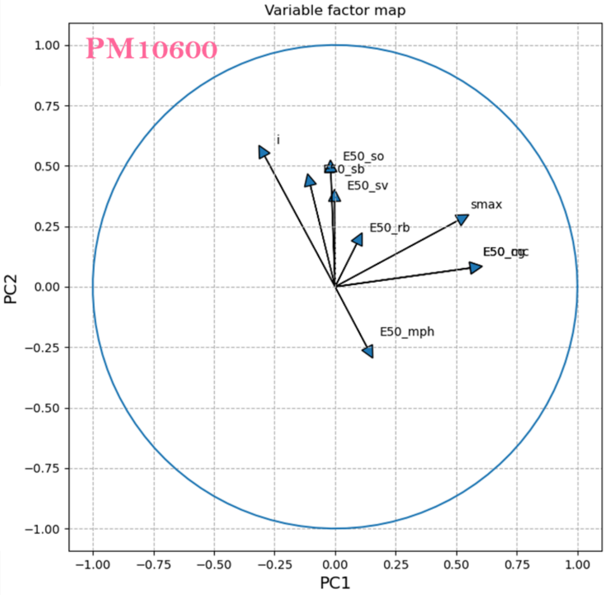
Variable factor map
PM10600
i
E50_so
E50_sb
E50_sv
smax
E50_rb
E50_ocg
E50_mph
PC1
PC2
−1.00
−0.75
−0.50
−0.25
0.00
0.25
0.50
0.75
1.00

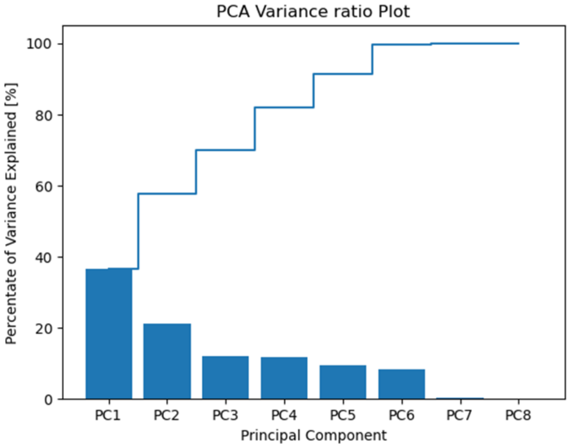
PCA Variance ratio Plot
Percentage of Variance Explained [%]
100
80
60
40
20
0
PC1
PC2
PC3
PC4
PC5
PC6
PC7
PC8
Principal Component

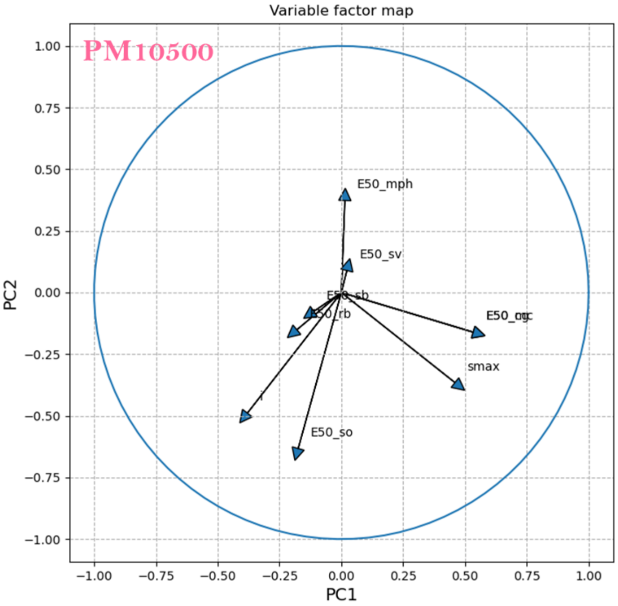
Variable factor map
PM10500
E50_mph
E50_sv
E50_sb
E50_rb
E50_oc
E50_og
smax
i
E50_so
PC2
PC1
1.00
0.75
0.50
0.25
0.00
−0.25
−0.50
−0.75
−1.00

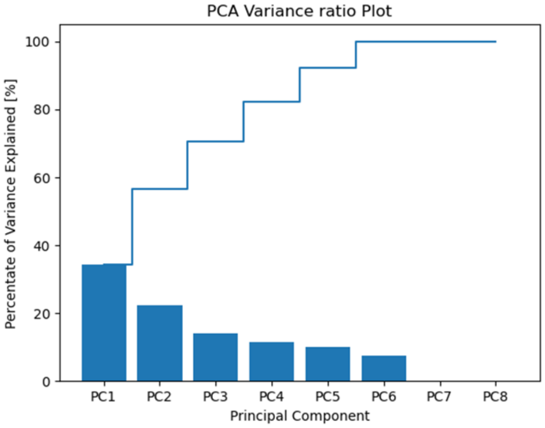
PCA Variance ratio Plot
Percentage of Variance Explained [%]
100
80
60
40
20
0
PC1
PC2
PC3
PC4
PC5
PC6
PC7
PC8
Principal Component

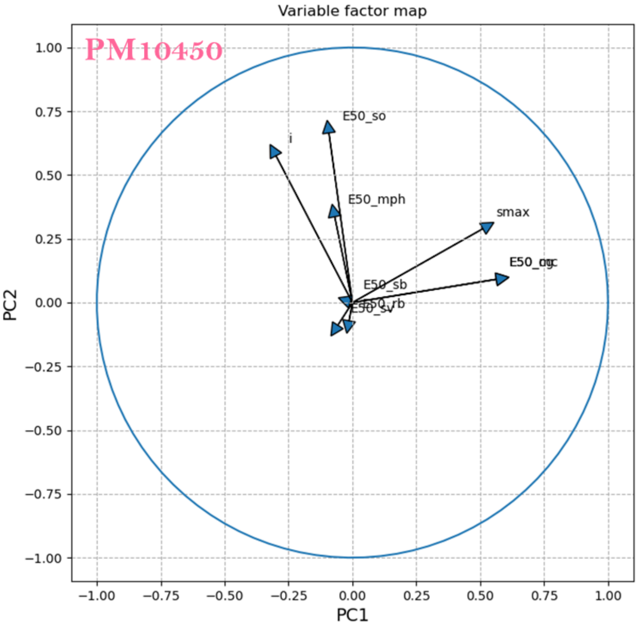
Variable factor map
PM10450
E50_so
i
E50_mph
smax
E50_oc
E50_og
E50_sb
E50_rb
E50_sv
PC2
PC1
1.00
0.75
0.50
0.25
0.00
−0.25
−0.50
−0.75
−1.00

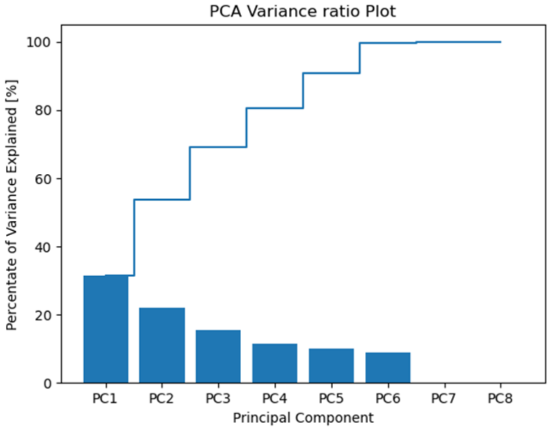
PCA Variance ratio Plot
Percentage of Variance Explained [%]
100
80
60
40
20
0
PC1
PC2
PC3
PC4
PC5
PC6
PC7
PC8
Principal Component

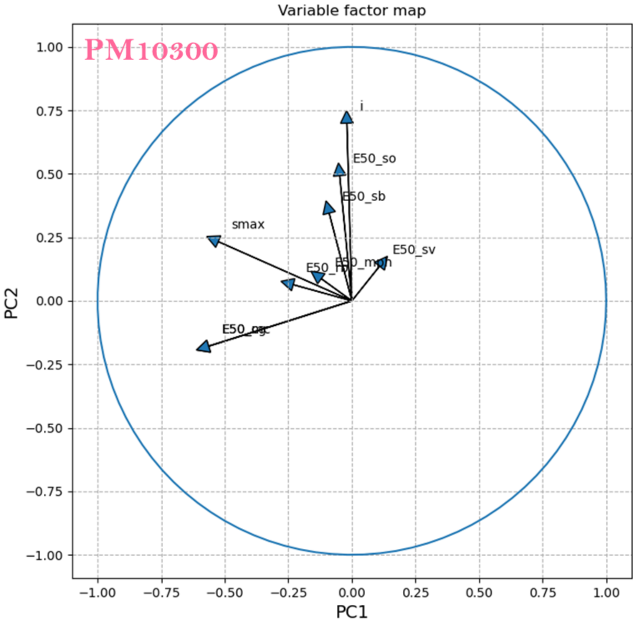
Variable factor map
PM10300
i
E50_so
E50_sb
smax
E50_sv
E50_rb
E50_mph
E50_og
E50_oc
PC2
PC1
1.00
0.75
0.50
0.25
0.00
−0.25
−0.50
−0.75
−1.00

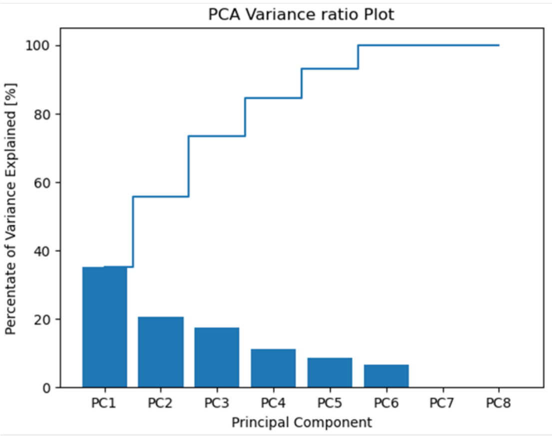
PCA Variance ratio Plot
Percentate of Variance Explained [%]
0
20
40
60
80
100
PC1
PC2
PC3
PC4
PC5
PC6
PC7
PC8
Principal Component

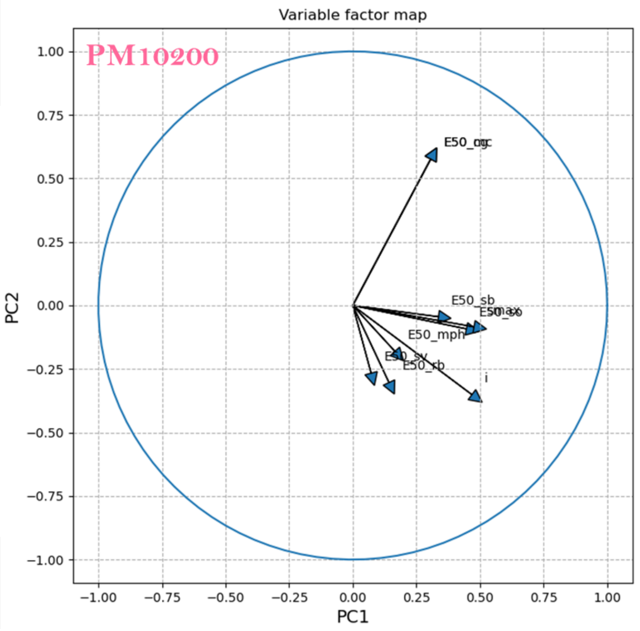
Variable factor map
PM10200
E50_σgc
E50_sb
smax
E50_so
E50_mph
E50_sv
E50_rb
i
PC2
PC1
1.00
0.75
0.50
0.25
0.00
−0.25
−0.50
−0.75
−1.00

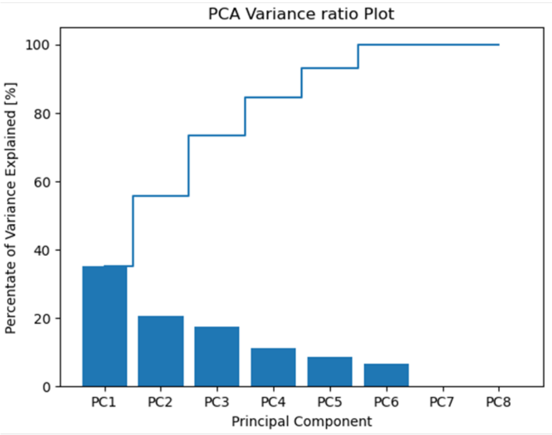
PCA Variance ratio Plot
Percentate of Variance Explained [%]
0
20
40
60
80
100
PC1
PC2
PC3
PC4
PC5
PC6
PC7
PC8
Principal Component

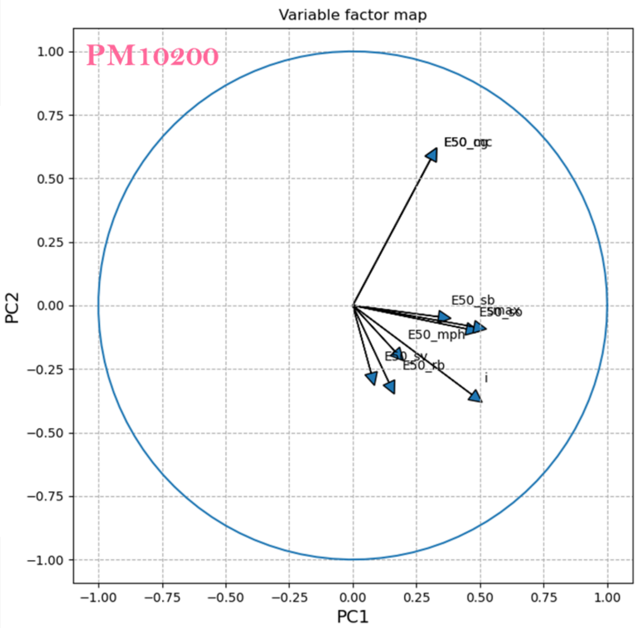
Variable factor map
PM10200
E50_σgc
E50_sb
smax
E50_so
E50_mph
E50_sv
E50_rb
i
PC2
PC1
1.00
0.75
0.50
0.25
0.00
−0.25
−0.50
−0.75
−1.00

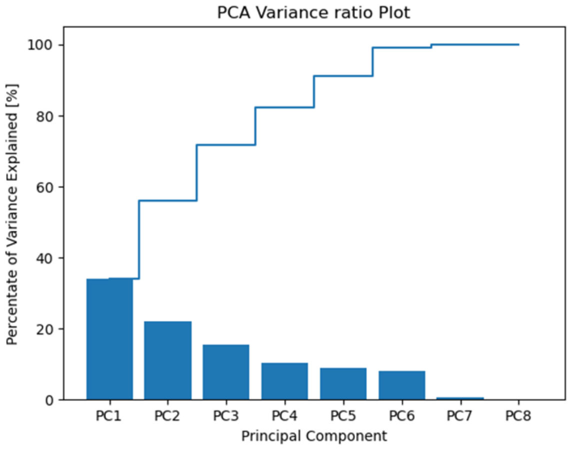
PCA Variance ratio Plot
Percentate of Variance Explained [%]
0
20
40
60
80
100
PC1
PC2
PC3
PC4
PC5
PC6
PC7
PC8
Principal Component

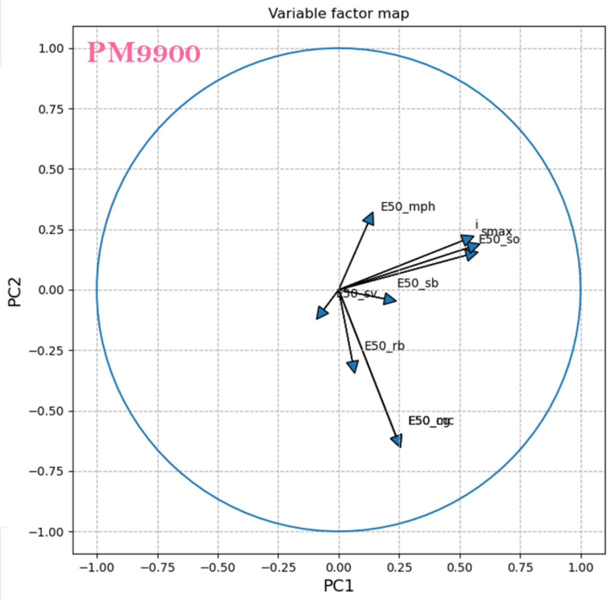
Variable factor map
PM9900
E50_mph
i
smax
E50_so
E50_sb
E50_sv
E50_rb
E50_σgc
PC2
PC1
1.00
0.75
0.50
0.25
0.00
−0.25
−0.50
−0.75
−1.00

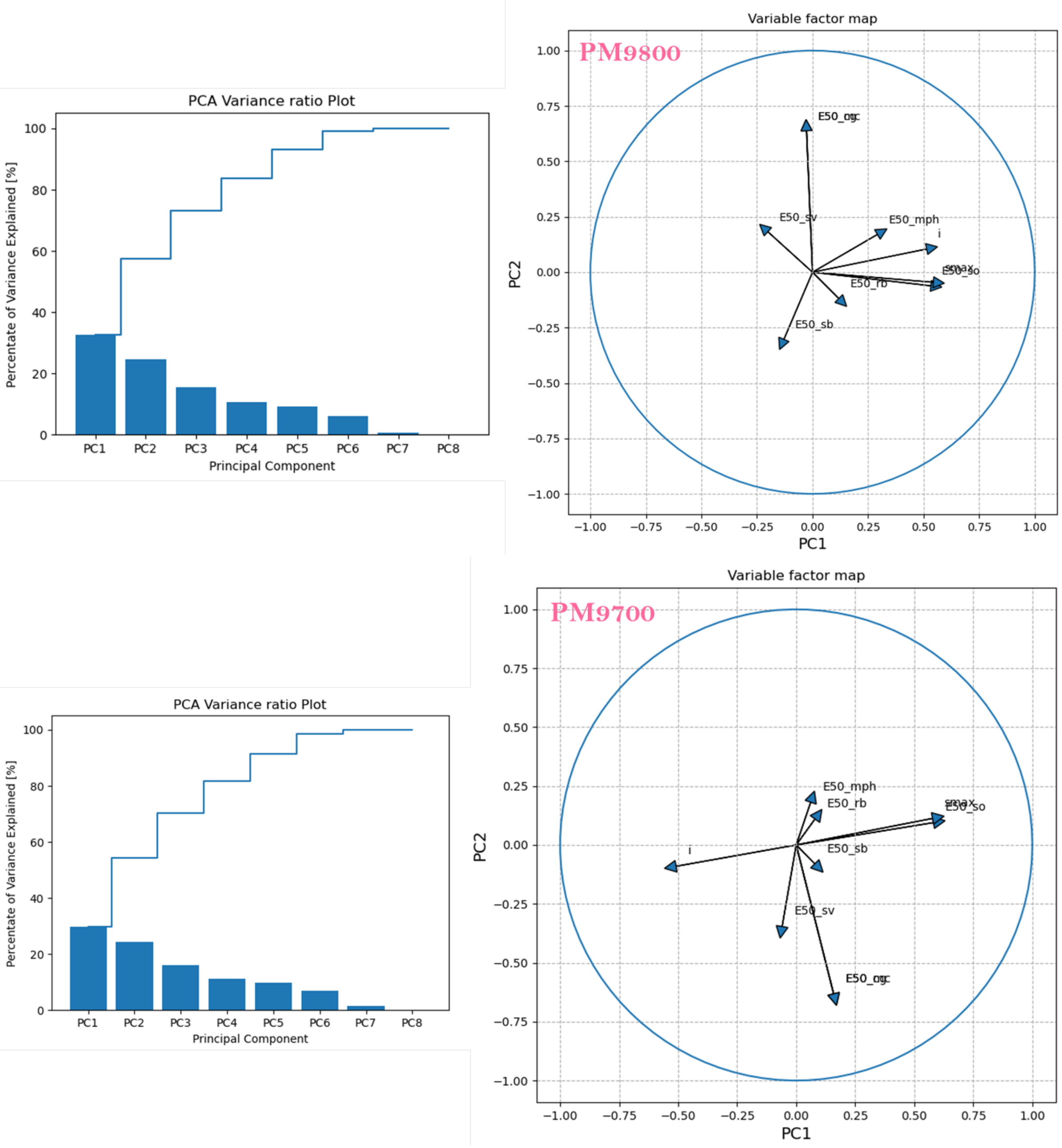

Figure B.4: The pareto diagram representing the variance of the principal components and the correlation circle formed by the two principal components at each cross-section profile